Multi-Region Boundary Element Analysis and Multi-Layered Green's Functions

Jiandong Xu

A thesis submitted for the degree of Doctor of Philosophy at the
University of Glasgow

Department of Civil Engineering
University of Glasgow
May 2007

To my family

Acknowledgements

My special thanks to my supervisor Dr Trevor G. Davies for his invaluable guidance during the study and thesis writing. He has inspired and informed my thinking, and my efforts would be diminished without his contribution to my work.

I would like to thank Cormack Professor S. J. Wheeler, Regius Professor N. Bicanic, Dr D. Philips and Professor A. Ervine for their help, encouragement and support.

I would also like to thank Mr. K. McColl, Mr. S.McLean and Ms. J. McCulloch for their computer facilities service and assistance; Department Administrator, Mrs E Davies, and the department secretaries, Ms B. Grant and Mrs. T. Bryden for their help in various ways.

I am grateful to Dr. E. Pan, Dr. B. S. Zhang, Dr. M. Karstunen and Dr. C. J. Pearce for valuable advice and suggestions.

Further thanks to my friends, Mrs. X. Y. Tao, Mr. Harold Krenn, Dr. B. Koelle, Dr. C. Davie and Dr. K. McGinty for their friendship and support.

I am grateful to the Vice-Chancellors and Principals of the Universities of the United Kingdom for their financial support through an ORS award, and the Faculty of Engineering, Glasgow University, for funding this work through a Faculty of Engineering Research Scholarship.

Finally, thanks to my wife Weina Chen and my daughters, Yuxuan Xu and Qingxuan Xu for their sacrifice, support and encouragement.

Abstract

This thesis aims to improve some aspects of the boundary element techniques in elastostatics and in particular its treatment of layered media. These include two areas of work:

1. The development of the partially discontinuous element method, that is, elements which are continuous on smooth boundaries but discontinuous at edges and corners, in order to address the well-known corner problem. This approach is relatively simple to implement whilst avoiding the computational disadvantages of discontinuous elements. We examine the effect of the offset distance between the free nodes and the element edges on accuracy and stability. This approach is implemented with automatic edge detection software, which incorporates partially discontinuous elements into BEM program without intervention by the user. This greatly reduces data preparation effort and makes the BEM an attractive option in practice.
2. In order to preserve the boundary-only discretization advantages of BEM, three–dimensional Green's functions in multi-layered systems are explored. These are computed using the cylindrical system of vector functions and the propagator matrix method. Numerical integration of these functions is problematic but a singularity extraction method is used to them accurately in the vicinity of the singularity. In this process, the Green's functions for the bi-material full space, are adopted instead of those for the homogeneous full space. The analytic work, which was necessary to derive the necessary transformed functions in cylindrical vector space, is described in some detail. Numerical trials show that the current method is accurate and efficient, and superior to the previous approaches.

Notation

Some of the key variables used in this thesis are listed here. Where appropriate, some symbols may have more than one meaning.

$[A]$	Assembled solution matrix after considering boundary conditions
$[K]$	'Stiffness matrix' used in multi-region analysis
t_i	Tractions
u_i	Displacement vector
N_a	Interpolation (shape) function of α-th node
$\boldsymbol{n}$ (or n_i)	Outward normal of the surface
$J(\xi)$	Jacobian of coordinate transformation in two dimensional problems
$J(\xi, \eta)$	Jacobian of coordinate transformation in three dimensional problems
U_{ij}	Kelvin's solutions (displacement)
T_{ij}	Kelvin's solutions (traction)
E	Young's modulus
ν	Poisson's ratio
G	Shear modulus
λ	Lame's constant, also integration parameter
$\{c\}$	Constant vector of system equation
$\{x\}$	Unknown vector of system equation
P, Q	Source and field point, respectively (on boundary)
p, q	Source and field point, respectively (arbitrary point of the body)
σ_{ij}	Stress tensor
σ_{rr}	Radial stress
σ_{rz}	Shear stress
σ_{zz}	Axial stress
$\sigma_{\theta\theta}$	Hoop stress

ε_{ij}	Strain tensor
ε_{rr}	Radial strain
ε_{rz}	Shear strain
ε_{zz}	Axial strain
$\varepsilon_{\theta\theta}$	Hoop strain
ξ, η	Intrinsic coordinates of the element
ξ', η'	Intrinsic coordinates of the sub-element
Γ	Surface or boundary of the physical body
Ω	Physical domain
δ	Kronecker delta (substitution tensor)
r	Distance between arbitrary points
w_i	Weights in Gaussian quadrature
d (d_i)	Parameters that indicate position of node inside element
$\boldsymbol{i}_r$, $\boldsymbol{i}_\theta$, $\boldsymbol{i}_z$	Unit vectors in r, θ, z, respectively.
$\tilde{f}^m(\lambda)$	m-th order Hankel transform of $f(r)$
J_m	Bessel function of m-th order
λ_n	The nth zero of $J_m(\lambda r)$ normalized by the range r

The subscripts

ijk	Cartesian co-ordinate system
α	α – th node of shape function
comma(,)	Differentiation with respect to a coordinate following the comma

CONTENTS

Chapter 1

Introduction

1.1. An overview of BEM in Elastostatics

The boundary element method (BEM) has continued to develop at a fast pace and has been extended to include a very wide range of continuum mechanics in the past four decades, although its roots lie much earlier. The first rigorous investigation of the classical kinds of integral equation was published by Fredholm(1905), who used discretized integral equations in potential problems which formed the basis for the 'indirect' BEM.

During the early years, the literature had concentrated on questions of existence and uniqueness, by distinguished mathematicians such as Oseen(1927), Kellogg(1929), Muskhelishvili(1953), Mikhlin(1957) and Kupradze(1965).

The boundary element method has evolved along two closely linked, but distinct, branches: 'indirect' and 'direct'. In the indirect formulation, fictitious density functions or sources that have no physical meaning are used, from which physical quantities such as displacements and stresses can be easily calculated(Massonet, 1965, Benjumea & Sikarskie, 1972). This method is spectacularly efficient for some special problems(Banerjee & Driscoll, 1976). One kind of indirect method; the 'displacement discontinuity' method has been used in the rock mechanics context, where slip takes place along pre-defined planes of weakness(Crouch & Starfield, 1983), its density functions are 'fictitious' displacements.

In the direct formulation(the one described throughout this thesis), the integral equations are expressed in terms of the actual physical variables, such as tractions and displacements. The first paper to use the direct approach in elastostatics was published by Rizzo(1967). The extension to three dimensional problems was obtained by Cruse(1969, 1973, 1974). Borrowing ideas from the finite element field, such as the concept of higher-order elements, Lachat & Watson (1976) developed more sophisticated algorithms. Cruse & Wilson (1978) and Tan & Fenner (1978, 1979) used isoparametric quadratic elements, where both the geometry and variables are allowed to change quadratically over each element, and demonstrated the high resolution of stress obtained in three-dimensional problems. Due to their accuracy and popularity in practical problems, these elements are adopted throughout this thesis.

Evaluation of the singular integrals arising in these algorithms is an important issue and was studied by many workers, like Cruse (1974), Hartman (1983), Guiggiani & Gigante (1990), Huber, Lang & Kuhn (1993), Mi & Aliabadi (1996), amongst others.

Ever since its early period of development (from 1967 to 1972), the integral equation formulations have been extended to a wide range of physical problems: e.g. those of non-homogeneous problems containing inclusions (Rizzo & Shippy, 1968), elastodynamic problems (Cruse, 1968 and Cruse & Rizzo, 1968), elastoplasticity (Swedlow & Cruse, 1971), anisotropic materials (Cruse & Swedlow, 1971) and three-dimensional fracture mechanics (Cruse & Van Buren, 1971 and Cruse, 1972). As a result, the method has gained popularity and offers a credible practical alternative to finite element analysis.

1.2. BEM and FEM

In the field of solid mechanics, BEM offers many advantages, and admittedly some disadvantages, over its rivals (e.g., the finite element and finite difference methods).

In the early sixties, high speed digital computers and numerical techniques started to find their way into engineering applications. In particular, the FEM attracted a great deal of interest and demonstrated both its applicability and accuracy in a wide range of engineering problems.

In this approach, the entire physical body is divided into elements of finite size, and over each element, the response satisfies the differential governing equations. All these finite elements are assembled together. The result is an overall system of linear algebraic equations (with a sparsely populated and usually symmetric solution matrix). After the boundary conditions of the actual problem are imposed, a unique solution can be obtained.

The range and power of finite element methods, together with its relative ease to incorporate realistic boundary conditions, presents a formidable challenge to any contending technique. Its weak aspect is also obvious; a whole body discretization scheme leads to very large numbers of finite elements, especially in three-dimensional problems with distant boundaries, within each of which the solution variables do not all vary continuously.

An obvious alternative approach would be to attempt to integrate the differential equations analytically in some way before either proceeding to any discretization scheme or to introduce any approximations. The essence of the BEM is the transformation of the differential equations into equivalent sets of boundary integral ones, either by means of a reciprocal identity (Cruse, 1969) or, more generally, by weighted residual and ‘integration by parts’ techniques (Brebbia, 1978). Only values of the variable at the extremes of the range of integration (i.e. on the boundaries of the body) are involved in these equations. This, in turn, implies that any discretization scheme needed would subdivide only the bounding surface of a body, rather than whole region. As in the other numerical approaches, provided that the boundary conditions are satisfied, a system of linear algebraic equations emerges for which a unique solution can be obtained. The solution variables will then vary continuously throughout the region and all approximations of geometry, etc., will only occur on its outer boundaries.

The advantages and disadvantages of BEM, compared to its main rival, FEM, can be summarized as follows.

Data preparation effort

BEM reduces the dimensionality of the basic process; i.e. for two-dimensional problems the analysis generates a one-dimensional boundary integral equation and for three-dimensional problems only two-dimensional equations arise. In the absence of body forces, we need only specify the boundary geometry data of a region (in addition to all necessary boundary conditions, material properties, etc.). thus the time required for data preparation for a given problem is greatly reduced.

Accuracy and Error distribution

Errors due to discretization and numerical approximations arise only on, and adjacent to, the boundaries of the body. The errors can be very small if we adopt sophisticated numerical integration procedures, for example, by using curved boundary elements and continuously varying distributions of both geometry and variables over elements. Once the necessary boundary information has been derived, values of the solution variables can then be calculated at any subsequently selected interior points.

Furthermore, since no further approximation is imposed on the solution at interior points, stresses are accurate and fully continuous inside the domain. These features appear to be unique to BEM and make it very suitable for modelling problems of rapidly changing stresses such as at stress concentrations, contact and fracture mechanics and dynamics.

Computer time and storage

The solution matrix resulting from the simple boundary discretization is very much smaller than any scheme of whole body discretization, although it is unsymmetric and fully populated for a homogeneous region. When more than one region is involved, it is block banded.

The evaluation of each component of the matrices in BEM does involve much more arithmetic calculation than its finite element counterpart. This may offset part of computer time saved by the much reduced matrix reduction requirements. Nevertheless, as problems become bigger, the overall computer costs in terms of data generation and processing for BEM increase less dramatically than for FEM. Particularly in three-dimensional problems solved with similar precision, the advantage of BEM can be substantial.

Further, the use of fundamental solutions automatically satisfies admissible boundary conditions at infinity, obviating the necessity to curtail such domains artificially, whereas with the finite element method, infinite boundaries have to be approximated by a considerable number of distant elements.

Multi-region problem

Based on the fundamental solutions in infinite space, all boundary element methods are applicable to either completely linear systems or those for which the differential equations can be approximated as a summation of linear and non-linear operators. However, where a solid is composed of distinct zones of different materials (i.e., a piece-wise inhomogeneous material), a multi-region approach is necessary. Examples may be found in the work of Lachat &Watson (1975), Banerjee & Butterfield (1981), Kane et al. (1990) and Gao & Davies (2000).

For some bodies with high aspect ratios (i.e., those with high surface-to-volume ratios), such as moderately thick plates and shells, narrow thin strips, etc), the BEM performs poorly. In these difficult cases, the use of artificial subdivisions can improve the stability of the equation set and overcome some of these limitations.

However, the application of the multi-region BEM has also its own limitations. The so-called 'corners and edges problem' which not only exists in multi-region cases but also in single-region ones has received a great deal of attention. Here, the difficulty is that, at corners, while displacements are unique, tractions are multi-valued. Depending on the corner boundary conditions, the integral equations may need to be augmented by additional auxiliary equations (Chaudonneret, 1978; Gao & Davies, 2000a) to close the equation set. Less satisfactorily, one can 'round off' the corner (Jaswon & Symm, 1977), use multiple nodes (Riccardella, 1973) or discontinuous elements (Brebbia & Dominguez, 1992). Using these latter approaches, either resolution of the corner tractions is diminished or the equation set becomes ill conditioned. An important consideration is that in multiple region problems 'rounding off' of corners and edges is impossible, and auxiliary equations methods become imperative. The partially discontinuous element method (PDE method) offers an alternative approach which will be developed and discussed in detail in this thesis.

A special case which is often encountered in engineering practice is the multi-layered problem. The beauty and main advantage of the BEM may be lost when multi-region approach is employed, as it requires discretization of interfaces between the layers combined with suitable continuity conditions there. Computational costs may be very high when a large number of layers are encountered.

However, some alternative approaches have been proposed to preserve the BEM's advantages, in both elastostatics and elastodynamics area, by authors such as Banitez & Lu (1993, 1996), Pan & Yang (2001), Zeng & Liang (2002), etc. The main idea is to apply the BEM formulation to the layered system with the Green's functions (or fundamental solution) being those for the layered system rather than a homogeneous infinite domain. The derivation and accurate evaluation of these special Green's function is critical, and a major topic of this thesis.

1.3. Scope of this thesis

Two main issues in BEM technology still need to be resolved. The first is the development of partially discontinuous elements (PDE) and their implementation to solve the long-standing corners/edges problem. The second is to develop a new algorithm for computing the Green's functions in multi-layered elastic systems, which is critical for a new BE formulation preserving the main beauty of BEM, that is, boundary discretization only when it is used to analyse the multi-layered problems.

In Chapter 2, the basic formulation and solution process for the BEM are introduced. Some important numerical implementation issues are also presented, such as the evaluation of singular integrals, etc. The corners/edges problem and some techniques proposed thus far for its solution are discussed.

Chapter 3 presents the application of the PDE method to two- and three-dimensional problems. Some numerical examples of these two cases are examined to verify the current method. The offset between the auxiliary nodes and the element edges, which is the key parameter controlling numerical stability and accuracy, is also investigated.

Chapter 4 is on the application of PDE method to multi-region problems. It is recognized that one important aspect of work is to make discontinuous elements opaque: once the geometry is defined (using continuous elements) the discontinuous elements are generated automatically by edge detection software and (once the equations are solved) the multi-valued tractions at the corners/edges are computed automatically. The main features of this software, which are developed first for two- and three-dimensional single region problems and then extended to two- and three-dimensional multi-region problems, are presented in this chapter, followed by several benchmark examples to demonstrate the potential of the technique.

In Chapter 5, three-dimensional Green's functions in multi-layered half spaces due to internal point loads are derived based on the cylindrical system of vector functions and the propagator matrix method. The transformed domain Green's functions obtained in this chapter need to be inverse transformed in order to get the corresponding functions in the physical domain, which is discussed in Chapter 6. In this process, suitable numerical quadrature techniques are necessary. The singularity extraction method is used to predict these functions values accurately in the vicinity of the singularity, in which the Green's functions for homogeneous full space are used.

It is shown in Chapter 7 that although the singularity extraction method presented in chapter 6 can obtain highly accurate Green's functions at singularity points within each layer, it fails to deal with the singularity points at the interface between two distinct layers with different material properties. In this circumstance the Green's functions for the bi-material full space offer a better choice, for which Guzina & Pak (1999) have derived closed-form representation. The corresponding integral representation expressed in the cylindrical system of vector functions, which is needed in the singularity extraction method, is derived in this chapter. Numerical trials show that current method is accurate and efficient. Suitable integration intervals of the transform parameter λ, which plays an important role on convergence of the integrals, is also investigated.

In Chapter 8 the multi-region BEM and Green's functions approaches are compared for a benchmark example of a three-layered half space under surface loading. Finally, the conclusions of the study and some suggestions for further work are given in chapter 9.

Chapter 2

Elastostatic BEM analysis and the corners/edges problem

Introduction

In this chapter, the classic BEM "edge and corner problem" is revisited and a new approach to solve it is discussed. It is necessary to introduce the fundamental theory of the boundary element method for elastostatics based on the boundary integral equations and the related general numerical technique used to solve the equations. Special techniques need to be employed when the load point P is located in the same element as the field point Q, as kernels become singular when these two points are close to each other. The edge and corner issue arises at the edges and corners of a physical body. In some cases as BEM can not provide enough equations to solve all the unknowns. To tackle this problem several techniques of more or less effectiveness are currently employed. Generally they either degrade the numerical accuracy or are inelegant. In this thesis, an improvement is adopted which use partially discontinuous elements only at edges and corners. As will be seen in the next two chapters, the advantage of this method lies in that it exploits the advantage of elements of both types (continuous and discontinuous) while avoiding most of their problems. This is further combined with the innovative edge detection software developed by the author which renders the process opaque to the user.

2.1. Boundary Integral Equations for Elasticity

The fundamental solution for a unit force in an infinite medium (the Green's functions) plays a central role in BEM analysis. Thomson (Lord Kelvin) derived the fundamental solution of the Navier-Cauchy equations of equilibrium for an infinitely extended three-dimensional elastic solid. His results yield the Cartesian components of the displacement field $u_j(q)$ and tractions $t_j(q)$ with respect to a plane defined by the outward normal $n(q)$ at the so-called field point q, due to a unit point force system $e_i(p)$ acting at the source point p, in the form:

$$\begin{aligned} u_j(q) &= U_{ij}(q,p)e_i(p) \\ t_j(q) &= T_{ij}(q,p)e_i(p) \end{aligned} \tag{2.1}$$

where,

$$\begin{aligned} U_{ij}(q,p) &= \frac{A}{r}(B\delta_{ij} + r_{,i}r_{,j}) \\ T_{ij}(q,p) &= -\frac{2GA}{r^2}[C(n_i r_{,j} - n_j r_{,i}) + (3r_{,i}r_{,j} + C\delta_{ij})n_m r_{,m}] \end{aligned} \tag{2.2}$$

and,

$$\begin{aligned} A &= \frac{1}{16\pi G(1-\nu)} \\ B &= 3-4\nu \\ C &= 1-2\nu \\ r_i &= x_i(q) - x_i(p) \\ r^2 &= r_i r_i \\ \delta_{ij} &= 1 \qquad (if\ i=j) \\ \delta_{ij} &= 0 \qquad (if\ i \neq j) \end{aligned} \tag{2.3}$$

Note that in the above equation as well as all the following equations, the repeated suffixes imply summation on them over their full range of values. In 3D, the range of i = 1, 2, 3, whereas in 2D the range would be i = 1, 2.

It is important to distinguish carefully between terms such as r_i (defined above) and $r_{,i}$ (which means $\partial r/\partial x_i\,(q)$ here); the latter quantity is equivalent to r_i/r.

By integrating Kelvin's solution for a line source $e_k(p)$, where k=1 & 2 only, along the x_3 axis, we obtain the displacement and traction kernel for plane strain, namely:

$$\begin{aligned} U_{ij}(q,p) &= -2A[B\delta_{ij}\log_e(r) - r_{,i}r_{,j}] \\ T_{ij}(q,p) &= -\frac{4GA}{r^2}[C(n_i r_{,j} - n_j r_{,i}) + (2r_{,i}r_{,j} + C\delta_{ij})n_m r_{,m}] \end{aligned} \tag{2.4}$$

The boundary element method for elastostatics is based on the boundary integral equations which provide the formal solution to the governing equations of elasticity and which relate the displacements and tractions at the surface (boundary). The derivation of the boundary integral equations can be found in many works. Here, we follow Gao & Davies (2002), who write this equation for elastostatic problem as (without body forces)

$$c_{ij}(P)u_j(P) + \fint_{\Gamma} T_{ij}(Q,P)u_j(Q)d\Gamma(Q) = \int_{\Gamma} U_{ij}(Q,P)t_j(Q)d\Gamma(Q) \tag{2.5}$$

where u_j and t_j are displacements and tractions on the bounding surface Γ, which contains the source point P and field point Q; $c_{ij}(P)$ are constants whose values depend on the geometric conditions of the point P. If P is on a smooth boundary, then $c_{ij}(P) = \delta_{ij}/2$. The notation $\fint$ signifies that the singular integral is to be interpreted in the Cauchy principal value sense. That is to say, although the integrand is strongly singular at P, the integral is finite if the limits of integration straddle P. This happy result arises from the fact that the integrand is asymmetrical about P and so this improper integration is perfectly valid

2.2. Boundary Discretisation

In solving the elastic problems by BEM, the boundary of the body is discretized into N_e elements (and N nodes). The displacement and traction fields within an element can then be interpolated between the element nodal values of displacements and tractions through interpolation functions, using the equations:

$$\begin{aligned} u_j(\xi) &= \sum_{\alpha=1}^{M} N_\alpha(\xi)u_j^\alpha \\ t_j(\xi) &= \sum_{\alpha=1}^{M} N_\alpha(\xi)t_j^\alpha \end{aligned} \tag{2.6}$$

where α denotes the α-th node in the M-noded element. The interpolations $N_\alpha(\xi)$ are commonly referred to as 'shape functions'. The parameter ξ is the local (intrinsic) coordinates, defined by the curvi-linear axis system which is tangential everywhere over the element. By definition, the intrinsic coordinates for an element normally take values in the range ± 1. The shape functions N_α can be thought of as functions which map the global coordinates of the element into the intrinsic coordinate system (ξ). For many purposes, quadratic interpolation functions work very well and these may be defined using the so-called 'Serendipity' eight-noded element in the three-dimensional problems. In the intrinsic coordinate system, this element is square (see Fig.2.1) and has three nodes per side.

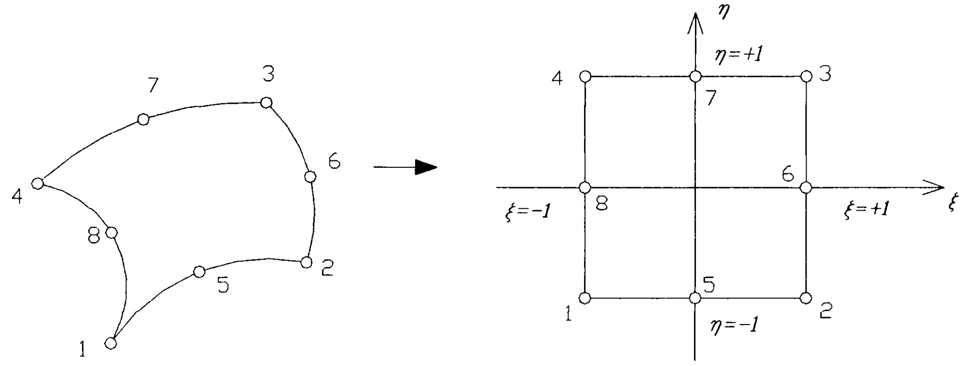

Fig. 2.1 The serendipity eight-noded element

Although the element is square in the intrinsic coordinate system, the quadratic mapping from the real element permits considerable latitude in the geometry of the latter. In general, the real element may be a curvilinear quadrilateral (as exemplified by Fig. 2.1). The four corner nodes are associated with the shape functions:

$$N_i(\xi,\eta)=\frac{1}{4}(1+\xi\xi_i)(1+\eta\eta_i)(-1+\xi\xi_i+\eta\eta_i) \tag{2.7}$$

where $N_i(\xi, \eta)$ is the shape function for a corner node with intrinsic coordinates ξ_i, η_i and $i = 1 - 4$. For example, if at node 1, then $\xi_1 = -1$ and $\eta_1 = -1$. The shape functions of the remaining mid-side nodes are:

$$\begin{aligned}
N_5(\xi,\eta)&=\frac{1}{2}(1-\xi^2)(1-\eta)\\
N_6(\xi,\eta)&=\frac{1}{2}(1+\xi)(1-\eta^2)\\
N_7(\xi,\eta)&=\frac{1}{2}(1-\xi^2)(1+\eta)\\
N_8(\xi,\eta)&=\frac{1}{2}(1-\xi)(1-\eta^2)
\end{aligned} \tag{2.8}$$

For one-dimensional quadratic interpolation, three nodes must be defined as depicted in Fig. 2.2.

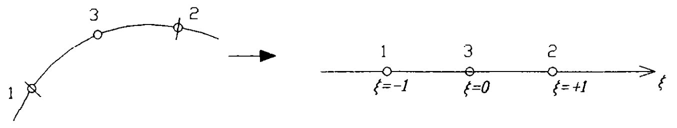

Fig. 2.2 The serendipity line element

The shape functions are:

$$
\begin{aligned}
N_1(\xi) &= \frac{1}{2}\xi(\xi-1) \\
N_2(\xi) &= \frac{1}{2}\xi(1+\xi) \\
N_3(\xi) &= 1-\xi^2
\end{aligned}
\tag{2.9}
$$

Once these nodal quantities are determined, displacements and tractions on the boundary are known everywhere. The boundary integral equation (2.5) can now be re-written in terms of these, yet undetermined, variables, as

$$
\begin{aligned}
c_{ij}(P)u_j(P) + \sum_{e=1}^{N_e}\left\{\sum_{\alpha=1}^{M} u_j^\alpha \oint_{\Gamma_e} T_{ij}(Q,P)N_\alpha(Q)d\Gamma(Q)\right\} \\
= \sum_{e=1}^{N_e}\left\{\sum_{\alpha=1}^{M} t_j^\alpha \int_{\Gamma_e} U_{ij}(Q,P)N_\alpha(Q)d\Gamma(Q)\right\}
\end{aligned}
\tag{2.10}
$$

Where Γ_e signifies the area of the e-th element, M is the number of element nodes in each element. u_j^α, t_j^α are nodal displacements and tractions. In order to produce a closed set of equations, we write this equation with source point P placed at each node in turn, i.e., we collocate at each of the nodes. It can be observed that the integrations of kernel function-shape function products are carried out over each of the elements.

The technique, employed to carry out these integrations, are critically important, in particular when the U_{ij} and T_{ij} kernels become singular. This will be discussed later. For the time being, we assume that the integrals have been computed and at each boundary node eqn. (2.10) can finally be transformed to the following form:

$$\sum_{m=1}^{N} T_{ij}^{nm} u_j^m = \sum_{m=1}^{N} U_{ij}^{nm} t_j^m \qquad (n = 1,2,\cdots\cdots N) \tag{2.11}$$

where u_j^m and t_j^m are the values of u_j and t_j at node Q_m, and

$$T_{ij}^{nm} = \sum_{e=1}^{N_e} \oint_{\Gamma_e} T_{ij}(Q,P_n) N(Q_m) d\Gamma(Q) + c_{ij}(P_n)\delta_{nm} \tag{2.12}$$

$$U_{ij}^{nm} = \sum_{e=1}^{N_e} \int_{\Gamma_e} U_{ij}(Q,P_n) N(Q_m) d\Gamma(Q) \tag{2.13}$$

in which $N(Q_m)$ is the shape function of the m-th node. Eqn. (2.11) can be written as its matrix equivalent:

$$[H]\{u\} = [G]\{t\} \tag{2.14}$$

On substituting the known boundary conditions into the discretised boundary integral equations (2.14), the matrices on either side of eqn. (2.14) can be rearranged such that all the known variables are on the right-hand side and all the unknown variables on the left-hand side which will result in the linear algebraic equations:

$$\begin{aligned} [A]\{x\} &= [B]\{y\} \\ &= \{c\} \end{aligned} \tag{2.15}$$

where $\{x\}$ contains all unknown variables (whether displacements or tractions), $\{y\}$ contains all known variables prescribed as boundary conditions. Eqn. (2.15) can be solved by standard techniques.

2.3 Numerical implementation

2.3.1. Gauss quadrature

The boundary integral equations presented in the previous section provide an exact description of an elastic continuum, and in principle an exact solution can be found for any well-posed set of boundary conditions. But for complex geometric features and boundary conditions, numerical solution techniques must be employed. These techniques involve; (a) interpolation, (b) numerical integration (quadrature) and, (c) matrix inversion. None of these introduces any fundamental approximations and hence solution accuracy is generally well preserved. The first of them (interpolation) has been described in the previous section. Matrix inversion may become problematic for large arrays but this question will not be explored here. Here we concentrate on numerical integration of T_{ij}^{nm} and U_{ij}^{nm}, using numerical quadrature methods.

By general consensus, we employ Gaussian quadrature rules (Stroud & Secrest, 1996). For simplicity, we use the example of integral of a function f(x) in one dimension, between arbitrary limits (a,b). To apply the Gauss quadrature rules, we need to map this interval into Gauss quadrature space, denoted by the symbol ξ, with due consideration for the scaling factor (Jacobian) that this introduces.

$$I = \int_a^b f(x)dx = \int_{-1}^{+1} f(x(\xi))J(x,\xi)d\xi \tag{2.16}$$

where $J(x, \xi)=dx/d\xi$. Thus, only in the case of linear mapping can the Jacobian be treated as a constant over the interval. Hence, after applying the Gauss rule we have

$$I \approx \sum_{i=1}^{n} w_i f(x(\xi_i))J(x,\xi_i) \tag{2.17}$$

where x_i and w_i are the i-th (of n) ordinates and weights, respectively. These ordinates and weights over the interval ±1 for various Gauss orders can be found in many publications (e.g., Gao & Davies 2001, Zienkiewicz, O. C. 1977).

Integration in two dimensions can be treated in much the same way, by making use of the so-called product rule.

$$I = \int_{a_2}^{b_2}\int_{a_1}^{b_1} f(x_1,x_2)dx_1dx_2 = \sum_{i_1=1}^{n_1}\sum_{i_2=1}^{n_2} w_{i1}w_{i2}f(x_1(\xi_1,\xi_2),x_2(\xi_1,\xi_2))J(x,\xi) \tag{2.18}$$

where

$$J(x,\xi) = \begin{vmatrix} \dfrac{\partial x_1}{\partial \xi_1} & \dfrac{\partial x_1}{\partial \xi_2} \\ \dfrac{\partial x_2}{\partial \xi_1} & \dfrac{\partial x_2}{\partial \xi_2} \end{vmatrix} \tag{2.19}$$

This two dimensional integration might also be employed to integrate a function over a surface in three dimensions if the axes x_1 and x_2 constitute a local (tangential) set. To make matters concrete, the integrals which we are concerned with are of the type:

$$I_i = \sum_{\alpha=1}^{M} t_j^{\alpha} \int_{-1}^{1}\int_{-1}^{1} U_{ij}(Q(\xi,\eta),P)N_{\alpha}(\xi,\eta)J(\xi,\eta)d\xi d\eta \tag{2.20}$$

where P is the collocation point and U_{ij} is the kernel function to be integrated over the element. We exclude here all singular integrals and hence there is nothing special in the choice of U_{ij} rather than T_{ij}. Since the surface is now divided into elements, the numerical integration is performed over each element using the local intrinsic coordinates ξ and η. In order to determine the components of the unit outward normal at any point on the boundary, as well as the Jacobian of the transformation from the global three-dimensional coordinate system to the intrinsic two-dimensional coordinate system of the surface patch, we define two vectors $\boldsymbol{r}_{\xi}$ and $\boldsymbol{r}_{\eta}$, which are tangential to the intrinsic coordinate ξ and η respectively (Fig. 2.1), as follows:

$$\begin{aligned} r_{\xi} &= \frac{\partial x_1(\xi,\eta)}{\partial \xi} i + \frac{\partial x_2(\xi,\eta)}{\partial \xi} j + \frac{\partial x_3(\xi,\eta)}{\partial \xi} k \\ r_{\eta} &= \frac{\partial x_1(\xi,\eta)}{\partial \eta} i + \frac{\partial x_2(\xi,\eta)}{\partial \eta} j + \frac{\partial x_3(\xi,\eta)}{\partial \eta} k \end{aligned} \tag{2.21}$$

where ***i***, ***j*** and ***k*** are the orthogonal unit basis vectors of the global coordinate axes.

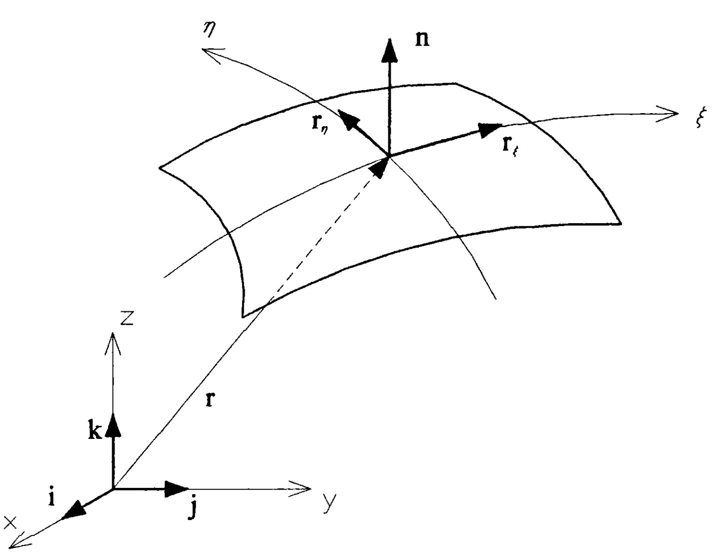

Fig. 2.1. Intrinsic coordinate system of a surface patch.

The normal vector, $\boldsymbol{n}^*$, is equal to the vector cross product of the vectors $\boldsymbol{r}_\xi$ and $\boldsymbol{r}_\eta$ (that is, $\boldsymbol{n}^* = \boldsymbol{r}_\xi \times \boldsymbol{r}_\eta$) and so this operation also yields the components, or 'direction cosines', (n_1, n_2, n_3) of the unit normal vector $\boldsymbol{n}$ ($= \boldsymbol{n} \,/\, |\, \boldsymbol{n}^* |$). These quantities are needed to calculate the kernel function T_{ij}^{nm} itself. In two dimensions, integration is carried out over a line element with intrinsic coordinate ξ, and again, the Jacobian is the magnitude of the normal vector $\boldsymbol{n}^*$, i.e., $J(\xi) = |\, \boldsymbol{n}^* |$, where:

$$n^* = \frac{\partial x_2}{\partial \xi} i - \frac{\partial x_1}{\partial \xi} j \tag{2.22}$$

The components of the unit normal vector $\boldsymbol{n}$ in this case are

$$\begin{aligned} n_1 &= \frac{\partial x_2}{\partial \xi} \Big/ J(\xi) \\ n_2 &= -\frac{\partial x_1}{\partial \xi} \Big/ J(\xi) \end{aligned} \tag{2.23}$$

2.3.2. Singular Integration

When the load point P is located in the same element as the field point Q, the U_{ij} and T_{ij} kernels become singular since they contain terms of order r^{-1} and r^{-2}, respectively. If we apply Gaussian quadrature directly in this case, it will lead to inaccurate results and special techniques must be employed, depending on the distance between P and Q.

Weakly singular integrals in three dimensions

An example of weakly singularity is when P and Q are in the same element (but $P \neq Q$). Since the functions to be integrated vary sharply in the vicinity of P, an element sub-division technique is employed (Lachat & Watson, 1976), as shown in Figure 2.2, in which elements containing the source node P are further subdivided into two triangular sub-elements (if P is located at a corner node) or three triangular sub-elements (if P is located at a mid-side node), with P located at the common vertex of these sub-elements.

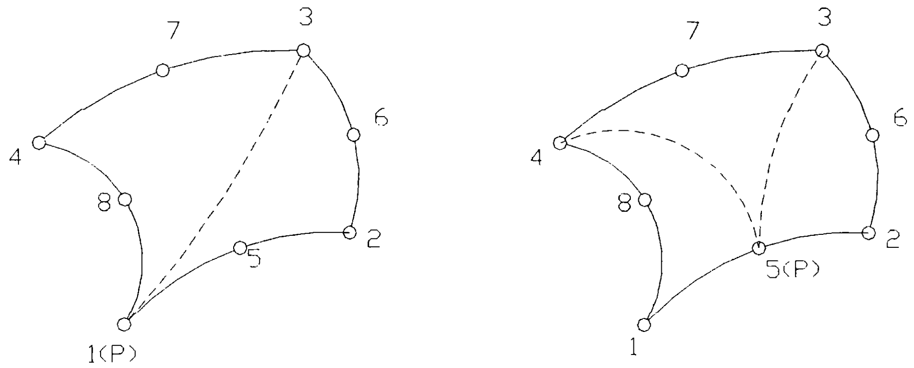

Fig. 2.2. Element sub-division for weakly singular integrals with P: (a) at a corner, and (b) at a mid-side node.

These sub-elements are in turn mapped into square intrinsic element space, as shown in Fig. 2.3.

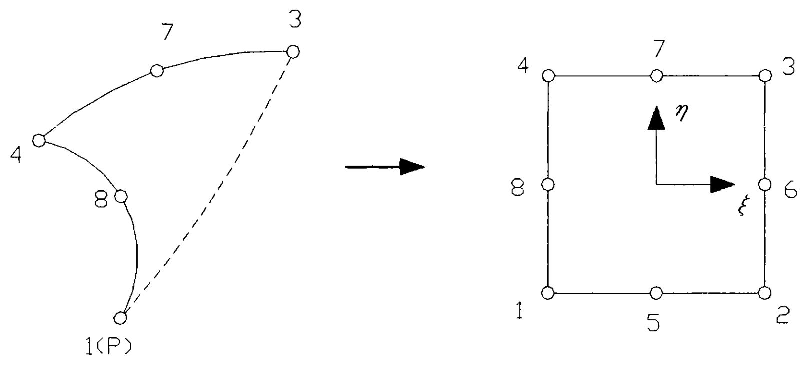

Fig. 2.3. Mapping of sub-element

Thus, nodes 1, 5, 2 of the intrinsic element are all coincident with P. Due to this degeneracy, it can be shown that the Jacobian of the transformation is of order r, where r is the distance from the vertex P (Gao & Davies, 2002). Consequently, the weak singularity is nullified and it can now be evaluated by normal Gauss quadrature.

Weakly Singular Integrals in Two Dimensions

In two-dimensional space, the displacement kernels U_{ij} are again weakly singular (of order $log_e r$), as shown in equation (2.5). This logarithmic singularity can be isolated and integrated directly using the Gauss integration rule for the logarithmically singular functions, which can be written as follows:

$$\int_0^1 f(\eta)\ln(\frac{1}{\eta})d\eta = \sum_{i=1}^{n} f(\eta_i)w_i \qquad (2.24)$$

where n is the total number of logarithmic Gaussian integration points, η_i is the Gaussian coordinate with an associated weighting function w_i, which can be found in other publications (Becker, 1992). It is noted the limits of integration is changed to become 0 to 1. Considering a three-noded element, a simple linear transformation can be used to accommodate the 0 to 1 integration limits as follows:

(a) When P is the first end node (node 1) of the element, $\eta = 0.5\ (1 + \xi)$.
(b) When P is the second end node (node 2) of the element, $\eta = 0.5\ (1 - \xi)$.
(c) When P is at mid-side node (node 3) of the element, the element is divided into two sub-elements centred on that node: $\eta = -\xi$ (for $-1 < \xi < 0$) and $\eta = \xi$ (for $0 < \xi < 1$).

At node 1, the distance r between an arbitrary point, defined by its intrinsic coordinate ξ, and the source may be obtained as follows:

$$r^2 = [x(\xi) - x_1]^2 + [y(\xi) - y_1]^2 \tag{2.25}$$

where x_1 and y_1 are the global coordinates of the source. Substituting the one-dimensional quadratic shape functions (from eqn. 2.9) into this equation, we obtain:

$$\begin{aligned} r^2 = [\ \frac{1}{2}(1+\xi)\ ]^2 \{\ &[-(2-\xi)x_1 + \xi x_2 + 2(1-\xi)x_3]^2 \\ &+ [-(2-\xi)y_1 + \xi y_2 + 2(1-\xi)y_3]^2\ \} \end{aligned} \tag{2.26}$$

Analogously, when P is located at node 2, we obtain:

$$\begin{aligned} r^2 = [\ \frac{1}{2}(1-\xi)\ ]^2 \{\ &[-(2+\xi)x_1 - \xi x_2 + 2(1+\xi)x_3]^2 \\ &+ [-(2+\xi)y_1 - \xi y_2 + 2(1+\xi)y_3]^2\ \} \end{aligned} \tag{2.27}$$

These two equations can be expressed in the unified form:

$$r^2 = \eta^2(\ f_1^2 + f_2^2\ ) \tag{2.28}$$

where

$$\eta = \frac{1}{2}(1 - \xi_i \xi) \tag{2.29}$$

in which ξ_i denotes the intrinsic coordinates of the i-th node. The above equation is equal to the linear mapping described in (a) and (b). The functions f_1 and f_2 are:

$$\begin{aligned} f_1 &= -(2+\xi_i\xi)x_1 - \xi_i\xi x_2 + 2(1+\xi_i\xi)x_3 \\ f_2 &= -(2+\xi_i\xi)y_1 - \xi_i\xi y_2 + 2(1+\xi_i\xi)y_3 \end{aligned} \tag{2.30}$$

For the case where P is located at node 3, we obtain:

$$r^2 = \xi^2 (g_1{}^2 + g_2{}^2) \tag{2.31}$$

where,

$$\begin{aligned} g_1 &= \frac{1}{2} [(\xi - 1)x_1 + (\xi + 1)x_2 - 2\xi x_3] \\ g_2 &= \frac{1}{2} [(\xi - 1)y_1 + (\xi + 1)y_2 - 2\xi y_3] \end{aligned} \tag{2.32}$$

Now, taking the logarithm of equation (2.29), we have:

$$\ln(\frac{1}{r}) = \ln(\frac{1}{\eta}) - \frac{1}{2}\ln(f_1^2 + f_2^2) \tag{2.33}$$

while a similar expression can be obtained from eqn. (2.31). In eqn. (2.33), only the first term needs to be integrated using a logarithmically weighted Gauss quadrature rule, whereas the second term is non-singular and can be integrated using the standard Gaussian quadrature.

To apply this method of integration to the mid-side node, the element must be divided into two sub-elements as described in (c). Using the mapping in (c), the Jacobian $J(\xi, \eta)$ is unity. For the end nodes, the integration can be done over the entire element, using the mapping as (2.29) and the Jacobian $J(\xi, \eta)$ now is two.

Strongly Singular Integrals

When P and Q are in the same element, in this case if the subdivision into triangular sub-elements is used, the product of the T_{ij} kernel (of order r^{-2}) and Jacobian (of order r) does not tend to a finite limit as P is approached. Therefore, this strongly singular integral can not be integrated by Gaussian quadrature. Furthermore, we also need to explicitly calculate the parameter $c_{ij}(P)$ in eqn. (2.12) because its contribution together with the strongly singular T_{ij} integrals yields the diagonal terms of the matrix T_{ij}^{nm} in equation (2.11). Accurate evaluation of these terms requires special treatment. Although direct evaluation is possible such as in the work by Theocris & Ioakimidis (1977) or Heise (1975) and by utilizing certain coordinate transformations (e.g., Guiggiani & Gigante,1990), an indirect method, which exploits the rigid body motion constraint, is far more popular. Three cases relating to: (a) finite regions, (b) infinite regions, and, (c) semi-infinite regions, are considered in turn below.

In a finite region, based on the fact that the BIE matrices must apply to any physical problem with a unique solution, any physical problem can be chosen as long as the solution does not depend on the geometry. In elastostatic problem the physical condition of rigid body motion (constant displacement of all the nodes in any direction) results in zero tractions everywhere. For example, if a finite region is subjected to a unit rigid body displacement in the *n*-th Cartesian direction, then at the *k*-th node, we generate $m = 2$ (in two-dimensions) or 3 (in three-dimensions) equations in the form:

$$\begin{aligned} u_j^k &= \delta_{jn} \qquad & j &= 1-m \\ t_j^k &= 0 \qquad & j &= 1-m \end{aligned} \tag{2.34}$$

Substituting these equations into equation (2.14), we obtain the matrix equations:

$$[H]\{I\}^m = \{0\} \tag{2.35}$$

where $\{I\}^{\mathrm{m}}$ is a set of m column vectors. In *n*-th column (for all nodes) unit displacements are prescribed in the *n*-th direction and zero displacements in all other directions. From (2.35) the coefficients of the singular sub-matrix for the *k*-th node (which appears on the leading diagonal of the matrix *H*) can be determined from the (negative) sum of the off-diagonal elements, thus:

$$[H]_{ij}^{kk} = (\delta_{kl} - 1)\sum_{l=1}^{N} [H]_{ij}^{kl} \tag{2.36}$$

where N is the number of nodes, the subscripts i & j range from 1 to m while the superscripts k and l refer to the nodes.

For infinite region problems, which can generally be understood as the complementary (or exterior) problems to their corresponding finite-region counterparts, their boundaries can in general be divided into a finite part Γ and an infinite part Γ_∞. Assuming rigid body displacement and substituting eqn. (2.34) into the boundary integral equation (2.1), we have:

$$c_{in}(\mathrm{P}) + \int_{\Gamma} T_{in}(Q,P)\,d\Gamma(Q) + \int_{\Gamma_\infty} T_{in}(Q,\mathrm{P})\,d\Gamma(Q) = 0 \tag{2.37}$$

The last integral on the left-hand side can be integrated analytically, thus:

$$\int_{\Gamma_\infty} T_{in}(Q,\mathrm{P})\,d\Gamma(Q) = -\delta_{in} \tag{2.38}$$

Consequently, the diagonal sub-matrix of the traction kernel can be calculated from the equation:

$$[H]_{ij}^{kk} = \delta_{ij} + (\delta_{kl} - 1)\sum_{l=1}^{N}[H]_{ij}^{kl} \tag{2.39}$$

Compared with finite region problems, the coefficients on the leading diagonal of the traction matrix are increased by unity.

For semi-infinite problems, a very similar approach can be adopted. The boundary of semi-infinite regions can be divided into a 'finite' part Γ, which includes the half-space surface, and an infinite part which includes the half-spherical boundary $\Gamma_{H\infty}$, as shown in Fig 2.4.

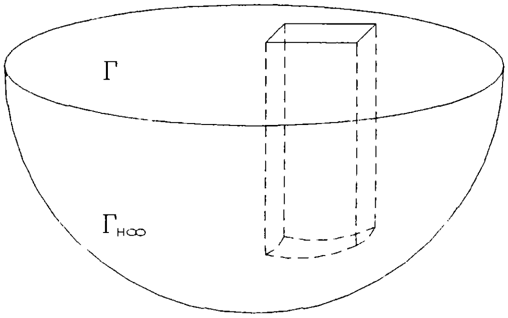

Fig. 2.4 Semi-infinite region boundaries.

Again, substituting equation (2.34) into the boundary integral equation (2.1), we obtain:

$$c_{in}(\mathrm{P}) + \int_{\Gamma} T_{in}(Q,P)d\Gamma(Q) + \int_{\Gamma_{H\infty}} T_{in}(Q,\mathrm{P})d\Gamma(Q) = 0 \tag{2.40}$$

The last integral on the left-hand side can be integrated (Gao & Davies, 1998) as follows:

$$\int_{\Gamma_\infty} T_{in}(Q,\mathrm{P})d\Gamma(Q) = -\frac{1}{2}\delta_{in} \tag{2.41}$$

$$\int_{\Gamma_\infty} \quad -\frac{1}{2}\delta_{in}$$

Consequently, the diagonal sub-matrix of the traction kernel can be calculated from the equation:

$$[H]_{ij}^{kk} = \frac{1}{2}\delta_{ij} + (\delta_{kl} - 1)\sum_{l=1}^{N}[H]_{ij}^{kl} \tag{2.42}$$

For all three cases, the use of the rigid body constraint obviates the necessity to integrate the strong singularity directly by rather complex methods, and as all the off-diagonal sub-matrices can be evaluated accurately as shown before, the use of the indirect method is justified for it involves only simple arithmetic.

2.3.2. System Equation Solution

The solution matrix [*A*] (equation 2.15) resulting after the application of the boundary conditions is not symmetric and is fully populated. The most commonly employed technique is Gaussian matrix reduction and back-substitution, usually with partial (or full) pivoting. In order to avoid numerical problems, associated with poor matrix conditioning, it is desirable that the magnitudes of the tractions and the displacements in the vector $\{x\}$ should be of the same order. This can be easily achieved by adopting dimensionless units for tractions and displacements. Thus, beginning with the system equations 2.15, we divide the tractions by a representative stress measure (usually, *E*, the Young's modulus of the elasticity) and the displacements by a representative length measure (usually the mean element length *L*). We obtain:

$$[H']\{u'\} = [G']\{t'\} \tag{2.43}$$

where $[G'] = E\,[G]$ and $[H] = L\,[H]$. Now the conditioning of the final system matrix [*A*] is much improved as the elements of the two coefficient matrices are of similar magnitude.

If numerical ill conditioning is suspected, this can be identified by resorting double-precision arithmetic or, better still, the well-known iterative improvement technique (Press et al, 1992). If we suppose on the *r*-th iteration, we obtain the solution $\{x\}^r$, the known error in the current solution $\{\delta c\}$ is:

$$\{\delta c\} = [A]\{x\}^r - \{c\} \tag{2.44}$$

From the above equation, we can obtain an estimate of the error in the solution $\{\delta x\}$ by solving the system equations:

$$[A]\{\delta x\} = \{\delta c\} \qquad (2.45)$$

So a new improved solution $\{x\}^{r+1}$ is obtained:

$$\{x\}^{r+1} = \{x\}^{r} - \{\delta x\} \qquad (2.46)$$

Usually, double-precision arithmetic is used in computing eqn. (2.44) to preserve accuracy. A matrix decomposition technique (such as the LU method) should be a better choice in this iterative technique as it offers re-solution of the iterative equations (2.45) in a fraction of the time. However, for large scale applications, where the number of degrees of freedom exceed several thousand, then equation solution time begins to dominate the solution process and, also, the accuracy of these direct methods may deteriorate. In such case, iterative methods such as the conjugate-gradient method and GMRES methods (Leung & Walker, 1997) offer the prospect of reduced computational cost and better accuracy.

In the above, we have sought to demonstrate the principal techniques which are employed to establish and solve the boundary integral equation solutions. Some related issues such as the evaluation of boundary and internal stresses are omitted in this thesis for brevity. Gao & Davies (2002) provide a detailed up-to-date account of these equations.

2.4. The corner/edge problem in BEM

Despite the elegance of the boundary element method, its application to solids that have sharp corners and edges introduces certain practical difficulties. For two-dimensional problems, if linear or higher order elements are adopted, some boundary nodes will be located at geometric corners. But it is well known that at corner nodes, the displacements are uniquely defined but the surface tractions are multi-valued, due to the different outward normal vectors. Since the boundary integral equations can yield only one equation per degree of freedom at each node, the number of equations is generally insufficient. Nevertheless, for some boundary conditions we can circumvent this difficulty easily by postponing assembly of the system equations (which are generated element-wise) until the boundary conditions are invoked.

In Fig. 2.5, all the six different possible boundary conditions are illustrated. In each of the cases (a), (b) and (c), on at least one side of the corner node all the tractions are prescribed. In eqn. (2.15), the $[A]$ matrix is assembled as a 'nodal' matrix of size $2N\times2N$. the $[B]$ matrix, however, can be assembled as an 'element' matrix of size $2N\times6N_e$, where N and N_e are the total numbers of nodes and elements, respectively. This effectively ensures that the displacements are continuous at the element junctions, but allows a corner node to be treated separately in each element, when tractions are considered. After moving all known variables to the right-hand side as shown in eqn. (2.15), then exactly $2N$ unknowns remain in the left-hand side.

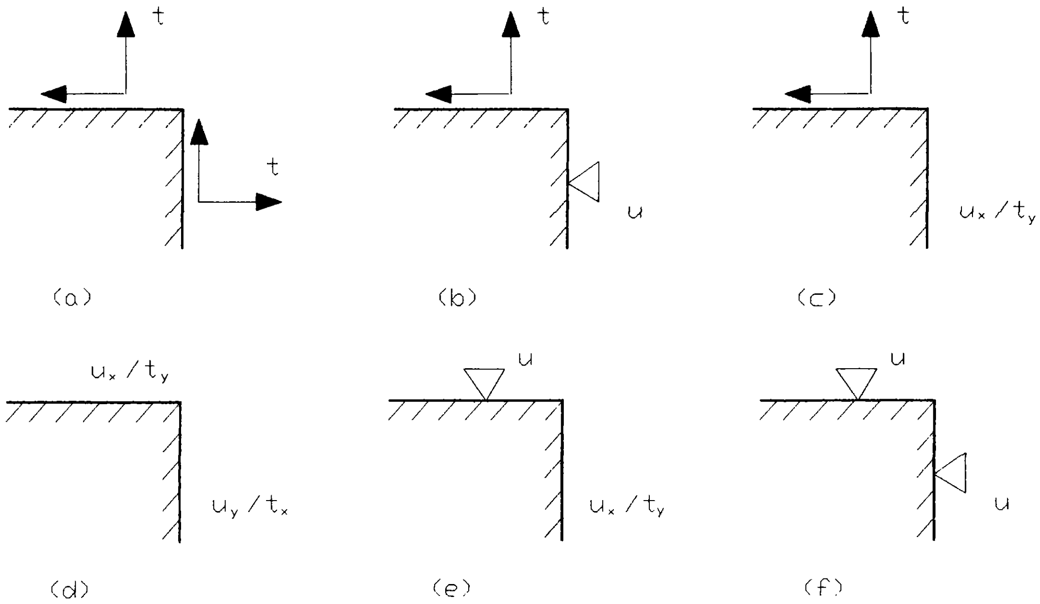

Fig. 2.5. Various boundary conditions at a corner.

But if at least one displacement is prescribed on both sides around a corner, as shown in case (d), (e) and (f) in Fig. 2.5, this technique fails since two unknown tractions are associated with the same degree of freedom at corner node. For example, in (d) the known boundary conditions are u_x and t_y in the one corner element and u_y and t_x in another one, therefore there are two unknown tractions (t_x and t_y) are associated with the same corner node.

This 'corner problem' has received a great deal of attention. Several techniques of varying effectiveness are currently employed.

One obvious way to tackle such problem is to 'round-off' corners and edges (Jaswon & Symm, 1977). Alternatively, one could simply adopt the 'unique traction' assumption (Cruse, 1974). Lachat & Watson (1976) suggested that the errors incurred by this treatment were mainly confined to the corner and were not significant at distant points. But Alarcon et al. (1979) pointed out that this could lead to significant errors in the evaluation of the solution at interior points.

Although it is not always necessary to obtain detailed results at or near a boundary discontinuity, these simple procedures can not be satisfactory since the results, even at some distance away from the rounded edges or corners, must be affected (Banerjee & Butterfield, 1981). On the other hand, in multi-zone problems it is evidently impossible to round off the interface corners and edges. In particular, for corners where more than two zones meet, the assumption of 'equal tractions' usually leads to unacceptable results.

In order to resolve the corner problem, Riccardella (1973) introduced the 'double-node' concept for two-dimensional (2D) problems, Brebbia & Dominguez (1977) later elaborated the use of this technique (which they term 'bi-nodes') for linear elements. However, if the separation between two corner nodes is too small, then serious numerical inaccuracies will be encountered.

Chaudonneret (1978), Zhang & Mukherjee (1991) introduce additional (coincident) nodes and develop auxiliary equations to determine the additional unknowns. Other works which fall into this category include: Yan & Lin (1994) derived two auxiliary relationships among the traction components, consistent with 2D linear elasticity. Gray & Luts (1990) obtained the auxiliary equations by differentiating the usual boundary integral equation.

One approach (Gao & Davies, 2000a) is derived from the stress tensor symmetry property and the equilibrium equations. The first auxiliary equation based on the stress equilibrium equation is:

$$\frac{\partial t_i}{\partial x_i} = 0 \tag{2.47}$$

where t_i , x_i are global tractions and coordinates.

Although this approach provides sufficient auxiliary equations in two dimensions, it may be insufficient in some three-dimensional problems. In such cases, the second auxiliary equation based on stress symmetry is derived:

$$n_i^b \, t_i^a = n_i^a \, t_i^b \tag{2.48}$$

For a corner, at the intersection of surface S_a and S_b, n_a and n_b are the unit outward normals on S_a and S_b, respectively.

Auxiliary equations based on Hooke's law implicitly assume isotropic elastic material properties. Extension to non-linear and dynamic problems may be difficult. Further, the assumption that the stress tensor is continuous at a corner (or edge) is not necessarily true (Zhang & Mukherjee, 1991). So the disadvantage of these approaches is obvious: they are based on restrictive assumptions or else they are impractical in complex problems.

As none of above methods is entirely satisfactory, a popular approach to treat the corner problems is the so-called non-conforming element method, in which discontinuous elements are used (Patterson & Sheikh, 1984; Manolis & Banerjee, 1986; Brebbia & Dominguez, 1992). In this method, the multiple nodes defined over different elements intersecting at a corner are moved inside their corresponding elements. In contrast to the FEM, topological inter-element continuity is not required. With discontinuous elements, the computational problems posed by sharp corners are circumvented, because discontinuous elements allow for multi-valued tractions. However, other disadvantages: high computational costs, numerical instability, inferior accuracy may be introduced.

Patterson & Elsebai (1982) used eight-noded quadrilateral non-conforming elements for three-dimensional potential problems. To deal with the singularities, the singular point is shifted to a point just "above" the element; thus eliminating the singularity. The offset distance is a function of the element dimensions. However, three unpleasant consequences arise:

(1) The method works only for moderate element aspect ratios and curvature.
(2) A trial and error process is needed to find the optimum offset distance.
(3) An ill-conditioned system of linear equations may be generated.

In the subsequent papers, the authors (1983, 1984) systematize their discussion of discontinuous elements based on the quadrilateral element by presenting families of elements with four, eight or twelve collocation nodes with four combinations of continuous and discontinuous sides. In this thesis, we develop these ideas further and introduce so-called partially discontinuous elements (PDEs): that is elements which are continuous on smooth boundaries but discontinuous at edges and corners. These elements exploit the advantages of elements of both types while avoiding most of their problems. In the next section, discontinuous elements of the quadratic type are developed with eight nodes in 3D and three nodes in 2D. Finally, the application of this type of element in multi-region analysis is explored.

Clearly discontinuous elements do not preserve strict inter-element geometric continuity. As noted earlier, this is not a significant problem and in any case C1 continuity is not preserved by existing elements.

In computer implementation, data preparation effort is often intolerably high if we need to input PDE data directly. Therefore, edge-detection software was developed to detect corners/edges and generate PDEs automatically based on the input information of the continuous elements. Once the equations are solved, the multi-valued tractions at the corners/edges are computed automatically. This approach offers a competitive alternative to other corners/edges treatment techniques. In the following chapter, we will discuss the application of PDEs (mainly of the quadratic type) in 2D and 3D problems: their performance will be illustrated through some numerical examples.

Chapter 3

Partially discontinuous elements for two and three-dimensional BEM analysis

This chapter is divided into two parts which describe the two-dimensional partially discontinuous elements (2D PDE) and three-dimensional partially discontinuous elements (3D PDE), respectively. The shape functions for 2D quadratic elements are obtained in terms of two parameters which signify the position of two free nodes inside the elements. The procedures to deal with singularities in these elements are discussed. Some numerical examples are examined to explore the performance of this element. The discussion of 3D PDE is carried out in parallel fashion. Four parameters (a more flexible 8-parameter PDE will be discussed in next chapter) are needed to determine the position of the free nodes. Some numerical examples are presented to show the effectiveness and accuracy of this method.

3.1. Partially discontinuous elements for two-dimensional BEM analysis

3.1.1. Interpolation functions for 2D Partially Discontinuous Elements

In the partially discontinuous element (PDE) method, which has been described in Chapter 2, the geometry of the problem is defined using straight or curved elements. At corners/edges, the multiple nodes defined over different elements intersecting at a corner may be moved inside their corresponding elements, to become 'free nodes'.

In the paper by Patterson & Sheikh (1984), the intrinsic coordinates of free nodes are given fixed values, i.e., the offset distance is assumed to be 1/3 (in the intrinsic coordinate system) from the edge of elements. However, in principle free nodes can be freely chosen anywhere over the element. Extending their work, generalized interpolation functions for PDE are derived here.

For many purposes, quadratic interpolation functions or shape functions work very well and these may be defined using the so-called "serendipity" three-noded element. In the intrinsic coordinate system, this element is straight line and has three nodes, as shown in Fig. 3.1. The shape functions are written as follows

$$
\begin{aligned}
N_1 &= c_0 + c_1\xi + c_2\xi^2 \\
N_2 &= c_3 + c_4\xi + c_5\xi^2 \\
N_3 &= c_6 + c_7\xi + c_8\xi^2
\end{aligned}
\tag{3.1}
$$

The nine constant parameters, c_0 - c_8, can be determined by the properties of shape functions.

$$
N_\alpha(\xi_\beta) = \delta_{\alpha\beta} \tag{3.2}
$$

where the subscript β denotes the value of the intrinsic coordinates at the β-th node.

$$
\begin{aligned}
\xi_1 &= -d_1 \\
\xi_2 &= +d_2 \\
\xi_3 &= 0
\end{aligned}
\tag{3.3}
$$

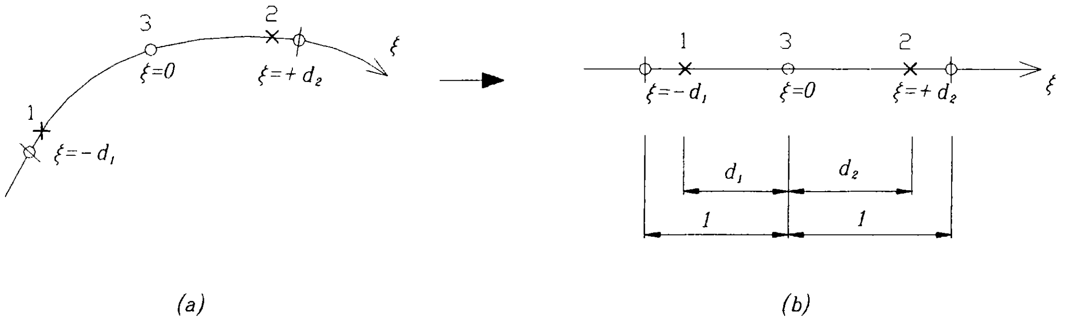

Fig 3.1. (a) Discontinuous quadratic element (b) Local (intrinsic) coordinate system

From eqn. (3.1) and (3.2), we can see that nine equations can be used to determine the nine constants. As a result, shape functions for 2D discontinuous elements are written as follows:

$$N_1 = \frac{\xi(\xi - d_2)}{d_1(d_1 + d_2)}$$
$$N_2 = \frac{\xi(\xi + d_1)}{d_2(d_1 + d_2)} \tag{3.3}$$
$$N_3 = \frac{-(\xi - d_2)(\xi + d_1)}{d_1 d_2}$$

where d_1 and d_2 are the parameters which indicate the positions of node 1 (start node) and node 2 (end node), respectively. If both of them are values other than unity, the shape functions describe discontinuous elements. If only one of them is not unity, the shape functions describe a PDE. If $d_1 = d_2 = 1$, eqn. (3.1) become the well-known forms of continuous elements, as shown in eqn. (2.9).

Fig. 3.2 shows a comparison between the shape functions for a discontinuous element ($d_1 = d_2 = 0.8$) and those for a continuous element.

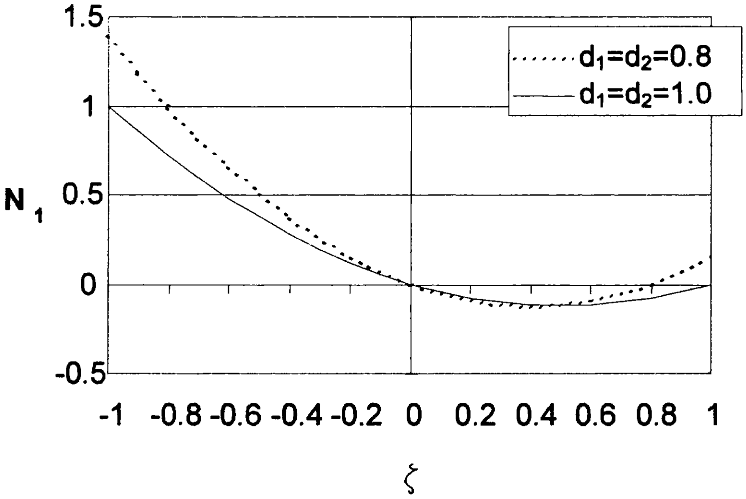

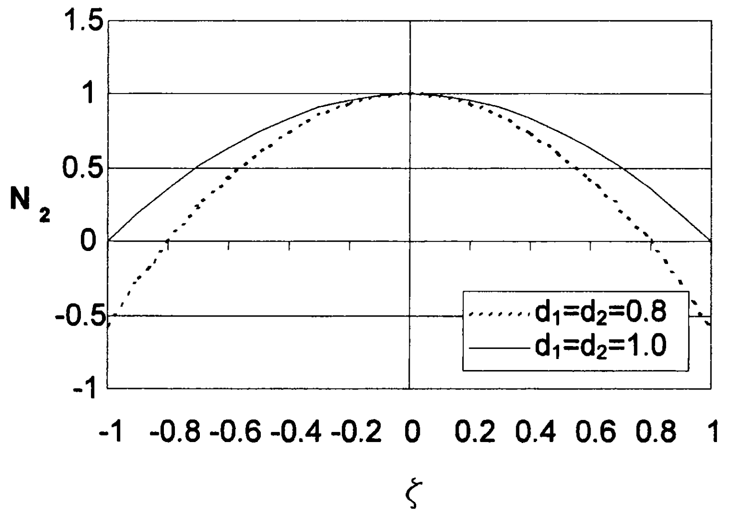

Fig 3.2. Quadratic interpolation: the comparison between the shape functions of continuous and discontinuous elements.

From Fig. 3.2, the difference between these two types of shape functions is obvious. For example, at the end point, the maximum value in the continuous element case is 1, but can be more than unity in the PDE case. It can also be a negative value in the mid node, as shown in the N_2, while in the continuous element, the minimum value is zero.

3.1.2 Boundary element equations in 2D

The discretized boundary integral equation for 2D elastostatics analysis can be written as:

$$\begin{aligned} c_{ij}(P)u_j(P)+\sum_{e=1}^{N_e}\Big(\int_{-1}^{+1}T_{ij}(Q,P)N_\alpha(\xi)J(\xi)d\xi\Big)u_j^\alpha \\ =\sum_{e=1}^{N_e}\Big(\int_{-1}^{+1}U_{ij}(Q,P)N_\alpha(\xi)J(\xi)d\xi\Big)t_j^\alpha \end{aligned} \tag{3.2}$$

To determine the unknown boundary displacements and tractions in terms of the prescribed values, we allow the point P to coincide sequentially with all the nodal points of the boundary used for defining the field variables. As a result, a closed set of simultaneous linear equations is generated, since the number of remaining unknowns (2×N tractions or displacements) is exactly the same as the number of equations. It may be observed that the integrals of the kernel function products are carried out over each element.

The numerical quadrature employed to carry out these integrations is critically important, and are discussed in some detail below. Two cases need to be considered:

Non-singular case

When the distance r between the source point P and the field point Q on the surface of element, i.e., $r = | Q - P |$, remains finite, the integrals in (3.2) can be evaluated by the application of standard Gauss-Legendre quadrature formula. For improved accuracy, an element could be subdivided into sub-elements whose number depends on the minimum distance $r_{\min}$ between P and the element, and on the order of the Gaussian quadrature formula used.

An adaptive integration scheme such as that employed by Gao & Davies (2001) in the conforming boundary element method can be developed. It can also be implemented in the partially discontinuous element method without much modification.

Singular case

When the source point P coincides with one of the collocation nodes of a boundary element, a singular case arises. The order of the singularity of the kernel integrals in 2D is as follows:

$$\begin{aligned} &U_{ij}(Q,P)N_\alpha(\xi) \sim O(\log_e r) \\ &T_{ij}(Q,P)N_\alpha(\xi) \sim O(1/r) \end{aligned} \tag{3.3}$$

when $r \to 0$.

The traction kernel integrand is strongly singular which can be solved using indirect method using the rigid body motion assumption, as discussed in detail in section 2.2.2. As far as the weakly singular displacement kernel integrand is concerned, the strategy which we adopt, as in the conforming element method, is to isolate the logarithmic singularity and integrate it using the Gauss integration rule for logarithmically singular functions. However, some special treatment is necessary for partially discontinuous elements.

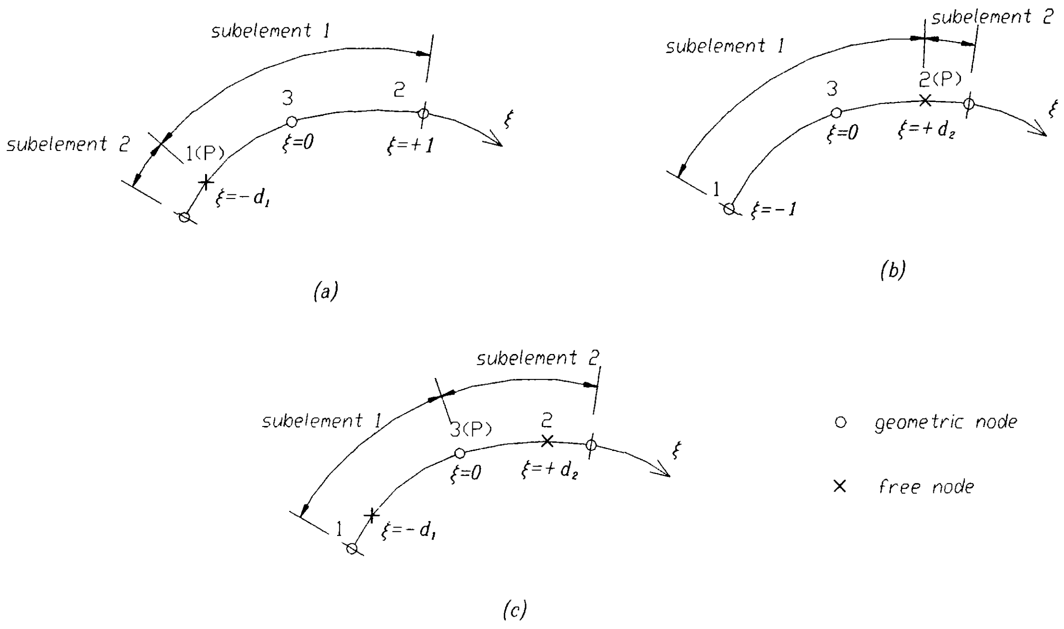

Fig 3.3. (a) Partially discontinuous quadratic element with source P locating at free node 1. (b) PDE with source P locating at free node 2. (c) PDE with source P locating at mid node 3.

In PDEs, the free nodes are not located at the element end. When this node is also the source point P, then the element must be divided into two sub-elements centred on P to cope with the weak singularity of the kernel integrals, as shown in Fig. 3.3.

For the three-noded element, three cases need to be considered: (a) source P locate at end node 1, (b) source P at the end node 2, (c) source P at mid-side node 3. These cases will be discussed in turn below. We assume that in both cases (a) and (b), the source P is located at a free node.

Case (a): with P at the start node 1

Following the development described in 2.2.2, substituting the quadratic shape functions (equation 3.1) into eqn. 2.25 results in:

$$r^2 = \eta^2\left[f_1^2 + f_2^2\right] \qquad (3.4)$$

where

$$\begin{aligned}
\eta &= \frac{\xi + d_1}{d_1 + d_2} \\
f_1 &= \frac{\xi - (d_1 + d_2)}{d_1} x_1 + \frac{\xi}{d_2} x_2 - (\xi - d_2)(\frac{1}{d_1} + \frac{1}{d_2}) x_3 \\
f_2 &= \frac{\xi - (d_1 + d_2)}{d_1} y_1 + \frac{\xi}{d_2} y_2 - (\xi - d_2)(\frac{1}{d_1} + \frac{1}{d_2}) y_3
\end{aligned} \tag{3.5}$$

For a PDE, then $d_2 = 1$, and $0 < d_1 < 1$. Now taking the logarithm of equation (3.4), we obtain:

$$\log_e(\frac{1}{r}) = \log_e(\frac{1}{\eta}) - \frac{1}{2}\log_e(f_1^2 + f_2^2) \tag{3.6}$$

The second term on the right hand side is non-singular and can be integrated without difficulty, while the first term can be integrated using the logarithmically weighted Gauss quadrature rule. To apply this method, the element must be divided into two sub-elements (or integration regions) centred on that free node, as shown in Fig. 3.3. (a).

Since the Gaussian interval of integration is from zero to unity (intrinsic coordinates), while the interval of integration region 1 is from $-d_1$ to 1, the mapping between these two systems is simply,

$$\eta = \frac{\xi + d_1}{d_1 + d_2} \tag{3.7}$$

for $\xi > -d_1$. For continuous elements eqn (3.7) reduces to equation (2.29). The Jacobian $J(\xi, \eta)$ is $d_1 + d_2$.

The interval of integration of region 2 is from $-d_1$ to -1. Therefore, the mapping is:

$$\eta' = \frac{\xi + d_1}{d_1 - 1} = \eta\frac{d_1 + d_2}{d_1 - 1} \tag{3.8}$$

for $\xi < -d_1$. The Jacobian $J(\xi, \eta')$ is $1 - d_1$. Thus, in this region the first term in equation (3.6) can be written:

$$\log_e \frac{1}{|\eta|} = \log_e \frac{1}{\eta'} + \log_e (\frac{d_1 + d_2}{1 - d_1}) \tag{3.9}$$

Here, the first term can be evaluated using logarithmically weighted Gauss quadrature rule, while the second term using standard Gauss quadrature formula with the mapping from (- 1, - d_1) to (- 1, + 1).

Case (b): with P at the end node 2

In this case, the distance r is:

$$r^2 = [x(\xi) - x_2]^2 + [y(\xi) - y_2]^2 \tag{3.10}$$

and, similar to case (a), we obtain:

$$r^2 = \eta^2 [f_1^2 + f_2^2] \tag{3.11}$$

where

$$\begin{aligned} \eta &= \frac{-\xi + d_2}{d_1 + d_2} \\ f_1 &= -\frac{\xi}{d_1} x_1 - \frac{\xi + d_1 + d_2}{d_2} x_2 + (\xi + d_1)(\frac{1}{d_1} + \frac{1}{d_2}) x_3 \\ f_2 &= -\frac{\xi}{d_1} y_1 - \frac{\xi + d_1 + d_2}{d_2} y_2 + (\xi + d_1)(\frac{1}{d_1} + \frac{1}{d_2}) y_3 \end{aligned} \tag{3.12}$$

Analogously, if a PDE is considered, then d_1=1, and $0 < d_2 < 1$.

After taking the logarithm of equation (3.11), we have the same equation as eqn. (3.6) but with the different formula for η, f_1 and f_2.

To integrate the first term in the right-hand side of eqn (3.6), the element is divided into two sub-elements or integration regions centred on free node 2, as shown in Fig. 3.3 (b).

In region 1, the interval of integration is from d_2 to –1. The mapping between η and ξ is,

$$\eta = \frac{-\xi + d_2}{d_1 + d_2} \tag{3.13}$$

for $\xi < d_2$, which in the case of continuous element reduces to equation (2.29). The Jacobian $J(\xi, \eta)$ is $d_1 + d_2$.

The interval of integration region 2 is from d_2 to 1, therefore, the mapping is:

$$\eta' = \frac{\xi - d_2}{1 - d_2} = \eta \frac{d_1 + d_2}{d_2 - 1} \tag{3.14}$$

for $\xi > d_2$, the Jacobian $J(\xi, \eta')$ is $1\text{-}d_2$. Thus, in this region, the first term in equation (3.6), which applies to both case (a) and (b), can be written as:

$$\log_e \frac{1}{|\eta|} = \log_e \frac{1}{\eta'} + \log_e (\frac{d_1 + d_2}{1 - d_2}) \tag{3.15}$$

Here, the first term can be evaluated using logarithmically weighted Gauss quadrature rule, while the second term can be evaluated using standard Gauss quadrature formula with the mapping from (d_2, 1) to (- 1, + 1).

Case (c) : with P at the mid-node 3

In this case, the distance r is:

$$r^2 = [x(\xi) - x_3]^2 + [y(\xi) - y_3]^2 \tag{3.17}$$

and also:

$$r^2 = \xi^2 [g_1^2 + g_2^2] \tag{3.18}$$

where

$$g_1 = \frac{\xi - d_2}{d_1(d_1 + d_2)} x_1 + \frac{\xi + d_1}{d_2(d_1 + d_2)} x_2 - \frac{\xi - d_2 + d_1}{d_1 d_2} x_3$$
$$g_2 = \frac{\xi - d_2}{d_1(d_1 + d_2)} y_1 + \frac{\xi + d_1}{d_2(d_1 + d_2)} y_2 - \frac{\xi - d_2 + d_1}{d_1 d_2} y_3 \qquad (3.19)$$

The next steps are similar to the continuous element case, which has been described in section 2.2.2. The element is divided into two sub-elements centred on the mid node, as shown in Fig. 3.3 (c). The mapping for these two sub-elements is simply, $x = -\xi$, for $\xi < 0$, and $x = +\xi$, for $\xi > 0$, and the Jacobian $J(x, \xi)$ is unity.

3.1.3 Numerical examples in 2D

We examine some two-dimensional elastostatic problems which will serve either as benchmark tests or possess some practical significance. We will also discuss the 'optimum' offset parameter. This is the distance in the intrinsic coordinate system of the free nodes from element edge. This parameter plays an important role in the numerical stability and accuracy of the PDE method.

(a) A benchmark example

To illustrate the relative merits of continuous and discontinuous elements, we first consider a thick plate which is subjected to a uniform pressure loading under plane strain conditions, as depicted in Fig. 3.4 (a). All surfaces except the top surface are constrained by roller supports. The elastic material properties are: Young's modulus of elasticity $E = 1.0\times10^8$, and, Poisson's ratio $\nu = 0.4$. Six elements are used to model each side AB, CD and AD, with ten along BC.

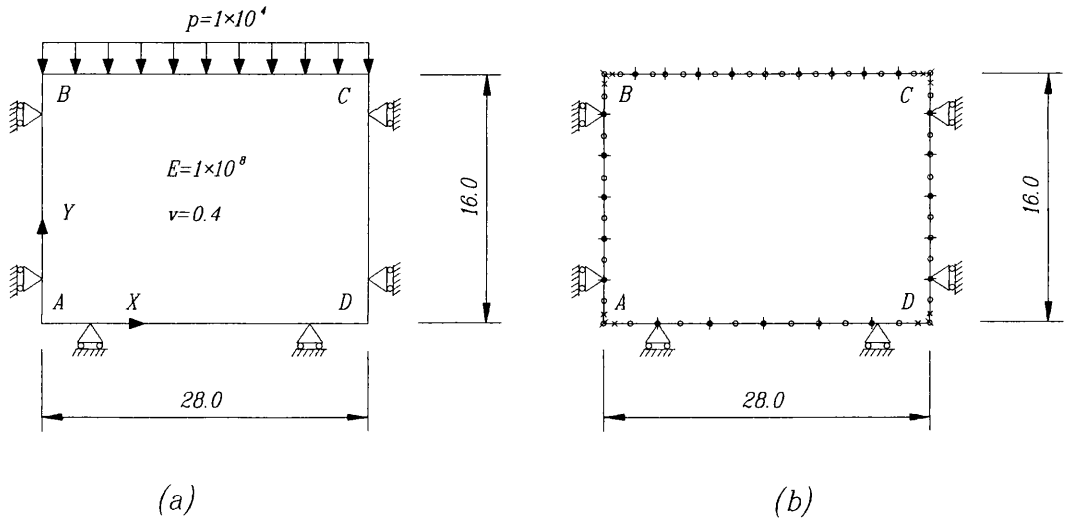

Fig. 3.4 Numerical model for a plane-strain problem

With such boundary conditions, the problem reduces to one-dimension. The analytical solution is:

$$\sigma_{xx}/\sigma_{zz} = \lambda/(\lambda+2G) = \nu/(1-\nu) \tag{3.20}$$

Thus if $\nu = 0.4$, $\sigma_{xx} = 6.67$.

Eight PDEs are generated automatically by edge detection software at the four corners (A, B, C, D). All other elements remain as continuous elements. The detection of corners (discussed in detail in Chapter 4) is based on the fact that at all corner nodes, the outward normals computed from two neighbouring elements at their common nodes are significantly different from each other.

The horizontal tractions on CD using the continuous element method and PDE method are listed in Table 3.1.

Table.3.1. Horizontal tractions on CD

Y coordinate	Traction (PDE)	Traction (continuous element)
16.0	-6.82	-9.64
15.0	-6.62	-6.90
14.0	-6.74	-6.40
13.0	-6.62	-6.69
12.0	-6.73	-6.74
10.5	-6.64	-6.65
9.0	-6.74	-6.72
7.0	-6.65	-6.62
5.0	-6.75	-6.67
3.5	-6.63	-6.67
2.0	-6.75	-6.23
1.0	-6.59	-8.16
0.0	-6.88	0.00

It can be seen that the PDE method gives results which agree well with the exact solution, even near the corners. By contrast, the continuous element gives poor results in these areas. This is due to its assumption of an 'unique traction' at corners. However, in this example, the error is mainly confined to the corner and is not significant elsewhere.

In the PDE method, we chose $d_1 = d_2 = 0.9$, which means that the offset distance between the free nodes and element edge (in intrinsic coordinates) is 0.1.

Here, we examine the effect of this offset parameter on numerical stability and accuracy. Fig. 3.5 shows the horizontal tractions at the corner point C against the value of the offset parameter. We can see that for a reasonably wide range of $d = 0.4\sim0.9$, results are satisfactorily stable and accurate. Specifically, if $d = 0.8$, the error is 2.7%.

We can also see that poor results are produced in the two extreme cases. One is when d approaches 1, which means free nodes are very close to the element edge. Another is that when d approach a very small value or 0, which means the free nodes are too far away from the element edge and too close to the mid element nodes. These two circumstances must be avoided therefore in the computation.

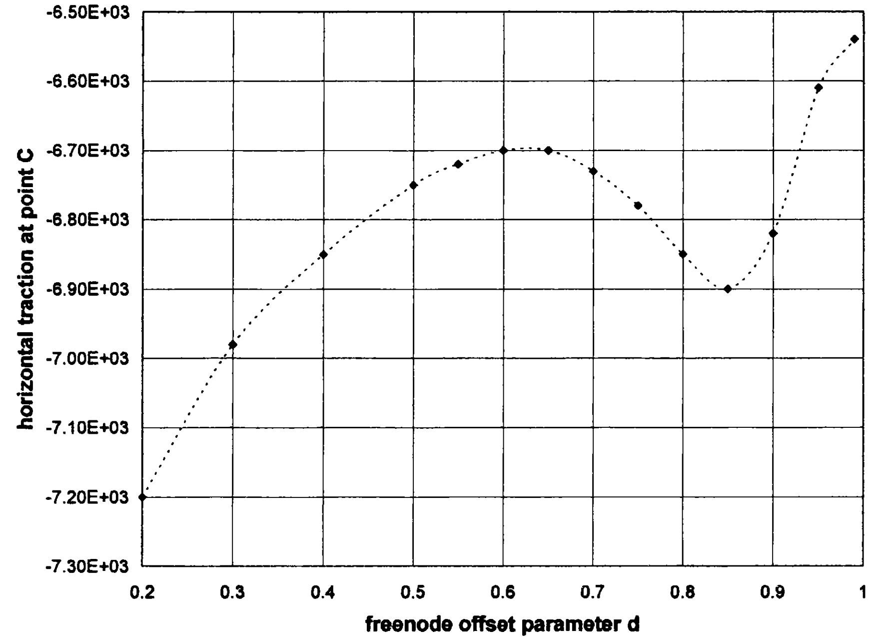

Fig.3.5. Stability of partial discontinuous element.

(b) Flexible strip foundation over a single finite layer

We now consider the plane problem illustrated as Fig. 3.6, which depicts uniform vertical loading of a (flexible) strip foundation, of width B, over a finite layer underlain by a rough rigid base.

(a)

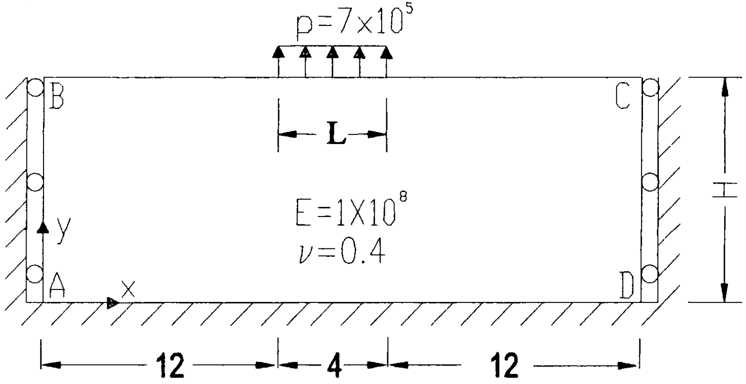

(b)

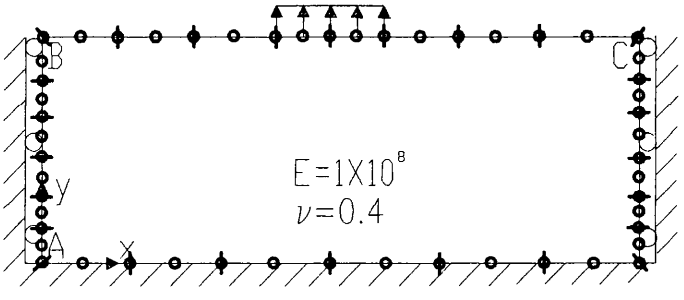

Fig. 3.6 (a) Flexible strip foundation on a finite elastic layer. (b)boundary element mesh.

The traction-free upper boundary is discretized into 8 quadratic boundary elements and the strip foundation is represented by two elements. The free surface discretization is truncated at a distance of 3L from the edge of the strip foundation. A further six elements are used to represent the rigid base boundary (assumed fixed) and the lateral boundaries (assumed smooth but laterally unyielding). Numerical results were obtained for : L = 4m, H = 8m, E = 100MN/m^2, v = 0.4, and, p = 700kN/m^2.

Computed values of displacement and traction are given in Fig.3.7. Results from both PDE and continuous elements are compared. Fig. 3.7 shows the horizontal and vertical displacements along the loaded surface (Line BC). Fig. 3.8 shows the vertical displacements and horizontal tractions along lateral line CD. We can see both methods yield sensibly the same results, except for some slight variation at the corners.

3.7 a)

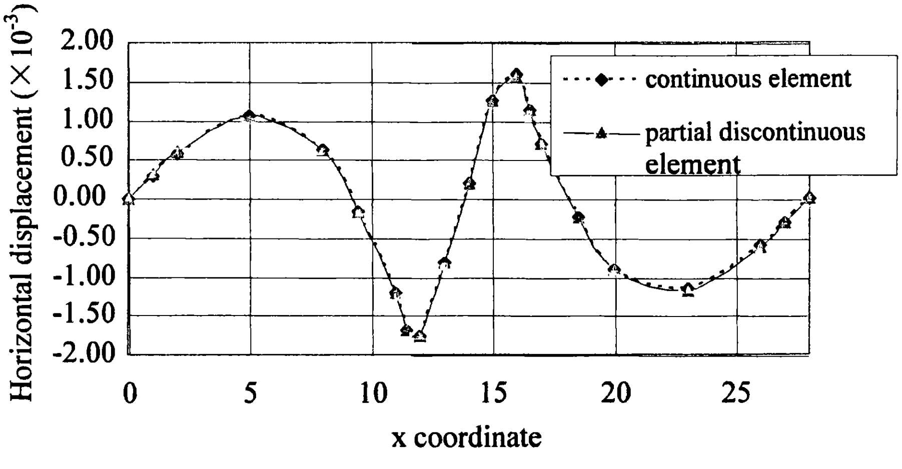

3.7 b)

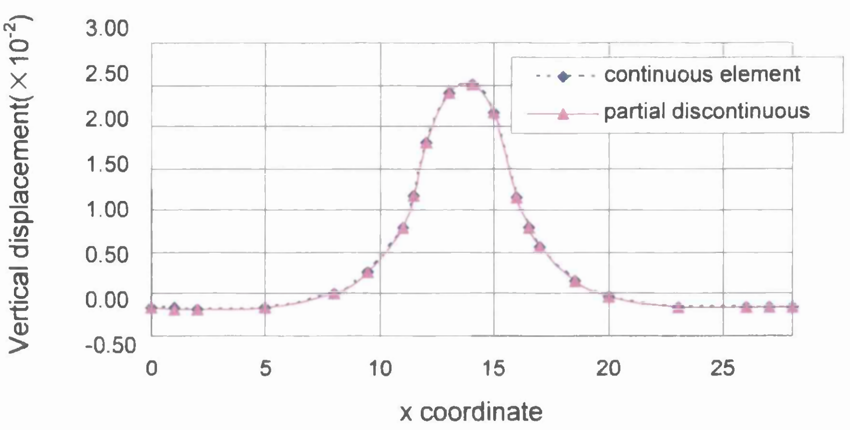

Fig. 3.7 a) Horizontal displacement along line BC
b) Vertical displacement along line BC

3.8 a)

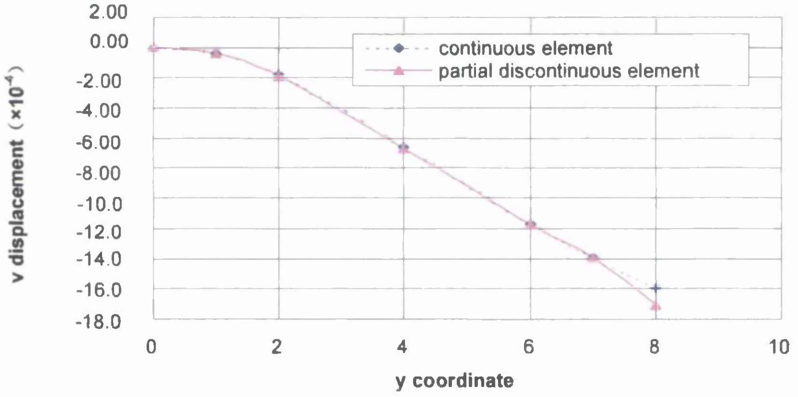

3.8 b)

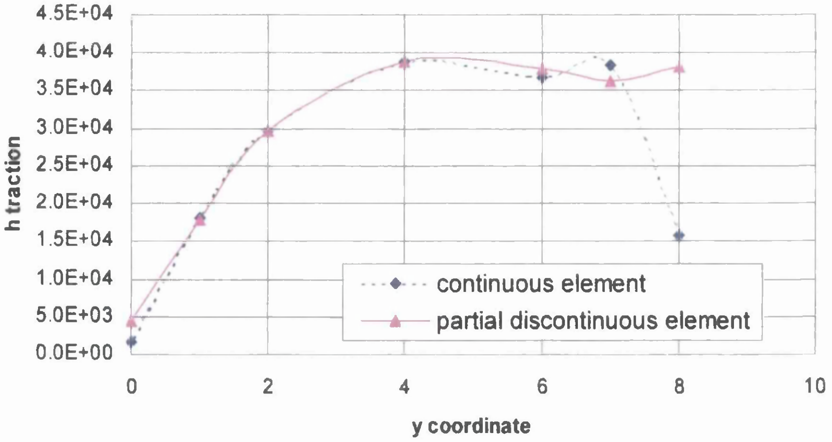

Fig. 3.8 a) Vertical displacement along line CD
b) Horizontal traction along line CD

The poor performance of the continuous elements at corners is abundantly evident in Fig. 3.8. Nevertheless, the effect is localised at the corners. The error is caused by the 'unique traction' assumption. However, the continuous element method can yield good results if assembly of the system equations (which are generated element-wise) is delayed until after the boundary conditions have been imposed. By this way, the independence of the tractions at any common node is temporarily retained. Then, if only one (or no) traction at a node (per degree of freedom) is unknown, the equations for that node can be assembled incorporating the known boundary conditions. The remaining unknowns at that node will then include no more than one traction (per degree of freedom), which may be obtained by solving the system equations in the normal way.

The PDE method can also deal with singularities caused by loading discontinuities. For example, strip centre-line vertical displacement of 25.1mm agrees well the theoretical solution of 25.0mm. However, the strip edge displacements predicted by a continuous element program are 18.1mm and 11.5mm for the left-hand edge and right-hand edge, respectively. The left-hand edge displacement is overstated because continuity between two elements imposes anomalous loading on left element. On the other hand, the right-hand edge displacement is understated because the traction-free condition over the right element erases part of the loading over the left element. As a comparison, the predicted strip centre-line vertical displacement from the partial discontinuous element program is 25.4mm, while the strip edge displacements are 15.8mm, and the left and right side results are the same. Again, this problem can be circumvented (using continuous elements) by delaying assembly of the system equations, but this is less efficient.

3.4 Partially discontinuous elements for three-dimensional BEM analysis

3.2.1. Interpolation functions for Partially Discontinuous Elements

Partially discontinuous elements in three-dimensions are much more complex than in two dimensions. Automatic detection of edges and corners (and re-meshing) is clearly more complex. In addition, the procedures for evaluating the integrals have to be revisited.

As in two-dimensional case, we only consider quadratic elements. The eight collocation nodes (free nodes) are located as shown in Fig.3.9, and are defined by the four parameters (d_1, d_2, d_3, d_4).

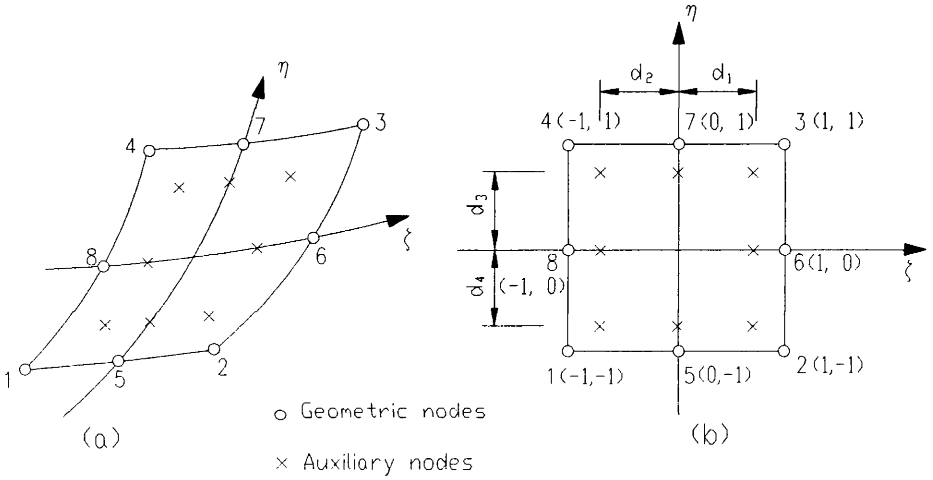

Fig 3.9. (a) Discontinuous quadratic element. (b) Local (intrinsic) coordinate system.

The edge-detection software detects edges between two neighbouring elements by comparing the outward normals at the mid-node at their common side. For example, if the element side 1-5-2 in Fig. 3.9 is an edge (detected by examining the outward normal at node 5), then the value of d_4 (originally unity) is changed, which means that all three geometric nodes 1, 5 and 2 are moved inside the element and become free nodes.

As in the two-dimensional case, we derive the interpolation functions for the 4-parameter discontinuous elements from the 'serendipity' expressions:

$$N_1(\xi,\eta) = c_0 + c_1\xi + c_2\eta + c_3\xi\eta + c_4\xi^2 + c_5\eta^2 + c_6\xi^2\eta + c_7\xi\eta^2 \qquad (3.21)$$

The above is only one of the eight shape functions. The other seven functions have the similar expressions. The eight constant parameters, $c_0 - c_7$, are to be determined by the properties of shape functions, which are

$$
\begin{aligned}
&N_1(-d_2,-d_4)=1\\
&N_1(\ 0,-d_4)=0\\
&N_1(\ d_1,-d_4)=0\\
&N_1(\ d_1,\ \ 0)=0\\
&N_1(\ d_1,\ d_3)=0\\
&N_1(\ 0,\ \ d_3)=0\\
&N_1(-d_2,\ d_3)=0\\
&N_1(-d_2,\ \ 0)=0
\end{aligned}
\tag{3.22}
$$

Solving the above eight equations, the eight unknowns can be determined. Analogously, the other seven shape functions can be derived and after some algebraic manipulation the interpolation functions are as follows:

$$
\begin{aligned}
N_1(\xi,\eta)&=\frac{1}{(d_1+d_2)(d_3+d_4)}(d_1-\xi)(d_3-\eta)(-1-\frac{\xi}{d_2}-\frac{\eta}{d_4})\\
N_2(\xi,\eta)&=\frac{1}{(d_1+d_2)(d_3+d_4)}(d_2+\xi)(d_3-\eta)(-1+\frac{\xi}{d_1}-\frac{\eta}{d_4})\\
N_3(\xi,\eta)&=\frac{1}{(d_1+d_2)(d_3+d_4)}(d_2+\xi)(d_4+\eta)(-1+\frac{\xi}{d_1}+\frac{\eta}{d_3})\\
N_4(\xi,\eta)&=\frac{1}{(d_1+d_2)(d_3+d_4)}(d_1-\xi)(d_4+\eta)(-1-\frac{\xi}{d_2}+\frac{\eta}{d_3})\\
N_5(\xi,\eta)&=\frac{1}{d_1d_2(d_3+d_4)}(d_1-\xi)(d_2+\xi)(d_3-\eta)\\
N_6(\xi,\eta)&=\frac{1}{d_3d_4(d_1+d_2)}(d_2+\xi)(d_3-\eta)(d_4+\eta)\\
N_7(\xi,\eta)&=\frac{1}{d_1d_2(d_3+d_4)}(d_1-\xi)(d_2+\xi)(d_4+\eta)\\
N_8(\xi,\eta)&=\frac{1}{d_3d_4(d_1+d_2)}(d_1-\xi)(d_3-\eta)(d_4+\eta)
\end{aligned}
\tag{3.23}
$$

We see that for $d_1=d_2=d_3=d_4=1$, the above equations reduce to the well-known shape functions for the continuous element.

3.2.2. Numerical integration techniques

The discretized boundary integral equation for three-dimensional elasto-statics analysis is:

$$c_{ij}(P)u_j(P)+\sum_{e=1}^{N_e}\left(\int_{-1}^{+1}\int_{-1}^{+1}T_{ij}(Q,P)N_\alpha Jd\zeta d\eta\right)u_{j\alpha}^e = \sum_{e=1}^{N_e}\left(\int_{-1}^{+1}\int_{-1}^{+1}U_{ij}(Q,P)N_\alpha Jd\zeta d\eta\right)t_{j\alpha}^e \tag{3.24}$$

where N_e is the total number of boundary elements, J is the determinant of the Jacobian matrix, N_α is the interpolation (shape) functions of PDEs, which have been written in eqn. (3.23), and Q and P are termed the field point and source point, respectively. Both points are on the boundary. U_{ij} and T_{ij} are the fundamental solutions in three dimensions, while $u_{j\alpha}^e, t_{j\alpha}^e$ are the nodal displacement and traction vectors, respectively.

The non-singular integrals in this equation can be evaluated by standard Gauss-Legendre quadrature formula, and just as in the two-dimensional case, the adaptive integration scheme proposed by Gao & Davies (2002) can be used to improve the accuracy of integration.

When the source point P coincides with one of the collocation nodes of boundary element, a singular case arises. The offset between the free nodes and the element edges introduces some difficulties in the singular integrals, but these can be easily overcome by standard numerical quadrature techniques. The order of the singularity of the kernel integrals in (3.24) is as follows:

$$\begin{aligned} &U_{ij}(Q,P)N_\alpha \sim O(1/r) \\ &T_{ij}(Q,P)N_\alpha \sim O(1/r^2) \end{aligned} \tag{3.25}$$

when $r \to 0$.

Again, the traction kernel integrand is a strongly singular case which can be solved by indirect method using the rigid body motion assumption.

As far as the weakly singular displacement kernel integrand is concerned, a quadrilateral element is divided into triangular sub-elements whose common apex is the singular node. If this node is a free node, then the whole element is now partitioned into four triangular sub-elements. Each triangular sub-element is in turn mapped from the (ξ,η) co-ordinate system on to a new set of intrinsic co-ordinate (ξ',η') with their origin at the centre of the element. This rather complicated process is shown in Figure 2.4 for the case of a PDE. After the triangular sub-element (2-3-1′) in (b) is mapped on to the square element in (c), the Gauss quadrature rule can be applied.

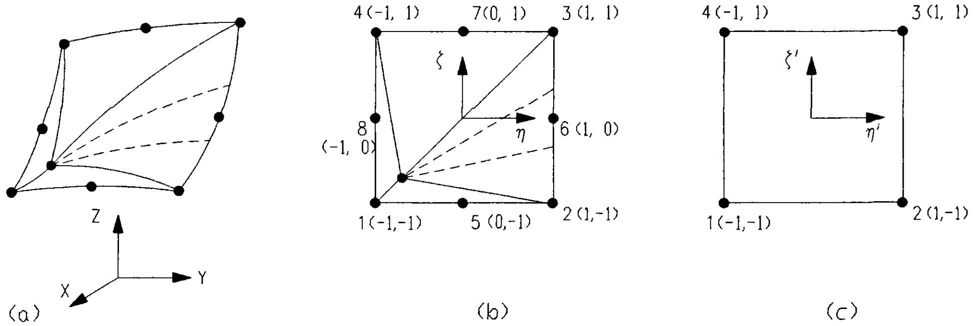

Fig. 3.10. Typical subdivision pattern for a boundary element – singular case

If we denote the weakly singular kernel integral by *f(Q,P)*, the above process can be expressed as follows:

$$\begin{aligned}\int_{\Gamma_s} f(Q,P)d\Gamma &= \int_{-1}^{1}\int_{-1}^{1} f(\xi,\eta)J(\xi,\eta)d\xi d\eta = \\ &= \sum_{s=1}^{4}\int_{-1}^{1}\int_{-1}^{1} f(\xi_f,\eta_f)J(\xi_f,\eta_f)J_s(\xi',\eta')d\xi' d\eta'\end{aligned} \tag{3.26}$$

where ξ_f signifies $\xi(\xi', \eta')$, η_f signifies $\eta(\xi', \eta')$ and $J_s(\xi', \eta')$ is the Jacobian of the transformation from the original to the new intrinsic co-ordinate system:

$$J_s(\xi',\eta') = \frac{\partial(\xi,\eta)}{\partial(\xi',\eta')} = \begin{vmatrix} \dfrac{\partial\xi(\xi',\eta')}{\partial\xi'} & \dfrac{\partial\eta(\xi',\eta')}{\partial\xi'} \\ \dfrac{\partial\xi(\xi',\eta')}{\partial\eta'} & \dfrac{\partial\eta(\xi',\eta')}{\partial\eta'} \end{vmatrix} \tag{3.27}$$

For illustration, we take one sub-element in Fig. 3.10, as shown in Fig.3.11. Since the transformation from element intrinsic coordinates to sub-element intrinsic coordinates is linear, an alternative strategy is possible (e.g., Becker, 1992). In this case, a new set of intrinsic co-ordinates ξ' and η' with their origin at the centre of the element is defined for each sub-element (refer to Fig. 3.11).

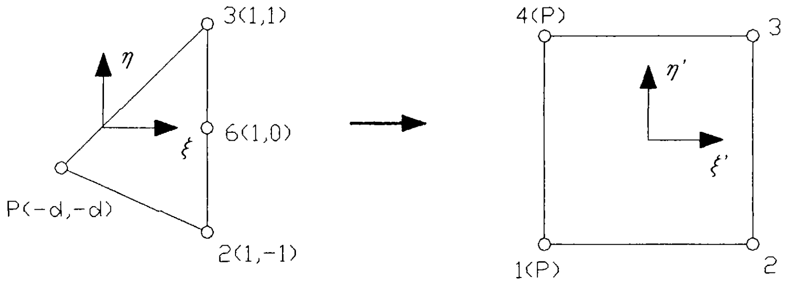

Fig 3.11. Sub- element intrinsic coordinate system

In Fig. 3.11, the intrinsic co-ordinates of free node *P* in (ξ, η) system are ($-d_2$, $-d_4$), as have been discussed before.

Linear shape functions are now used to determine the original intrinsic co-ordinates for a point in the new intrinsic co-ordinate system, as follows:

$$\begin{aligned} \xi(\xi',\eta') &= \sum_{\alpha=1}^{4} N'_\alpha(\xi',\eta')\,\xi_\alpha \\ \eta(\xi',\eta') &= \sum_{\alpha=1}^{4} N'_\alpha(\xi',\eta')\,\eta_\alpha \end{aligned} \tag{3.28}$$

where the linear shape functions are:

$$\begin{aligned} N'_1(\xi',\eta') &= \frac{1}{4}(1-\xi')(1-\eta') \\ N'_2(\xi',\eta') &= \frac{1}{4}(1+\xi')(1-\eta') \\ N'_3(\xi',\eta') &= \frac{1}{4}(1+\xi')(1+\eta') \\ N'_4(\xi',\eta') &= \frac{1}{4}(1-\xi')(1+\eta') \end{aligned} \tag{3.29}$$

and the parameters ξ_α and η_α are the nodal values of the original intrinsic co-ordinates.

As before, the Jacobian $J_s(\xi', \eta')$ tends to zero as $O(r)$ as $r \to 0$, since the original intrinsic co-ordinates of the two nodes associated with P take the same values in the transformed sub-element. In Fig. 3.11, node 1 and 4 are made coincident by setting:

$$\begin{aligned} \xi_1 &= \xi_4 = -d_2 \\ \eta_1 &= \eta_4 = -d_4 \end{aligned} \tag{3.30}$$

For added accuracy, each triangular sub-element could be further subdivided into triangles (shown in broken lines in Fig. 3.10) whose number depends on the angle subtended at the singular node in the (ξ, η) co-ordinate parent triangle. This detailed subdivision of the element ensures accurate integration of the sharply varying displacement kernel.

3.2.3. Symmetry

Implementation of symmetry is essential if large problems that exhibit symmetry are to be solved. If both the geometry and the boundary conditions are symmetric, the considerable savings in computational time, as well as data preparation effort, can be gained by taking advantage of this fact. The detail of the symmetry option in BEMECH is described by Gao & Davies, 2002. Here, we only introduce some main features. The BEMECH is a two- and three-dimensional BEM program written in Fortran 90, and is used and modified by the author to include more features like PDE and multi-region analysis in this thesis.

We assume that in a global Cartesian frame, the body is symmetric about a plane which is normal to the r-th Cartesian axes with an intersection point as $x_r = x_r^s$. In the image elements, the displacements and tractions in the direction normal to the symmetry plane are equal in value but with reverse sign to those in the original elements, while those in the tangential directions are unaltered. Therefore, the displacements and tractions at the image nodes can be expressed by the equations:

$$\begin{aligned} u_i^m &= u_i^o - 2\delta_{ir} u_r^o \\ t_i^m &= t_i^o - 2\delta_{ir} t_r^o \end{aligned} \tag{3.31}$$

where the superscript o signifies the original node values, m signifies the image node values.

For assembly of the system of equations, this means that the coefficients of the image nodes can be assembled in the same location as for the original nodes. In this process, the negative signs of the displacements and tractions should be considered during assembly. As a result of this assembly procedure, the number of unknowns for the problem is reduced to those on the original side of the symmetry plane and on the plane itself.

In three-dimensional problem, there can be single, two-fold and three-fold symmetry. The greater the degree of symmetry, the lesser is the proportion of the domain which must be discretized. For example, in three-fold symmetry, we need only discretize one-eighth of the domain.

However, the reduction of unknowns does not mean that no integrations are necessary over the image elements. The integration of the kernel shape function products over the image elements must still be evaluated but collocation is necessary only on the original elements.

In image elements (refer to Fig. 3.12), we note that the incidence of the element nodes has to be reversed in order to maintain a consistent outward normal, e.g., 1 and 2, 3 and 4, 6 and 8, and so will be the parameters which are used in 4-parameter quadrilateral elements to determine the intrinsic co-ordinates of free nodes. As shown in Fig. 3.12, d_1 and d_2 should be reversed.

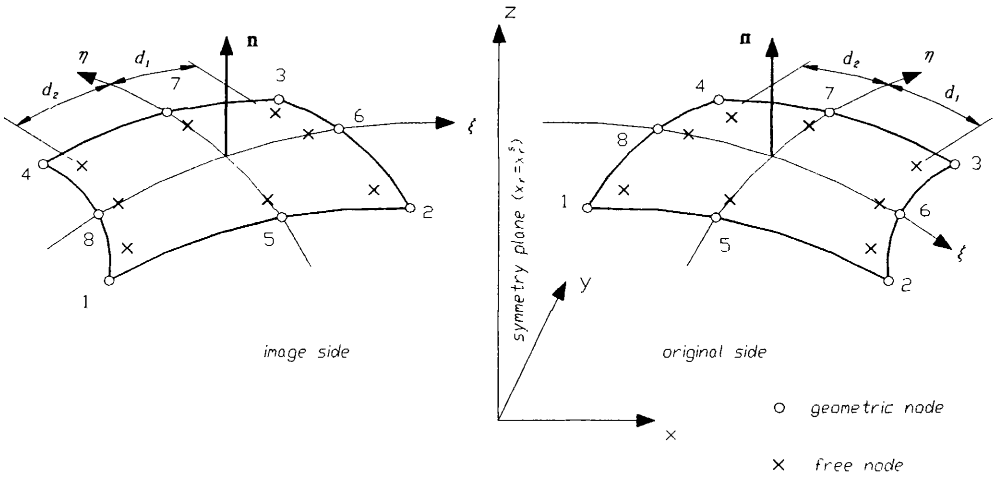

Fig 3.12. Three dimensional PDE with one plane of symmetry

3.2.4. Numerical examples

(a) Cube under tension

Fig.3.13 shows a cube subjected to a uniformly distributed traction of $P_1 = 1$ on the top surface (z^+) and $P_2 = 2$ on the right surface (x^+), subjected to the boundary conditions that the front (y^-), back (y^+) and left (x^-) surfaces are roller supports and the bottom surface (z^-) is fixed.

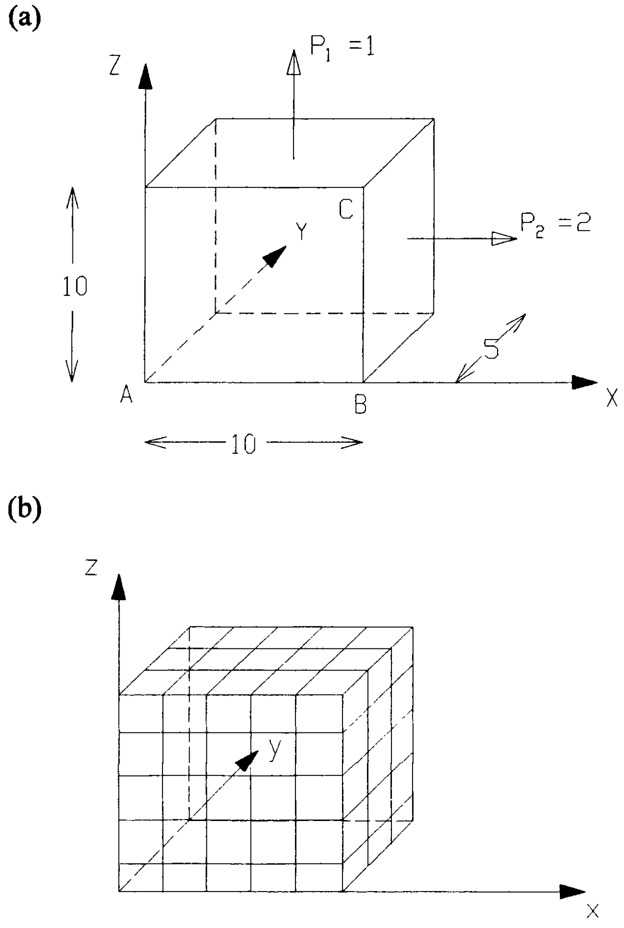

Fig 3.13. (a) A cube under tension. (b) Boundary element mesh.

In Fig.3.13, points A and B are corner nodes where three boundary surfaces intersect (defined on the surfaces z^-, x^- and y^- for point A, and z^-, x^+ and y^- for point B).

The surfaces of the cube are discretized using three elements in the y-direction and five elements in the x and z directions. The Young's modulus E and Poisson's ratio ν are assumed to be unity and 0.3 respectively. The results of current method were compared with other methods, i.e., BEM using auxiliary equations to treat edges and corners (Gao & Davies, 2002), standard plane-strain finite element (FE) program (OASYS), and an elementary 3D-BEM program (BEM3D). These results have been reported by Gao & Davies (2002). Table 3.1 and 3.2 show the calculated tractions and displacements for some selected points.

Table 3.1. Traction at Selected Points

	Program	Point A			Point B		
		Face z^-	Face x^-	Face y^-	Face z^-	Face x^+	Face y^-
t_x	Current	0.00017	-0.590	0*	-2.666	2.0*	0*
	Gao&Davies	-0.002	-0.619	0*	-1.712	2.0*	0*
	FEM	-0.007	-0.612	0*	-1.696	2.010	0*
	BEM3D	-0.217	-0.217	-0.217	-3.149	-3.149	-3.149
t_y	Current	-0.0005	0*	-0.592	0.019	0*	0.458
	Gao&Davies	-0.003	0*	-0.642	-0.005	0*	0.457
	FEM	0*	0*	-0.632	0*	0*	0.515
	BEM3D	-0.229	-0.229	-0.229	0.351	0.351	0.351
t_z	Current	-1.379	0*	0*	2.987	0*	0*
	Gao&Davies	-1.385	0*	0*	3.830	0*	0*
	FEM	-1.432	-0.007	0*	3.396	0*	0*
	BEM3D	-1.399	-1.399	-1.399	3.831	3.831	3.831

Note: The superscript * indicates a prescribed value.

Table 3.2. Displacements at Selected Point C

Program	u_x	u_y	u_z
Current	15.3857	0.0000*	-0.096
Gao&Davies	15.3302	0.0000*	0.0078
FEM	15.3800	0.0000*	-0.0699
BEM3D	15.3338	0.0000*	0.0102

The results shown in Tables 3.1 and 3.2 illustrate the very good results obtained using the current program. Program BEM3D often yields poor results at corners, because it essentially ignores the corner problem ("equal traction" assumption). The lack of agreement on face z- at B is because there is a stress concentration (singularity) there. This is apparent if we adopt a 10×10×5 mesh (400 boundary elements). The tractions (Face z-) along the bottom line AB are shown in Fig. 3.14. We can see the stress increases rapidly as the edge of the cube is approached.

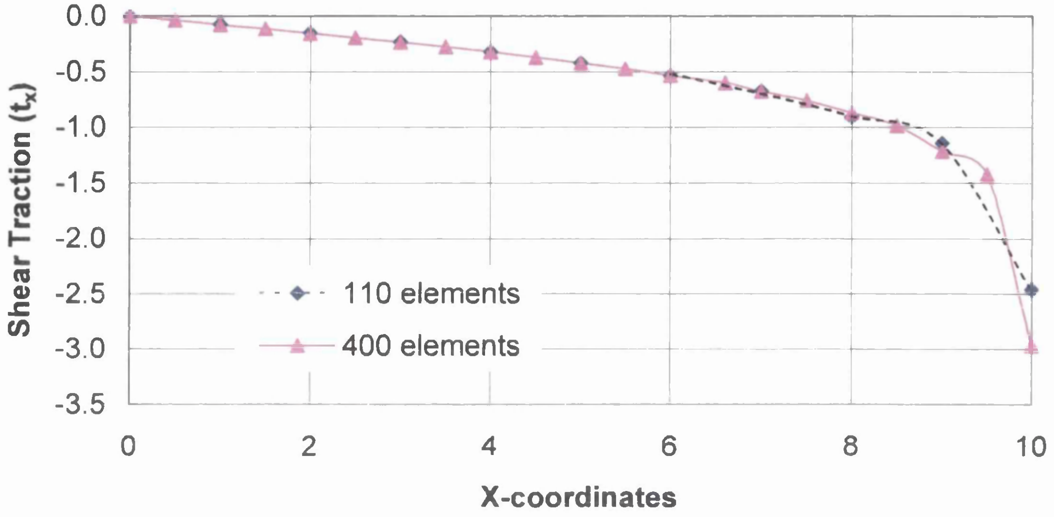

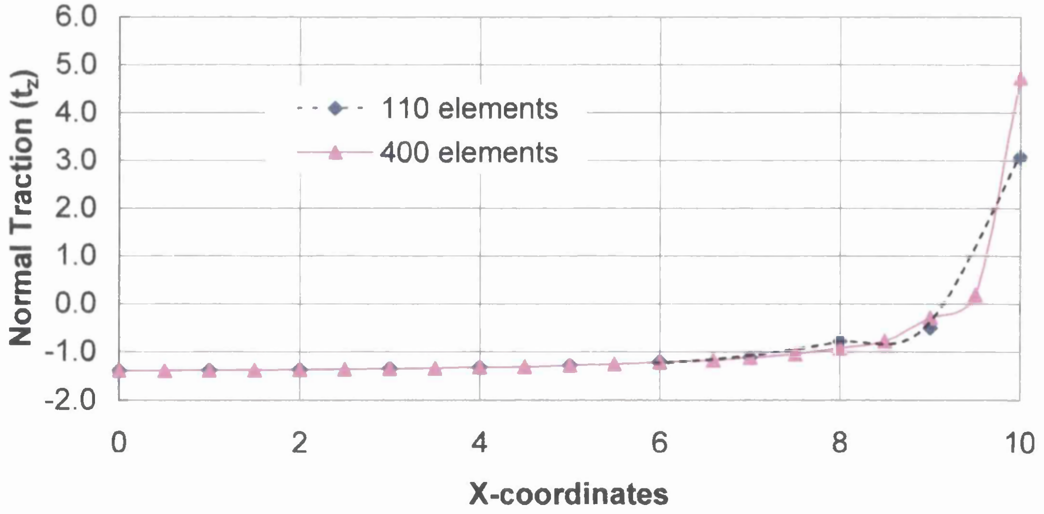

Fig 3.14. *a) Shear tractions along bottom of the cube.*

b) Normal tractions along bottom of the cube.

Again, we examine the effect of the offset between the free nodes and element edges on numerical stability and accuracy. We now consider a cube with the same geometry as Fig.3.13 but with $E = 10^8$ and $\nu = 0.3$. The cube is subjected to a uniformly distributed pressure of $P = 1000$ on the top surface: all other surfaces are subjected to roller constraint. Thus, this example is the confined compression test in which the analytical solution is available, e.g., the lateral pressure is $P\nu/(1-\nu) = 4286$.

The displacements and tractions along CB line parallel to axis z are listed in Table 3.3.

Table 3.3 Displacement and traction along CB, Fig. 3.13

z coordinate along CB	Vertical displacement $\times 10^{-3}$	Horizontal traction
10.0	-0.743	4285.4
9.0	-0.669	4284.6
8.0	-0.594	4286.3
7.0	-0.520	4284.8
6.0	-0.446	4286.5
5.0	-0.371	4284.4
4.0	-0.297	4286.5
3.0	-0.223	4284.8
2.0	-0.149	4286.3
1.0	-0.074	4284.0
0.0	0.000	4283.7

As shown in Table 3.3, the current results agree very well with the analytical solution. Note that at the corner nodes, the results are extrapolated values.

We examine the effect of the offset parameter on the horizontal traction at a corner node (point C in Fig. 3.13). It can be seen that stable and accurate results can be obtained over a very wide range of the offset distance (Fig. 3.15).

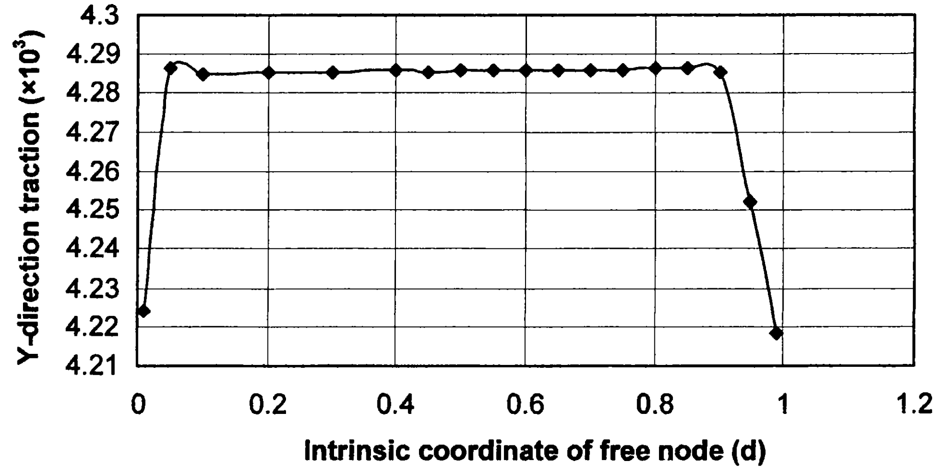

Fig. 3.15. Horizontal traction (y-direction) versus free node intrinsic coordinate (d).

Analysis and numerical trials suggest that the optimal value of the offset parameter (d) lies in the range 0.7 to 0.8 in the intrinsic co-ordinate system. One important consideration is to avoid overcrowding of collocation points at corners, especially in large-scale problem, because the results may diverge. When two equations are generated by placing the collocation points on the two free nodes which are very close to each other (as they are both very near to the same element edge), it becomes possible to obtain two rows with weak pivots that result in ill-conditioning of equation systems.

(b) Pressurized spherical cavity

The examples so far only concern the discretization of flat surfaces. In the following example, the performance of PDE on curved surfaces is investigated.

An example which has been used by Manolis & Banerjee (1986) to establish the relative merit of conforming (continuous) and non-conforming (discontinuous) elements is used here. This is a spherical cavity in an infinite domain, as shown in Fig. 3.16.

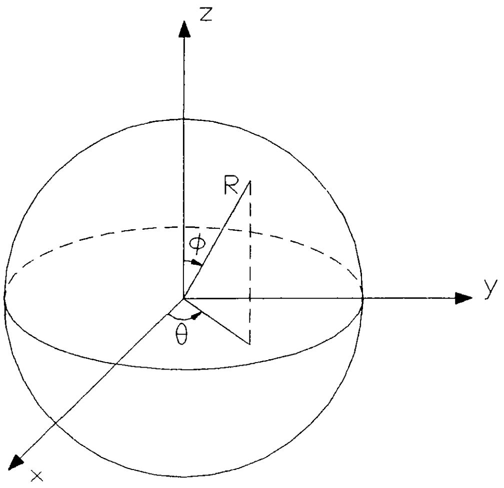

Fig. 3.16 Spherical cavity embedded in an infinite continuum

The radius of the cavity is $R = 212$ in. The surrounding material is granite with $E =$ 8,993,000 lbf/in.^{2} and $\nu = 0.25$. The surface of cavity is under uniform internal radical pressure $p = 1000$ lbf/in.^{2}. Since it is a three-fold symmetric problem, only one-eighth of the domain has to be considered. We use only three elements to model this structure. The mesh is shown in Fig. 3.17.

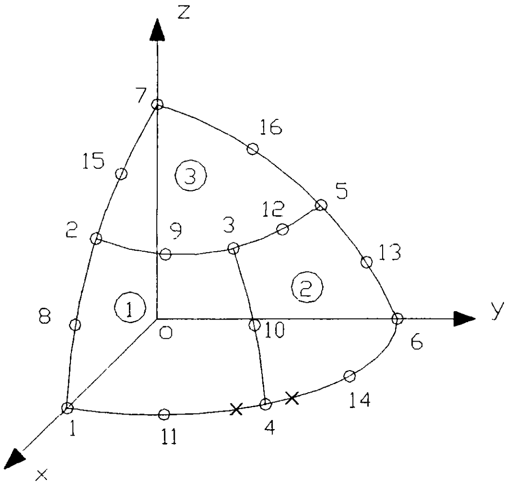

- *Fig. 3.17 Boundary element mesh*

In Table 3.4, we list the cartesian co-ordinates of some critical nodes in the mesh.

For this problem, the exact solution for the radial displacement at the cavity surface is:

$$u_r = pR(1+\nu)/(2E) \qquad at \;\; r = R \tag{3.32}$$

and the only non-zero stresses at the surface of the cavity are:

$$\begin{aligned} \sigma_{rr} &= -p \\ \sigma_{\phi\phi} &= \sigma_{\theta\theta} = p/2 \end{aligned} \tag{3.33}$$

Table 3.4. Cartesian co-ordinates of some nodes.

Node	x	y	z
3	122.4	122.4	122.4
4	149.9	149.9	0.0
2	149.9	0.0	149.9
5	0.0	149.9	149.9

If we use 15° as the 'threshold' angle for a corner, then in this example no corners will be detected, and so no PDEs will be generated. Here the 'threshold' angle means that when the subtended angle between normal of two connecting elements exceeds it then a corner or edge is detected. To compare the results between PDE and those of conforming elements, we change the threshold angle to 5°. Table 3.5 lists the displacements and stresses obtained at points 6 & 7. One is the polar point (node 7 in Fig. 3.17) which has Cartesian co-ordinate (0.0, 0.0, 212.0); the other is the equatorial point (node 6) whose co-ordinate is (0.0, 212.0, 0.0).

In the paper by Manolis & Banerjee (1986), who used non-conforming elements, the new collocation nodes which replace these two points are (21.23, 21.44, 209.31) and (21.23, 208.86, 21.23) respectively.

In Table 3.5, the results obtained by using conforming and non-conforming elements are those reported by Manolis & Banerjee (1986).

Table 3.5. BEM results for spherical cavity under radial expansion.

	u_r at pole (7) (10^{-2} in.)	u_r at equator (6) (10^{-2} in.)	σ_{rr} at pole (7) (10^3lbf/in.^{2})	$\sigma_{\varphi\varphi}$ at pole (7) (10^3lbf/in.^{2})	$\sigma_{\theta\theta}$ at equator (6) (10^3 lbf/in.^{2})
conforming	1.441	1.457	-1.000	0.481	0.489
non-conforming	0.610	0.639	-0.975	0.286	0.201

PDE	1.440	1.440	-1.000	0.512	0.510
exact	1.473	1.473	-1.000	0.500	0.500

From Table 3.5, we can see the poor performance of the non-conforming elements. Manolis & Banerjee gave two reasons of this. The first is that the quadrilateral surface elements have a parabolic curvature which does not exactly match the spherical curvature of the cavity. As a result, some errors are introduced in the numerical computation of the outward normal vector at the collocation nodes. The second is that only the nodes used for description of the geometry lie exactly on the surface of the sphere, since piecewise matching of the element's curvature with the cavity's curvature occurs at these location. In the case of non-conforming elements, the co-ordinates of the collocation nodes are interpolated from the geometry nodes. This process introduces some small inaccuracies, and as a result the collocation nodes are misplaced from their proper location by an amount around 0.02 times the radius of the cavity. This mesh distortion could result in a severe convergence problem for non-conforming elements.

From Table 3.5, we can see that the PDE gives far more accurate results than non-conforming elements. It is noted these results are associated with the geometric nodes. The problems caused by introducing the free nodes into elements still exist in the PDE method. In other words, unsatisfactory results may emerge at the location where 'corners' are detected. For example, in node 4, two free nodes are generated inside the element 1 and 2, as shown in Fig. 3.17. The results at node 4 are actually the extrapolated values from eight collocation nodes in one element, and depend on which element is used. Some results are listed in Table 3.6.

Table 3.6. BEM results for an equatorial point (node 4 in Fig. 3.17).

	u_r (10^{-2} in.)	$\sigma_{\varphi\varphi}$ (10^3 lbf/in.^{2})	$\sigma_{\theta\theta}$ (10^3 lbf/in.^{2})
PDE	1.4482	0.42053	0.5109
exact	1.4734	0.50000	0.5000

Since the quadrilateral surface elements do not exactly match the curvature of the cavity, some error will be introduced in the computation of the outward normal vector at the collocation node as in non-conforming elements. For example, at node 4, the outward normal should be (n_1, n_2, n_3) = (-0.707, -0.707, 0.0) in a spherical surface. However, from element 1 the normal is (-0.711, -0.691, -0.126), while from element 2 it is (-0.691, -0.711, -0.126). Conforming elements can yield relatively good results at such nodes if the outward normal is averaged between the surrounding elements. This can not be done directly with the free nodes as they are never shared between adjacent elements, although one could of course make the assumption that the outward normal at the free node should be the same as that of the corner node. As usual better results can be obtained by employing more elements.

Chapter 4

Partially discontinuous elements for multi-region BEM analysis

In this chapter, the Partially Discontinuous Element (PDE) method is extended and implemented in multi-region problems. In the numerical implementation, the stiffness matrix assembly method developed by Beer (2001) is adopted, which is different from the multi-region assembly method commonly used in most BEM techniques. The essence of this method is similar to that used in the FEM. In the edge detection software, PDEs are generated automatically from the normal continuous elements if corners and edges are detected, using the same criteria as those developed for single region 2D and 3D problems. The main aim of this software is to reduce the burden of the data preparation effort when PDEs are used. Some benchmark examples are examined to verify the accuracy and effectiveness of the current method. The effect of the offset parameter on numerical stability and accuracy when solving the assembly boundary element integral equations is examined in multi-region problems. In general, numerical trials show that stable and accurate results can be obtained over a reasonably wide range of the offset parameter in multi-region analysis. However, more severe restrictions on the offset parameter in multi-region case may be necessary than those in the homogeneous case, in order to avoid the over crowding of collocation points at corners, in particular at a corner where several regions meet. Tentative optimal values for the offset parameter are suggested.

4.1. Multi-region Boundary Element Methods

Multi-region BEM is necessary to analyse problems which involve materials consisting of several contiguous zones of different properties. Moreover, some homogeneous regions with a high surface-to-volume ratio should be artificially subdivided into sub-domains in order to improve the conditioning of the system equations as well as reducing computational costs. For large complex regions, such subdivision may be justified on the grounds that the resulting block-banded system equations may be generated and solved faster than the fully populated original set. Multi-region techniques can also be useful in the areas of fracture and non-linear analysis. Some fracture problems have been analysed by multi-region approach with an interface centred on the crack (Blandford et al, 1981).

In the context of multi-region problem, corners and edges occur not only at geometrical discontinuities but also at regional interfaces. It is known that at corners and edges, the displacements are uniquely defined but the surface tractions are multi-valued. Although rounding off corners and edges can give good results for some single region problems, it is impossible to round off corners and edges formed by the interfaces of different sub-domains. The unique traction assumption can provide reasonable approximate solutions for a two-zone intersecting edge and corner, but usually leads to unacceptable results for corners where more than two zones meet.

One commonly accepted method for the treatment of multi-region corners and edges problems is to introduce additional nodes at the edges and corners, and then develop auxiliary equations to determine the additional unknowns (Gao & Davies, 1999a). Banerjee (1994) introduced a resistance relationship, for potential problems, at each node of each interface element to eliminate the additional unknowns. Rudolphi (1983) described an implementation using quadratic elements for multi-region problems, including discontinuous stress components.

There are advantages in using partially discontinuous elements together with sub-domain models to treat edges/corners problem. With the abandonment of the complete inter-element continuity and free nodes being moved away from the singular locations, the difficulties which arise from using continuous elements at edges/corners disappear. By contrast, if an auxiliary equation approach is used, it introduces certain restrictive assumptions and makes the assembly process more difficult. In particular, in the case when more than two zones meet, the system may be over-determined at the interface and require special solution methods (Beer, 2001).

4.2. Stiffness matrix assembly method for multi-region problem

In multi-region BEM, we consider a number of homogeneous regions connected to each other. Each region is treated in the same way as discussed for the single region case. Since at the interfaces between the regions, both tractions $\{t\}$ and displacements $\{u\}$ are unknown, additional equations are required to close the equation set. These equations can be obtained from the conditions of equilibrium and compatibility at the region interfaces, and may be expressed in the following form:

$$\begin{aligned} \{t\}_i^{I} + \{t\}_i^{\mathrm{II}} &= \{t\}_i \\ \{u\}_i^{I} &= \{u\}_i^{\mathrm{II}} \end{aligned} \tag{4.1}$$

where $\{t\}_i$ is applied traction vector at the i-th interface. The Roman superscript denotes region number.

We introduce the subscript because in many cases we have problems where not all boundary nodes of the regions are connected. We refer to these problems as partially coupled, and we distinguish the boundary nodes which are at the interface from those which are not by assigning them a subscript i and e respectively. Various approaches have been established for the assembly of the multi-region system equations. For example, those proposed by Banerjee & Butterfield (1981), Brebbia et al (1984), Kane et al (1990), Gao & Davies (2000a). All these methods are similar as the assembly procedure is modified, so that a larger system of equations is formed including the additional unknowns at the interfaces. Although the multi-region assembly is easy to implement and solve, it is not very efficient in some special cases, (e.g., for modelling the sequential excavation/construction processes in tunnelling), since the coefficient matrices of all regions have to be computed and assembled every time a region is added or removed. Mainly aimed at these problems, Beer (2001) proposed the stiffness matrix assembly method which utilises a philosophy similar to that used by the FEM. As will be discussed later in section 4.3.3, this method can be easily combined with PDE implementation in multi-region BEM analysis.

In this method, we first construct a 'stiffness matrix' $[K]_i$ for all interface nodes of each region. The coefficients of $[K]_i$ are the tractions $\{t\}$ due to unit displacements of the interface nodes. To obtain these coefficients in one region, we need to solve a number of so-called Dirichlet problems, in which unit displacements are prescribed in one direction at each interface node in turn. This means we must solve the Dirichlet problem M times, where M is the number of degrees of freedom of all interface nodes in one region.

For partially coupled problems, apart from solving the first Dirichlet problem as discussed above, we need to solve an extra second Dirichlet problem with prescribed zero values of $\{u\}$ at all interface nodes in one region. The interface matrices $[K]$ for all regions are then assembled in the same way as with the FEM. The whole procedure can be divided into four stages.

Stage 1: solution of the first Dirichlet problem with unit values applied at each of interface nodes

The stiffness matrix is obtained for each region for the Dirichlet condition, with unit displacement value applied at each of the interface nodes in turn and zero values at all the other nodes, as shown in Fig. 4.1.

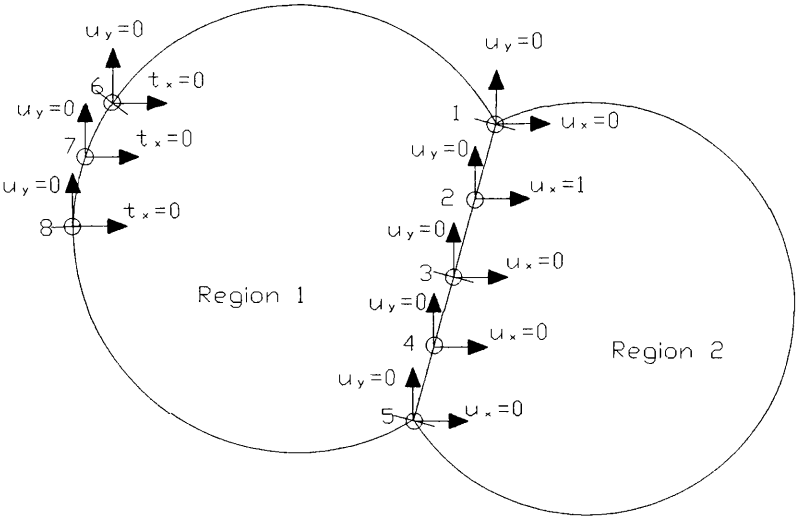

Fig 4.1. First Dirichlet problem

Fig. 4.1 shows the case when ux=1 for node 2 and zero values for all the other nodes. For external nodes, the zero value does not necessarily mean displacement but depends on the boundary condition prescribed at this node. For example, in one external element of region 1 as shown in Fig. 4.1, the x-direction traction is known, at this stage we temporarily assign a zero value to this traction, and not to the x-direction displacement which is unknown. In elastostatics problems, two or three degrees of freedom exist at each node, depending on the dimensionality. Every degree of freedom corresponds to one direction of unit displacement. The equation set to be solved at this stage can be written as:

$$[A]\begin{Bmatrix} t_{in} \\ x_{en} \end{Bmatrix} = \{B\}_n \qquad n = 1,2,\cdots\cdots, M = (2\ or\ 3)\times N_i \tag{4.2}$$

where $[A]$ is assembled solution matrix, $\{B\}_n$ is the known coefficient vector for each Dirichlet condition, computed with a unit displacement value at node n and zero values for all other nodes, so in this case it is simply the n-th column of the traction matrix $[H]$. N_i denotes the number of interface nodes. M is the number of degrees of freedom for all interface nodes. The unknown vector t_{in} contains the tractions at interface nodes and x_{en} either displacements or tractions at the external nodes, depending on the boundary conditions specified. The first subscript i and e signify the interface and external nodes respectively. The second subscript n signifies that the n-th Dirichlet condition is imposed.

Stage 2: solution of the second Dirichlet problem with 'fixed' interface nodes

The given boundary conditions are applied at the nodes which are not connected to other regions (external nodes) and Dirichlet conditions with zero values are applied at interface nodes (coupled nodes), as shown in Fig.4.2.

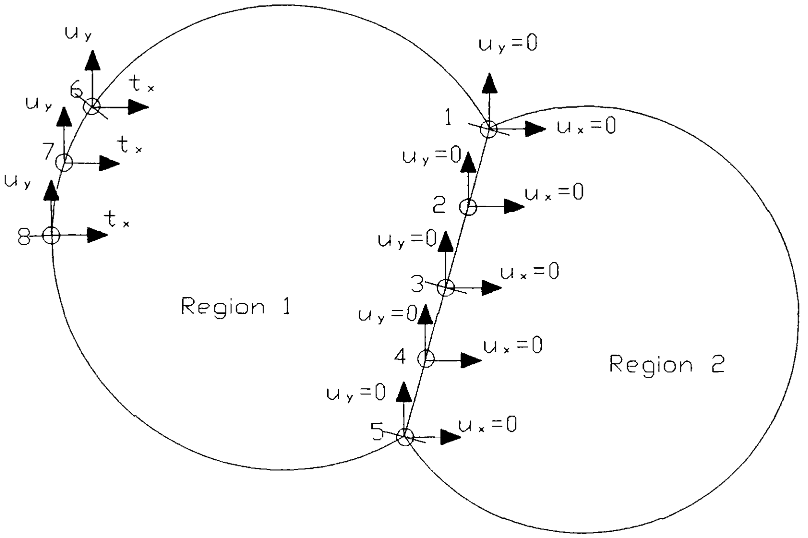

Fig 4.2. Second Dirichlet problem

For each region we can write the following equation set:

$$[A]\begin{Bmatrix} \boldsymbol{t}_{i0} \\ \boldsymbol{x}_{e0} \end{Bmatrix} = \{B\}_0 \tag{4.3}$$

where $[A]$ is the same as in the first stage and $\{B\}_0$ is a vector with known coefficients (the right-hand side) due to given boundary conditions. The unknown vector $\boldsymbol{t}_{i0}$ and $\boldsymbol{x}_{e0}$ has the same meaning as in the first stage but correspond to different Dirichlet conditions.

In the computer implementation, equation (4.2) and (4.3) can be solved once and for all with the same $[A]$ on the left-hand side and combined $(M+1)$ known vectors at the right-hand side.

After solution $\boldsymbol{t}_i$ and $\boldsymbol{x}_e$ for each region can be expressed in terms of $\boldsymbol{u}_i$ by:

$$\begin{Bmatrix} \boldsymbol{t}_i \\ \boldsymbol{x}_e \end{Bmatrix} = \begin{Bmatrix} \boldsymbol{t}_{i0} \\ \boldsymbol{x}_{e0} \end{Bmatrix} + \begin{bmatrix} T \\ X \end{bmatrix} \boldsymbol{u}_i \tag{4.4}$$

where $\boldsymbol{u}_i$ is the unknown vector of the interface node displacement, which is to be solved in the third stage. The matrix T and X are defined by:

$$T = [\boldsymbol{t}_{i1} \cdots\cdots \boldsymbol{t}_{iM}]$$
$$X = [\boldsymbol{x}_{i1} \cdots\cdots \boldsymbol{x}_{iM}] \tag{4.5}$$

where $\boldsymbol{t}_{in}$ and $\boldsymbol{x}_{in}$ (n = 1,2,...,M) are the solutions from equation (4.2).

Stage 3: Assembly of interface stiffness matrix and calculation of interface node displacements

After the interface stiffness matrices for each region have been obtained, they are assembled into a whole interface stiffness matrix $\boldsymbol{K}$ for all regions. Using the condition of equilibrium and uniqueness of displacement at the interface nodes, the following equation set is obtained:

$$\boldsymbol{K}\,\boldsymbol{u} = \boldsymbol{F} \tag{4.6}$$

where $\boldsymbol{F}$ is assembled known vector which reflect the reaction of the given boundary conditions at the interface nodes, and $\boldsymbol{u}$ refers to displacements of all interface nodes.

Stage 4: Calculation of other unknowns for each region

After stage 3, the unknown vector $\{u\}$ at the nodes of all interfaces has been determined, which can be substituted back to equation (4.4) to obtain the values of $\{t\}_i$ at the interface nodes and $\{x\}_e$ at the external nodes for each region. Thus every unknown at the boundary of the problem is determined. Note that $\boldsymbol{u}_i$ in equation (4.4) can be obtained from the interface node displacement vector $\boldsymbol{u}$, which is the solution of equation (4.6). Note that $\boldsymbol{u}_i$ include only the interface node displacements in each single region, while $\boldsymbol{u}$ involves all interface nodal displacements of the whole multi-region problem.

After all the boundary unknowns have been obtained, other results of interest may also be determined. For example, stresses on the boundary and at points inside the domain.

The method adopted here is the same as that used in the homogeneous problem, i.e., 'traction recovery' method (Cruse, 1974, Telles & Brebbia, 1979, Banerjee & Davies, 1984, Kane, 1994), to determine the boundary stress tensor. The strategy of this method is to determine the tangential strains (from the displacements) at the point of interest and, hence, using Hooke's law and the known tractions, recover the stresses. However, differences arise when dealing with interface nodes. Where both displacement and traction vectors at interface nodes are unknown, both the coefficient matrices of displacement [G] and traction [H], must be preserved in memory beforehand. After all the interface unknowns are determined, both of these can be recovered from memory to compute any internal variables.

4.3. Edge detection software

4.3.1. Edge detection software for 3D problems

The software automatically generates the PDE from the input data of continuous elements. In the author's view this is a critical aspect of the work. and make it a truly competitive approach compared with other existing corner treatment techniques. Obviously, the non-conforming or partially non-conforming method introduces more degrees of freedom than the continuous element method, particularly in 3D problems. This is a disadvantage which increases the computation cost, but more importantly, if no edge detection software is adopted, it will also dramatically increase the burden of data preparation. The only solution is to make discontinuous elements opaque: once the geometry is defined (using continuous elements) any PDEs are generated automatically by edge detection software and (once the equations are solved) the multi-valued tractions at the corners/edges are computed automatically.

While the edge detection software is relatively simple in 2D problems, it is much more complicated in 3D. However, the number of possible cases of corners/edges is limited, as shown in Fig. 4.1.

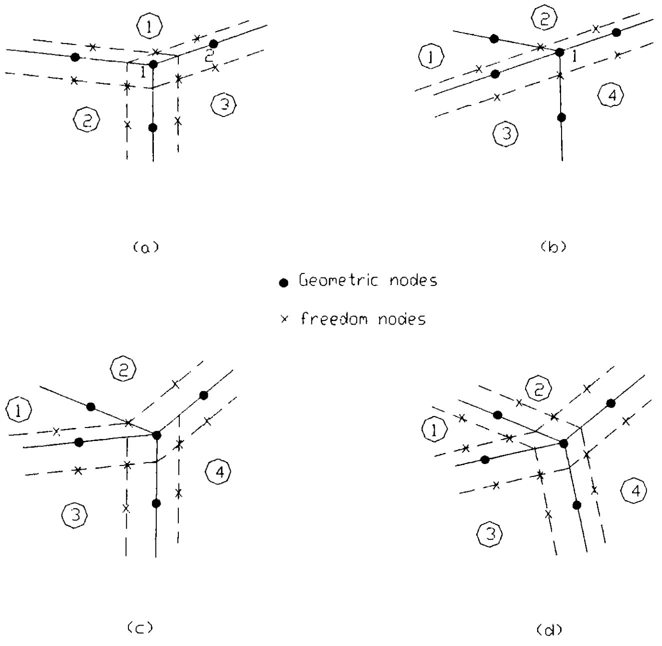

Fig 4.3. Model for edges and corners in three-dimensional problem

The corners/edges shown in Fig. 4.3 are all of convex shape, the corresponding cases for concave shape are omitted as they can be detected using the same principles.

Edge detection software for 3D problems can be developed based on the common geometrical features illustrated in Fig. 4.3. The objective of this software is to detect all edges existing in a 3D body, based on the comparison of the outward normals of two connecting elements. Once an edge is detected, the geometric nodes which are located at these edges are moved inside the element to become so-called free nodes, and then, if necessary, additional new free nodes are assigned node numbers. This process goes on until all edges are detected and all free nodes (including intrinsic coordinates and node number) are determined.

In the computer implementation, based on the 4-parameter PDE defined in section 3.2.1, this process can be realized by two steps.

(1) Element-wise edge detection is performed by comparing the outward normals at the mid-node of each element side (node 5,6,7,8 in Fig. 3.9) with those of neighbouring elements. After all four sides are considered the intrinsic coordinates of all nodes can be determined.

(2) Assign node numbers to every free node. This is realized by a node-wise searching procedure through the existing numbering system. Free nodes can be distinguished from the unchanged geometric nodes by their intrinsic coordinates. In the first step, the intrinsic co-ordinates of free nodes has already been determined. For geometric nodes, the values of intrinsic co-ordinates are either ±1 or 0. By contrast, free nodes have at least one of their intrinsic coordinates different from 0, ± 1. Thus, free nodes can be readily detected.

During the node-wise searching procedure, we find out which elements share particular nodes. Of those nodes which share the same node number currently, the free nodes are detected based on the criteria mentioned above and given new node numbers. A restriction of the current program means that one free node must inherit the current node number in order to preserve the serial node numbering system.

For example, in Fig. 4.3 (a), three elements 1, 2 and 3 intersect the corner node 1, and three element nodes at this corner all become free nodes. So two of them will be assigned two new node numbers, while the third node inherits the current node number (1).

A more complex case arises in Fig. 4.3 (b). Here we can see four elements 1~4 intersect at node 1, and all four element nodes at this edge point become free nodes. But two free nodes of element 1 and 2 are in fact in the same position and should share a common node number. Similarly, the free nodes of element 3 and 4 are also the same node.

In the program code, this indexing process can be realized by two methods.

Method I

After the intrinsic co-ordinates of the free nodes have been determined in the first step, their Cartesian co-ordinates can be computed by interpolation from those of the eight original element nodes. In this case, the Cartesian co-ordinates of all four free nodes can be obtained. The distance between any two of them can also be calculated. The distance of two free nodes which share the same position should be zero in theory, but we allow for an approximation error, e.g., one percent of the element length. If this happens, the two nodes are assigned the same node number.

Method II

In this method, one free node is chosen and its normal is compared with those of the other three nodes. If the angle subtended by them is less than 15°, these two nodes can be judged to share the same position, and are assigned the same node number.

Other possible cases of corners formed by four elements are listed in Fig. 4.3 (c) and (d). All these cases are different and should be treated separately in the computer program. The criteria to distinguish between them are also based on the intrinsic co-ordinates of free nodes. For example, in the cases where four elements intersect, we can distinguish between them by calculating the number of free nodes which have at least one unit value in their intrinsic co-ordinates. There are four in case (b), two in case (c), and none in case (d).

The four-parameter quadratic PDE is useful for geometrically simple 3D bodies. But for more complex objects, a more flexible approach must be adopted, e.g., eight-parameter PDE, which will be discussed in next section.

4.3.2. Eight-parameter interpolation functions

The 4-parameter PDE can not deal with some complicated 3D objects. This is because it adopts only one parameter on each element side. If this side is an edge, all three nodes at this side must be moved inside the element to become free nodes.

If five elements intersect at a node, as shown in Figure 4.4, the five elements 1~5 have a common node. According to the procedure described before, the sides between elements 1 and 4, elements 3 and 5 will be detected as edges, so the free nodes at these two sides are moved inside the elements. But no edge is detected between elements 1 and 2, nor is between elements 2 and 3, because all three elements (element 1, 2, 3) lie on a flat surface. Therefore, the free nodes generated from the previous detection process are not moved inside these elements. As a consequence, in element 2, a contradiction arises.

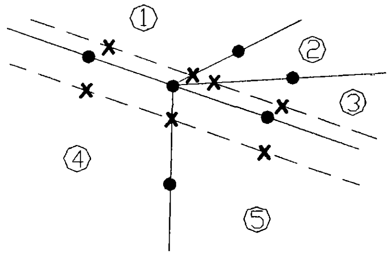

Fig 4.4. Model for edges/ corners node where 5 elements intersect.

To overcome the limitations of the four-parameter PDE method, a more flexible eight-parameter PDE is adopted. The intrinsic coordinates of the eight free nodes inside the element are determined by eight parameters (d_1~d_8), as shown in Fig. 4.5.

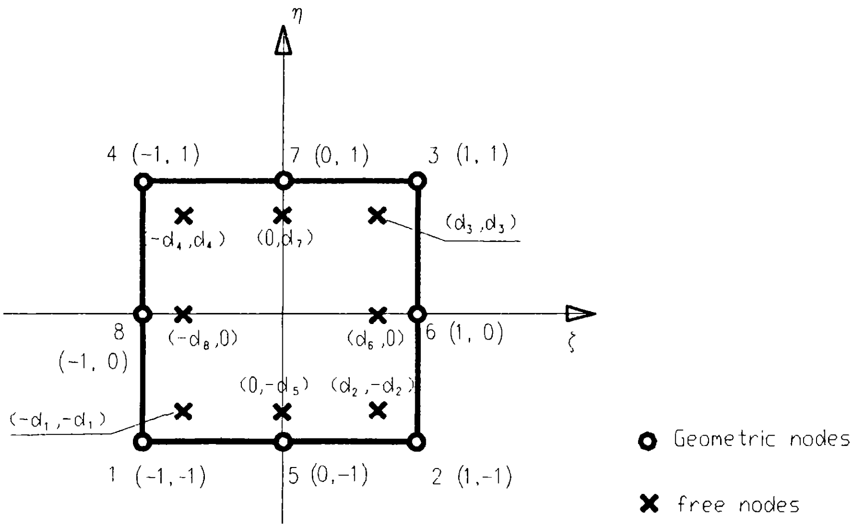

Fig 4.5. Local (intrinsic) coordinate system for 8-parameter PDEs

We can see that each free node is defined by one parameter. The interpolation functions for this element are much more complex, the detail of which is listed in Appendix A.

The advantage of the eight-parameter PDE is obvious. With more parameters, the three free nodes along an element side are no longer required to move inside together once an edge is detected. In some ways this element is easier to handle because each node is dealt with independently of all other nodes. The difficulties associated with applying the four-parameter PDE are overcome. The edge detection software using the eight-parameter PDE is similar to that of four-parameter PDE except in the first step.

Instead of an element-wise detection procedure in which the outward normals at the mid-nodes in every element side is compared with those of contiguous elements, a node-by-node detection approach is adopted, involving a search through the existing node system to detect whether each individual node is located at an edge or corner. For this to be done, we find out which elements are connected to this node, and their outward normals at the node are compared to each other. If a corner or edge is detected, a free node is generated inside every element and their intrinsic co-ordinates are determined. The node number indexing process in the second step becomes much simpler. Every newly generated free node is assigned a new node number (except one, which inherits the current number of the geometric node).

The greater simplicity of this detection scheme means it is now possible to implement edge detection software into 3D multi-region problems, which will be discussed later. However, despite these advantages, it introduces more degrees of freedom, e.g., in Fig.4.3 (b), four free nodes are generated instead of two nodes when the four-parameter PDE is used.

4.3.3. Edge detection software for multi-region problems

In the context of multi-region problems, corners and edges occur not only at geometrical discontinuities but also at regional interfaces.

For simplicity, we describe the edge detection software only for two-dimensional multi-region problems. The principles are also valid for 3D cases.

First, we define two node numbering systems for all element nodes: a local one, specified for each region, as shown in Fig. 4.6 (b), and a global one, as shown in Fig. 4.6 (a).

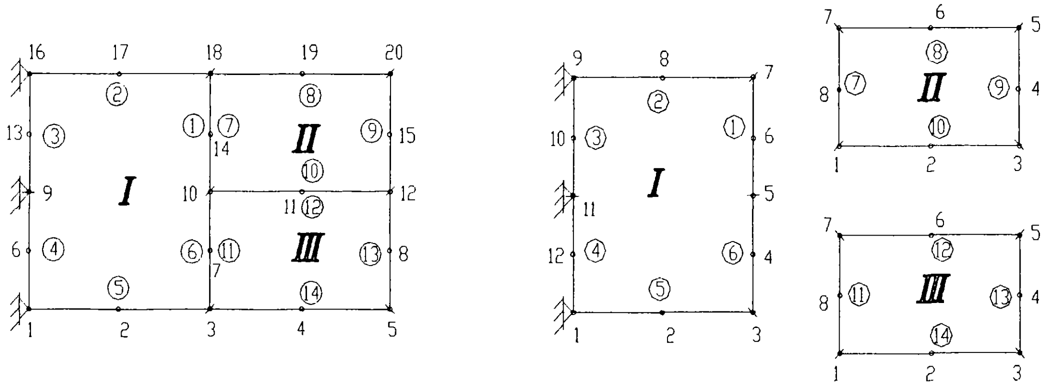

(a)

(b)

Fig. 4.6 (a) Global numbering system for the three-region model
(b) Local numbering system for each region

The local numbering systems are independent of each other. Each region is defined by quadratic boundary elements on its boundary. These elements are assigned global index numbers only. This means nodes may be both globally and locally numbered, but elements are only numbered globally. In our example, region I consists of element 1~6, region II of elements 7~10 and region III, 11~14. At the interface between the two regions, there is one boundary element but it is numbered twice, as shown in Fig.4.6. This is called an "element pair", which belongs to both regions. These two elements are identical except that the outward normal is reversed, e.g., element pairs 1&7, 6&11, 10&12 in Fig. 4.6. This definition of the "element pair" has two purposes: one is to preserve the continuity of element numbering for each region, and to simplify the computer code. When one interface element is considered, it is easy to find the corresponding one belonging to opposite region. This step plays an important role in re-indexing the global numbers of free nodes. After each element pair has been specified in the data input, incidences of elements in the global and local (region) numbering are shown in Table 4.3.

Table 4.1 Incidences of boundary elements in global and local numbering schemes.

Region	Element	Global			Local		
		1 (start)	2 (end)	3 (mid)	1 (start)	2 (end)	3 (mid)
I	1	10	18	14	5	7	6
	2	18	16	17	7	9	8
	3	16	9	13	9	11	10
	4	9	1	6	11	1	12
	5	1	3	2	1	3	2
	6	3	10	7	3	5	4
II	7	18	10	14	7	1	8
	8	20	18	19	5	7	6
	9	12	20	15	3	5	4
	10	10	12	11	1	3	2
III	11	10	3	7	7	1	8
	12	12	10	11	5	7	6
	13	5	12	8	3	5	4
	14	3	5	4	1	3	2

This numbering system was used by Beer (2001) in a multi-region BEM. The definition of double node numbering but single element numbering is also suitable for generating PDEs using the edge detection software. In the stiffness matrix assembly method, this makes it possible to assemble and compute the matrix of each region separately. The edge detection software, with the introduction of the local node numbering, now involves further steps:

Step 1: Detection of corners and PDE generation in individual regions

The edge detection scheme developed for homogeneous problems can be used here. But it is used to modify the current local node numbering system for every region. Obviously, this adjusted system involves the new free nodes generated in each region.

Step 2: Indexing the global node numbers for the multi-region model

In this step, the global number indexing procedure is done for the whole body. A node-by-node search similar to that used in the homogeneous case is performed. However, this time it is done through a global node numbering search. At each node, all elements associated with it are found. If a node is located at a corner, there must be some nodes, among all those found, which have already become free nodes during the step 1, and perhaps have been assigned a new local node number. However, they still have the same global number as the current corner node.

Now the global number for any new free node can be assigned. If this node is on an interface element, its counterpart of the element pair belonging to another region should also be a free node. If it is also at a corner of this region, then this is already true. What remains to be done is to assign the same global number to these two nodes. But in some cases, as shown in Fig. 4.7, the corresponding node may not be located at a corner. Then this node is also changed to a free node, and the local numbering system for this region is modified accordingly.

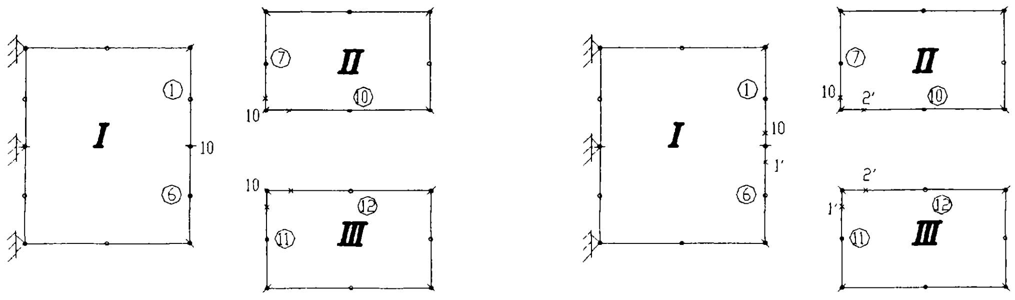

(a) (b)

Fig. 4.7. (a) Free nodes determined in the first step (only node 10 is considered).
(b) Free nodes determined in the second step.

In Fig. 4.7, all three regions intersect at node 10. At the second step, when the node-by-node search reaches this node, element 1, 6, 7, 10, 11 and 12 are found to be connected to this common node. In region *II*, node 2 of element 7 and node 1 of element 10 become free nodes at the first step. In region *III*, node 1 of element 11 and node 2 of element 12 are free nodes. All of these elements are interface elements. Thus in region *I*, node 1 of element 1 and node 2 of element 6 should also be free nodes, but they have not become free nodes after the first step because no corner exists at node 10 in region I. As a result, in the second step we change not only the intrinsic and global coordinates of these two element nodes, but also the local numbering system for region *I* in order to incorporate them. After all free nodes are determined we assign a new global number 1' (assumed) to the free nodes of interface element 6 and 11, 2' to those of element 10 and 12, while those of element 1 and 7 inherit the current global number 10, to preserve the serial global node numbering system.

One more advantage of using the PDE method in multi-region problems over the auxiliary equation method is that, the total unknowns at the interface will be equal to the number of equations. In the auxiliary equation method (Beer, 2001), the system is over-determined and can not be solved directly.

To illustrate this point, we adopt an example which is similar to the above but with linear elements discretizing the boundary, as shown in Fig. 4.8.

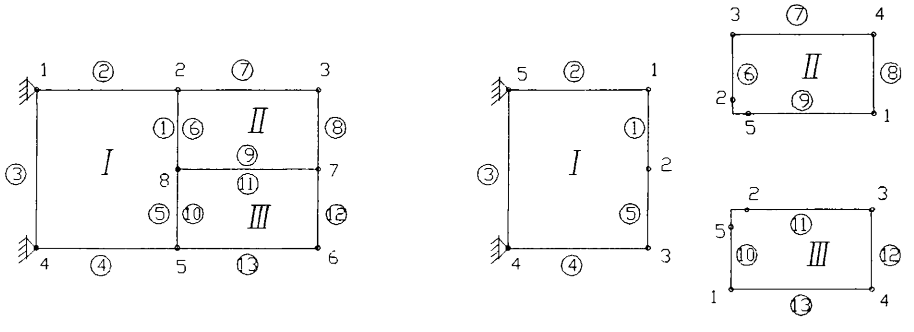

(a) (b)

Fig. 4.8 (a) Global numbering system for the three-region model(linear element)
(b) Local node numbering system for each region(linear element)

In Fig. 4.8 (b), local node number 2 and 5 refers in fact to one node. However, because it is a corner node we define two nodes to represent the multi-value tractions.

In the stiffness matrix assembly method, the equations of equilibrium and compatibility are used for assembly of regions. Assuming that no net tractions are applied at the interface, the equations of equilibrium in terms of tractions are:

$$\begin{aligned} t_1^{I} + t_3^{II} &= 0 \\ t_2^{I} + t_2^{II} &= 0 \\ t_2^{I} + t_5^{II} &= 0 \\ t_2^{III} + t_5^{II} &= 0 \\ t_3^{I} + t_1^{III} &= 0 \\ t_3^{III} + t_1^{II} &= 0 \end{aligned} \tag{4.7}$$

In the above equations, the subscript signifies the node number, while the superscript signifies region number. There are 6×2 equations but at the interface only 4×2 unknowns exist (u_2, u_8, u_5, u_7). The system is over-prescribed. Borrowing an idea from the finite element method, Beer (2001) used equivalent nodal forces to reduce the number of equilibrium equations and made it equal to the number of unknowns. However, this over-description problem does not arise using the PDE method and therefore, the solution procedure is straightforward.

For the 3D case, we adopt the eight-parameter quadrilateral PDE. In the edge detection software, if one node is detected as a corner node in one region, then all elements (in this and other regions) which intersect at this node are found, and their corresponding nodes are changed to free nodes. This procedure may introduce some unnecessary extra degrees of freedom. However, this disadvantage is offset by simplicity of the detection and indexing procedures, especially in 3D.

Fig. 4.9 shows a typical example of 3D multi-region body where five regions meet.

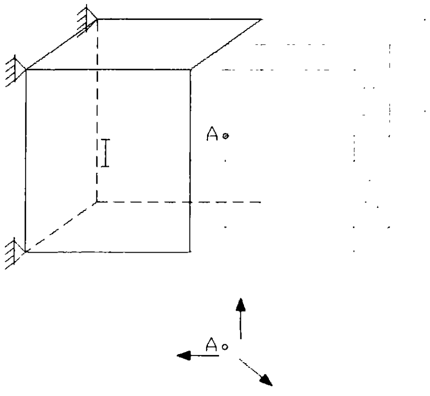

Fig. 4.9 Three-dimensional model of cantilever beam with five regions

At node A where five regions meet, in the four regions II~IV, their corresponding element nodes are all detected as corner nodes. Therefore, the element nodes at this point all become free nodes, and are moved inside their respective elements. For region I, however, the node A is not a corner, so no free nodes are generated at this location at the first step. In a second step, we artificially change the element nodes in region I into free nodes, and update its local node numbering system. Finally, a global number can be assigned to all new free nodes.

4.4. Numerical examples

We now consider a benchmark multi-region example, a thick circular cylinder subjected to internal pressure $p = 1$. This is a two-dimensional plane strain problem. Fig. 4.10 shows a quarter of the cylinder is divided into four regions.

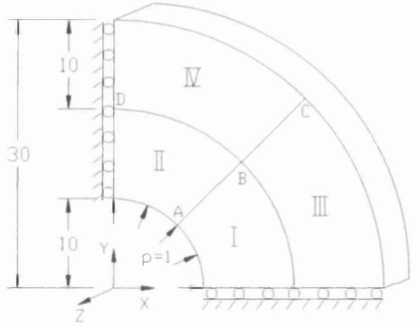

Fig. 4.10 Cylinder subjected to internal pressure

The vertical ($x = 0$) and horizontal ($y = 0$) boundaries are constrained by 'roller' supports (i.e., $u_x = 0$ and $u_y = 0$, respectively). To begin with, we assume that all four regions have the same material properties (i.e., an homogeneous problem), for which an analytical solution is available. We define $E_1 = E_2 = E_3 = E_4 = 1$ and $v_1 = v_2 = v_3 = v_4 = 0.3$ (the subscript indicates the region number). Figs4.11. (a) and (b) show the variations of the radial displacements and circumferential stresses along the radial (ABC) direction.

(a)

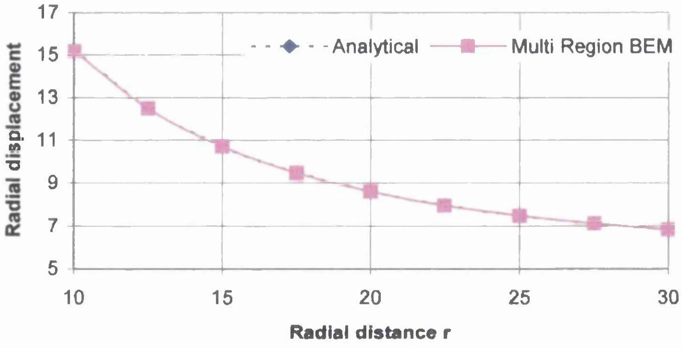

(b)

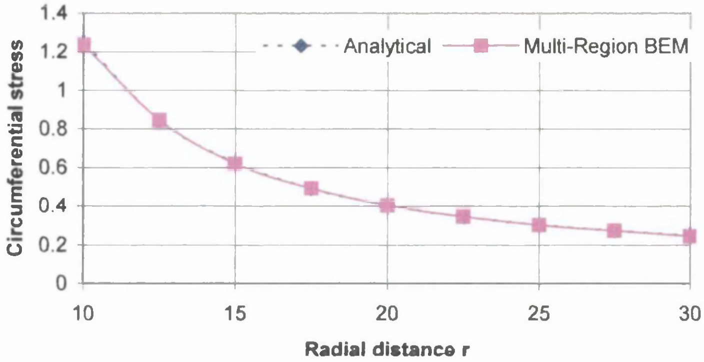

Fig. 4.11 (a) Variation of radial displacement along radius ABC
(b) Variation of circumferential stress along radius ABC
(E_1=E_2=E_3=E_4=1, v_1= v_2= v_3= v_4=0.3)

We observe that results obtained from multi-region BEM using partially discontinuous element method match almost exactly the analytical solution. This verifies the high accuracy of the PDE method.

Table 4.2 lists some results obtained by different edge/corner methods compared with the analytical solutions; we can see that unique traction assumption gives poor results, while the current method produces the most accurate results.

Table 4.2. Radial displacements by different methods (E_1=E_2=E_3=E_4=1)

Point	Analytical solution	Partially discontinuous element	Auxiliary equation (Gao&Davies,2001)	'Unique traction' at D	'Unique traction' at B
A	15.275	15.207	15.124	14.691	14.540
B	8.613	8.617	8.587	8.107	7.731
C	6.825	6.829	6.796	6.334	5.928

As an example of piece-wise (zonal) inhomogeneity, we consider two cases:
(1) $E_1 = E_2 = 1$, $E_3 = E_4 = 3$,
(2) $E_1 = E_3 = 3$, $E_2 = E_4 = 1$,

Poisson's ratio is 0.3 in all regions.

Figure 4.12 shows radial displacements and circumferential stresses along the radius ABC for these two cases. Naturally, displacement remains continuous in the case when the outer ring is stiffened and, as expected, there is a pronounced change in the gradient of the displacement. We can see from Fig. 4.12 (b) that for case (1) the circumferential stress is discontinuous at the interface, where the material properties change. The ordinary BEM fails to catch this phenomenon if the “equal traction” assumption is invoked.

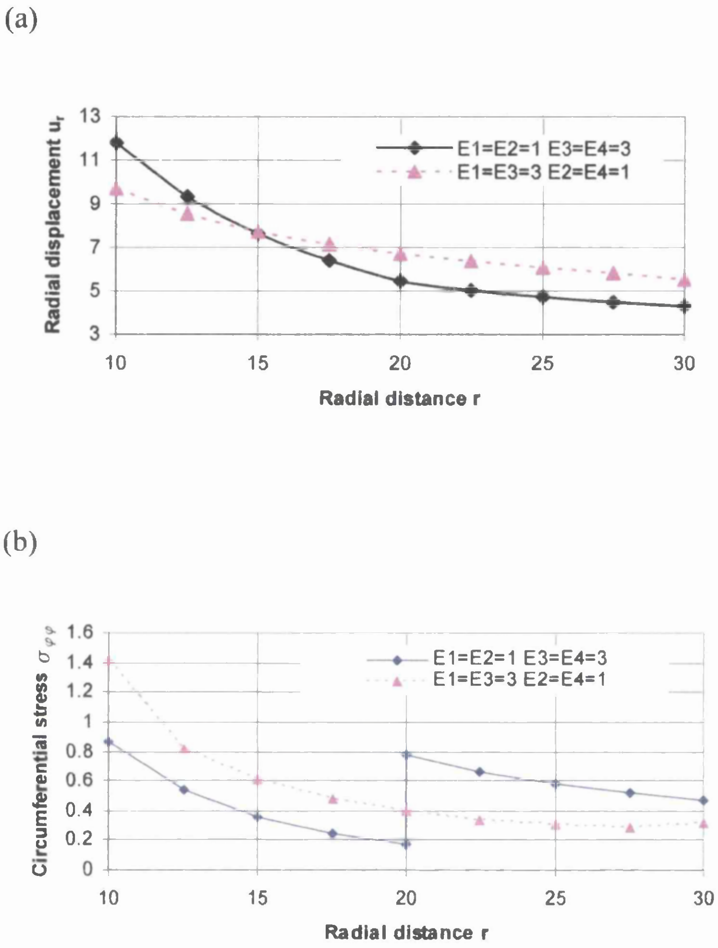

Fig. 4.12 (a) Variation of radial displacement along radius ABC

(b) Variation of circumferential stress along radius ABC

To verify the multi-region formulation, we also compare the results with those computed from FEM. Case (2) is considered. The results are shown in Fig. 4.13, which shows the results from the two methods match very well.

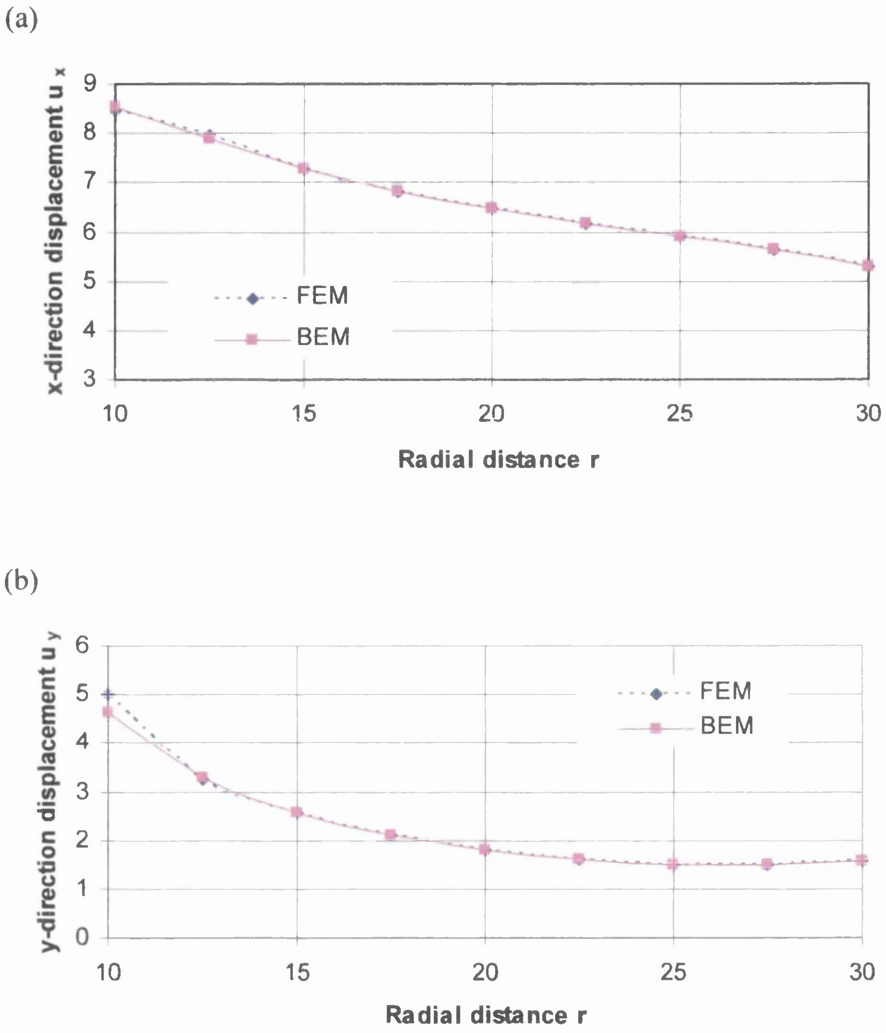

Fig. 4.13 (a) x-direction displacement along radius ABC
(b) y-direction displacement along radius AB
(E_1=E_3=3, E_2=E_4=1)

The effect of the offset parameter on numerical stability and accuracy is now examined for this multi-region problem. For case (1), some results are shown in Fig.4.14 and 4.15.

(a)

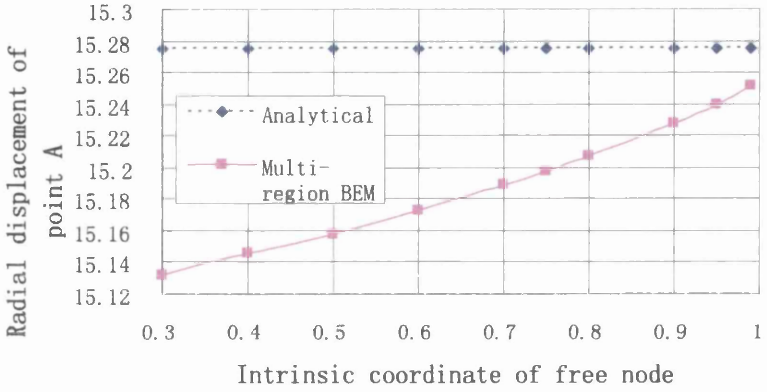
Radial displacement of point A
15.3
15.28
15.26
15.24
15.22
15.2
15.18
15.16
15.14
15.12
Analytical
Multi-region BEM
0.3
0.4
0.5
0.6
0.7
0.8
0.9
1
Intrinsic coordinate of free node

(b)

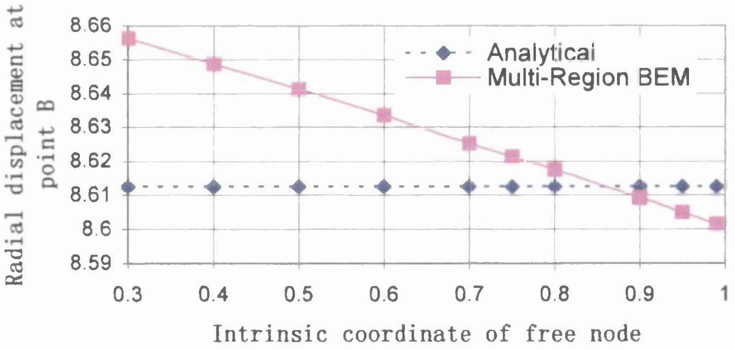
Radial displacement at point B
8.66
8.65
8.64
8.63
8.62
8.61
8.6
8.59
Analytical
Multi-Region BEM
0.3
0.4
0.5
0.6
0.7
0.8
0.9
1
Intrinsic coordinate of free node

(c)

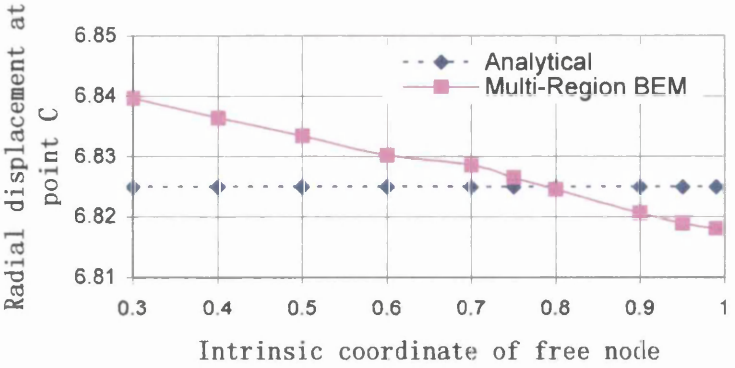

Fig. 4.14 Radial displacement at (a) point A, (b) point B and (c) point C vs. the offset parameter d of free node

Fig. 4.14 shows the variation of radial displacement at the points *A*, *B* and *C* vs. the offset parameter. The position of points *A*, *B* and *C* is shown in Fig. 4.10. In this example, it can be seen that within range of d = 0.3~0.99, the maximum error percentage is only 0.93% at point *A*, 0.51% at point *B* and 0.21% at point *C*, respectively. Therefore, the results are very stable and accurate over a wide range of the offset parameter *d*. The displacements here are computed from the interpolated value of only one element from one region (here, it is region I), rather than the average value calculated from those of all four regions.

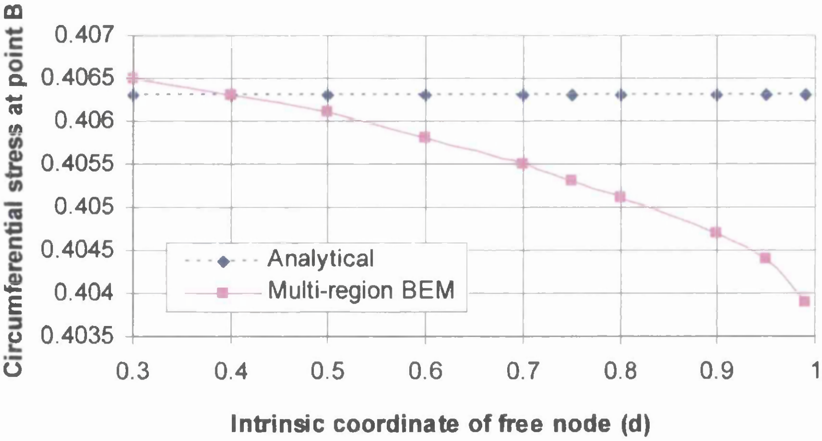

Fig. 4.15 Circumferential stress $\sigma_{\theta\theta}$ vs. the offset parameter (d) of free nodes.

Fig. 4.15 shows the variation of circumferential stress $\sigma_{\theta\theta}$ at point *B* vs. location of the free nodes. Accuracy decreases from the most accurate at $d = 0.3$ to a maximum error of 0.59% at $d = 0.99$, where the free nodes are very close to the element edge. The stresses are computed from the extrapolated values of only one element; the average value from all elements intersecting at B should be more accurate. This is shown in Fig. 4.16.

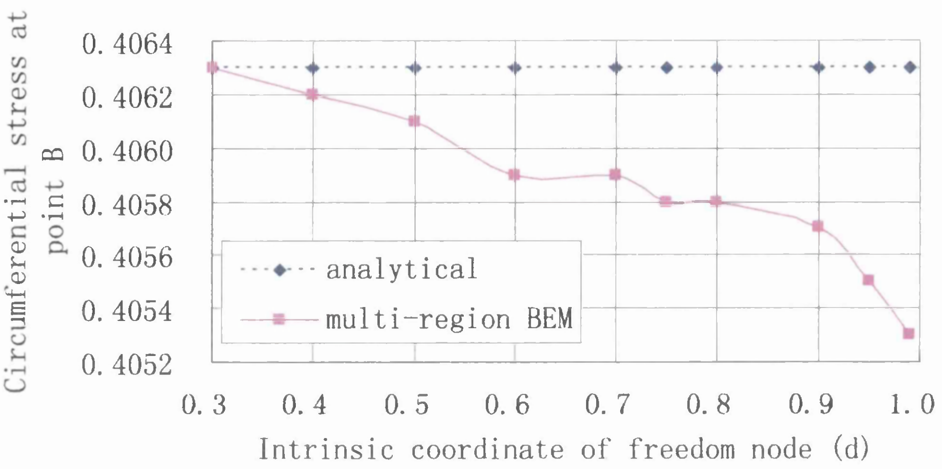

Fig. 4.16 Circumferential stress $\sigma_{\theta\theta}$ vs. the offset parameter d of free nodes(average value).

A similar trend appears in from both Fig. 4.15 and 4.16. However, the average value is much more accurate: the maximum error is 0.25%.

The numerical trials show that stable and accurate results can be obtained over a reasonably wide range of the offset parameter in multi-region analysis. However, greater caution should be exercised in the multi-region case, in order to avoid the over crowding of collocation points at corners, where several regions meet. Since the contributions of collocation points are never added together, it becomes possible to obtain equations with weak pivots, which may result in an ill-conditioning of the system equations. As a consequence, the results may become unstable. In the above example, the deterioration of results at the corner point *B* when the free nodes move extremely near to the element edge (see Fig. 4.15 and 4.16), may be partly attributed to the overcrowding of free nodes, as all four regions meet at this point.

Chapter 5

Green's functions for multi-layered systems: I - Analytical

In the previous chapter, we examined the multi-region BEM for layered systems. In addition to the discretization of the outside boundary of the system, the interfaces between each layer must also be discretized. Thus, an advantage of BE analysis namely boundary-only discretization is to some extent lost. However, if we develop Green's functions for a multi-layered system, and use them instead of the Kelvin's solution, interface discretization can be eliminated. In this chapter, the popular propagator matrix method, which incorporates the Fourier and Hankel transforms into the cylindrical system of vector functions, is described and used to derive the Green's functions for a transversely isotropic multi-layered half-space. These analytical results will be employed to calculate the Green's functions using numerical integration techniques in the next chapter.

5.1. Background

Multi-layered systems are frequently encountered in geotechnical engineering. In soil, natural deposition process often results in the formation of multi-layered soil structures. Thus, it is often necessary to analyze systems consisting of a stack of horizontal layers over an elastic homogeneous half space.

Layered systems can of course be analysed using the Boundary Element Method (BEM). However, one of the main advantages of BEM (discretization only along the boundary) is significantly reduced if such problems are treated as piece-wise homogeneous, since this approach requires discretization of the interfaces between the soil strata in addition to the boundary. This can become computationally cumbersome when a large number of layers are encountered.

Layered elastic systems can be handled much more effectively by BEM if the corresponding Green's functions are available. Since layered Green's functions satisfy exactly the continuity conditions along the interfaces, discretization is restricted to the problem boundary. Developing the Green's functions for layered systems is therefore key to the success of the approach.

However, whereas the Green's functions for homogeneous media may be evaluated in closed forms, the corresponding solutions for inhomogeneous media are far less tractable.

Green's functions for layered half-spaces or multi-layered composites are relevant to many engineering branches. Consequently, many approaches have been suggested for calculating the required Green's functions. In the case of horizontally infinite and layered system, the most popular approach is the propagator matrix method, which originated with the work of Thomson (1950), Haskell (1953), and Gilbert & Beckus (1966) for elasto-dynamics. The fundamental solutions in the frequency or wave-number domain have been recently derived (Kausel & Peek 1982, Luco & Apsel 1983, Franssenns 1983, Beskos 1987, Bouden et al. 1990).

For the corresponding elastostatic problems, the propagator matrix is often derived directly instead of obtaining it from its dynamic counterpart by taking the limit as frequency close to zero. Direct solutions were derived by Singh (1970), Jovanovich et al. (1974), and Sato & Mutsu'ura (1973) for the isotropic medium; and by Singh (1986), Yue & Wang (1988) for the transversely isotropic medium.

Pan (1989) introduced a Cartesian and cylindrical system of vector functions for layered structures to obtain solutions for surface loadings and internal dislocations. The static Green's functions in multi-layered transversely isotropic and isotropic half spaces have also been derived.

Yuan & Yang (2003) presented a formulation for the Green's displacement and stress using the generalized Stroth formalism. Using a similar methods, Yang & Pan (2002) derived the complete set of the Green's functions including displacement, stress and their derivatives for anisotropic elastostatic multi-layered composites using the tri-material expansion solutions recently developed by the Yang & Pan (2002). These solutions were illustrated by applications to multi-layer composite structures.

This chapter deals in some detail with the principle of the propagator matrix method. With the cylindrical system of vector functions, the Green's functions in a multi-layered transversely isotropic half space are obtained in the transformed domain. The derivation process mainly follows the work of Pan (1989, 1997). The derivation of the corresponding functions in the physical domain will be discussed in the next chapter.

5.2. The cylindrical system of vector functions

Perhaps the most popular approach for dealing with horizontally infinite and layered systems is the transformation method in which Fourier or Hankel transforms are used to suppress the horizontal variables (*x*, *y* in Cartesian coordinate system or *r*, θ in cylindrical system). The transformed coefficients can be obtained by solving a linear set of first-order differential equations, which are combinations of exponential terms of the vertical variable z.

An alternative approach is to define a cartesian or cylindrical system of vector functions (Pan 1997, 1989). These two vector systems are in fact an extension of the Fourier and Hankel transform methods, but possess two advantages: (1) any integrable vector function such as displacements and tractions can be expressed in terms of these vector function systems, (2) for elastic problems with relatively higher material symmetry, the propagator matrices derived in these two vector systems are exactly the same. In the following discussion, we only consider the cylindrical system.

5.2.1. Cylindrical system of vector functions

The cylindrical system of vector functions is as follows

$$\begin{aligned} &\boldsymbol{L}(r,\theta;\lambda,m) = \boldsymbol{i}_z S(r,\theta;\lambda,m) \\ &\boldsymbol{M}(r,\theta;\lambda,m) = grad\ S = (\boldsymbol{i}_r \frac{\partial}{\partial r} + \boldsymbol{i}_\theta \frac{\partial}{r\partial\theta}) S(r,\theta;\lambda,m) \qquad (5.1) \\ &\boldsymbol{N}(r,\theta;\lambda,m) = curl(\boldsymbol{i}_z S) = (\boldsymbol{i}_r \frac{\partial}{r\partial\theta} - \boldsymbol{i}_\theta \frac{\partial}{\partial r}) S(r,\theta;\lambda,m) \end{aligned}$$

where $\boldsymbol{i}_r$, $\boldsymbol{i}_\theta$ and $\boldsymbol{i}_z$ are unit vectors in (r, θ, z) directions, respectively, of the cylindrical coordinate system. The cylindrical coordinate (r, θ) and transform parameter (λ, m) are separated by the semicolon (;) to indicate that they belong to different systems. The scalar function

$$S(r,\theta;\lambda,m) = \frac{1}{\sqrt{2\pi}} J_m(\lambda r) e^{im\theta} \qquad (5.2)$$

also satisfies the Helmholz equation

$$\frac{\partial^2 S}{\partial r^2} + \frac{\partial S}{r\partial r} + \frac{\partial^2 S}{r^2\partial\theta^2} + \lambda^2 S = 0 \qquad (5.3)$$

where $i = \sqrt{-1}$, $J_m(\lambda r)$ is the Bessel function of order m, with m=0 corresponding to axially symmetric deformation.

Because this cylindrical system (5.1) forms an orthogonal and complete space, any integrable vector function can be expressed in terms of it. In particular, for the unknown displacement and traction vectors, we have

$$\boldsymbol{u}(r,\theta,z) = \sum_m \int_0^\infty \left[U_L(z)\boldsymbol{L}(r,\theta) + U_M(z)\boldsymbol{M}(r,\theta) + U_N(z)\boldsymbol{N}(r,\theta)\right]\lambda d\lambda \tag{5.4a}$$

$$\begin{aligned} \boldsymbol{t}(r,\theta,z) &= \sigma_{rz}\boldsymbol{i}_r + \sigma_{\theta z}\boldsymbol{i}_\theta + \sigma_{zz}\boldsymbol{i}_z \\ &= \sum_m \int_0^\infty \left[T_L(z)\boldsymbol{L}(r,\theta) + T_M(z)\boldsymbol{M}(r,\theta) + T_N(z)\boldsymbol{N}(r,\theta)\right]\lambda d\lambda \end{aligned} \tag{5.4b}$$

where $U_L(z), U_M(z), U_N(z)$ are the transformed displacement coefficients (expansion coefficients) in the cylindrical system, $T_L(z), T_M(z), T_N(z)$ are the transformed traction coefficients. For brevity, the parameters λ and m in the vector functions $\boldsymbol{L}$, $\boldsymbol{M}$ and $\boldsymbol{N}$ are omitted.

We may visualize $\boldsymbol{L}$, $\boldsymbol{M}$ and $\boldsymbol{N}$ as three axes of the transformed space, and U_L, U_M and U_N as the projection of the displacement vector on these three axes respectively.

5.2.2. Transversely isotropic elastic material

The well-known transversely isotropic material is characterized by five elastic coefficients (Lekhnitskii, 1963). This material exhibits isotropic behaviour in a plane (x-y plane) and anisotropic behaviour perpendicular to this plane (z axis). In other words, the material coefficients remain invariant under a rotation through any angle θ about the axis of symmetry (z axis). The propagator matrices used for deriving Green's functions for multi-layered systems can easily handle transversely isotropic elastic materials. Of course, the isotropic elastic material is only a special case of the transversely isotropic elastic one. In the following sections, we deal with the propagator matrices for the transversely elastic case. The generalized Hooke's law in cylindrical coordinates (r, θ, z) can then be expressed as

$$\begin{aligned}
\sigma_{rr} &= C_{11}e_{rr} + C_{12}e_{\theta\theta} + C_{13}e_{zz} \\
\sigma_{\theta\theta} &= C_{12}e_{rr} + C_{11}e_{\theta\theta} + C_{13}e_{zz} \\
\sigma_{zz} &= C_{13}e_{rr} + C_{13}e_{\theta\theta} + C_{33}e_{zz} \\
\sigma_{\theta z} &= 2C_{44}e_{\theta z} \\
\sigma_{rz} &= 2C_{44}e_{rz} \\
\sigma_{r\theta} &= 2C_{66}e_{r\theta}
\end{aligned} \tag{5.5}$$

where

$$C_{66} = (C_{11} - C_{12})/2 \tag{5.6}$$

In Eqn. (5.5) σ_{ij} and e_{ij} are stress and strain tensors in the cylindrical coordinate system, respectively. The range of i, j = r, θ, z here. C_{11}, C_{12}, C_{13}, C_{33} and C_{44} are five elastic coefficients of the material. In terms of engineering parameters, they are:

$$\begin{aligned}
C_{11} &= \frac{(1-n\nu_{zx}^2)E_x}{AB} \\
C_{12} &= \frac{(\nu_{xy}+n\nu_{zx}^2)E_x}{AB} \\
C_{13} &= \frac{\nu_{zx}E_x}{B} \\
C_{33} &= \frac{(1-\nu_{xy})E_z}{B} \\
C_{44} &= G_{xz} = G_{yz}
\end{aligned} \tag{5.7}$$

where

$$\begin{aligned}
A &= 1 + \nu_{xy} \\
B &= 1 - \nu_{xy} - 2n\nu_{zx}^2 \\
n &= E_x / E_z
\end{aligned} \tag{5.8}$$

The ratio n is a measure of the degree of anisotropy. The symbols E, G and ν with appropriate subscripts denote Young's moduli, shear moduli and Poisson's ratios associated with the corresponding axes. The coefficients C_{66} is determined from C_{11} and C_{12} by eqn. (5.6). In terms of engineering parameters

$$C_{66} = \frac{E_x}{2A} \tag{5.9}$$

The remaining engineering coefficients G_{xy} and ν_{xz} are related to the four coefficients E_x, E_z, ν_{xy} and ν_{zx}; thus they are not independent.

$$\begin{aligned} G_{xy} &= \frac{E_x}{2(1+\nu_{xy})} \\ \nu_{xz} &= n\nu_{zx} \end{aligned} \tag{5.10}$$

The strain-displacement relations in cylindrical coordinates are:

$$\begin{aligned} e_{rr} &= \frac{\partial u_r}{\partial r} \\ e_{\theta\theta} &= \frac{\partial u_\theta}{r\partial\theta} + \frac{u_r}{r} \\ e_{zz} &= \frac{\partial u_z}{\partial z} \\ 2e_{r\theta} &= \frac{\partial u_r}{r\partial\theta} + \frac{\partial u_\theta}{\partial r} - \frac{u_\theta}{r} \\ 2e_{\theta z} &= \frac{\partial u_\theta}{\partial z} + \frac{\partial u_z}{r\partial\theta} \\ 2e_{rz} &= \frac{\partial u_z}{\partial r} + \frac{\partial u_r}{\partial z} \end{aligned} \tag{5.11}$$

where u_r, u_θ and u_z are the displacement components in the r, θ and z direction respectively. The equilibrium equations, in the absence of body forces, are:

$$\begin{aligned} &\frac{\partial\sigma_{rr}}{\partial r} + \frac{\partial\sigma_{r\theta}}{r\partial\theta} + \frac{\partial\sigma_{rz}}{\partial z} + \frac{\sigma_{rr}-\sigma_{\theta\theta}}{r} = 0 \\ &\frac{\partial\sigma_{r\theta}}{\partial r} + \frac{\partial\sigma_{\theta\theta}}{r\partial\theta} + \frac{\partial\sigma_{\theta z}}{\partial z} + \frac{2\sigma_{r\theta}}{r} = 0 \\ &\frac{\partial\sigma_{rz}}{\partial r} + \frac{\partial\sigma_{\theta z}}{r\partial\theta} + \frac{\partial\sigma_{zz}}{\partial z} + \frac{\sigma_{rz}}{r} = 0 \end{aligned} \tag{5.12}$$

5.3. General solutions and propagator matrices

In this and the next two sections, we follow the procedure described by Pan (1997) to derive the propagator matrix in terms of the cylindrical system of vector functions. This matrix is needed to derive Green's functions in a multi-layered transversely isotropic or isotropic half space.

Substituting (5.4a) into eqn. (5.11) and then into eqn. (5.5), we obtain the stresses in terms of the transformed components of displacement (U_L, U_M, U_N). Comparing the stresses σ_{rz}, $\sigma_{\theta z}$ and σ_{zz} with those derived from eqn. (5.4b), we can obtain three equations which express the relationship between the expansion coefficients.

$$
\begin{aligned}
T_L &= -\lambda^2 C_{13} U_M + C_{33}\frac{\partial U_L}{\partial z} \\
T_M &= C_{44}(U_L + \frac{\partial U_M}{\partial z}) \\
T_N &= C_{44}\frac{\partial U_N}{\partial z}
\end{aligned}
\tag{5.13}
$$

In the above, T_L, T_M and T_N are the transformed components of traction in the cylindrical system of vector functions. Substituting all the stresses into the equations of equilibrium (5.12) and with the use of (5.13), we finally derive another three equations (the details are given in Appendix B):

$$
\begin{aligned}
&\frac{\partial T_L}{\partial z} - \lambda^2 T_M = 0 \\
&\frac{\partial T_N}{\partial z} - \lambda^2 C_{66} U_N = 0 \\
&- \lambda^2 C_{11} U_M + C_{13}\frac{\partial U_L}{\partial z} + \frac{\partial T_M}{\partial z} = 0
\end{aligned}
\tag{5.14}
$$

No matter whether we operate in a cylindrical or a Cartesian coordinate system, eqns. (5.13) and (5.14) are obtained in each case. In fact, operating in Cartesian system is far more simple than in cylindrical one.

Equations. (5.13) and (5.14) can be divided into two independent sets of simultaneous linear differential equations for U_L, U_M, T_L, T_M, and U_N, T_N respectively. We call the former Type I equations; the latter, Type II equations.

For Type I

$$
\begin{aligned}
\frac{\partial U_L}{\partial z} &= \lambda^2 \frac{C_{13}}{C_{33}} U_M + \frac{1}{C_{33}} T_L \\
\frac{\partial U_M}{\partial z} &= -U_L + \frac{1}{C_{44}} T_M \\
\frac{\partial T_L}{\partial z} &= \lambda^2 T_M \\
\frac{\partial T_M}{\partial z} &= \lambda^2 \frac{C_{11}C_{33} - C_{13}^2}{C_{33}} U_M - \frac{C_{13}}{C_{33}} T_L
\end{aligned}
\tag{5.15}
$$

For Type II:

$$
\begin{aligned}
\frac{\partial U_N}{\partial z} &= \frac{1}{C_{44}} T_N \\
\frac{\partial T_N}{\partial z} &= \lambda^2 C_{66} U_N
\end{aligned}
\tag{5.16}
$$

From (5.16), the general solution for type II can be easily found

$$\left\{E^{II}(z)\right\} = \left[Z^{II}(z)\right]\left\{K^{II}\right\} \tag{5.17}$$

where

$$\left\{E^{II}(z)\right\} = \left\{U_N, T_N / \lambda\right\}^T \tag{5.18}$$

and

$$\left\{K^{II}\right\} = \left\{a^{II}, b^{II}\right\}^T \tag{5.19}$$

where a^{II} and b^{II} are two arbitrary coefficients, and also functions of λ, and

$$\left[Z^{II}(z)\right] = \begin{bmatrix} \exp(\lambda s z) & \exp(-\lambda s z) \\ \lambda \bar{s} \exp(\lambda s z) & -\lambda \bar{s} \exp(-\lambda s z) \end{bmatrix} \tag{5.20}$$

where s and $\bar{s}$ are two constants relating to the material elastic coefficients.

$$s = \sqrt{\frac{C_{66}}{C_{44}}} \qquad (5.21)$$
$$\bar{s} = C_{44}s = \sqrt{C_{44}C_{66}}$$

The derivation of the general solution of the Type I equation involves considerable algebraic manipulation and the results depend on the two roots of the "characteristic equation":

$$(C_{44}x^2 - C_{11})(C_{33}x^2 - C_{44}) + (C_{13} + C_{44})^2 x^2 = 0 \qquad (5.22)$$

In the first case the two roots of this equation are different. In the second case, the roots are identical. In isotropic materials the roots are equal. And, specifically, both roots are equal to unity. With careful manipulation, the general homogeneous solution (type I) can be cast into a compact form:

$$\left\{E^I(z)\right\} = \left[Z^I(z)\right]\left\{K^I\right\} \qquad (5.23)$$

where

$$\left\{E^I(z)\right\} = \left\{U_L, \lambda U_M, T_L/\lambda, T_M\right\}^T \qquad (5.24)$$

where $\left\{E^I(z)\right\}$ are the transformed expansion coefficients, and

$$\left\{K^I\right\} = \left\{a, b, c, d\right\}^T \qquad (5.25)$$

where $\left\{K^I\right\}$ are unknown constants to be determined, and are the arbitrary functions of λ. The solution matrix $[Z^I(z)]$ which takes two forms for the two different characteristic roots are given in Appendix B.

We now consider a semi-infinite linearly elastic medium made up of j-1 parallel, homogeneous and transversely isotropic (isotropy can be seen as a special case) layers lying over a homogeneous, transversely isotropic (or isotropic) half space. The interfaces are parallel to the top surface of the medium and are perfectly bonded. The top surface is traction-free, except in the case of surface loading. The layers are numbered serially from 1 at the top (j is the half space).

The coordinate system is shown in Fig. 5.1, and we assume that $Z_0 = 0$ and $Z_{j-1} = h$.

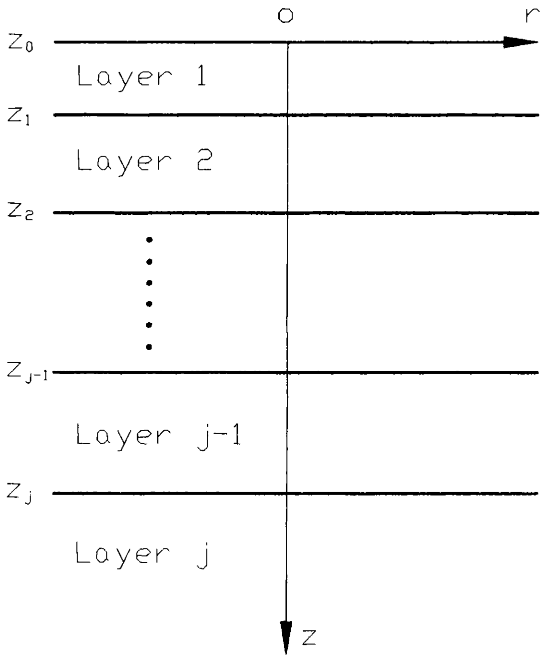

Fig. 5.1 Geometry of layered half space

In the propagator matrix method, the transformed coefficients for each layer are related to each other by the multiplication of layer matrices (or propagator matrices), which relate the expansion coefficients at the top of any single layer to those at the bottom of it. From equation (5.17), we can construct the following propagator matrices:

$$\begin{aligned} \{E^{I}(z_{k-1})\} &= [A_k^{I}]_u \{E^{I}(z_k)\} \\ \{E^{II}(z_{k-1})\} &= [A_k^{II}]_u \{E^{II}(z_k)\} \end{aligned} \tag{5.26}$$

where z_{k-1} and z_k are the depth of the top and bottom interfaces of layer k. the components in the vectors of $\{E^I\}$ and $\{E^{II}\}$ are all functions of λ. The propagator matrices $[A^I]_u$ and $[A^{II}]_u$ are also called layer matrices of type I and II respectively. The elements of these matrices are also functions of λ. The subscript u indicates that the matrices propagate upwards. Thus

$$[A_k^{II}]_u = \begin{bmatrix} \cosh(\lambda s_k h_k) & -\sinh(\lambda s_k h_k)/\bar{s}_k \\ -\bar{s}_k \sinh(\lambda s_k h_k) & \cosh(\lambda s_k h_k) \end{bmatrix} \tag{5.27}$$

where $h_k = z_k - z_{k-1}$, s_k and $\bar{s}_k$ are corresponding values of s and $\bar{s}$ in layer k. The elements of $\left[A_k^I\right]_u$ are given in Appendix C.

The multiplication of layer matrices implies the imposition of interfacial continuity conditions between layers, which are assumed to be perfectly bonded. The main advantage of the propagator method is that no global matrix system for the layered structure needs to be formed. Instead, what is required is only the solution of 4×4 and 2×2 linear algebraic equations.

5.4. Green's functions in the transformed domain

We now assume, without loss of generality, that a unit concentrated point load is located at depth $z = s$ along the z-axis. We consider horizontal and vertical unit point loads separately. These forces can be expressed (as body-force fields), in cylindrical coordinates, as

$$\begin{aligned} \boldsymbol{f}_h(r,\theta,z) &= \frac{1}{2\pi r}\delta(r)\delta(z-s)\boldsymbol{i}_h \\ \boldsymbol{f}_z(r,\theta,z) &= \frac{1}{2\pi r}\delta(r)\delta(z-s)\boldsymbol{i}_z \end{aligned} \tag{5.28}$$

where, δ is the one-dimensional Dirac delta function. $\boldsymbol{i}_z$ is the unit vector in the vertical direction, $\boldsymbol{i}_h$ is the horizontal unit vector in the $\theta = \theta_0$ direction (Fig 5.2) given by

$$\boldsymbol{i}_h = n_r \boldsymbol{i}_r + n_\theta \boldsymbol{i}_\theta = \cos(\theta - \theta_0)\boldsymbol{i}_r - \sin(\theta - \theta_0)\boldsymbol{i}_\theta \tag{5.29}$$

In equation (5.29); n_r, n_θ are the direction cosines of the unit force vector in cylindrical coordinates, and $\boldsymbol{i}_r, \boldsymbol{i}_\theta$ are the unit vectors in the radial and circumferential directions, respectively.

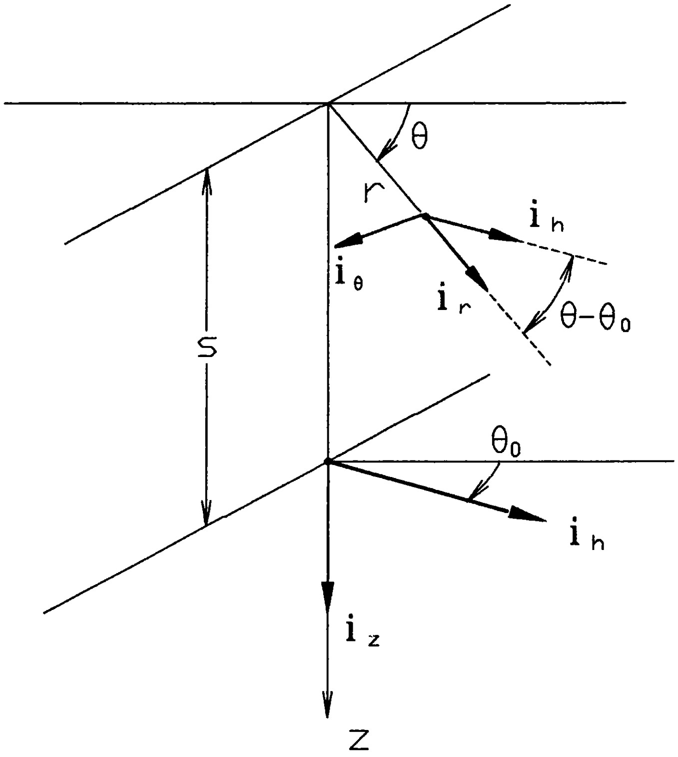

Fig. 5.2. Configuration of the point loads

These unit forces, which are also integrable vector functions, can be written in terms of the cylindrical system of vector functions in the form:

$$f(r,\theta,z) = f_h \cdot i_h + f_z \cdot i_z = \sum_m \int_0^{+\infty} \left[F_L(z) L(r,\theta) + F_M(z) M(r,\theta) + F_N(z) N(r,\theta) \right] \lambda d\lambda \tag{5.30}$$

After some manipulation (see Appendix C), the transformed body force coefficients are then given by

$$\begin{aligned} F_L &= \int_0^{2\pi} \int_0^{+\infty} f \cdot L^*(r,\theta) r dr d\theta \\ F_M &= \lambda^{-2} \int_0^{2\pi} \int_0^{+\infty} f \cdot M^*(r,\theta) r dr d\theta \\ F_N &= \lambda^{-2} \int_0^{2\pi} \int_0^{+\infty} f \cdot N^*(r,\theta) r dr d\theta \end{aligned} \tag{5.31}$$

in the cylindrical system. In the above equations, the asterisk signifies the complex conjugate.

By substituting (5.28) into (5.31), we get (see Appendix D)

$$
\begin{aligned}
F_L &= \frac{n_z}{\sqrt{2\pi}} && m = 0 \\
F_M &= \frac{\pm e^{\mp i\theta_0}}{2\lambda\sqrt{2\pi}} && m = \pm 1 \\
F_N &= \frac{-ie^{\mp i\theta_0}}{2\lambda\sqrt{2\pi}} && m = \pm 1
\end{aligned}
\tag{5.32}
$$

The action of a concentrated point load across the plane $z = s$ can be represented as a set of prescribed stress discontinuities across the plane (Pak, 1987). In cylindrical coordinates (r, θ, z), this can be written as:

$$
\begin{aligned}
\sigma_{zr}(r,\theta,s-) - \sigma_{zr}(r,\theta,s+) &= P(r,\theta) \\
\sigma_{z\theta}(r,\theta,s-) - \sigma_{z\theta}(r,\theta,s+) &= Q(r,\theta) \\
\sigma_{zz}(r,\theta,s-) - \sigma_{zz}(r,\theta,s+) &= R(r,\theta)
\end{aligned}
\tag{5.33}
$$

In eqn. (5.33), P, Q and R represent the stress discontinuity caused by a concentrated point load in r, θ, z directions respectively.

By virtue of the angular expansions of the stress discontinuities across the plane z=s and the orthogonality of the angular eigenfunctions $\left\{e^{im\theta}\right\}_{m=-\infty}^{\infty}$, we can write:

$$
\begin{aligned}
P(r,\theta) &= \sum_{m=-\infty}^{\infty} P_m(r)e^{im\theta} \\
Q(r,\theta) &= \sum_{m=-\infty}^{\infty} Q_m(r)e^{im\theta} \\
R(r,\theta) &= \sum_{m=-\infty}^{\infty} R_m(r)e^{im\theta}
\end{aligned}
\tag{5.34}
$$

The m-th order Hankel transform with respect to the radial coordinate is:

$$
\tilde{f}^m(\lambda) = \int_0^\infty f(r)rJ_m(\lambda r)dr
\tag{5.35}
$$

where, $\tilde{f}^m(\lambda)$ represents the m-th order Hankel transform of $f(r)$. The inverse transformation may be written as

$$f(r) = \int_0^\infty \tilde{f}^m(\lambda)\lambda J_m(\lambda r)d\lambda \tag{5.36}$$

From (5.28), (5.29) and (5.34) we can find

$$\begin{aligned}
&P_{\pm 1}(r) = e^{\mp i\theta_0}\frac{\delta(r)}{4\pi r}, && P_m(r) = 0 \quad for \quad m \neq \pm 1 \\
&Q_{\pm 1}(r) = \pm i\, e^{\mp i\theta_0}\frac{\delta(r)}{4\pi r}, && Q_m(r) = 0 \quad for \quad m \neq \pm 1 \\
&P_0(r) = \frac{\delta(r)}{2\pi r}, && R_m(r) = 0 \quad for \quad m \neq 0
\end{aligned} \tag{5.37}$$

We now define (Guzina et al, 1999)

$$\begin{aligned}
X_m(\lambda) &= \tilde{P}_m^{m-1}(\lambda) - i\tilde{Q}_m^{m-1}(\lambda) \\
Y_m(\lambda) &= \tilde{P}_m^{m+1}(\lambda) + i\tilde{Q}_m^{m+1}(\lambda) \\
Z_m(\lambda) &= \tilde{R}_m^{m}(\lambda)
\end{aligned} \tag{5.38}$$

Substituting eqn. (5.37) into (5.38), and with some manipulations we can derive:

$$\begin{aligned}
&X_1(\lambda) = \frac{1}{2\pi}e^{-i\theta_0}, && X_m(\lambda) = 0 && m \neq 1, \\
&Y_{-1}(\lambda) = \frac{1}{2\pi}e^{i\theta_0}, && Y_m(\lambda) = 0 && m \neq -1, \\
&Z_0(\lambda) = \frac{1}{2\pi}, && Z_m(\lambda) = 0 && m \neq 0.
\end{aligned} \tag{5.39}$$

We can see from equations (5.32) and (5.37) that there is a relationship between the expansion coefficients of body force (F_L, F_M, and F_N) and the angular expansion coefficients of stress discontinuities (P_m, Q_m and R_m). With some manipulation on the equations (5.38) and (5.39), we can obtain the following relations:

$$
\begin{aligned}
X_1(\lambda) &= \widetilde{P}_1^0(\lambda) - i\widetilde{Q}_1^0(\lambda) = \frac{\lambda}{\sqrt{2\pi}}(F_{M+1} + iF_{N+1}) \\
Y_{-1}(\lambda) &= \widetilde{P}_{-1}^0(\lambda) + i\widetilde{Q}_{-1}^0(\lambda) = \frac{\lambda}{\sqrt{2\pi}}(-F_{M-1} + iF_{N-1}) \\
Z_0(\lambda) &= \widetilde{R}_0^0(\lambda) = \frac{1}{\sqrt{2\pi}}F_{L0}
\end{aligned}
\tag{5.40}
$$

The subscript m in F_{Lm}, F_{Mm} and F_{Nm} signifies the m-th expansion coefficient of F_L, F_M and F_N, respectively. In the case of a point load, m takes the values of ±1 and zero only, as shown above.

With some simple manipulation on equation (5.32), we can also get the following relations:

$$
\begin{aligned}
&F_{M+1} + iF_{N+1} = 2F_{M+1} = 2iF_{N+1} \\
&-F_{M-1} + iF_{N-1} = -2F_{M-1} = 2iF_{N-1}
\end{aligned}
\tag{5.41}
$$

From the definition of stress discontinuities (equation 5.33), we see that the point force vector described above will cause a corresponding discontinuity in the expansion coefficients of the traction vector. This can be seen as a reflection of real stress field discontinuities in the transform domain:

$$
\begin{aligned}
\Delta T_L &\equiv T_L(s-) - T_L(s+) = F_L = \frac{n}{\sqrt{2\pi}} & m &= 0 \\
\Delta T_M &\equiv T_M(s-) - T_M(s+) = F_M = \frac{\pm e^{\mp i\theta_0}}{2\lambda\sqrt{2\pi}} & m &= \pm 1 \\
\Delta T_N &\equiv T_N(s-) - T_N(s+) = F_N = \frac{-ie^{\mp i\theta_0}}{2\lambda\sqrt{2\pi}} & m &= \pm 1
\end{aligned}
\tag{5.42}
$$

The above equations are written in terms of the cylindrical coordinate system.

5.5. The derivation of the propagation matrix

It was shown in Section 5.3 that, two independent sets of simultaneous linear differential equations, for U_L, U_M, T_L, T_M and U_N, T_N, are obtained.

The corresponding two sets of solutions for the multi-layered half space can then be derived using the propagator matrix method. For example, the expansion coefficients in eqn. (5.18) and (5.24) at any depth for z ⩾ s, in layer k, i.e., $z_{k-1} \le z \le z_k$ can be derived as

$$\{E(z)\} = [A_k(z_k - z)]_u [A_{k+1}]_u \cdots\cdots [A_{n-1}]_u [Z_n(h)] \{K\} \tag{5.43}$$

The above equation is a unified form of both types of equations. In the type *I* case, $\{E(z)\}$ should be $\{E^I(z)\}$. In type *II*, it is $\{E^{II}(z)\}$. The other terms should be changed in the same manner. This also applies to the following equations. Equation (5.43) is applicable when the field point is below or at the source point level, i.e., $z \geqslant s$. If the field point is above the source level, similar expressions are derived but with downward propagator matrices $[A^I]_d$ and $[A^{II}]_d$, from the top surface.

$$\begin{aligned}\{E\ (z)\} = [A_k(z - z_{k-1})]_d [A_{k-1}(z_{k-1} - z_{k-2})]_d \cdots\cdots \\ [A_1(z_1 - z_0)]_d \{E\ (0)\}\end{aligned} \tag{5.44}$$

For a traction-free top surface, we have:

$$\begin{aligned}\{E^I(0)\} &= \{U_L(0), \lambda U_M(0), 0, 0\}^T \\ \{E^{II}(0)\} &= \{U_N(0), 0\}^T\end{aligned} \tag{5.45}$$

For large number of layers, numerical overflow may result from these matrix multiplications. Taking the isotropic case as a example, it can be shown that matrix multiplication (from layer *k* to layer *n*-1) yields $\exp\{\lambda(h\text{-}z)\}$.

To overcome this problem, two new propagator matrices $[B^I]$ and $[B^{II}]$ can be introduced, which are related to the old ones by

$$[A_k(z_k - z_{k-1})] = [B_k(z_k - z_{k-1})] \exp\{\lambda(z_k - z_{k-1})\} \tag{5.46}$$

After matrix multiplication, the exponentially growing term on the right-hand side of the above equation yields

$$\exp\{\lambda(z_k - z)\} \exp\{\lambda(z_{k+1} - z_k)\} \cdots\cdots \exp\{\lambda(h - z_{n-1})\} = \exp\{\lambda(h - z)\}$$

This scaling can be applied to both upward and downward propagator matrices. The exponentially growing term is cancelled out largely by $\exp\{-\lambda h\}$ in $[Z_j^I(h)]$ or $[Z_j^{II}(h)]$, as shown in the Appendix F. This process is done with some careful re-arrangement of algorithm. Thus in terms of these new propagator matrices the equation (5.43) can be recast into

$$\begin{aligned}\{E\ (z)\} = \exp\{-\lambda d_{zs}\}[B_k(z_k - z)]_u [B_{k+1}]_u \cdots\cdots \\ [B_{n-1}]_u \exp\{\lambda(h-s)\}[Z_n(h)]\{K^I\}\end{aligned} \tag{5.47}$$

where $d_{zh} = z - s$, which is the vertical distance between the field point and the source point.

Similar expressions can be derived in which matrices $[B^I]$ and $[B^{II}]$ will propagate from the top surface (z=0) downwards.

$$\begin{aligned}\{E\ (z)\} = \exp\{\lambda z\}[B_k(z - z_{k-1})]_d [B_{k-1}(z_{k-1} - z_{k-2})]_d \cdots\cdots \\ [B_1(z_1 - z_0)]_d \{E\ (0)\}\end{aligned} \tag{5.48}$$

5.6. The solution procedure

The constant vector $\{K^I\}$ and $\{K^{II}\}$ in eqn. (5.43) must be determined in order to obtain $\{E^I(z)\}$ and $\{E^{II}(z)\}$. At layer interface $z_{n-1} = h$ In the case of a multi-layered half space, the coefficients in the $\{K\}$ can be written as

$$\{K^I\} = \{a_n, b_n, c_n, d_n\}^T$$
$$\{K^{II}\} = \{a_n^{II}, b_n^{II}\}^T$$

a_n and c_n in $\{K^I\}$ and a_n^{II} in $\{K^{II}\}$ should be zero in order to satisfy the admissible boundary conditions at infinity. Therefore, the remaining unknowns are b_n and d_n in $\{K^I\}$ and b_n^{II} in $\{K^{II}\}$. In the following discussion, we assume that the field point is below or at the source point level.

5.6.1. Solution for $\{E^I\}$

From eqn. (5.47), we can derive the expansion coefficients at depth z = s, i.e., source point level in layer p, and $z_{p-1} \leq z \leq z_p$.

$$\begin{aligned}\{E^I(s+)\} = \exp\{\lambda(h-s)\}[B_p^I(z_p - z)]_u [B_{p+1}^I(z_{p+1} - z_p)]_u \cdots\cdots \\ [B_{n-1}^I(h - z_{n-2})]_u [Z_n^I(h)]\{K^I\}\end{aligned} \tag{5.49}$$

where

$$\left\{E^I(s+)\right\} = \left\{U_L(s+), \lambda U_M(s+), T_L(s+)/\lambda, T_M(s+)\right\}^T \tag{5.50}$$

and

$$\left\{K^I\right\} = \left\{0, b_n, 0, d_n\right\}^T \tag{5.51}$$

Considering the two zero values in $\{K^I\}$, the first and third column of $\left[Z_n^I(h)\right]$ can be omitted in the calculation, and the $e^{-\lambda h}$ in the second and fourth column can be cancelled by item $e^{\lambda h}$ in eqn. (5.49). So eqn. (5.49) can be rewritten as

$$\left\{E^I(s+)\right\} = [B]\left[\bar{Z}_n^I(h)\right]\left\{\bar{K}^I\right\} \tag{5.52}$$

where

$$\left\{\bar{K}^I\right\} = \exp(-\lambda s)\left\{K^I\right\} \tag{5.53}$$

and

$$[B] = \left[B_p^I(z_p - s)\right]_u \left[B_{p+1}^I(z_{p+1} - z_p)\right]_u \cdots\cdots \left[B_{n-1}^I(h - z_{n-2})\right]_u \tag{5.54}$$

is the multiplication of propagator matrices (4×4) from layer *n-1* to *p* upwards. The elements in matrix $\left[\bar{Z}_n^I(h)\right]$ are the same as those in $\left[Z_n^I(h)\right]$ but without the exponential parts $exp(\pm\lambda h)$.

If we define

$$[G] = [B]\left[\bar{Z}_n^I(h)\right] \tag{5.55}$$

Then eqn. (5.52) can be written in more compact form

$$\left\{E^I(s+)\right\} = [G]\left\{\bar{K}^I\right\} \tag{5.56}$$

Similarly, we derive the expansion coefficients at depth $z = s$ again, but this time from eqn. (5.48), in which the matrices $[B^I]$ propagate downwards from the surface (z = 0).

$$\begin{aligned}\left\{E^I(s-)\right\} = \exp\{\lambda s\}\left[B_p^I(s - z_{p-1})\right]_d \left[B_{p-1}^I(z_{p-1} - z_{p-2})\right]_d \cdots\cdots \\ \left[B_1^I(z_1 - z_0)\right]_d \left\{E^I(0)\right\}\end{aligned} \tag{5.57}$$

where

$$\left\{E^I(s-)\right\} = \{U_L(s-), \lambda U_M(s-), T_L(s-)/\lambda, T_M(s-)\}^T \tag{5.58}$$

$$\left\{E^I(0)\right\} = \{U_L(0), \lambda U_M(0), 0, 0\}^T \tag{5.59}$$

Eqn. (5.57) can be rewritten as

$$\left\{E^I(s-)\right\} = [R]\left\{\bar{E}^I(0)\right\} \tag{5.60}$$

where

$$\left\{\bar{E}^I(0)\right\} = \exp(\lambda s)\left\{E^I(0)\right\} \tag{5.61}$$

and

$$[R] = \left[B_p^I(s - z_{p-1})\right]_d \left[B_{p-1}^I(z_{p-1} - z_{p-2})\right]_d \cdots\cdots \left[B_1^I(z_1 - z_0)\right]_d \tag{5.62}$$

is the product of downwards propagating matrices (4×4) from layer 0 to p.

Now according to the discontinuity condition (5.42) and the continuity of displacement across the plane $z = s$, we have

$$U_L(s-) = U_L(s+)$$
$$U_M(s-) = U_M(s+)$$
$$T_L(s-) - T_L(s+) = \Delta T_L$$
$$T_M(s-) - T_M(s+) = \Delta T_M$$

Substituting equations (5.56) and (5.60) into the above formula we can obtain the following equation:

$$[G]\{0, \bar{b}_n, 0, \bar{d}_n\}^T - [R]\{\bar{U}_L(0), \lambda\bar{U}_M(0), 0, 0\}^T = \{0, 0, \Delta T_L/\lambda, \Delta T_M\}^T \tag{5.63}$$

where

$$\begin{aligned} \bar{b}_n &= \exp(-\lambda s)b_n, \\ \bar{d}_n &= \exp(-\lambda s)d_n, \\ \bar{U}_L(0) &= \exp(\lambda s)U_L(0), \\ \bar{U}_M(0) &= \exp(\lambda s)U_M(0) \end{aligned} \tag{5.64}$$

Multiplying by $[R]^{-1}$ both sides of eqn.(5.63), we have

$$[Q]\{0, \bar{b}_n, 0, \bar{d}_n\}^T - \{\bar{U}_L(0), \lambda\bar{U}_M(0), 0, 0\}^T = [R]^{-1}\{0, 0, \Delta T_L/\lambda, \Delta T_M\}^T \tag{5.65}$$

where $[Q] = [R]^{-1}[G]$. Since the upwards propagator matrix is the inverse matrix of the corresponding downwards propagator matrix, $[R]^{-1}$ in equation (5.65) can be derived by the multiplication of upwards propagator matrices $[B]_u$ from the source level $z = s$ to the surface $z = 0$. Therefore, $[Q]$ is in fact the multiplication of all the upwards propagator matrices from layer n-1 (starting at the depth of last interface $z_{n-1} = h$) to layer 1 (end at the surface $z = 0$). Taking out the third and fourth equations from equation set (5.65) we have:

$$\begin{bmatrix} Q_{32} & Q_{34} \\ Q_{42} & Q_{44} \end{bmatrix} \begin{Bmatrix} \bar{b}_n \\ \bar{d}_n \end{Bmatrix} = \begin{bmatrix} R_{33} & R_{34} \\ R_{43} & R_{44} \end{bmatrix} \begin{Bmatrix} \Delta T_L/\lambda \\ \Delta T_M \end{Bmatrix} \tag{5.66}$$

where Q_{ij} ($i = 3, 4,\ j = 2, 4$) and R_{ij} ($i = 3, 4,\ j = 3, 4$) are the elements of $[Q]$ and $[R]^{-1}$ respectively.

Solving this 2×2 matrix explicitly, we find that:

$$\begin{aligned} \bar{b}_n &= \frac{R_{33}Q_{44} - R_{43}Q_{34}}{Q_{32}Q_{44} - Q_{42}Q_{34}} \Delta T_L / \lambda \\ \bar{d}_n &= \frac{R_{43}Q_{32} - R_{33}Q_{42}}{Q_{32}Q_{44} - Q_{42}Q_{34}} \Delta T_L / \lambda \end{aligned} \tag{5.67}$$

for the case of $m = 0$. In the case of $m = \pm 1$, the solutions are the same as eqn. (5.67) except that $\Delta T_L / \lambda$ is replaced by ΔT_M . Analogously, the solution of $\bar{U}_L(0)$ *and* $\lambda \bar{U}_M(0)$ can also be obtained from the first and second equations in eqn. (5.65). Substituting eqn. (5.67) into eqn. (5.47), we can obtain the expansion coefficients $\{E^I(z)\}$ at any level of $z \geqslant s$. Substituting the solutions of $\bar{U}_L(0)$ *and* $\lambda \bar{U}_M(0)$ into eqn. (5.48) we can obtain $\{E^I(z)\}$ at any level of $z < s$.

5.6.2. Solution for $\{E^{II}\}$

The procedure for obtaining $\{E^{II}(z)\}$is similar to that for $\{E^I(z)\}$. According to eqn. (5.47), the expansion coefficients at the depth $z = s$ in layer p can be obtained as

$$\begin{aligned} \{E^{II}(s+)\} = \exp\{\lambda(h-s)\}[B_p^{II}(z_p - s)]_u [B_{p+1}^{II}(z_{p+1} - z_p)]_u \cdots\cdots \\ [B_{n-1}^{II}]_u [Z_n^{II}(h)]\{K^{II}\} \end{aligned} \tag{5.68}$$

where

$$\{E^{II}(s+)\} = \{U_N(s+), T_N(s+)/\lambda\}^T \tag{5.69}$$

and

$$\{K^{II}\} = \{0, b_n^{II}\}^T \tag{5.70}$$

and eqn. (5.68) can be written as

$$\{E^{II}(s+)\} = [G^{II}]\{\bar{K}^{II}\} \tag{5.71}$$

where

$$\{\bar{K}^{II}\} = \exp(-\lambda s)\{K^{II}\} \tag{5.72}$$

and

$$[G^{II}] = [B^{II}][\bar{Z}_n^{II}(h)] \tag{5.73}$$

$$[B^{II}] = [B_p^{II}(z_p - z)]_u [B_{p+1}^{II}(z_{p+1} - z_p)]_u \cdots\cdots [B_{n-1}^{II}(h - z_{n-2})]_u \tag{5.74}$$

is the product of 2×2 propagating matrices from layer *n-1* to layer *p* upwards, and the elements of $[\bar{Z}_n^{II}(h)]$ are the same as those in $[Z_n^{II}(h)]$ except that the exponential parts $exp(\pm\lambda h)$ are discarded.

Similarly, from eqn. (5.48) we can also obtain the expansion coefficients at depth $z = s$ from the surface $z = 0$ as

$$\begin{aligned}\{E^{II}(s-)\} = \exp\{\lambda s\}&[B_p^{II}(s - z_{p-1})]_d [B_{p-1}^{II}(z_{p-1} - z_{p-2})]_d \cdots\cdots \\ &[B_1^{II}(z_1 - z_0)]_d \{E^{II}(0)\}\end{aligned} \tag{5.75}$$

where

$$\{E^{II}(s-)\} = \{U_N(s-), T_N(s-)/\lambda\}^T \tag{5.76}$$

and

$$\{E^{II}(0)\} = \{U_N(0), 0\}^T \tag{5.77}$$

Equation (5.75) can be written in more compact form as

$$\{E^{II}(s-)\} = [R^{II}]\{\bar{E}^{II}(0)\} \tag{5.78}$$

where

$$\{R^{II}\} = [B_p^{II}(s - z_{p-1})]_d [B_{p-1}^{II}(z_{p-1} - z_{p-2})]_d \cdots\cdots [B_1^{II}(z_1 - z_0)]_d \tag{5.79}$$

is the product of downwards 2×2 propagating matrices from layer 1 to layer p, and

$$\{\bar{E}^{II}(0)\} = \exp(\lambda s)\{E^{II}(0)\} \tag{5.80}$$

From the discontinuity conditions

$$U_N(s-) = U_N(s+)$$
$$T_N(s-) - T_N(s+) = \Delta T_N$$

we obtain:

$$\left[G^{II}\right]\left\{0, \bar{b}_n^{II}\right\}^T - \left[R^{II}\right]\left\{\bar{U}_N(0), 0\right\}^T = \left\{0, \Delta T_N / \lambda\right\}^T \tag{5.81}$$

where

$$\begin{aligned} \bar{b}_n^{II} &= \exp(-\lambda s) b_n^{II}, \\ \bar{U}_N(0) &= \exp(\lambda s) U_N(0) \end{aligned} \tag{5.82}$$

Multiplying by $[R^{II}]^{-1}$ both sides of eqn. (5.81), we have

$$\left[Q^{II}\right]\left\{0, \bar{b}_n^{II}\right\}^T - \left\{\bar{U}_N(0), 0\right\}^T = \left[R^{II}\right]^{-1}\left\{0, \Delta T_N / \lambda\right\}^T \tag{5.83}$$

where

$$\left[Q^{II}\right] = \left[R^{II}\right]^{-1}\left[G^{II}\right] \tag{5.84}$$

and from the second equation in (5.84) the solution of $\bar{b}_n^{II}$ is obtained:

$$\bar{b}_n^{II} = \frac{R_{22} \cdot \Delta T_N}{\lambda Q_{22}} \tag{5.85}$$

In the above, Q_{ij} and R_{ij} are the elements of $[Q^{II}]$ and $[R^{II}]^{-1}$ respectively. Similarly, $\bar{U}_N(0)$ can be obtained from the first equation in (5.83).

And again, substituting eqn. (5.85) into eqn. (5.47) the expansion coefficients $\{E^{II}(z)\}$ at any level of $z \geqslant s$ can be solved. Substituting the solution of $\bar{U}_N(0)$ into eqn. (5.48) we can obtain $\{E^{II}(z)\}$ at any level of $z < s$.

Chapter 6

Green's functions for multi-layered systems: II - Numerical

In this chapter, the Green's functions in the physical domain are obtained using numerical integration. Bessel functions are involved in the integral kernels: these are oscillatory and may be only slowly convergent particularly at singular points. Therefore, acceleration techniques may be necessary. One effective approach, called the continued fraction method, is adopted here together with a singularity extraction method. The latter method removes the singularity in the layered Green's functions in the transformed domain by subtraction of the full-space Green's functions. Adaptive integration is then performed on these reduced functions, and the result added to the explicit full-space Green's functions.

As demonstrated here by numerical examples, this approach works well at singular points, except at the free surface of half spaces and the interfaces between two layers of different material properties. An approach to solve this problem is discussed in the next chapter.

6.1. Displacement and stress formulation

In Chapter 5, we derived the expansion coefficients of the transformed Green's functions $\{E^{I}(z)\}$ and $\{E^{II}(z)\}$ in the cylindrical coordinate system. To find the displacement and traction vectors in the physical domain, the expansion coefficients in the transformed domain need to be integrated numerically.

Under the action of an internal point load, the Green's functions for displacements in cylindrical coordinates can be written as:

$$
\begin{aligned}
u_r ={}& \frac{U_{M-1}(z)}{\sqrt{2\pi}}\left[J_1(\lambda r)/r-\lambda J_0(\lambda r)\right]e^{-i\theta}+\frac{U_{N-1}(z)}{\sqrt{2\pi}}i\frac{J_1(\lambda r)}{r}e^{-i\theta}+ \\
& \frac{U_{M+1}(z)}{\sqrt{2\pi}}\left[\lambda J_0(\lambda r)-J_1(\lambda r)/r\right]e^{i\theta}+\frac{U_{N+1}(z)}{\sqrt{2\pi}}i\frac{J_1(\lambda r)}{r}e^{i\theta}- \\
& \frac{U_{M0}(z)}{\sqrt{2\pi}}\lambda J_1(\lambda r) \\
u_\theta ={}& \frac{U_{M-1}(z)}{\sqrt{2\pi}}i\frac{J_1(\lambda r)}{r}e^{-i\theta}-\frac{U_{N-1}(z)}{\sqrt{2\pi}}\left[J_1(\lambda r)/r-\lambda J_0(\lambda r)\right]e^{-i\theta}+ \\
& \frac{U_{M+1}(z)}{\sqrt{2\pi}}i\frac{J_1(\lambda r)}{r}e^{i\theta}-\frac{U_{N+1}(z)}{\sqrt{2\pi}}\left[\lambda J_0(\lambda r)-J_1(\lambda r)/r\right]e^{i\theta}+ \\
& \frac{U_{N0}(z)}{\sqrt{2\pi}}\lambda J_1(\lambda r) \\
u_z ={}& -\frac{U_{L-1}(z)}{\sqrt{2\pi}}J_1(\lambda r)e^{-i\theta}+\frac{U_{L+1}(z)}{\sqrt{2\pi}}J_1(\lambda r)e^{i\theta}+\frac{U_{L0}(z)}{\sqrt{2\pi}}J_0(\lambda r)
\end{aligned}
\tag{6.1}
$$

Where, for convenience, we write only the functions $f(\lambda)$ on the right-hand-side. In reality, of course, the right hand sides should be $\int_0^{+\infty} f(\lambda)\,\lambda d\lambda$. We follow this convention in the following equation too.

$$
\begin{aligned}
\sigma_{rz} ={}& \frac{T_{M-1}(z)}{\sqrt{2\pi}}\left[J_1(\lambda r)/r-\lambda J_0(\lambda r)\right]e^{-i\theta}+\frac{T_{N-1}(z)}{\sqrt{2\pi}}i\frac{J_1(\lambda r)}{r}e^{-i\theta}+ \\
& \frac{T_{M+1}(z)}{\sqrt{2\pi}}\left[\lambda J_0(\lambda r)-J_1(\lambda r)/r\right]e^{i\theta}+\frac{T_{N+1}(z)}{\sqrt{2\pi}}i\frac{J_1(\lambda r)}{r}e^{i\theta}- \\
& \frac{T_{M0}(z)}{\sqrt{2\pi}}\lambda J_1(\lambda r) \\
\sigma_{\theta z} ={}& \frac{T_{M-1}(z)}{\sqrt{2\pi}}i\frac{J_1(\lambda r)}{r}e^{-i\theta}-\frac{T_{N-1}(z)}{\sqrt{2\pi}}\left[J_1(\lambda r)/r-\lambda J_0(\lambda r)\right]e^{-i\theta}+ \\
& \frac{T_{M+1}(z)}{\sqrt{2\pi}}i\frac{J_1(\lambda r)}{r}e^{i\theta}-\frac{T_{N+1}(z)}{\sqrt{2\pi}}\left[\lambda J_0(\lambda r)-J_1(\lambda r)/r\right]e^{i\theta}+ \\
& \frac{T_{N0}(z)}{\sqrt{2\pi}}\lambda J_1(\lambda r) \\
\sigma_{zz} ={}& -\frac{T_{L-1}(z)}{\sqrt{2\pi}}J_1(\lambda r)e^{-i\theta}+\frac{T_{L+1}(z)}{\sqrt{2\pi}}J_1(\lambda r)e^{i\theta}+\frac{T_{L0}(z)}{\sqrt{2\pi}}J_0(\lambda r)
\end{aligned}
\tag{6.2}
$$

for tractions. In eqn. (6.1), the subscript -1 of U_{M-1} means the value of U_M in the case of $m = -1$ (similarly for the subscript 0 and 1). From eqn. (6.1) and (6.2) we can derive the following relations:

$$
\begin{aligned}
\tilde{u}_{rm}^{m+1} + i\tilde{u}_{\theta m}^{m+1} &= \frac{\lambda}{\sqrt{2\pi}}(-U_{Mm} + iU_{Nm}) \\
\tilde{u}_{rm}^{m-1} - i\tilde{u}_{\theta m}^{m-1} &= \frac{\lambda}{\sqrt{2\pi}}(\ U_{Mm} + iU_{Nm}) \\
\tilde{u}_{zm}^{m} &= \frac{1}{\sqrt{2\pi}}U_{Lm}
\end{aligned}
\tag{6.3}
$$

and

$$
\begin{aligned}
\tilde{\sigma}_{rzm}^{m+1} + i\tilde{\sigma}_{\theta zm}^{m+1} &= \frac{\lambda}{\sqrt{2\pi}}(-T_{Mm} + iT_{Nm}) \\
\tilde{\sigma}_{rzm}^{m-1} - i\tilde{\sigma}_{\theta zm}^{m-1} &= \frac{\lambda}{\sqrt{2\pi}}(\ T_{Mm} + iT_{Nm}) \\
\tilde{\sigma}_{zzm}^{m} &= \frac{1}{\sqrt{2\pi}}T_{Lm}
\end{aligned}
\tag{6.4}
$$

In the above, m can take values of 0 and ±1.

The remaining stress components can be obtained from the generalized Hooke's law in cylindrical coordinates.

$$
\begin{aligned}
\sigma_{rr} &= \sum_m [T_L(z)C_{13}/C_{33} + U_N(z)(C_{11} - C_{12})\Delta_1 + U_M(z) \\
&\qquad \lambda^2 (C_{13}^2 - C_{11}C_{33})/C_{33} - U_M(z)(C_{11} - C_{12})\Delta_2]\, S(r,\theta;\lambda,m) \\
\sigma_{\theta\theta} &= \sum_m \ [T_L(z)C_{13}/C_{33} - U_N(z)(C_{11} - C_{12})\Delta_1 + U_M(z) \\
&\qquad \lambda^2 (C_{13}^2 - C_{12}C_{33})/C_{33} + U_M(z)(C_{11} - C_{12})\Delta_2]\, S(r,\theta;\lambda,m) \\
\sigma_{r\theta} &= C_{66}\sum_m \left[U_N(z)(\lambda^2 + 2\Delta_2) + 2U_M(z)\Delta_1\right] S(r,\theta;\lambda,m)
\end{aligned}
\tag{6.5}
$$

In (6.5), the operators are:

$$
\begin{aligned}
\Delta_1 &= \frac{1}{r}\frac{\partial^2}{\partial r \partial\theta} - \frac{1}{r^2}\frac{\partial}{\partial\theta} \\
\Delta_2 &= \frac{1}{r^2}\frac{\partial^2}{\partial\theta^2} + \frac{1}{r}\frac{\partial}{\partial r}
\end{aligned}
\tag{6.6}
$$

Parameters $C_{11}, C_{12}, C_{13}, C_{33}$ and C_{44} are the five elastic constants of the transversely isotropic medium. In the case of an isotropic medium

$$\begin{aligned} C_{11} &= C_{33} = \frac{E(1-\nu)}{(1+\nu)(1-2\nu)} \\ C_{12} &= C_{13} = \frac{E\nu}{(1+\nu)(1-2\nu)} \\ C_{44} &= \frac{E}{2(1+\nu)} \end{aligned} \tag{6.7}$$

where E is the Young's modulus and v is the Poisson ratio, and

$$C_{66} = (C_{11} - C_{12})/2 \tag{6.8}$$

6.2. Numerical integration techniques

From eqns. (6.1), (6.2) and (6.5) it is found that of the 27 individual Green's functions (or Hankel transforms), only 15 integrals need to be evaluated (Pan, 1997).

In the Hankel transform, the oscillation of the integral kernels (due to the Bessel functions) and the infinite upper limit of the integrals pose major difficulties. Further, the Bessel functions converge slowly. Thus, the common numerical integration methods, such as Simpson's rule, are not suitable here.

The Hankel transforms are frequently encountered in the mathematical treatment of physical problems involving cylindrical symmetry. For the elastostatic case, some numerical methods have been proposed, such as Lipshitz-Hankel-type integral in which the least squares method is used (Jovanovich et al, 1974, Sato & Matsu'ura, 1973, Chan et al, 1974). Two popular approaches are fast Hankel transform and Gauss quadrature.

6.2.1. Fast Hankel transform

The standard numerical approach to the computation of Hankel transforms is the digital filter method following the work of Ghosh (1971).

Design criteria for the filter are of necessity largely ad hoc and were discussed by Anderson (1979). More developments including adaptive and lagged convolution to minimize kernel function evaluations were discussed by Anderson (1982). Reasonable (5 figure) accuracy is typically achieved for monotonic, rapidly decreasing kernel functions at moderate values of λ.

However, for some types of problem the digital filter method is less useful; for example, when the kernel function changes rapidly compared to the Bessel function, and when high numerical precision is required.

6.2.2. Adaptive Gauss quadrature

Gauss quadrature can yield high accuracy but re-computation of integrands is expensive. An adaptive Gauss quadrature, developed by Patterson (1968, 1973) and implemented by Chave (1983) into a program for the numerical integration of Hankel transform, is adopted here for the evaluation of Green's functions. This method saves computational effort by avoiding re-computation of all integrands when the order of Gauss quadrature is changed.

We first express the infinite integral for each Green's function component as a finite summation of partial integration terms:

$$\int_0^\infty f(\lambda,z)J_m(\lambda r)d\lambda \approx \sum_{n=1}^{N}\int_{\lambda_n}^{\lambda_{n+1}} f(\lambda,z)J_m(\lambda r)d\lambda \tag{6.9}$$

where $f(\lambda, z)$ represents the integrand which may including one of the expansion coefficients derived from the propagator matrix method in Chapter 5. λ_n is the nth zero of $J_m(\lambda r)$ normalized by the range r, and $\lambda_1 = 0$.

In each subinterval of integration a three-point Gauss quadrature is first applied to calculate the integral, using the interlacing quadrature method (Patterson, 1968). This process can be expressed as the approximation of the linear functional (6.9) by

$$\int_0^{+\infty} f(\lambda,z)J_m(\lambda r)d\lambda \approx \sum_{i=1}^{N} w_i f(\lambda_i,z)J_m(\lambda_i r) \tag{6.10}$$

where λ_i is the abscissa and w_i is the weight. Then a combined relative-absolute error criterion is used to check the convergence. If it is not satisfied, in the case of most Gauss rules the recomputation of all of the integrands is required when the order is changed. In Patterson's method, new Gauss points are added into the interval between the old Gauss points, so that only the new integrand values need to be calculated when the order of quadrature is increased.

In this algorithm, the weights w_i and λ_i in eqn. (6.10) consist of a three-point Gauss rule with extension to 7, 15, 31, 63, 127 and 255 common-point, interlacing forms. These correspond to integrating polynomials of degree 5, 11, 23, 47, 95, 191 and 383, respectively. In practice, each of the partial integrations is computed by adding new weights to the quadrature rule, and the kernel and Bessel function values obtained in the previous step are retained so that none of these costly evaluations need to be repeated. This procedure continues until the error criterion is satisfied.

Direct summation of sub-integrals is feasible only for rapidly convergent integrals. However, the terms in the series in (6.9) usually alternate in sign due to the Bessel function's oscillatory behaviour, and the result may be very slowly convergent and diverge if the kernel increases faster than $\lambda^{1/2}$.

To solve this problem, acceleration is necessary. A continued fraction expansion approach has been adopted to accelerate the convergence for slowly convergent series (Patterson, 1968, 1973, Hanggi et al, 1980, Chave, 1983). Experience with this novel numerical quadrature shows that it can yield very accurate results while using fewer Gauss points simple numerical quadrature (Pan, 1997).

Here, we adopt the continued fraction approach which is equivalent to an analytic continuation of the series. Divergent series suggests the presence of singularities can be removed by transformation.

The principle of the continued fraction method is to recast a series of partial integrations

$$S = \sum_{i=0}^{N} a_i \tag{6.11}$$

into the "continued fraction" form

$$S = \frac{d_0}{1+}\frac{d_1}{1+}\frac{d_2}{1+}\cdots\cdots \tag{6.12}$$

The right hand side of above equation denotes the continued fraction:

$$\cfrac{d_0}{1+\cfrac{d_1}{1+\cfrac{d_2}{1+\cfrac{d_3}{1+\cdots\cdots}}}}$$

where there is a direct correspondence between the continued fraction coefficients d_i and the summands a_i. The parameters $\{d_i\}$ in equation (6.12) can be calculated from the set $\{a_i\}$ in a straightforward way by using a recursive algorithm, called the P-algorithm by Hänggi et al (1978, 1980). Equation 6.11 can be recast in the form

$$S(y) = \sum_{i=0}^{\infty} \frac{a_i}{y^{2i-1}} \tag{6.13}$$

Obviously, when y = 1, the above series S(y) is reduced to S in equation 6.11. If S(y) is an asymptotic series, S(y) can be transformed into the continued fraction

$$S(y) = \frac{d_1}{y+}\frac{d_2}{y+}\frac{d_3}{y+}\cdots\cdots$$

Starting from the first coefficients, we have

$$\begin{array}{ll}
d_1 = D_1, & D_1 = a_1, \\
d_2 = -D_2/D_1, & D_2 = a_2, \\
d_3 = -D_3/D_2, & D_3 = a_3 + a_2 d_2, \\
d_4 = -D_4/D_3, & D_4 = a_4 + a_3(d_2 + d_3), \\
d_3 = -D_5/D_4, & D_5 = a_5 + a_4(d_2 + d_3 + d_4) + a_3 d_2 d_4, \\
\cdots\cdots &
\end{array} \tag{6.14}$$

The further coefficients D_n, n = 6, 7, ..., can be determined recursively by using the vector X of dimension

$$L = 2 \cdot [(n-1)/2] \tag{6.15}$$

In the above, the notation [] implies that only the integer part is taken.
Starting from n = 4:

$$X(1) = d_2, \qquad X(2) = d_2 + d_3 \tag{6.16}$$

Interchanging X(1) and X(2), as shown below

$$X(1) \to X(2), \qquad X(2) \to X(1) \tag{6.17}$$

Now working upwards for $n \geqslant 5$, in the process we set X(L-1) = 0, we have

$$\begin{array}{ll}
X(k) = X(k-1) + d_{n-1}X(k-2), & k = L, L-2, \ldots, 4, \\
X(2) = X(1) + d_{n-1}, &
\end{array} \tag{6.18}$$

After each recursion step, we interchange the odd and even components:

$$\begin{array}{ll}
X(1) \to X(2), & X(3) \to X(4); \\
X(2) \to X(1), & X(4) \to X(3); \\
\cdots\cdots &
\end{array} \tag{6.19}$$

Then D_n is given by

$$D_n = a_n + \sum_{i=1}^{L/2} a_{n-1} X(2i-1) \tag{6.20}$$

and the coefficient d_n is obtained from:

$$d_n = \frac{D_n}{D_{n-1}} \tag{6.21}$$

In practice, only the last coefficient in equation (6.12) is computed as terms are added to equation (6.11). The continued fraction is re-evaluated as additional partial integrations are added to the series (6.11), and this process terminates when the error criterion is satisfied. From experience, the continued fraction converges quite rapidly, and more than 30 or so terms are almost never required.

6.3. Treatment of singularity in layered Green's functions

6.3.1. Singularity extraction method

Some difficulties may be encountered during numerical integration when the field point is close to the source point (singular point), especially when these two points are on the same level. Some methods have been proposed to evaluate these singular values accurately, e.g., Singularity Extraction Method. In this method, we first remove the singularity in the layered Green's functions in the transformed domain by subtracting from them the full-space Green's functions (e.g., Kelvin's solution, assuming the material property of the source layer). Adaptive integration is then performed on these reduced functions, and the result added to the explicit full-space Green's functions.

Formally, we write the displacements, U_{ij}^* and tractions, T_{ij}^*, as

$$\begin{aligned} U_{ij}^* &= (U_{ij}^* - U_{ij}^{\inf}) + U_{ij}^{\inf} \\ T_{ij}^* &= (T_{ij}^* - T_{ij}^{\inf}) + T_{ij}^{\inf} \end{aligned} \tag{6.13}$$

where $U_{ij}^{\inf}$ and $T_{ij}^{\inf}$ are the displacements and tractions in the full space. For the transversely isotropic case, these Green's functions were derived by Pan and Chou. In the isotropic case, these functions simply reduce to the well-known Kelvin's solution.

Since in the source layer, the layered Green's functions and the full-space Green's functions possess the same singular behaviour, their difference is non-singular. We assume that the corresponding terms in the transformed domain are also non-singular and apply numerical integration to these non-singular functions only. In the transformed domain, eqn. (6.13) can be written as:

$$\begin{aligned} \tilde{U}^{*}_{ij} &= (\tilde{U}^{*}_{ij} - \tilde{U}^{\mathrm{inf}}_{ij}) + \tilde{U}^{\mathrm{inf}}_{ij} \\ \tilde{T}^{*}_{ij} &= (\tilde{T}^{*}_{ij} - \tilde{T}^{\mathrm{inf}}_{ij}) + \tilde{T}^{\mathrm{inf}}_{ij} \end{aligned} \tag{6.14}$$

where ~ indicates the corresponding transformed Green's functions. Applying the adaptive numerical integration to the difference terms in Eqn.(6.14), we obtain the non-singular part of the Green's functions in the physical domain. Finally, the explicit expression of the full-space Green's functions are superimposed to obtain the layered half-space solutions.

6.3.2. Green's functions for full space in transformed domain

We now need to obtain $\tilde{U}^{\mathrm{inf}}_{ij}$ *and* $\tilde{T}^{\mathrm{inf}}_{ij}$, which are the expansion coefficients of the full-space Green's functions in terms of the cylindrical system of vector functions. These can be easily derived in the similar way as that used for layered Green's functions by the propagator matrix method.

Fig. 6.1 shows the model of a full space, and we assume that the loaded plane is located at $z = h$. For convenience, we denote that the upper half-space as Region *I* ($z < h$), and the lower half-space as Region *II* ($z < h$).

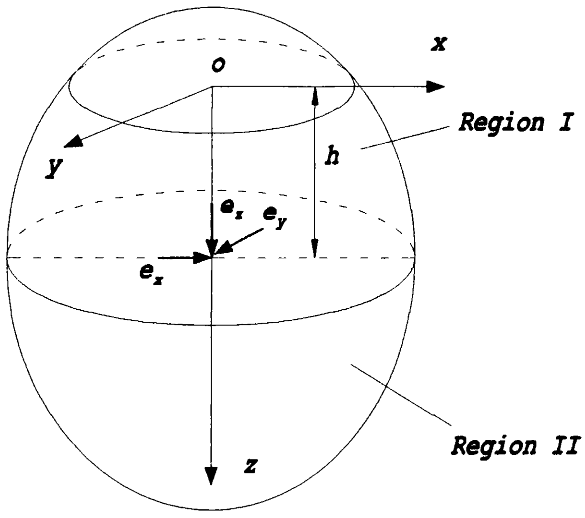

Fig. 6.1 Full space: transversely isotropic elastic material

Using equation (5.17) and (5.23), and considering the regularity conditions at infinity, the expansion coefficients can be written as:

$$\begin{Bmatrix} U_N(z) \\ T_N(z)/\lambda \end{Bmatrix} = \left[Z^{II}(z)\right]\begin{Bmatrix} a_1^{II} \\ 0 \end{Bmatrix}$$

$$\begin{Bmatrix} U_L(z) \\ \lambda U_M(z) \\ T_L(z)/\lambda \\ T_M(z) \end{Bmatrix} = \left[Z^{I}(z)\right]\begin{Bmatrix} a_1 \\ 0 \\ c_1 \\ 0 \end{Bmatrix} \tag{6.15}$$

in region I ($-\infty < z < h$), and:

$$\begin{Bmatrix} U_N(z) \\ T_N(z)/\lambda \end{Bmatrix} = \left[Z^{II}(z)\right]\begin{Bmatrix} 0 \\ b_2^{II} \end{Bmatrix}$$

$$\begin{Bmatrix} U_L(z) \\ \lambda U_M(z) \\ T_L(z)/\lambda \\ T_M(z) \end{Bmatrix} = \left[Z^{I}(z)\right]\begin{Bmatrix} 0 \\ b_2 \\ 0 \\ d_2 \end{Bmatrix} \tag{6.16}$$

in Region 2 ($h < z < +\infty$). In the above, $a_1^{II}, a_1, c_1, b_2^{II}, b_2, d_2$ are six unknown constants which need to be determined from the boundary conditions.

By means of the interfacial conditions (5.42), together with the continuity of displacements, six equations can be developed in these constants:

$$\begin{aligned}
&U_N(h-) = U_N(h+) \\
&T_N(h-)/\lambda - T_N(h+)/\lambda = \Delta T_N/\lambda \\
&U_L(h-) = U_L(h+) \\
&\lambda U_M(h-) = \lambda U_M(h+) \\
&T_L(h-)/\lambda - T_L(h+)/\lambda = \Delta T_L/\lambda \\
&T_M(h-) - T_M(h+) = \Delta T_M
\end{aligned} \tag{6.17}$$

When solving these equations, the three different cases of $m = 0, \pm 1$ must be considered separately. Substituting these results into eqn. (6.15) and (6.16) yields the expansion coefficients of the displacements and tractions in transversely isotropic material. These are listed in Appendix H.

6.4. Numerical examples

In this section, we will examine several numerical examples to verify the formulations presented thus far. Results are presented in non-dimensional form.

We assume a three-layered half space with elastic properties listed in Table 6.1. The interfaces of the layers are at $z = 0.25$ and 1.5 (see Fig.6.2).

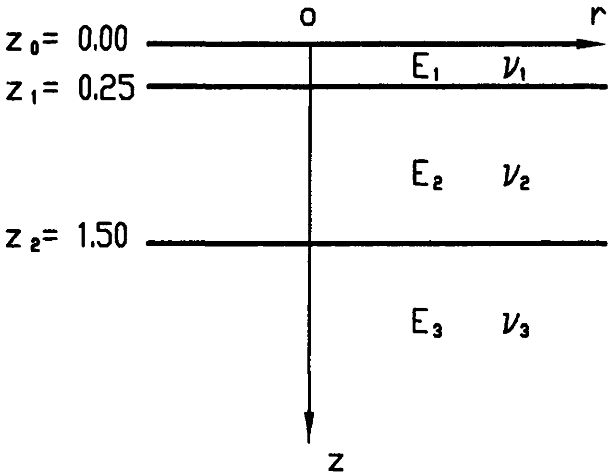

Fig.6.2 Geometry of a three-layered half space

Although the layered half-space Green's functions were derived in cylindrical coordinates, Cartesian components of the displacement Green's function U_i^* and the stress Green's function S_{ij}^* are presented here (A superscript x, y or z indicates the direction of point force). The Cartesian and cylindrical functions are related by:

$$\begin{aligned} U_i^*(x_1,x_2,x_3) &= q_{ik}u_k^*(r,\theta,z) \\ S_{ij}^*(x_1,x_2,x_3) &= q_{ik}q_{jl}\sigma_{kl}^*(r,\theta,z) \end{aligned} \tag{6.18}$$

where $k, l = r, \theta, z$ and

$$q_{i1} = \frac{\partial x_i}{\partial r}, \qquad q_{i2} = \frac{\partial x_i}{\partial \theta}, \qquad q_{i3} = \frac{\partial x_i}{\partial z} \tag{6.19}$$

Table 6.1. Elastic properties in a three layered half space.

	Case 1		Case 2		Case 3	
	E	v	E	v	E	v
layer 1	1.0	0.25	1.0	0.25	1.0	0.25
layer 2	1.0	0.25	2.0	0.25	5.0	0.25
layer 3	1.0	0.25	4.0	0.25	25.0	0.25

6.4.1. Comparison with Mindlin's (1936) solution

Case 1 corresponds to the well-known Mindlin solution. As usual, we assume that the source point is at the origin. The stresses and displacements at two field points near the source point are calculated, i.e., (0.01, 0.0, 0.0) and (0.05, 0.0, 0.0). The first one is very near to the force (i.e. near singular). Table 6.2 lists the displacement and Table 6.3 lists the stresses (overleaf).

From Table 6.2 and 6.3, when the field point is 0.05 from the source, the results obtained by the propagator matrix method agree with Mindlin's solution to a relative error of better than 10^{-15}.

When the field point is moved closer to the source (r = 0.01), we also get highly accurate results (relative error less than 10^{-6}). Although the loss of accuracy in this case is not significant, some integrals (among the 15 integrals) do not converge. This only occurs at the surface of the half-space. This is because we use the full-space Green's functions to extract the singularity from the layered Green's functions, and at the surface the full-space model does not share the same singular behaviour as the half-space model. In the next chapter, we will find that in the multi-layered system with different material properties, this problem arises not only at the free surface, but also at the interface between two layers.

Table 6.2. Displacements at two surface field points (0.01, 0.0, 0.0) and (0.05, 0.0, 0.0) in a three-layered half space. Source point is at the origin.

	X-load			Y-load			Z-load		
		Current Method	Mindlin Solution		Current Method	Mindlin Solution		Current Method	Mindlin Solution
field point at (0.01,0,0)	U_1^1	39.7887359	39.7887358	U_1^2	0.0	0.0	U_1^3	-9.9471832	-9.9471839
	U_2^1	0.0	0.0	U_2^2	29.8415518	29.8415518	U_2^3	0.0	0.0
	U_3^1	9.9471838	9.9471839	U_3^2	0.0	0.0	U_3^3	29.8415520	29.8415518
field point at (0.05,0,0)	U_1^1	7.95774715	7.95774715	U_1^2	0.0	0.0	U_1^3	-1.9894368	-1.9894368
	U_2^1	0.0	0.0	U_2^2	5.96831036	5.96831037	U_2^3	0.0	0.0
	U_3^1	1.98943679	1.98943679	U_3^2	0.0	0.0	U_3^3	5.9683104	5.9683104

Table 6.3. Stresses at two surface field points (0.01, 0.0, 0.0) and (0.05, 0.0, 0.0) in a three-layered half space. Source point is at the origin.

	X-load			Y-load			Z-load		
		Current Method	Mindlin Solution		Current Method	Mindlin Solution		Current Method	Mindlin Solution
field point at (0.01,0,0)	S_{11}^1	-3978.873466	-3978.873577	S_{11}^2	0.0	0.0	S_{11}^3	795.7756	795.7747
	S_{22}^1	0.5×10^{-4}	0.0	S_{22}^2	0.0	0.0	S_{22}^3	-795.7761	-795.7747
	S_{33}^1	-0.6×10^{-7}	0.0	S_{33}^2	0.0	0.0	S_{33}^3	-0.3×10^{-8}	0.0
	S_{23}^1	0.0	0.0	S_{23}^2	-0.3×10^{-8}	0.0	S_{23}^3	0.0	0.0
	S_{13}^1	-0.2×10^{-8}	0.0	S_{13}^2	0.0	0.0	S_{13}^3	0.6×10^{-7}	0.0
	S_{12}^1	0.0	0.0	S_{12}^2	-795.773026	-795.774715	S_{12}^3	0.0	0.0
field point at (0.05,0,0)	S_{11}^1	-159.1549431	159.1549431	S_{11}^2	0.0	0.0	S_{11}^3	31.83099	31.83099
	S_{22}^1	-0.7×10^{-7}	0.0	S_{22}^2	0.0	0.0	S_{22}^3	-31.83099	-31.83099
	S_{33}^1	-0.3×10^{-8}	0.0	S_{33}^2	0.0	0.0	S_{33}^3	-0.1×10^{-9}	0.0
	S_{23}^1	0.0	0.0	S_{23}^2	-0.1×10^{-9}	0.0	S_{23}^3	0.0	0.0
	S_{13}^1	-0.1×10^{-9}	0.0	S_{13}^2	0.0	0.0	S_{13}^3	0.3×10^{-8}	0.0
	S_{12}^1	0.0	0.0	S_{12}^2	-31.83098867	-31.83098861	S_{12}^3	0.0	0.0

6.4.2. Layered half-space

We now study the effect of material layering on displacements and stresses. Using the three-layered isotropic half space (Fig. 6.2), three cases are considered. The layer elastic properties are listed in Table 6.1; case 1 is simply a homogeneous half space; cases 2 and 3 are more general.

(a)

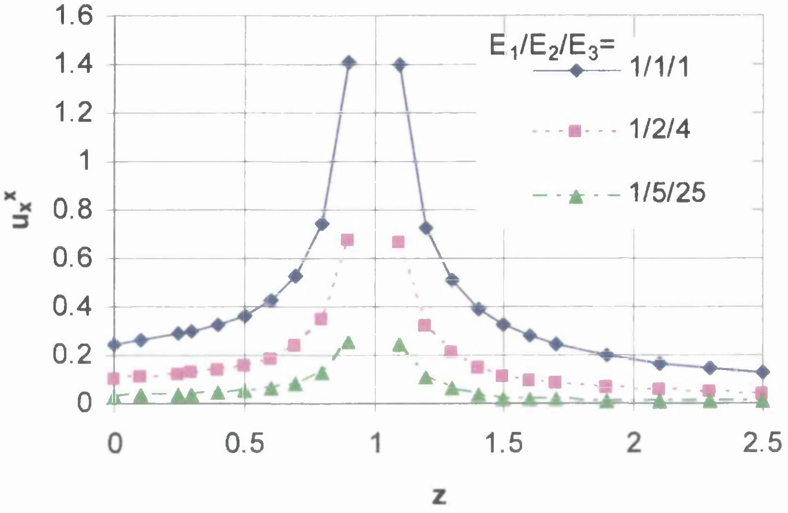

(b)

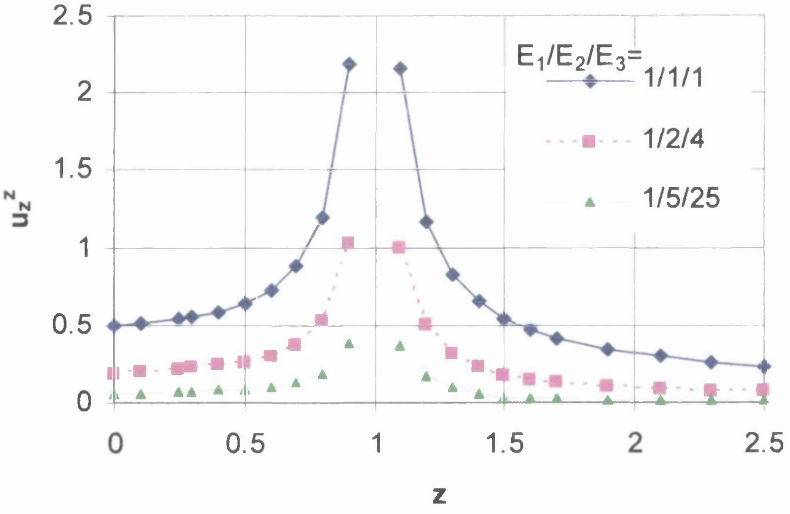

Fig.6.3. Variation of displacements along the z-axis.
(a) Displacement u_x^x, (b) Displacement u_z^z

Figures 6.3 (a) and (b) show, respectively, the variation of the displacement components u_x^x and u_z^z along the vertical line (0, 0, 0 → 2.5). The point force is located at (0, 0, 1). The values in the range $z = 0.9 \rightarrow 1.1$ are omitted, since they increase very quickly towards the singularity.

In Fig. 6.4 (overeleaf), we compare case 1 and case 2 except in (a), where all three models are compared. The horizontal stress is discontinuous at the layer interfaces while all the displacements and the other stress components like σ_{zz}^z and σ_{xz}^x are continuous. Some values of stresses around the source point are listed in Table 6.4.

It may be observed that displacements, as expected, are strongly affected by layering but, stresses are less affected. Since stress distributions are primarily constrained by equilibrium conditions, this latter observation also agrees with expectations.

Table 6.4. Stresses at two field points (0.0, 0.0, 0.9) and (0.0, 0.0, 1.1) for three different layered models.

z_f	stresses	Case 1 1/1/1	Case 2 1/2/4	Case 3 1/5/25
0.9	σ_{xx}^z	-2.67333	-2.67909	-2.67707
	σ_{zz}^z	18.45875	18.37133	18.29559
	σ_{xz}^x	2.63021	2.60459	2.57957
1.1	σ_{xx}^z	2.63922	2.62149	2.61490
	σ_{zz}^z	-18.65879	-18.77617	-18.87798
	σ_{xz}^x	-2.67030	-2.70654	-2.74086

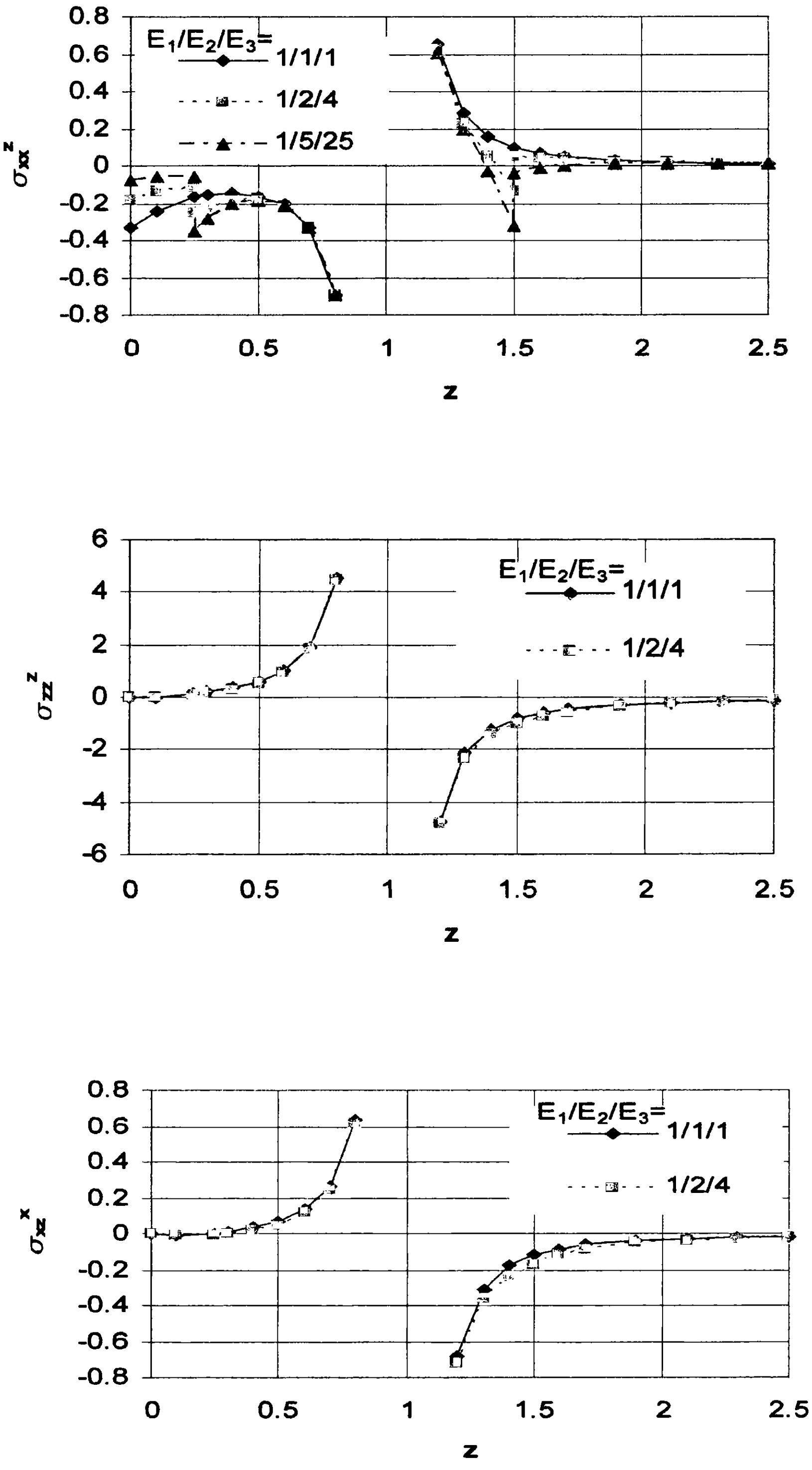

Fig.6.4. Variation of stress components along the z-axis: (a) *stress components* σ^z_{xx}, (b) *stress components* σ^z_{zz}, *(c) stress components* σ^x_{xz}

Chapter 7

Green's functions for the bi-material full space

For cases where the numerical methods described in the last chapter fail, an alternative is proposed here in which the Green's function for the bi-material full-space is used in the singularity extraction method. For this purpose, the transformed domain Green's functions for the bi-material full-space need to be derived. They must be expressed in cylindrical vector form. Numerical examples are examined to verify the effectiveness of this approach.

The Green's functions for the bi-material full-space (expressed in cylindrical vector form) are obtained in this chapter for the first time by the author, and are implemented in the singularity extraction method. Both integral forms and closed-forms of the Green's functions for the bi-material full-space are needed. A similar approach by has been used by Guzina & Pak (1999) to obtain these functions. However, the integral form is not expressed in terms of cylindrical system of vector function, so it can not be used directly in the singularity extraction method here, although its closed-form formulation can be used. Some results obtained by the author have a close relationship with those of Guzina. However, the author's method is simpler compared with Guzina's approach as no displacement potential functions are employed.

7.1. Green's functions: closed form and integral representations

In Chapter 6, full-space Green's functions were used in the numerical calculation of layered Green's functions, exploiting the fact that these two functions share the same singular behaviour. However, as described in section 6.4.1, this method fails in two special circumstances; (a) when source and field points are both at the free surface, and (b) source and field points are located near the interface between two different materials. In some cases, accuracy is degraded, while in others the method fails to converge and leads to gross errors.

The reason for this loss of accuracy lies in the fact that full-space Green's functions do not share the same singular behaviour as those of layered Green's functions at an interface. The Green's function for a bi-material full space is the natural choice for more accurate evaluation of layered Green's functions at the layer integrals.

To use bi-material Green's functions we need two representations for them, i.e., the closed-form and the integral representation. The former is expressed as U_{ij}^{inf} and T_{ij}^{inf} (in eqn. 6.13), and the latter as $\widetilde{U}_{ij}^{\mathrm{inf}}$ and $\widetilde{T}_{ij}^{\mathrm{inf}}$ (in eqn. 6.14). It may be noted that this dual format is also useful to deal with the singular behaviour of dynamic Green's functions (Pak, 1987; Guzina, 1996), and the derivation of certain boundary integral formulations (Sladek and Sladek, 1991; Tanaka et al., 1994).

A number of approaches to the bi-material problems have been proposed. Rongved (1955) first derived the static fundamental solutions for an isotropic, bi-material full-space by means of Papkovitch functions. Following his work, Vijayakumar & Cormack (1987) presented matrix representations of displacements and stresses. Pan & Chou (1979) and Konguchi et al. (1990) extended the Mindlin solution (1936) for a homogeneous isotropic half-space to a transversely isotropic two-phase material. Yu and Sanday (1991) developed the Galerkin vector method for a number of nuclei of strain in an isotropic bi-material full-space. However, none of these solutions is in the form of an integral representation.

Guzina & Pak (1999) applied the method of integral transforms and Fourier decomposition, in the context of displacement potentials, to the point-load problem for an elastic bi-material full-space, and obtained new results in the form of integral representations of the displacements and stresses. Closed-form solutions were also derived. Unfortunately, the integral representations in Guzina's approach are not expressed in terms of the cylindrical system of vector functions which are needed here. These representations of Green's functions for the bi-material full-space in the transformed domain are derived here for the first time.

7.2. Closed form Green's functions for the bi-material full-space

Guzina's approach

The physical domain of interest is taken to be composed of two dissimilar isotropic elastic half-spaces which are fully bonded across the plane $z = 0$ (see Fig. 7.1). The Lame's constants of the upper half space (referred to as Region 1) are denoted as λ_1 and μ_1, and the ones of the lower half-space as λ_2 and μ_2.

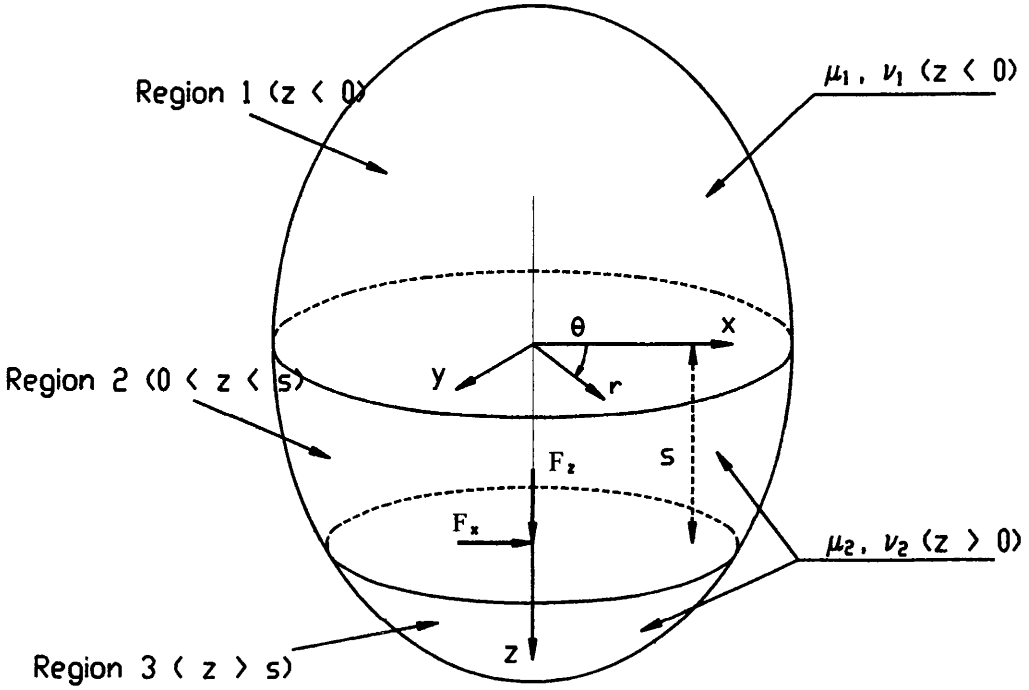

Fig. 7.1. Bi-material full space.

In Guzina's approach, the action of an arbitrary distributed source (concentrated point load can be seen as a special case) across the plane $z = s$ can be represented as a set of prescribed stress discontinuities across the corresponding planar region, as follows

$$\begin{aligned}
&\sigma_{zr}(r,\theta,s-)-\sigma_{zr}(r,\theta,s+)=P(r,\theta)\\
&\sigma_{z\theta}(r,\theta,s-)-\sigma_{z\theta}(r,\theta,s+)=Q(r,\theta)\\
&\sigma_{zz}(r,\theta,s-)-\sigma_{zz}(r,\theta,s+)=R(r,\theta)
\end{aligned} \tag*{(5.33) bis}$$

Without loss of generality, it is assumed that the loaded plane is located in the lower half-space, i.e., $s > 0$ (see Fig. 7.1). For convenience, we suppose that lower half-space is composed of two parts, Region 2 ($0 < z < s$) and Region 3 ($z > s$), as indicated in Fig. 7.1.

By means of Fourier decomposition and the Hankel transform method, Guzina & Pak (1999) obtained the transformed Fourier components of the displacement field in the form:

$$
\begin{aligned}
\tilde{u}_{zm}^{m} \quad &= \Omega_1(\lambda,z;s)\frac{X_m-Y_m}{2\mu_2}+\Omega_2(\lambda,z;s)\frac{Z_m}{\mu_2} \\
\tilde{u}_{rm}^{m+1}+i\,\tilde{u}_{\theta m}^{m+1} &= -\gamma_1(\lambda,z;s)\frac{X_m-Y_m}{2\mu_2}+\gamma_2(\lambda,z;s)\frac{X_m+Y_m}{2\mu_2} \\
&\quad -\gamma_3(\lambda,z;s)\frac{Z_m}{\mu_2} \qquad (7.1) \\
\tilde{u}_{rm}^{m-1}-i\,\tilde{u}_{\theta m}^{m-1} &= \gamma_1(\lambda,z;s)\frac{X_m-Y_m}{2\mu_2}+\gamma_2(\lambda,z;s)\frac{X_m+Y_m}{2\mu_2} \\
&\quad +\gamma_3(\lambda,z;s)\frac{Z_m}{\mu_2}
\end{aligned}
$$

The expression for X_m, Y_m and Z_m has been given as follows

$$
\begin{aligned}
X_m(\lambda) &= \tilde{P}_m^{m-1}(\lambda)-i\tilde{Q}_m^{m-1}(\lambda) \\
Y_m(\lambda) &= \tilde{P}_m^{m+1}(\lambda)+i\tilde{Q}_m^{m+1}(\lambda) \qquad (5.38)\text{ bis} \\
Z_m(\lambda) &= \tilde{R}_m^{m}(\lambda)
\end{aligned}
$$

The notation ~ and *m*, as has been explained section 5.4, represent the *m*-th order Hankel transform. The terms Ω_1, Ω_2, γ_1, γ_2, γ_3 are auxiliary functions and are defined as follows:

For Region 1,

$$
\begin{aligned}
\Omega_1 &= \frac{\mu_2\exp(-\lambda d_1)}{2\lambda M_1 M_2}\{\lambda(zM_2-sM_1)-(\mu_1(3-4\nu_2)(1-2\nu_1) \\
&\quad -\mu_2(3-4\nu_1)(1-2\nu_2))\} \\
\Omega_2 &= \frac{-\mu_2\exp(-\lambda d_1)}{2\lambda M_1 M_2}\{\lambda(zM_2-sM_1)-(\mu_1(3-4\nu_2)(2-2\nu_1) \\
&\quad +\mu_2(3-4\nu_1)(2-2\nu_2))\} \qquad (7.2) \\
\gamma_1 &= \frac{\mu_2\exp(-\lambda d_1)}{2\lambda M_1 M_2}\{\lambda(zM_2-sM_1)+(\mu_1(3-4\nu_2)(2-2\nu_1) \\
&\quad +\mu_2(3-4\nu_1)(2-2\nu_2))\} \\
\gamma_2 &= \frac{\mu_2\exp(-\lambda d_1)}{\lambda(\mu_1+\mu_2)} \\
\gamma_3 &= \frac{-\mu_2\exp(-\lambda d_1)}{2\lambda M_1 M_2}\{\lambda(zM_2-sM_1)+(\mu_1(3-4\nu_2)(1-2\nu_1) \\
&\quad -\mu_2(3-4\nu_1)(1-2\nu_2))\}
\end{aligned}
$$

where

$$\begin{aligned} d_1 &= \left|z-s\right| \\ d_2 &= z+s \\ M_1 &= \mu_1 + (3-4\nu_1)\mu_2 \\ M_2 &= \mu_2 + (3-4\nu_2)\mu_1 \end{aligned} \tag{7.3}$$

For Region 2 and 3,

$$\begin{aligned}
\Omega_1 &= \frac{\exp(-\lambda d_1)}{8\lambda(1-\nu_2)M_1M_2}\{\lambda d_3 M_1 M_2\} + \frac{\exp(-\lambda d_2)}{8\lambda M_1 M_2(1-\nu_2)}\{-4\mu_2(1-\nu_2) \\
&\quad (\mu_1(3-4\nu_2)(1-2\nu_1) - \mu_2(3-4\nu_1)(1-2\nu_2)) - M_1(\mu_1-\mu_2) \\
&\quad (3-4\nu_2)\lambda d_3 + 2\lambda^2(\mu_1-\mu_2)M_1 sz\} \\
\Omega_2 &= \frac{\exp(-\lambda d_1)}{8\lambda(1-\nu_2)M_1M_2}(3-4\nu_2+\lambda d_1)M_1M_2 + \frac{\exp(-\lambda d_2)}{8\lambda M_1 M_2(1-\nu_2)} \\
&\quad \{-2\lambda^2(\mu_1-\mu_2)M_1 zs - M_1(\mu_1-\mu_2)(3-4\nu_2)\lambda d_2 - \\
&\quad (\mu_1^2(3-4\nu_2)^2 - \mu_2^2(3-4\nu_1)(5-12\nu_2+8\nu_2^2) \\
&\quad + \mu_1\mu_2(3-4\nu_2)(2-4\nu_1)(1-2\nu_2))\} \\
\gamma_2 &= \frac{\exp(-\lambda d_1)}{8\lambda(1-\nu_2)M_1M_2}(3-4\nu_2-\lambda d_1)M_1M_2 + \frac{\exp(-\lambda d_2)}{8\lambda M_1 M_2(1-\nu_2)} \\
&\quad \{-2\lambda^2(\mu_1-\mu_2)M_1 zs + M_1(\mu_1-\mu_2)(3-4\nu_2)\lambda d_2 - \\
&\quad (\mu_1^2(3-4\nu_2)^2 - \mu_2^2(3-4\nu_1)(5-12\nu_2+8\nu_2^2) \\
&\quad + \mu_1\mu_2(3-4\nu_2)(2-4\nu_1)(1-2\nu_2))\} \\
\gamma_2 &= \frac{\exp(-\lambda d_1)}{2\lambda} - \frac{\exp(-\lambda d_2)}{2\lambda(\mu_1+\mu_2)}\{\mu_1-\mu_2\} \\
\gamma_3 &= \frac{\exp(-\lambda d_1)}{8\lambda(1-\nu_2)M_1M_2}\{-\lambda d_3 M_1 M_2\} + \frac{\exp(-\lambda d_2)}{8\lambda M_1 M_2(1-\nu_2)}\{-4\mu_2(1-\nu_2) \\
&\quad (\mu_1(3-4\nu_2)(1-2\nu_1) - \mu_2(3-4\nu_1)(1-2\nu_2)) + M_1(\mu_1-\mu_2) \\
&\quad (3-4\nu_2)\lambda d_3 + 2\lambda^2(\mu_1-\mu_2)M_1 sz\}
\end{aligned} \tag{7.4}$$

where

$$d_3 = z - s \tag{7.5}$$

From the stress-displacement relationship and the displacement solutions (equation 7.1), the stress components in transformed domain can also be derived as follows (Guzina & Pak, 1999)

$$
\begin{aligned}
\tilde{\tau}_{zzm}^{m} &= \left[(\Lambda_b + 2\mu_b)\frac{d\Omega_1}{dz} - \Lambda_b \xi \gamma_1\right]\frac{X_m - Y_m}{2\mu_2} + \\
&\quad \left[(\Lambda_b + 2\mu_b)\frac{d\Omega_2}{dz} - \Lambda_b \xi \gamma_3\right]\frac{Z_m}{\mu_2} \\
\tilde{\tau}_{zrm}^{m+1} + i\,\tilde{\tau}_{z\theta m}^{m+1} &= -\mu_b\left(\frac{d\gamma_1}{dz} + \xi\Omega_1\right)\frac{X_m - Y_m}{2\mu_2} + \mu_b\frac{d\gamma_2}{dz}\frac{X_m + Y_m}{2\mu_2} \\
&\quad - \mu_b\left(\frac{d\gamma_3}{dz} + \xi\Omega_2\right)\frac{Z_m}{\mu_2} \\
\tilde{\tau}_{zrm}^{m-1} - i\,\tilde{\tau}_{z\theta m}^{m-1} &= \mu_b\left(\frac{d\gamma_1}{dz} + \xi\Omega_1\right)\frac{X_m - Y_m}{2\mu_2} + \mu_b\frac{d\gamma_2}{dz}\frac{X_m + Y_m}{2\mu_2} \\
&\quad + \mu_b\left(\frac{d\gamma_3}{dz} + \xi\Omega_2\right)\frac{Z_m}{\mu_2}
\end{aligned}
\tag{7.6}
$$

Where the subscript b of the piecewise constant Lamé's moduli Λ and μ takes value of 1 when in region I ($z < 0$), and 2 in region II and III ($z > 0$).

In particular, considering the bi-material medium under the action of horizontal and vertical unit point loads as shown in Chapter 5

$$
\begin{aligned}
\boldsymbol{f}_h(r,\theta,z) &= \frac{1}{2\pi r}\delta(r)\delta(z-s)\boldsymbol{i}_h \\
\boldsymbol{f}_z(r,\theta,z) &= \frac{1}{2\pi r}\delta(r)\delta(z-s)\boldsymbol{i}_z
\end{aligned}
\tag*{(5.28) bis}
$$

the transformed loading coefficients X_m, Y_m and Z_m have also been obtained as

$$
\begin{aligned}
X_1(\lambda) &= \frac{1}{2\pi}e^{-i\theta_0}, & X_m(\lambda) &= 0 & m &\neq 1, \\
Y_{-1}(\lambda) &= \frac{1}{2\pi}e^{i\theta_0}, & Y_m(\lambda) &= 0 & m &\neq -1, \\
Z_0(\lambda) &= \frac{1}{2\pi}, & Z_m(\lambda) &= 0 & m &\neq 0.
\end{aligned}
\tag*{(5.39) bis}
$$

Substituting these coefficients into eqn. (7.1) and inverting the transformed expression result in the closed-form representation of displacement (U_{ij}^*) and generalized stresses (S_{ij}^*) for the joined half spaces, which can be readily used in the singularity extraction method.

Numerical example

The closed-form bi-material Green's functions can be verified in part by examining two limiting cases resulting from them by setting: (1) the modulus of the upper half space ($z < 0$) equate to zero, (2) the moduli of both media equal. Guzina (1999) shows that the functions are correct for these two cases, which correspond to the Mindlin solution and Kelvin's solution, respectively.

Self-consistency can be verified by numerical differentiation. The differentials of displacement can be approximated by:

$$\begin{aligned}\frac{\partial U_i^*(x,y,z)}{\partial x} &\approx \frac{U_i^*(x+\Delta x,y,z)-U_i^*(x,y,z)}{\Delta x}\\ \frac{\partial U_i^*(x,y,z)}{\partial y} &\approx \frac{U_i^*(x,y+\Delta y,z)-U_i^*(x,y,z)}{\Delta y}\\ \frac{\partial U_i^*(x,y,z)}{\partial z} &\approx \frac{U_i^*(x,y,z+\Delta z)-U_i^*(x,y,z)}{\Delta z}\end{aligned} \tag{7.6}$$

Where Δx (Δy or Δz) is optimally chosen to be $10^{-6}r$ where r is the separation of the load and field point. The selection of this value takes into account of the machine precision.

Using the strain-displacement relation and Hooke's law, we can then obtain the corresponding stresses. These can be compared to those obtained directly from the closed-form formulations to verify self-consistency.

As an example, we assume a bi-material full-space with $E_1 = 5$, $\nu_1 = 0.1$ in the upper half space and $E_2 = 1$, $\nu_2 = 0.4$ in the lower one. The source (a unit vertical force) is located at (0, 0, 8). The field point is located at coordinates (1, 3, 5), so the horizontal distance r between source and field points is 3.16. The stresses calculated from the two methods are listed in Table 7.1.

Table 7.1. Stresses ($\times 10^3$) at field point due to vertical unit load.

	closed-form	numerical differentiation
S_{11}^3	0.3098 44	0.3098 50

S^3_{22}	3.3918 15	3.3918 21
S^3_{33}	5.0185 84	5.0185 86
S^3_{23}	-3.6817 32	-3.6817 29
S^3_{13}	-1.2272 44	-1.2272 46
S^3_{12}	1.1557 39	1.1557 40

As shown in Table 7.1., the data demonstrates that the self-consistency test is satisfied. We now examine a special case where the source and field points are both at the interface level between the two media, i.e., $z = s = 0$. Expressed in the cylindrical coordinate system, a unit horizontal load acts in the $\theta_0 = 0$ direction at the origin. Two field points are considered: one is located at $(r, \theta, z) = (3.1623, 71.565, 0)$, while the second (singular) one is located at $(r, \theta, z) = (1.0\times10^{-5}, 71.565, 0)$. The resulting stresses are listed in Table 7.2.

Table 7.2 Stresses at two field points in a bi-material full space.

	field point 1 stresses ($\times10^{-4}$)		field point 2 stresses ($\times10^{7}$)	
	closed-form	numerical differentiation	closed-form	numerical differentiation
S^1_{11}	-10.1323 6	-10.1323 7	-10.1323 6	-10.1323 8
S^1_{22}	- 8.8488 25	- 8.8488 25	- 8.8488 25	- 8.8488 26
S^1_{33}	4.7597 13	4.7597 20	4.7597 20	4.7597 14
S^1_{23}	5.6996 57	5.6996 47	5.6996 57	5.6996 47
S^1_{13}	- 7.5995 43	- 7.5995 45	- 7.5995 43	- 7.5995 45
S^1_{12}	- 1.4592 93	- 1.4592 92	-14.5929 3	-14.5929 2

From Table 7.2, we can see at both the singular and the non-singular point, the closed-form formulation are self-consistent.

7.3. Green's functions for the bi-material full-space in the transformed domain

It now remains to derive the transformed domain representations expressed in terms of the cylindrical system of vector functions. Similar to the process described in section 6.3, in which the Green's functions for full-space are derived, here also from eqn. (5.17) and (5.23), and considering the regularity conditions at infinity, the relevant expansion coefficients can be written as

$$\begin{Bmatrix} U_N(z) \\ T_N(z)/\lambda \end{Bmatrix} = \left[Z^{II}(z)\right]\begin{Bmatrix} a_1^{II} \\ 0 \end{Bmatrix}$$

$$\begin{Bmatrix} U_L(z) \\ \lambda U_M(z) \\ T_L(z)/\lambda \\ T_M(z) \end{Bmatrix} = \left[Z^{I}(z)\right]\begin{Bmatrix} a_1 \\ 0 \\ c_1 \\ 0 \end{Bmatrix} \qquad (7.7)$$

in Region 1(-∞<z<0)

$$\begin{Bmatrix} U_N(z) \\ T_N(z)/\lambda \end{Bmatrix} = \left[Z^{II}(z)\right]\begin{Bmatrix} a_2^{II} \\ b_2^{II} \end{Bmatrix}$$

$$\begin{Bmatrix} U_L(z) \\ \lambda U_M(z) \\ T_L(z)/\lambda \\ T_M(z) \end{Bmatrix} = \left[Z^{I}(z)\right]\begin{Bmatrix} a_2 \\ b_2 \\ c_2 \\ d_2 \end{Bmatrix} \qquad (7.8)$$

in Region 2 (0<z<s), and

$$\begin{Bmatrix} U_N(z) \\ T_N(z)/\lambda \end{Bmatrix} = \left[Z^{II}(z)\right]\begin{Bmatrix} 0 \\ b_3^{II} \end{Bmatrix}$$

$$\begin{Bmatrix} U_L(z) \\ \lambda U_M(z) \\ T_L(z)/\lambda \\ T_M(z) \end{Bmatrix} = \left[Z^{I}(z)\right]\begin{Bmatrix} 0 \\ b_3 \\ 0 \\ d_3 \end{Bmatrix} \qquad (7.9)$$

in Region 3 (s<z<+∞). In the above, $a_1^{II}, a_1, \cdots\cdots d_3$ are the unknown constants to be determined from the boundary conditions.

Combining eqn. (7.7)-(7.9), the interface conditions (see eqn. 5.42), as well as the continuity of displacements and tractions between the two half spaces across the plane $z = 0$, twelve equations can be developed which can be used to determine the twelve unknown coefficients ($a_1^{II}, a_1, \cdots\cdots d_3$). These twelve equations are:

On the plane $z = 0$:

$$\begin{aligned}
U_N(0-) &= U_N(0+) \\
T_N(0-)/\lambda &= T_N(0+)/\lambda \\
U_L(0-) &= U_L(0+) \\
\lambda U_M(0-) &= \lambda U_M(0+) \\
T_L(0-)/\lambda &= T_L(0+)/\lambda \\
T_M(0-) &= T_M(0+)
\end{aligned} \tag{7.10}$$

On the plane $z = s$:

$$\begin{aligned}
U_N(s-) &= U_N(s+) & & \\
T_N(s-)/\lambda - T_N(s+)/\lambda &= F_N/\lambda & & m = \pm 1 \\
U_L(s-) &= U_L(s+) & & \\
\lambda U_M(s-) &= \lambda U_M(s+) & & \\
T_L(s-)/\lambda - T_L(s+)/\lambda &= F_L/\lambda & & m = 0 \\
T_M(s-) - T_M(s+) &= F_M & & m = \pm 1
\end{aligned} \tag{7.11}$$

After the twelve constants are determined, they are then substituted back into eqns. (7.7)-(7.9), which yields the transformed expansion coefficients of the displacements and tractions, as follows:

For Region 1,

$$\begin{aligned}
U_{N0}(z) &= 0 \\
T_{N0}(z)/\lambda &= 0 \\
U_{L0}(z) &= \frac{F_{L0}\exp(-\lambda d_1)}{2\lambda M_1 M_2}[2\mu_1(3-4\nu_2)(1-\nu_1) + 2\mu_2(3-4\nu_1)(1-\nu_2) \\
&\qquad + \lambda(sM_1 - zM_2)] \\
\lambda U_{M0}(z) &= \frac{F_{L0}\exp(-\lambda d_1)}{2\lambda M_1 M_2}[-\mu_1(3-4\nu_2)(1-2\nu_1) + \mu_2(3-4\nu_1)(1-2\nu_2) \\
&\qquad + \lambda(sM_1 - zM_2)] \\
T_{L0}(z)/\lambda &= \frac{\mu_1 F_{L0}\exp(-\lambda d_1)}{2\lambda M_1 M_2}[M_1(3-4\nu_2) + M_2 + 2\lambda(sM_1 - zM_2)] \\
T_{M0}(z) &= \frac{\mu_1 F_{L0}\exp(-\lambda d_1)}{2\lambda M_1 M_2}[\mu_2(3-4\nu_1)(3-4\nu_2) - \mu_2 + 2\lambda(sM_1 - zM_2)]
\end{aligned} \tag{7.12}$$

$$U_{N+1}(z)=\frac{F_{N+1}\exp(-\lambda d_1)}{\lambda(\mu_1+\mu_2)}$$

$$T_{N+1}(z)/\lambda=\frac{\mu_1F_{L+1}\exp(-\lambda d_1)}{\lambda(\mu_1+\mu_2)}$$

$$U_{L+1}(z)=\frac{F_{M+1}\exp(-\lambda d_1)}{4M_1M_2}[M_1(3-4\nu_2)-M_2(3-4\nu_1)+2\lambda(zM_2-sM_1)]$$

$$\lambda U_{M+1}(z)=\frac{F_{M+1}\exp(-\lambda d_1)}{4M_1M_2}[M_1(3-4\nu_2)+M_2(3-4\nu_1)+2\lambda(zM_2-sM_1)]$$

$$T_{L+1}(z)/\lambda=\frac{\mu_1F_{M+1}\exp(-\lambda d_1)}{2M_1M_2}[M_1(3-4\nu_2)-M_2+2\lambda(zM_2-sM_1)]$$

$$T_{M+1}(z)=\frac{\mu_1F_{M+1}\exp(-\lambda d_1)}{2M_1M_2}[M_1(3-4\nu_2)+M_2+2\lambda(zM_2-sM_1)]$$

for Region 2 and 3,

$$\begin{aligned}
&U_{N0}(z)=0\\
&T_{N0}(z)/\lambda=0\\
&U_{L0}(z)=\frac{F_{L0}\exp(-\lambda d_1)}{8\mu_2\lambda(1-\nu_2)}(3-4\nu_2+\lambda d_1)+\frac{F_{L0}\exp(-\lambda d_2)}{8\mu_2\lambda M_1M_2(1-\nu_2)}\\
&\qquad[-2\lambda^2(\mu_1-\mu_2)M_1zs-M_1(\mu_1-\mu_2)(3-4\nu_2)\lambda d_2-\\
&\qquad(\mu_1^2(3-4\nu_2)^2-\mu_2^2(3-4\nu_1)(5-12\nu_2+8\nu_2^2)\\
&\qquad+\mu_1\mu_2(3-4\nu_2)(2-4\nu_1)(1-2\nu_2))]\\
&\lambda U_{M0}(z)=-\frac{F_{L0}\exp(-\lambda d_1)}{8\mu_2(1-\nu_2)}d_3+\frac{F_{L0}\exp(-\lambda d_2)}{8\mu_2\lambda M_1M_2(1-\nu_2)}[-4\mu_2(1-\nu_2)\\
&\qquad(\mu_1(3-4\nu_2)(1-2\nu_1)-\mu_2(3-4\nu_1)(1-2\nu_2))+M_1(\mu_1-\mu_2)\\
&\qquad(3-4\nu_2)\lambda d_3+2\lambda^2(\mu_1-\mu_2)M_1sz]
\end{aligned}\tag{7.13}$$

$$\begin{aligned}
T_{L0}(z)/\lambda = {} & -\frac{F_{L0}\exp(-\lambda d_1)}{4\lambda(1-\nu_2)} sign(z-s)(2-2\nu_2+\lambda d_1) + \frac{F_{L0}\exp(-\lambda d_2)}{4\lambda M_1 M_2(1-\nu_2)} \\
& [2\mu_1^2(3-4\nu_2)(1-\nu_2) - 2\mu_2^2(3-4\nu_1)(1-\nu_2) + \lambda s M_1(\mu_1-\mu_2) + \\
& \lambda z M_1(\mu_1-\mu_2)(3-4\nu_2) + 2\lambda^2(\mu_1-\mu_2)M_1 sz]
\end{aligned}$$

$$\begin{aligned}
T_{M0}(z) = {} & \frac{F_{L0}\exp(-\lambda d_1)}{4\lambda(1-\nu_2)}(1-2\nu_2+\lambda d_1) + \frac{F_{L0}\exp(-\lambda d_2)}{4\lambda M_1 M_2(1-\nu_2)}[2\mu_1\mu_2 \\
& (3-4\nu_2)(1-2\nu_1) - \mu_1^2(3-4\nu_2)(1-2\nu_2) - \mu_2^2(3-4\nu_1)(1-2\nu_2) \\
& + \lambda s M_1(\mu_1-\mu_2) - \lambda z M_1(\mu_1-\mu_2)(3-4\nu_2) - 2\lambda^2(\mu_1-\mu_2)M_1 sz]
\end{aligned}$$

$$U_{N+1}(z) = \frac{F_{N+1}\exp(-\lambda d_1)}{2\mu_2\lambda} - \frac{F_{N+1}\exp(-\lambda d_2)(\mu_1-\mu_2)}{2\mu_2\lambda(\mu_1+\mu_2)}$$

$$T_{N+1}(z)/\lambda = -\frac{F_{L+1}\exp(-\lambda d_1)}{2\lambda} sign(z-s) + \frac{F_{N+1}\exp(-\lambda d_2)(\mu_1-\mu_2)}{2\lambda(\mu_1+\mu_2)}$$

$$\begin{aligned}
U_{L+1}(z) = {} & \frac{F_{M+1}\exp(-\lambda d_1)}{8\mu_2(1-\nu_2)}\lambda d_3 + \frac{F_{M+1}\exp(-\lambda d_2)}{8\mu_2\lambda M_1 M_2(1-\nu_2)}[-4\mu_2(1-\nu_2) \\
& (\mu_1(3-4\nu_2)(1-2\nu_1) - \mu_2(3-4\nu_1)(1-2\nu_2)) - M_1(\mu_1-\mu_2) \\
& (3-4\nu_2)\lambda d_3 + 2\lambda^2(\mu_1-\mu_2)M_1 sz]
\end{aligned}$$

$$\begin{aligned}
\lambda U_{M+1}(z) = {} & \frac{F_{M+1}\exp(-\lambda d_1)}{8\mu_2(1-\nu_2)}(3-4\nu_2-\lambda d_1) + \frac{F_{M+1}\exp(-\lambda d_2)}{8\mu_2 M_1 M_2(1-\nu_2)} \\
& [-2\lambda^2(\mu_1-\mu_2)M_1 zs + M_1(\mu_1-\mu_2)(3-4\nu_2)\lambda d_2 - \\
& (\mu_1^2(3-4\nu_2)^2 - \mu_2^2(3-4\nu_1)(5-12\nu_2+8\nu_2^2) \\
& + \mu_1\mu_2(3-4\nu_2)(2-4\nu_1)(1-2\nu_2))]
\end{aligned}$$

$$\begin{aligned}
T_{L+1}(z)/\lambda = {} & \frac{F_{M+1}\exp(-\lambda d_1)}{4(1-\nu_2)}(1-2\nu_2+\lambda d_1) + \frac{F_{M+1}\exp(-\lambda d_2)}{4M_1 M_2(1-\nu_2)} \\
& [-2\mu_1^2(3-4\nu_2)(1-\nu_2) + 2\mu_2^2(3-4\nu_1)(1-\nu_2) + M_1(\mu_1-\mu_2) \\
& (3-4\nu_2) + M_1(\mu_1-\mu_2)(-\lambda s + \lambda z(3-4\nu_2) - 2\lambda^2 sz)]
\end{aligned}$$

$$\begin{aligned}
T_{M+1}(z) = {} & -\frac{F_{M+1}\exp(-\lambda d_1)}{4(1-\nu_2)} sign(z-s)(2-2\nu_2-\lambda d_1) + \frac{F_{M+1}\exp(-\lambda d_2)}{4M_1 M_2(1-\nu_2)} \\
& [2\mu_1^2(3-4\nu_2)(1-\nu_2) - 2\mu_2^2(3-4\nu_1)(1-\nu_2) - M_1(\mu_1-\mu_2) \\
& (\lambda s + \lambda z(3-4\nu_2) - 2\lambda^2 sz)]
\end{aligned}$$

In the above, the definition of parameters like d_1, d_2, d_3, M_1, M_2 are the same as those in eqn. (7.3) and (7.5). The second subscript m designates the m-th Fourier decomposition component. We give the equations for m = 0 and 1 only. To obtain the equations for m = -1 terms we simply replace all subscripts +1 in the above equations by -1.

Comparing the above displacement expansion coefficients with the earlier auxiliary functions in eqn. (7.2) and (7.4), one may find the following relations:

$$
\begin{aligned}
U_{L+1}(z) &= \Omega_1 \frac{\lambda F_{M+1}}{\mu_2} \\
\lambda U_{M+1}(z) &= \gamma_1 \frac{\lambda F_{M+1}}{\mu_2} \\
U_{N+1}(z) &= \gamma_2 \frac{F_{N+1}}{\mu_2} \\
U_{L0}(z) &= \Omega_2 \frac{F_{L0}}{\mu_2} \\
\lambda U_{M0}(z) &= \gamma_3 \frac{\lambda F_{L0}}{\mu_2}
\end{aligned}
\qquad (7.14)
$$

In the above, we can see a one-to-one relationship exists between the expansion coefficients and the auxiliary functions described by Guzina & Pak(1999). Substituting these coefficients into eqn. (6.1) and (6.2), we obtain the same closed-form representations of Green's functions for the bi-material full space as those by Guzina's approach. However, although Guzina and the author both obtain the integral representation of Green's function for bi-material full-space, the difference lies in the fact that the author's method is expressed in the cylindrical system of vector functions while Guzina's method is not. Moreover, the current approach is simpler as it does not apply the integral transforms and Fourier decompositions in the context of displacement potentials. Most importantly, since it expands the displacements and tractions in terms of the cylindrical system of vector functions, the coefficients are ready to be used to extract the singularity in the Green's functions for multi-layered half-space from the propagator matrix method which, as described in Chapter 5 and 6, are also based on the cylindrical system of vector functions.

7.4. Numerical examples

For convenience, we denote the singularity extraction method based on Kelvin's solution as method *I* here. As noted earlier, this method is unsatisfactory in some (singular) cases. The alternative method described here, which makes use of the Green's functions for bi-material full-space, is denoted as method *II*. In this section, we compare these two methods. The results are presented in non-dimensional form.

We use the three-layered half-space problem described in section 6.4 (see Fig. 6.2); the material properties are listed in Table 6.1 and reproduced here for convenience.

Table 6.1. Elastic properties in a three layered half space.

	Case 1		Case 2		Case 3	
	E	ν	E	ν	E	ν
layer 1	1.0	0.25	1.0	0.25	1.0	0.25
layer 2	1.0	0.25	2.0	0.25	5.0	0.25
layer 3	1.0	0.25	4.0	0.25	25.0	0.25

For case 1, the Mindlin problem, the solution is essentially exact. Next we consider Case 3. The point source is located at (0.0, 0.0, 1.5), Two field points are considered: (0.01, 0.0, 1.5) and (0.05, 0.0, 1.5). Both source and field points are at the same interface z = 1.5, which is between layer 2 and 3. The first field point is more nearly singular.

Before examining the results in detail, we first discuss some aspects of the numerical integration technique. We recall that we integrate between the successive zeros of the Bessel function. High accuracy is achievable but the process may not converge at singularities.

We take a closer look at the 15 kernel functions, and select two of them as examples. Kernel 1 is $U_{M0}\lambda J_1(\lambda r)$, and kernel 4 is $T_{L0}J_0(\lambda r)$. Consider a source point at (0.0, 0.0, 1.5) and field point at (0.01, 0.0, 1.5). A plot of these kernel functions versus λ is shown in Fig. 7.2. The increment of the abscissa λ is 50, and the starting value is 0.5.

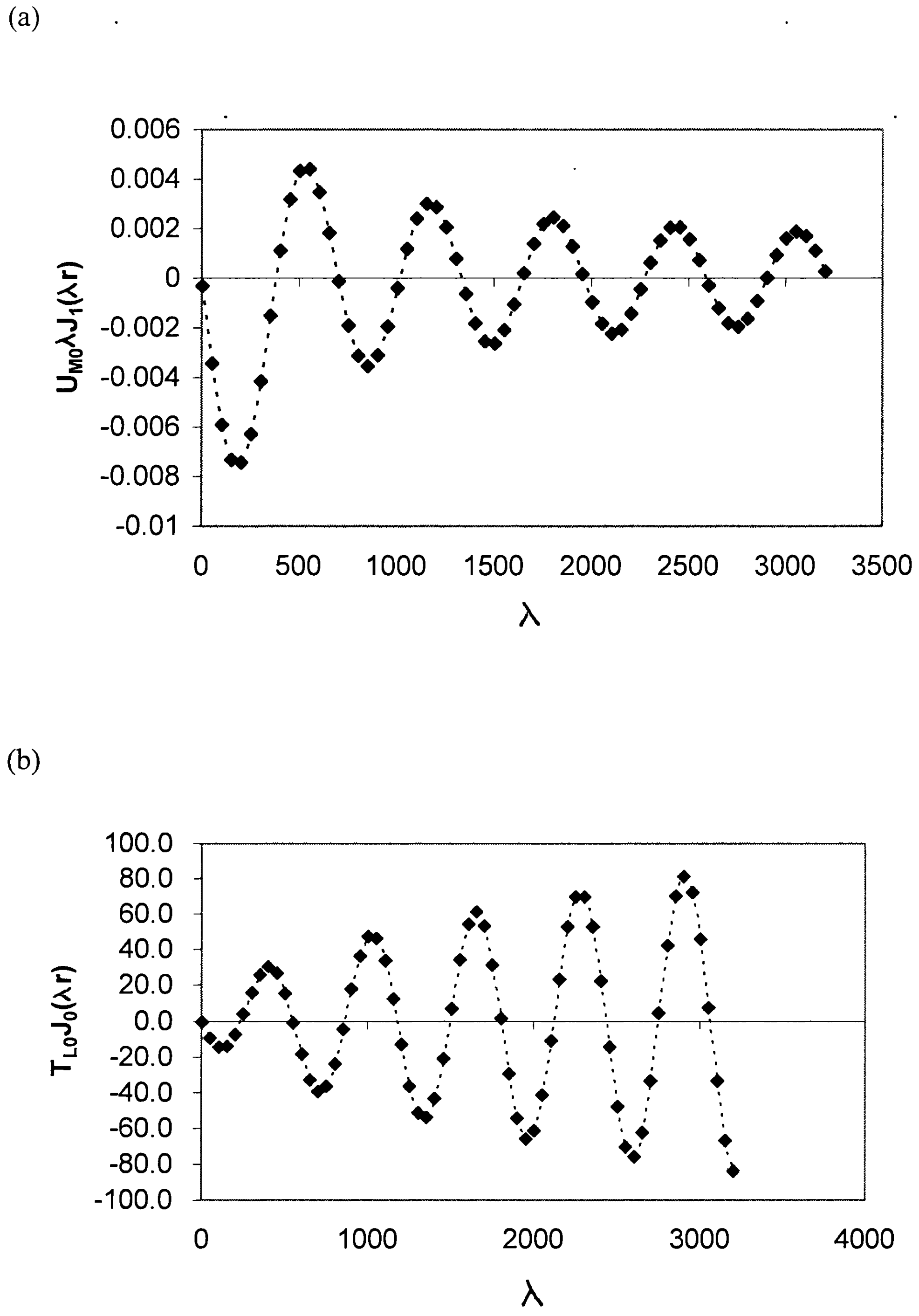

Fig. 7.2. (a) Kernel function $U_{M0}\lambda J_1(\lambda r)$ *and (b) kernel function* $T_{L0}J_0(\lambda r)$

Fig. 7.2 shows clearly that these kernel functions are oscillatory, and either (a) converge slowly or (b) diverge slowly.

In method II, we subtract the singular components of bi-material full-space kernel (U_{M0}^{ful} for kernel 1 and T_{L0}^{ful} for kernel 4, from eqns 7.12 and 7.13 respectively), from U_{M0} and T_{L0} respectively (which are derived by the propagator matrix method). Plots of the resulting regularized kernel functions are shown in Fig. 7.3.

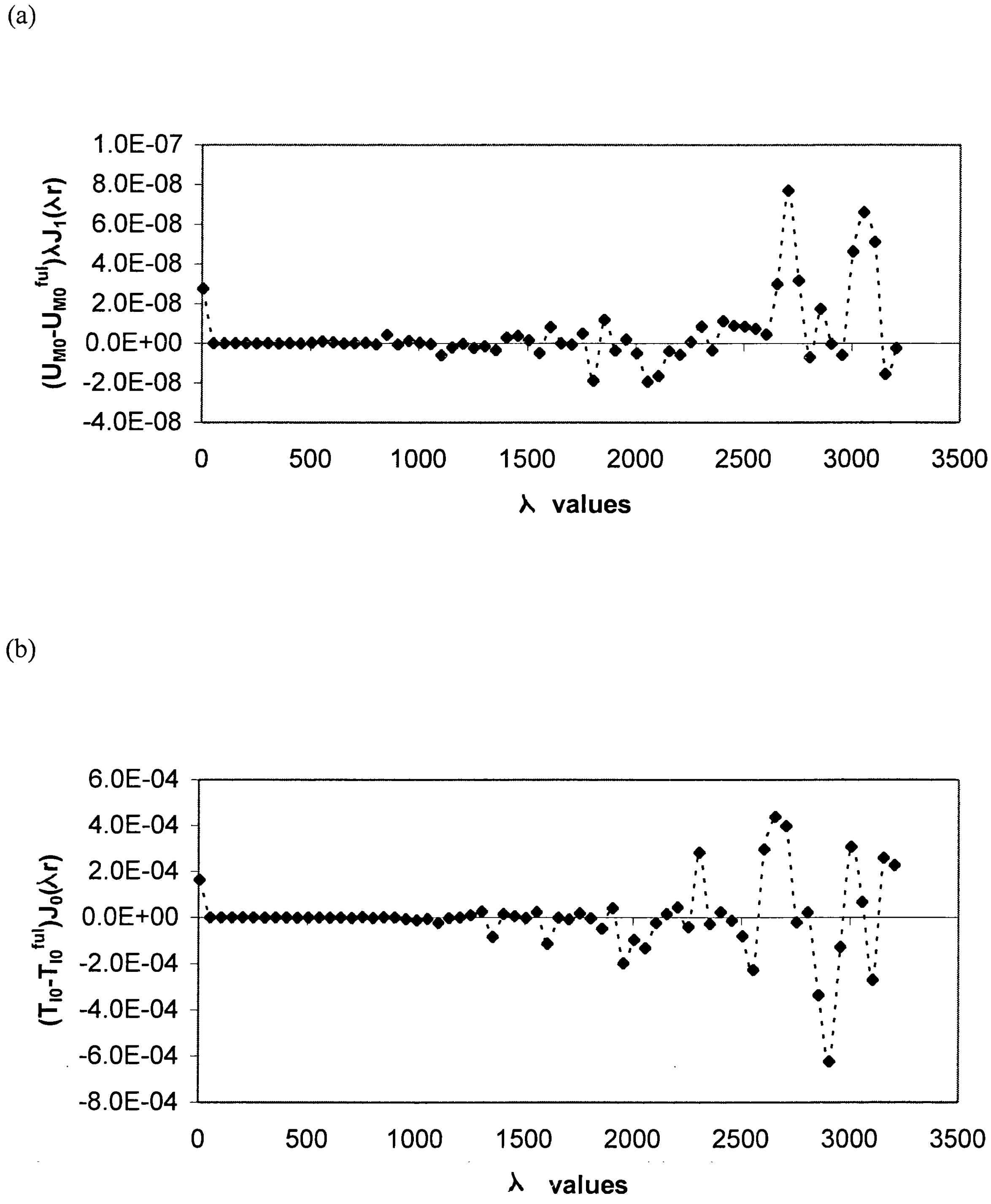

Fig. 7.3. Regularized kernel functions: (a) $\cdot(U_{M0}-U_{M0}^{ful})\cdot\lambda J_1(\lambda r)$ *, and, (b)* $(T_{L0}-T_{L0}^{ful})\cdot J_0(\lambda r)$.

Fig. 7.3 was obtained using a rather coarse interval along λ. It is clear that the integral of these regularized kernels are readily computable (i.e., the singularities cancel). However, a difficulty arises when λ approaches infinity, and unstable oscillatory values appear. These arise because of subtraction of very large, nearly equal, numbers. It can be argued that these values are spurious and that the upper limit of integration may be taken to be a value curtailed by the observation that the integral is constant (or nearly so) over a wide range of values. Formally,

$$I = \int_0^\infty F(\lambda)d\lambda \approx \int_0^{\lambda_1} F(\lambda)d\lambda$$

Where λ_1 is established by some appropriate convergence criterion. Some care is necessary to ensure that the criterion is robust.

The results from both method I and II are compared: the Cartesian components of displacements U_i^* are given in Table 7.3, and the stresses S_{ij}^* in Table 7.4, where i, $j = 1, 2, 3$. The superscript indicates the direction of the point force.

Table 7.3. Displacements

		Due to load in direction 1			Due to load in direction 2			Due to load in direction 3	
		Method I (full space)	Method II (bi-material)		Method I (full space)	Method II (bi-material)		Method I (full space)	Method II (bi-material)
Field point at (0.01,0.0,1.5)	U_1^1	1.32734 5668	1.32734 5821	U_1^2	0.0	10^{-16}	U_1^3	-0.20669 51958	-0.20669 52266
	U_2^1	0.0	0.0	U_2^2	0.93118 09255	0.93118 09160	U_2^3	0.0	0.0
	U_3^1	0.20669 53526	0.20669 52266	U_3^2	0.0	10^{-16}	U_3^3	0.93252 02605	0.93252 00001
Field point at (0.05,0.0,1.5)	U_1^1	0.26631 27083	0.26631 27078	U_1^2	0.0	10^{-16}	U_1^3	-0.04134 14285	-0.04134 14280
	U_2^1	0.0	0.0	U_2^2	0.18707 96425	0.18707 96420	U_2^3	0.0	0.0
	U_3^1	0.04134 14274	0.04134 14280	U_3^2	0.0	10^{-17}	U_3^3	0.18841 78094	0.18841 78094

Table 7.4. Stresses

		Due to load in direction 1		Due to load in direction 2		Due to load in direction 3	
		Method I (full-space)	Method II (bi-material)	Method I (full-space)	Method II (bi-material)	Method I (full-space)	Method II (bi-material)
Field point at (0.01,0.0,1.5)	S_{11}	-603.271	-602.859	0.0	10^{-13}	82.646	82.669
	S_{22}	86.304	86.122	0.0	10^{-14}	- 82.722	- 82.686
	S_{33}	155.289	155.021	0.0	10^{-14}	- 0.142	- 0.024
	S_{23}	0.0	0.0	34.4395 1190	34.4446 9827	0.0	0.0
	S_{13}	-34.865	-34.453	0.0	10^{-14}	-154.897	-155.021
	S_{12}	0.0	0.0	-106.7926 160	-106.7922 812	0.0	0.0
Field point at (0.05,0.0,1.5)	S_{11}	-24.1143 90	-24.1143 86	0.0	10^{-14}	3.2988 06	3.2988 12
	S_{22}	3.4449 41	3.4449 44	0.0	10^{-15}	-3.3154 29	-3.3154 17
	S_{33}	6.2009 27	6.2009 37	0.0	10^{-15}	-0.0239 43	-0.0239 13
	S_{23}	0.0	0.0	1.3736 70131	1.3735 45074	0.0	0.0
	S_{13}	- 1.3823 80	- 1.3823 83	0.0	10^{-16}	-6.2011 64	-6.2011 54
	S_{12}	0.0	0.0	-4.2717 07816	-4.2717 07800	0.0	0.0

We can see that accuracy is much better in the lower half of the table (less singular case); nearly 6 digits in relation to the magnitude of the largest quantity. Some of the kernel functions do not converge using Method 1 and the computational costs are consequently very high. Even for the "less singular" point, some kernel integrals still fail to converge, although accurate results are produced. This is not a satisfactory state of affairs. We conclude that use of the Green's functions for the bi-material full-space yields significant improvements in accuracy and solution reliability. Since the singular values of multi-layered Green's functions can now be evaluated accurately, we now compute the displacements and stresses over a range of distances from the source point. Fig. 7.4 shows results over the range from (0.01, 0.0, 1.5) to (1.0, 0.0, 1.5). We can see as the singular point is approached, the values of these functions increase rapidly and their amplitudes depend on the layer stiffnesses.

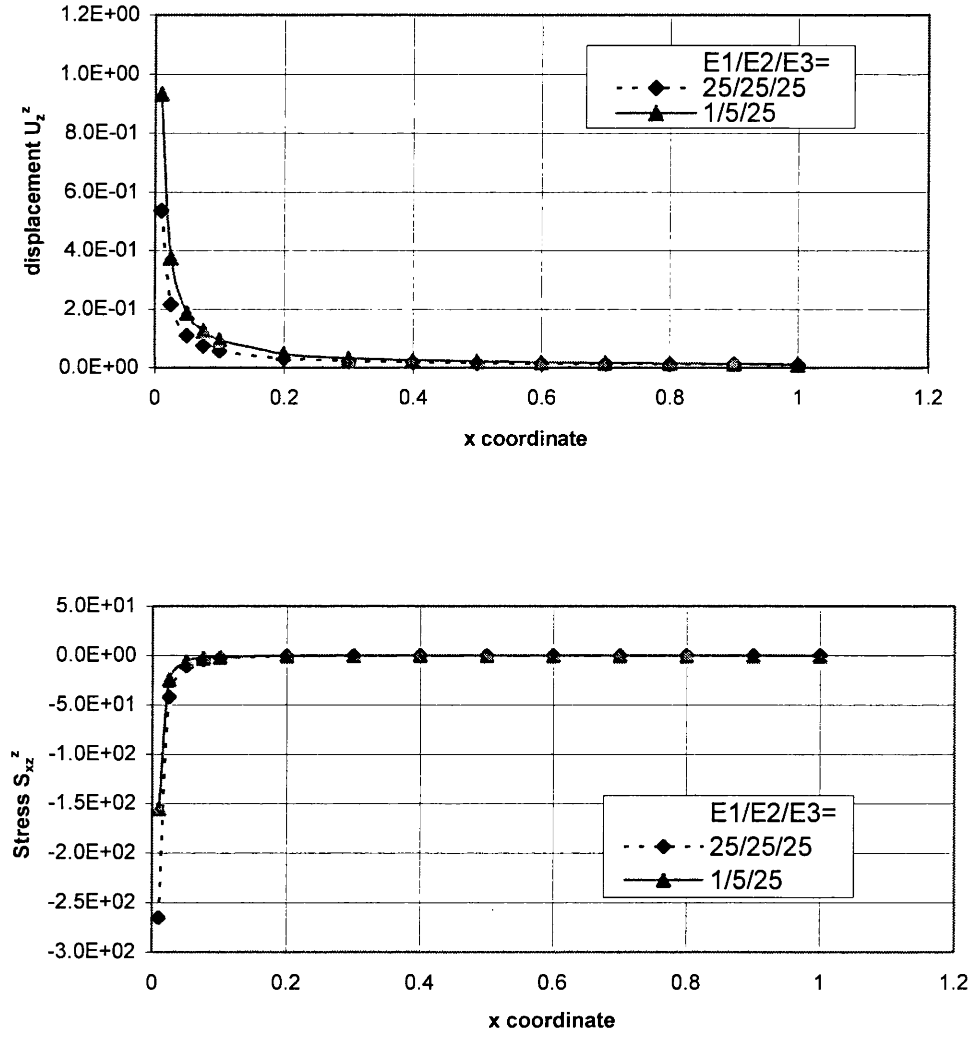

Fig. 7.4. Variation of (a)vertical displacement u_z^z *and (b)shear stress* σ_{xz}^z*, along the x-axis on the interface (0.01~1.0, 0.0, 1.5). (The point force is located at (0.0, 0.0, 1.5) in the three-layered half-space of Fig. 6.2).*

Chapter 8

Multi-region analysis – by two methods

In this chapter, we compare results obtained by using the Green's functions for a multi-layered half space with those obtained by using a multi-region BEM analysis (with Kelvin's solution). A three-layer model is adopted for the purpose to verify both the multilayer Green's functions and the multi-region boundary element method.

In this Chapter, we consider the three-layered model, shown in Fig. 8.1. At the upper free surface, there acts a uniform vertical distributed source p = 1, over a unit area. The resultant force will be assumed to be approximately equivalent to a concentrated unit force at some reasonable distance (say 3 units) from the centre of the loaded area (according to St Venant's principle). To model a three-layered half space, infinite elements should be adopted on the free surface and interfaces. But here we are satisfied to adopt a sufficiently large domain for this purpose. The lateral dimensions of this domain are taken to be 20, the thickness of each layer is 3, so the total thickness of the domain is H = 9. Thus, the infinite (free) surface is truncated at a distance of about 10 times the source dimension.

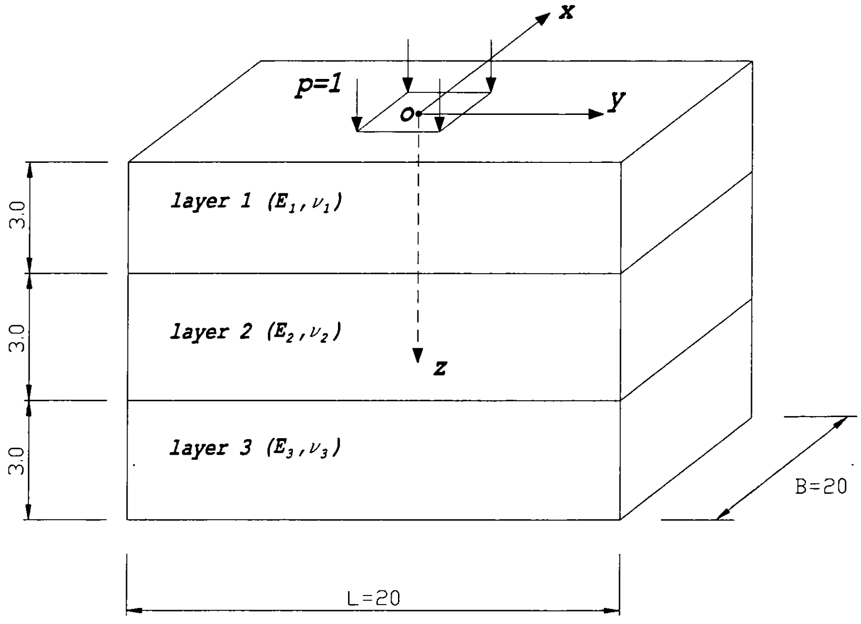

Fig. 8.1. Three-layered model for multi-region BEM analysis.

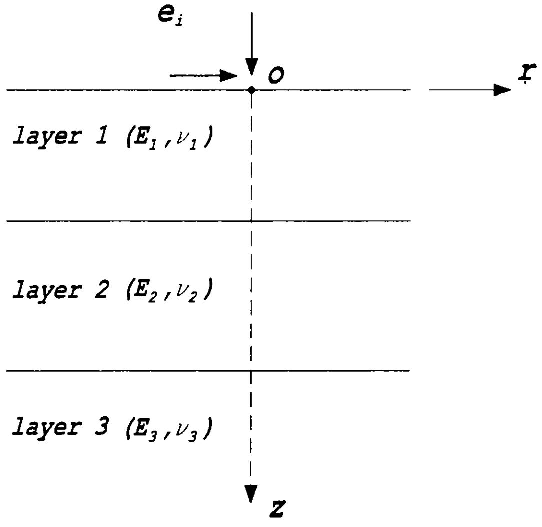

Fig. 8.2. The three-layered half space

Table 8.1. Elastic properties in a three layered half space.

	Case 1		Case 2		Case 3	
	E	ν	E	ν	E	ν
layer 1	1.0	0.25	1.0	0.25	1.0	0.25
layer 2	1.0	0.25	2.0	0.25	5.0	0.25
layer 3	1.0	0.25	4.0	0.25	25.0	0.25

Again all results are presented in non-dimensional form. The elastic properties are shown in Table 8.1. The base boundary is assumed to be fixed; the lateral boundaries are assumed to be smooth but laterally unyielding. This problem is then analysed by multi-region BEM (described in Chapter 4) and the results are compared with those obtained by Green's functions for the layered half space.

For multi-region BEM analysis, 213 quadratic elements are used. The total number of nodes is 476. Fig. 8.3 shows the surface mesh.

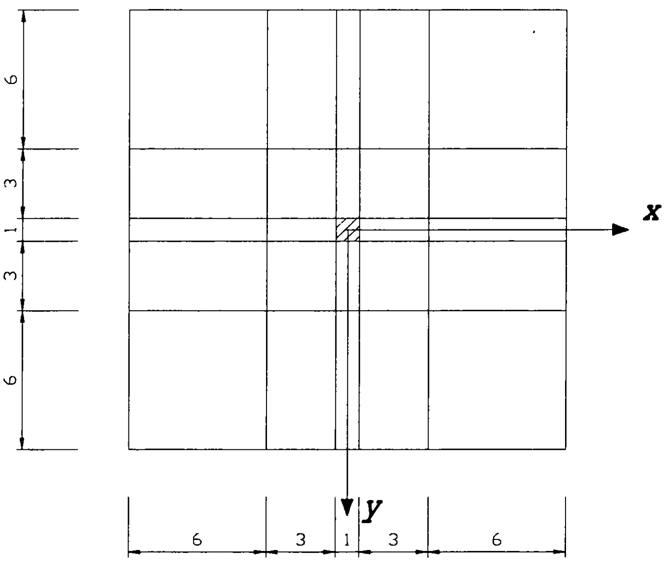

Fig. 8.3. The discretized mesh for the surface.

Firstly, we compare the results from the two methods along the z-axis (i.e., directly under the centre of the source). Fig 8.4a shows the distribution of vertical displacements, while Fig 8.4b shows the stresses σ_{zz}, and Fig 8.4c shows the stresses σ_{xx}.

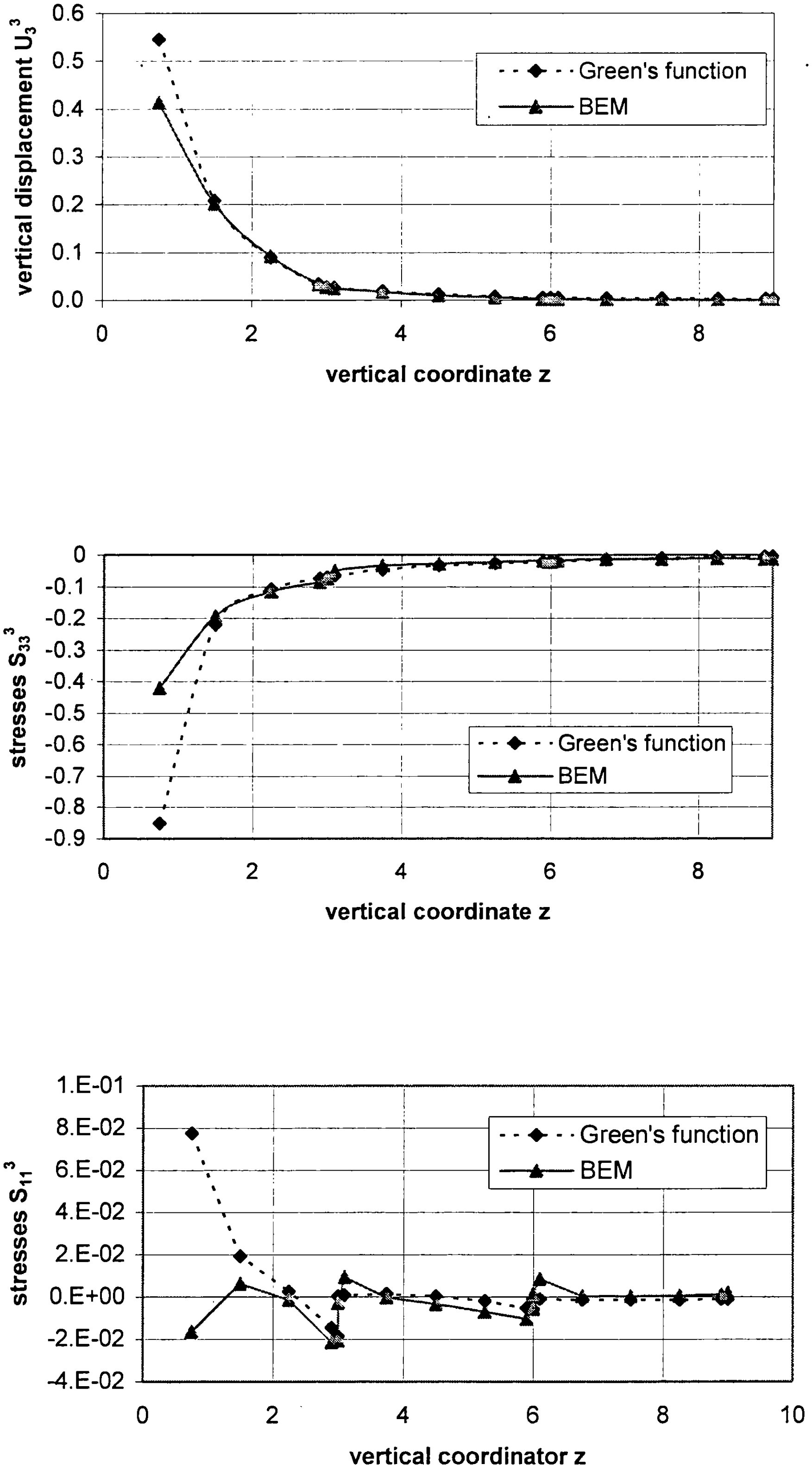

Fig. 8.4. Displacements and stresses in a three-layered half-space: (a) vertical displacement U_3^3*, (b) direct stress* S_{33}^3*, and (c) direct stress* S_{11}^3

We see from Fig. 8.4 that the results from multi-region BEM analysis and Green's function agree very well, except at points near to the surface. The discrepancies near to the surface may be attributed to the difference between a point load and a distributed load, and also the coarse discretisation. This also serves as a verification of the Green's functions formulations developed in Chapter 5 and 6, and the discontinuous elements.

To address the second of these issues, we adopt a finer discretization mesh in the BEM analysis, using 426 elements, as shown in Fig. 8.5.

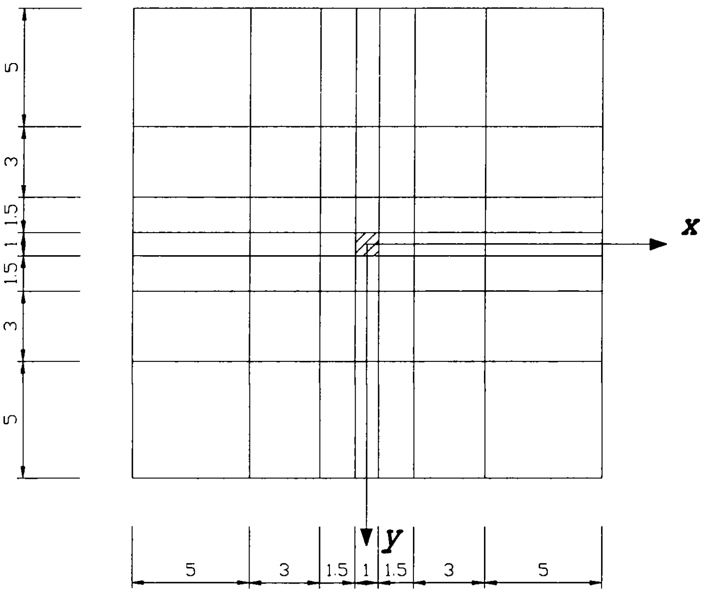

Fig. 8.5. The finer mesh on the surface.

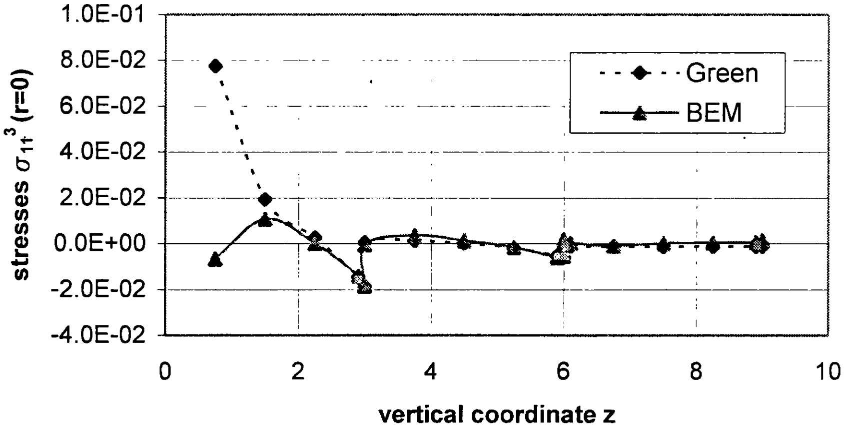

Fig. 8.6. Variation of stress component S_{11}^{3} *along the z-axis*

Fig 8.6 shows that the agreement between the results from BEM and Green's functions analysis is improved by adopting this finer discretisation. However, as the area of load distribution is still unit, the difference between the two approaches near the top surface appears to still exist.

A multi-region BEM can in principle resolve the discontinuous stresses across the interface between two material layers, e.g., at $z = 3$ and $z = 6$ in Figure 8.4 (c) and 8.6. However, it is difficult to determine stresses accurately very near to a boundary using the BEM, because the integrals are nearly singular. We have therefore omitted calculation of stresses at these points, except at the interface itself (and for those stress components which are equal to the tractions). It is of course possible to devise more sophisticated integration routines for this purpose, but this is beyond the scope of this thesis.

Fig. 8.7 shows results for a horizontal load (x-direction) at surface. Fig 8.7a shows the horizontal displacements U_{1}^{1} along the z-axis directly beneath the source, while 8.7b shows the shear stress S_{13}^{1} along this axis. We see again good agreement as in the vertical load case.

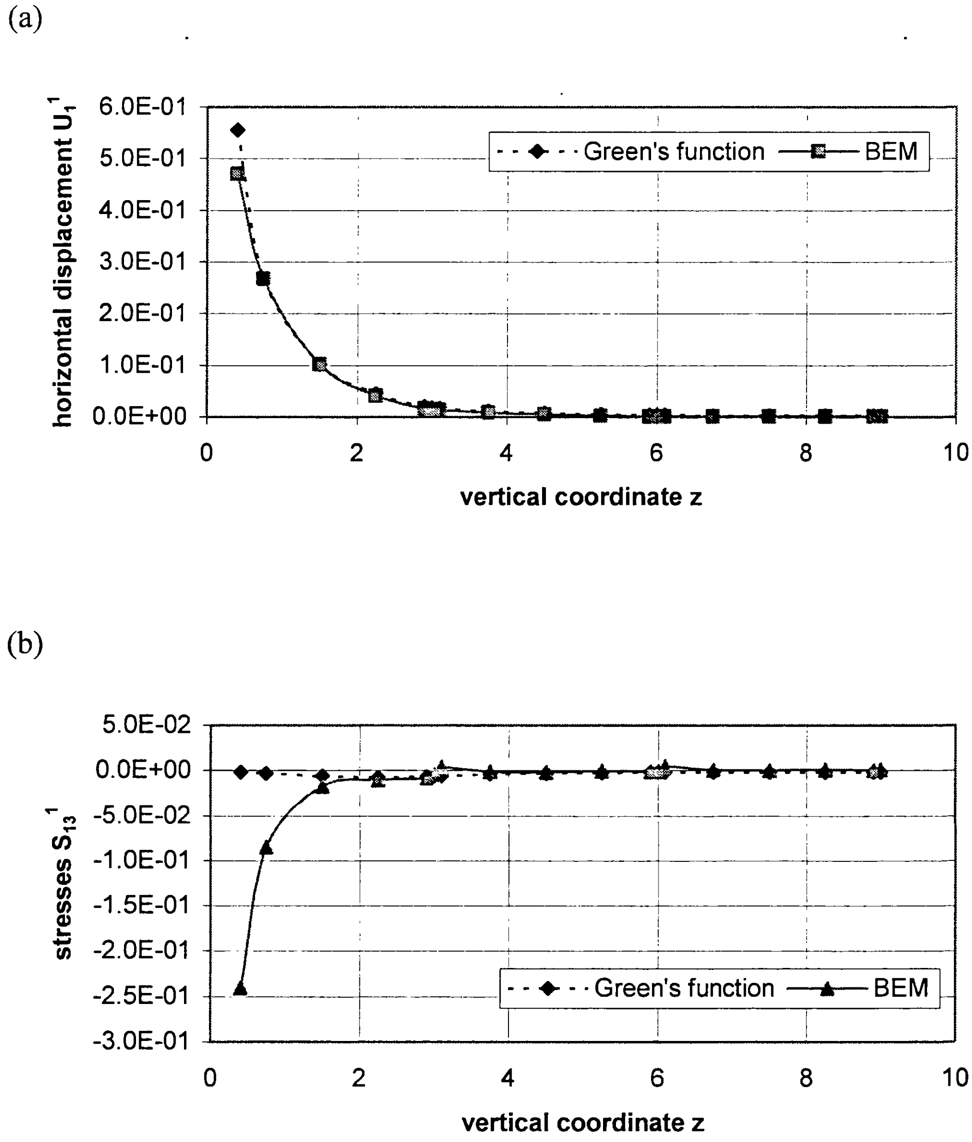

Fig. 8.7 Displacement and shear stresses beneath lateral point load

Next, we compare results on the z-axis through (0.5, 0.5, 0), i.e., beneath one corner of the distributed load area. Our purpose is to ensure that the results are correct not only for the special case examined so far, but also for a more general case. Fig 8.8 shows displacements along that axis.

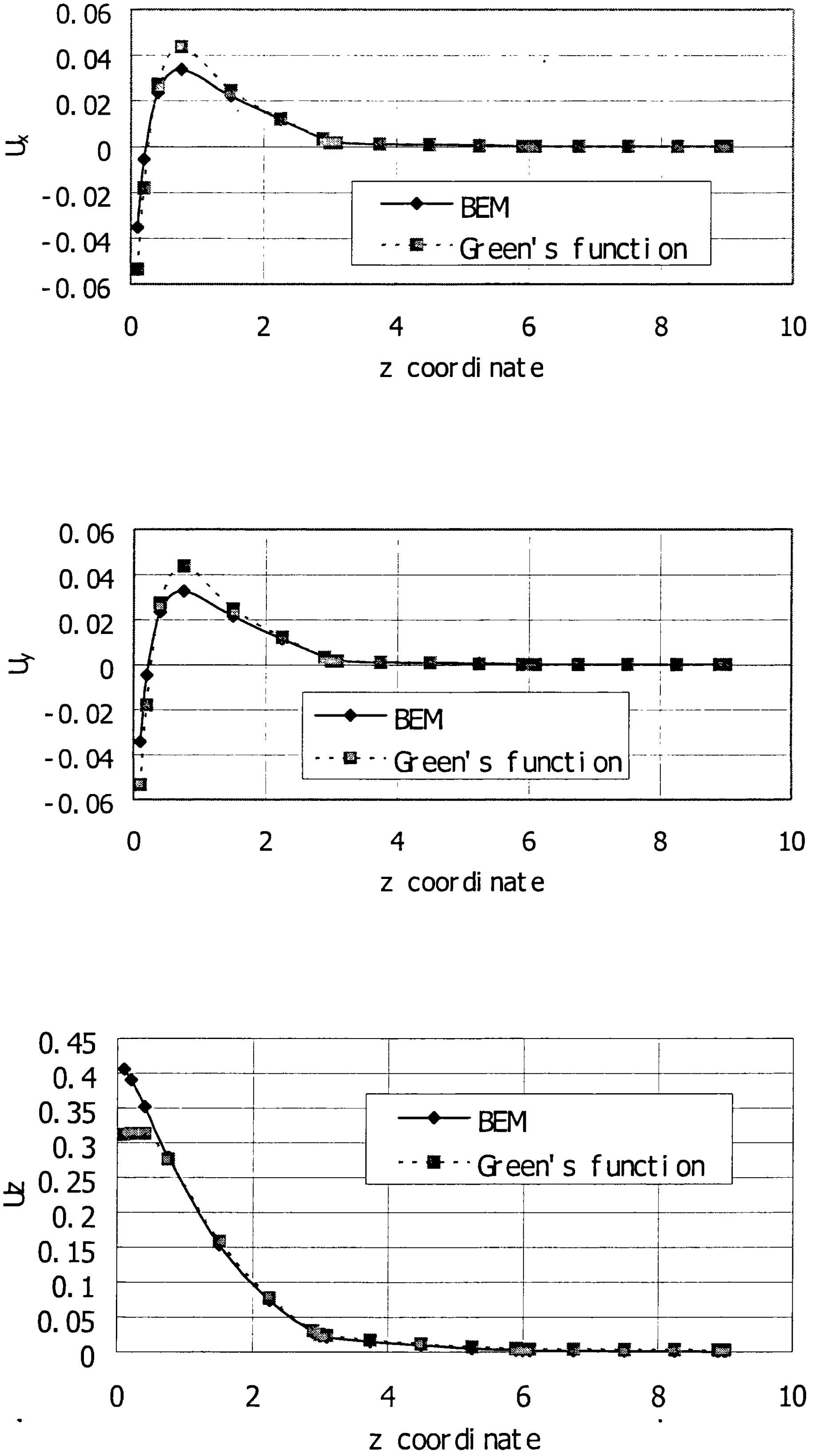

Fig. 8.8. Displacement component along z-axis

The results from both approaches are in very good agreement. Moreover, on this axis, there is no singularity and consequently the coincidence of the data is approached at lesser depths. The corresponding stresses are shown in Fig. 8.9.

(a)

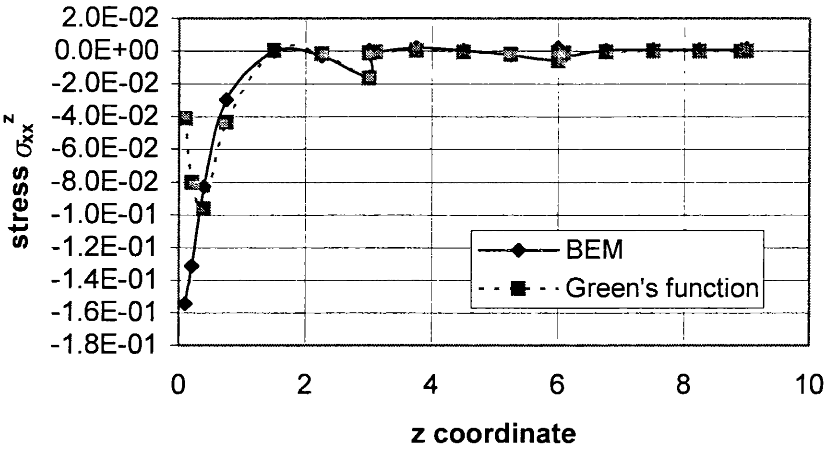

(b)

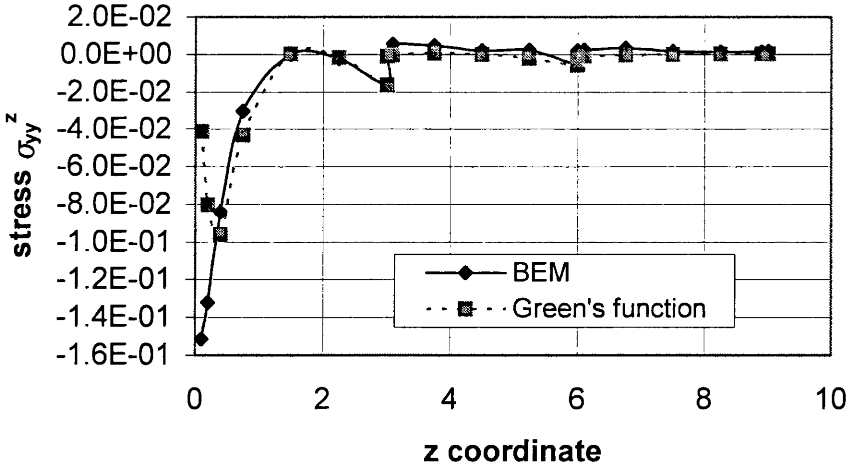

(c)

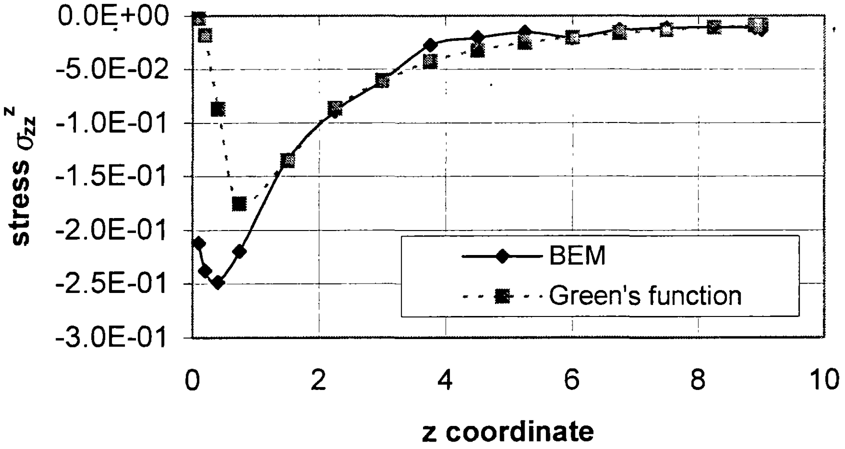
0.0E+00
-5.0E-02
-1.0E-01
-1.5E-01
-2.0E-01
-2.5E-01
-3.0E-01
stress σ_{zz}^{z}
0
2
4
6
8
10
z coordinate
BEM
Green's function

(d)

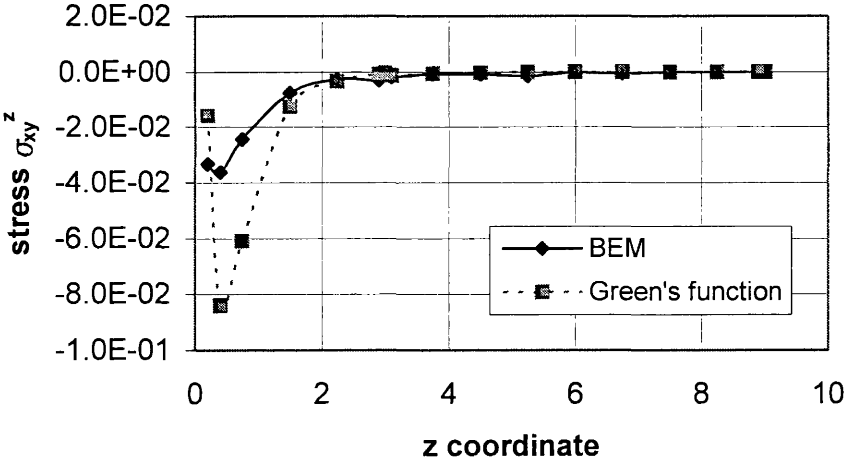
2.0E-02
0.0E+00
-2.0E-02
-4.0E-02
-6.0E-02
-8.0E-02
-1.0E-01
stress σ_{xy}^{z}
0
2
4
6
8
10
z coordinate
BEM
Green's function

(e)

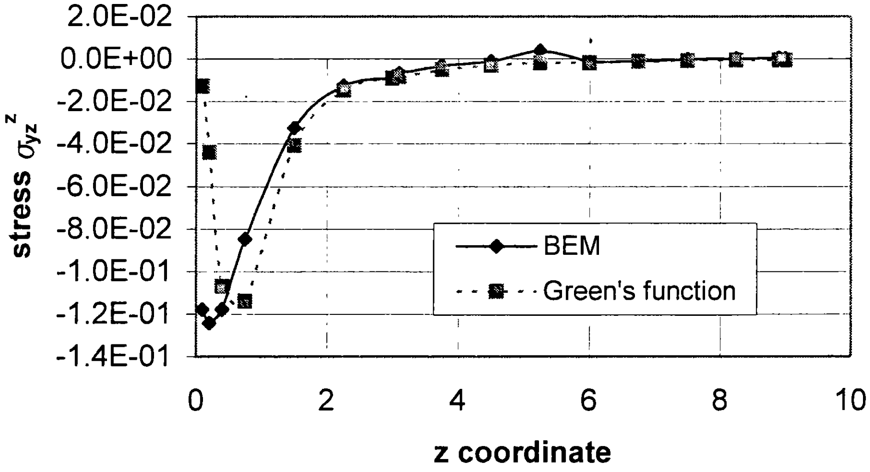

(f)

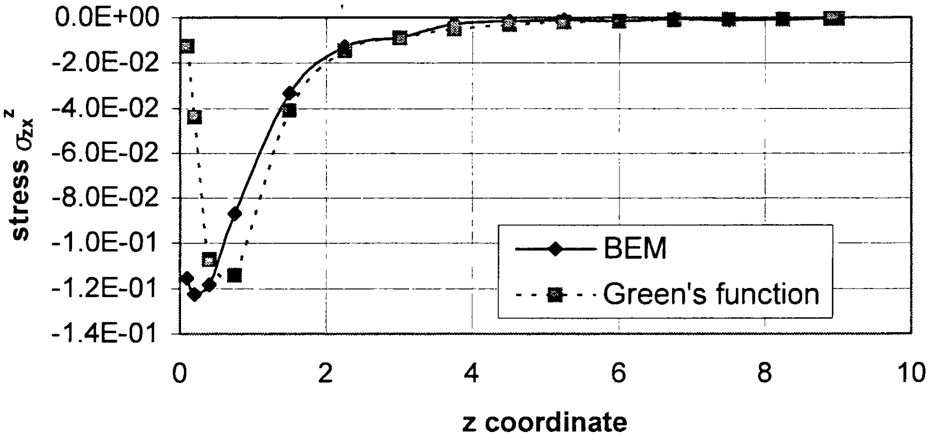

Fig. 8.9. Variation of stresses along z-axis.

These results again confirm the observation made earlier and lend confidence to the validity of both the multilayer Green's functions and the multi-region boundary element method.

Chapter 9

Conclusions and recommendations for further work

9.1 Summary and conclusions

This thesis aimed at solving some fundamental problems which exist in the implementation of boundary element techniques in solid mechanics. In particular, a unified approach to treat corners/edges problems is proposed and employed for 2D, 3D single-region and multi-region BEM analysis. Also, we report development of Green's functions for multi-layered system which can be applied to the BE analysis of the multi-layered structures or laminates, thus preserving boundary-only character. The main conclusions of the thesis are:

- Partially discontinuous element method provides a simple and accurate approach, compared with other techniques proposed so far to deal with the edges/corners problem: a long-standing difficulty in the BEM analysis. In this thesis, the potential of partially discontinuous elements is explored: These elements not only circumvent the traction-discontinuity difficulty associated with the continuous element method, but also to a large extent overcome the disadvantages of the non-conforming element method, such as inaccuracy and high computational cost (Manolis & Banerjee, 1986). In other words, they exploit the advantages of both approaches while avoiding most of their problems.

- An important aspect of work of implementing the partially discontinuous element method in BEM analysis, is that the discontinuous elements must be opaque: once the geometry is defined (using continuous elements), any partially discontinuous elements are generated automatically by edge detection software, and (once the equations are solved) the multi-valued tractions at the corners/edges are computed automatically. This edge detection software is quite easy to develop in 2D problems, where only corners (but no edges) exist. But its application in 3D problems is more complicated. A general 4-parameter interpolation function for partially discontinuous elements is developed in Chapter 3, which can be applied in 3D too. To simplify the edge detection process, a 8-parameter interpolation function for PDEs is introduced, although it is a more complex element. This shape function is especially useful for multi-region BEM analysis.

- When partially discontinuous elements are used, the offset between the free nodes and the element edges is a key parameter which controls numerical stability and accuracy. This introduces certain difficulties in singular integrals, but they can be easily overcome by standard numerical quadrature techniques. Analysis and numerical trials show that stable and accurate results can be obtained over a reasonably wide range of the offset parameter. Although the PDE method is generally accurate, crowding of collocation points at corners may result in unstable results, as the system equation may become ill conditioned. Numerical experience suggests an optimum offset distance of 0.2~0.3 from the perimeter of the elements.

- The partially discontinuous element method has also been explored in the case of multi-region BEM analysis, where corners and edges exist not only in the normal sense but also at regional interfaces. New edge detection software based on the eight-parameter partially discontinuous elements has been developed. This software has been proven to be crucial for the implementation of PDEs into the multi-region BEM analysis, and thus making this technique of practical value. For example, comparing this method to the auxiliary equation method, it greatly simplifies the system equations assembly process, and the difficulties associated with over-prescribed system of auxiliary equations are overcome.

- Green's functions for multi-layered system preserve the "boundary-only" nature of BEM. To obtain three-dimensional Green's functions for multi-layered half-spaces, one approach is the propagator matrix method, in terms of the cylindrical system of vector functions. As described in Chapters 5 and 6, the analytical Green's functions in the transformed domain have to be inversely transformed numerically to yield the Green's functions in the physical domain. During this process, infinite integrals must be evaluated. In order to get high accurate results, an adaptive Gauss quadrature is used, which is also combined with a continued fraction expansion approach to accelerate convergence.

- For singular points, a method for evaluating the singularity must be developed. The singularity extraction method is useful for this purpose. However, as normally applied, its performance is not satisfactory at interfaces between layers. This is because the Green's function does not share the same singular behaviour. The Green's functions for the bi-material full space are better choice in these cases. In order to apply these functions, both integral and close-form representations of them are necessary. The latter was obtained by Guzina (1999), while the former one (expressed in terms of cylindrical system of vector functions) has been obtained by the author in Chapter 7. By inversely transforming the integral representations, we can derive the same closed-form formulations as those by Guzina. However, the current approach is simpler as no displacement potentials are involved.

9.2 Recommendations for further work

The work described in this thesis offers significant improvement over current boundary element techniques. It also provides basis for further research:

- The adaptive Gauss quadrature used for computing the Green's functions for multi-layered half space yields results with high numerical precision, but computational costs are relatively high. Further effort can be expected to reduce this cost. Some other fast algorithms other than Gauss quadrature, such as fast Bessel transform method, might be developed.

- This work could be extended to transversely isotropic multi-layered systems, if the corresponding integral representations of the Green's functions for the bi-material full space can be developed. The closed-form representation has been derived by Pan and Chou (1979). The derivation of the integral representation would follow the method described in this thesis, although it would require considerable algebra.

- It may be worthwhile to develop a twelve-parameter partially discontinuous element, and corresponding edge detection software, to reduce the extra free nodes generated. In order to do this the software should be able to distinguish between different types of geometric feature in 3D and multi-region problems.

- The edge/corner problem in BEM only occurs when at least two tractions components of two elements intersecting at a corner are unknown. In the edge detection software we should develop a mechanism which can detect different boundary conditions on the contiguous surfaces around a corner or edge, and thus determine whether partially discontinuous elements must be generated to avoid the edge/corner problem. This would reduce the number of free nodes and improve the conditioning of system equations.

- In this thesis, the partially discontinuous element method has been successfully applied to single- and multi-region (2D and 3D) elastostatic BEM analysis. Further work can be done to apply it in the elastoplastic problems. A multi-region BEM analysis may be used here either to cope with the inhomogeneous material.

References

1. Anderson, W. L. (1979) Numerical integration of related Hankel transforms of orders 0 and 1 by adaptive digital filtering. *Geophysics.* 44, 1287-1305.

2. Anderson, W. L. (1982) Fast Hankel transforms using related and lagged convolutions: *ACM Trans. on Math. Software.* 8, 344-368.

3. Banerjee, P. K., Driscoll, R.M.C. (1976) Three-dimensional analysis of raked pile-groups, *Proc. Institution of Civil Engineers*, Part 2, 61, 653-671.

4. Banerjee, P. K., Henry, D. P. & Raveendra, S. T. (1989) Advanced inelastic analysis of solids by the boundary element method. *Int. J. Mech. Sci.*, 31, 309-322.

5. Banerjee, P. K. (1994) "The boundary element methods in engineering", McGraw-Hill book Co, London.

6. Becker, A.A. (1992) "The boundary element method in engineering", McGraw-Hill book Co, London.

7. Beer, G. & Watson, J.O. (1989) "Infinite boundary elements", *Int. J. Num. Meth. Engng.*, 28, 1233-1247.

8. Beer, G. (2001) "Programming the Boundary Element Method: An Introduction for Engineers", John Wiley & Sons, Ltd.

9. Beskos D. E. (1987) Boundary element methods in dynamic analysis, *Appl. Mech. Rev.*, 40, 1-23.

10. Blandford, G. E., Ingraffea, A. R. & Liggett, J. A. (1981) Two-dimensional stress intensity factor computations using the boundary element method, *Int. J. Numerical Methods in Engng.*, 17, 387-404.

11. Bouden M., Khair K. R., & Datta S. K. (1990) Ground motion amplification by cylindrical valleys embedded in a layered medium. *Earthquake Engng. Struc. Dyn.*, 19, 497-512.

12. Boresi, A. P. (1987) "Elasticity in Engineering Mechanics".

13. Brebbia, C. A., & Walker, S. (1980) "Boundary element techniques in Engineering". London: Newnes-Butterworths.

14. Brebbia, C. A., Telles, J.C.F. & Wrobel, L. C. (1984) "Boundary Element Techniques",

Springer-Verlag, Berlin and New York.

15. Brebbia, C.A. & Dominguez, J. (1992) "Boundary Elements: an Introductory Course", Computational Mechanics Publications, McGraw-Hill.

16. Chan, K. S., Karasudhi, P. & Lee, S. L. (1974) Force at a point in the interior of a layered elastic half space. *Int. J. Solids Struct.*, 10, 1179-1199.

17. Chaudonneret, M. (1978) "On the discontinuity of the stress vector in the boundary integral equation method for elastic analysis", in *Recent Advances in Boundary Element Methods*, ed C. A. Brebbia, Pentech Press, London.

18. Chave, A. D. (1983) Numerical integration of related Hankel transforms by quadrature and continued fraction expansion. *Geophys.*, 48, 1671-1686.

19. Franssenns G. R., (1983) Calculation of the elastodynamic Green's function in layered media by means of a modified propagator matrix method. *Geophys. J. R. Astr. Soc.*, 75, 669-91.

20. Gao X.W. & Davies T.G. (2002) "Boundary element programming in mechanics". Cambridge University Press, New York.

21. Gao X.W. & Davies T.G. (1998) "3-D infinite boundary elements for half-space problems", *Engineering Analysis with Boundary Elements*, 21, 207-213.

22. Gao, X.W. (1999) "3D non-linear and multi-region boundary element stress analysis", PhD thesis, University of Glasgow.

23. Ghosh, P. P. (1971) The application of linear filter theory to the direct interpretation of geoelectrical resistivity sounding measurements. *Geophys. Prosp.*, 19, 192-217.

24. Gibert, F. & Backus, G. (1966) Propagator matrices in elastic wave and vibration problems. *Geophys.*, 31, 326-332.

25. Gray, L. J. & Lutz, E. (1990) On the treatment of corners in the boundary element method. *J. Comp. Appl. Math.*, 32, 369-386.

26. Guzina B. & Pak R. (1999) Static fundamental solutions for a bi-material full-space. *Int. J. Solid. Struct.*, 36, 493-516.

27. Hanggi, P., Roesel, F. & Trautmann, P. (1980) Evaluation of infinite series by use of continued fraction expansions: A numerical study. *J. Comp. Phys.*, 37, 252-258.

28. Haskell, A. (1953) The dispersion of surface waves on a multilayered media, *Bull. Seism. Soc. Am.*, 43, 17-34.

29. Hu, Q. S. (1999) Distributed algorithm for multi-region problem in BEM. Journal of Computer Science and Technology, V14, n6, 558-564.

30. Jiandong Xu & Davies T.G. (2002) Multi-region BEM in solid mechanics. Proceedings of the Third International Conference on BeTeQ, Sept, Beijing, China, 335-340.

31. Jovanovich, D. B., Husseini, M. I. & Chinnery, M. A. (1974) Elastic dislocations in a layered half-space -I. Basic theory and numerical methods. *Geophys. J. R. Astro. Soc.*, 39, 205-217.

32. Kane, J. H. (1994) Boundary Element Analysis in Engineering Continuum Mechanics, Prentice-Hall, Englewood Cliffs, New Jersey.

33. Kane, J. H., Kumar, B. L. K. & Saigal, S. (1990) An Arbitrary condensing, noncondensing solution strategy for large scale, multi-zone boundary element analysis. Computational Methods in Applied Mechanics and Engng, 79, 219-244.

34. Kausel E, & Peek R. (1982) Dynamic loads in the interior of a layered stratum: an explicit solution. *Bull. Seismol. Soc. Am.*, 72, 1459-81.

35. Luco J. E. & Apsel R. J. (1983) On the Green's functions for a layered half-space. Part I. *Bull. Seismol. Soc. Am.*, 73, 909-29.

36. Malen K. (1971) A unified six-dimensional treatment of elastic Green's functions and dislocations. *Phys. Status solids* (*B*), 44, 661-72.

37. Manolis, G.D. & Banerjee, P. K. (1986) Conforming versus non-conforming boundary elements in three-dimensional elstostatics. *Int. J. Num. Meth. Engng.*, 23, 1885-1904.

38. Manolis, GD & Davies, TG. (1993) "Boundary Element Techniques in Geomechanics", Computational Mechanics Publications, Southampton.

39. Pak, R. Y. S. (1987) Asymmetric wave propagation in a half-space by a method of potential. *Journal of Applied Mechanics*, ASME 54, 121-126.

40. Pan, E. (1989) Static response of a transversely isotropic and layered half-space to general surface loads. *Phys. Earth Planet. Inter.*, 54, 353-363.

41. Pan, E. (1989) Static response of a transversely isotropic and layered half-space to general dislocation sources. *Phys. Earth Planet. Inter.*, 58, 103-117.

42. Pan, E. (1989) The static response of multilayered foundations to general surface loading and body force. *Acta Mechanica Sinica*, 21, 344-353.

43. Pan, E. (1997) Static Green's functions in multilayered half spaces. *Applied Mathematical Modelling*, 21, 509-521.

44. Pan E., Yang B et al (2001) Stress analysis around holes in composite laminates using boundary element method, *Engineering Analysis with Boundary Elements*, 25, 31-40.

45. Pan Y. C. & Chou, T. W. (1979) Green's function solutions for semi-infinite transversely isotropic materials. *Int. J. Eng. Sci.*, 17, 545-551.

46. Patterson, T. N. L. (1968) The optimum addition of points to quadrature formulae. *Math. Comp.*, 22, 847-856.

47. Patterson, T. N. L. (1973) Algorithm for automatic numerical integration over a finite interval [D1]. *Commun. ACM*, 16, 694-699.

48. Patterson, C. & Sheikh, M.A. (1984) "Interelement Continuity in the Boundary Element Method", In Topics in Boundary Element Research, Vol. 1, ed. C. A. Brebbia. Springer-Verlag, Berlin.

49. Press, W. H., Teukolsky, S. A., Vetterling, W. T. & Flannery, B. P. (1992) Numerical Recipes in FORTRAN: The Art of Scientific Computing, Second Edition, Cambridge University Press, New York.

50. Rudolphi, T. J. (1983) "An Implementation of the Boundary Element for Zoned Media with Stress Discontinuities". *Int. J. Num. Meth. Engng.*, Vol.19, pp.1-15.

51. Sato, R. (1971) Crustal deformation due to dislocation in a multi-layered medium. *J. Phys. Earth*, 19, 31-46.

52. Sato, R. & Matsu'ura, M. (1973) Static deformations due to the fault spreading over several layers in a multi-layered medium, Part I: Displacement. *J. Phys. Earth*, 21, 227-249.

53. Singh, S. J. (1970) Static deformation of a multilayered half space by internal sources. *J. Geophys. Res.*, 75, 3257-3263.

54. Singh, S. J., (1986) Static deformation of a transversely isotropic multilayered half-space by surface loads. *Phys. Earth Planet. Inter.*, 42, 263-273.

55. Sladek, V. & Sladek, J. (1998) Singular Integrals in Boundary Element Methods, WIT Press, Southampton.

56. Small, J. C. & Booker, J. R. (1984) Finite layer analysis of layered elastic materials using a flexibility approach. Part 1 – strip loadings. *Int. J. Numer. Methods Eng.*, 20, 1025-1037.

57. Small, J. C. & Booker, J. R. (1984) Finite layer analysis of layered elastic materials using a flexibility approach. Part 2 – circular and rectangular loadings. *Int. J. Numer. Methods Eng.*, 23, 959-978.

58. Stoer, J. & Bullrsch, R. (1980) Introduction to Numerical Analysis, New York: Springer-verlag.

59. Telles J. C. F. & Brebbia C. A. (1979) On the Application of the Boundary Element Method to Plasticity. *Appl. Math. Modelling*, 3, 466-470.

60. Thomson, W. T. (1950) Transmission of elastic waves through a stratified medium, *J. Appl. Phys.*, 21, 89-93.

61. Ting TCT & Lee VG. (1997) The three-dimensional elastostatic Green's function for general anisotropic linear elastic solids. *Quart. J. Mech. Appl. Math.* 50, 407-426.

62. Watson, J. O. (1979) Advanced implementation of the boundary element method for two- and three-dimensional elasto-statics', in P. K. Banerjee and R. Butterfield (eds.), Developments in Boundary Element Methods – 1, Applied Science, London, 31-63.

63. Wilde, A. J. (1998) "A hypersingular dual boundary element formulation for three-dimensional fracture analysis". PhD thesis, Wessex Institute of Technology, University of Wales, UK.

64. Yan, G. & Lin, F. B. (1994) Treatment of corner node problems and its singularity. Engineering Analysis with Boundary Elements, 13, 75-81.

65. Yang B. & Pan E. (2002) Efficient evaluation of three-dimensional Green's functions in anisotropic elastostatic multilayered composites, *Engineering Analysis with Boundary Elements*, 26, 355-366.

66. Yang B. & Pan E. (2002) Three-dimensional Green's functions in anisotropic trimaterials. *Int. J. Solids. Struct.*, 39, 2235-2255.

67. Yuan F. G., et al. (2003) Three-dimensional Green's functions for composite laminates. *Int. J. Solids. Struct.*, 40, 331-342.

68. Yu, H. Y. & Sanday, S. C. (1993) Elastic fields due to centers of dilation and thermal in homogeneities in plane-layered solids. *Journal of the Mechanics and Physics in Solids*, 41, 267-296.

69. Yue, Z. Q. & Wang, R. (1988) Static solution for transversely isotropic elastic n-layered system. *Acta Scientiarum Naturalium, Universitatis Pekinensis*, 24, 202-211.

70. Zhang, Q. & Mukherjee, S. (1991) Design sensitivity coefficients for linear elastic bodies with zones and corners by the derivative boundary element method. *Int. J. Solids Structures*, 27, 983-998.

Appendix A. Shape functions for the eight-parameter partially discontinuous element.

The quadratic shape functions N_i (i = 1 - 8) can be expressed in the form:

$$N_i = C_1 + C_2\xi + C_3\eta + C_4\xi\eta + C_5\xi^2 + C_6\eta^2 + C_7\xi^2\eta + C_8\xi\eta^2$$

For i = 1, the constants are:

$$C_1 = -d_{22333445678} / [(d_1 + d_3) Q]$$
$$C_2 = d_{223334457}(-d_6 + d_8) / [(d_1 + d_3) Q]$$
$$C_3 = d_{223334468} \quad (d_5 - d_7) / [(d_1 + d_3) Q]$$
$$C_4 = [d_{333}\{ -d_{445678} - d_{24}Q_1 + d_{22} (Q_1 + d_{4457} + d_{4468}) \}] / [(d_1 + d_3) Q]$$
$$C_5 = d_{223334457} / [(d_1 + d_3) Q]$$
$$C_6 = d_{223334468} / [(d_1 + d_3) Q]$$
$$C_7 = -[d_{3345678}(d_3 - d_4) + d_{233}(d_3 - d_4)Q_1 \quad + Q_2] / [2(d_1 + d_3)Q]$$
$$C_8 = [d_{3345678}(d_3 + d_4) + d_{233}(d_3 + d_4)Q_1 - Q_2 \quad] / \quad [2(d_1 + d_3) Q]$$

where $d_{ijk...n}$ signifies the product $d_i d_j d_k \ldots d_n$, and the constants Q, Q_1, Q_2, Q_3 are as follows:

$$Q = -d_{2233445678} + d_{122344} \quad Q_3 \quad + \quad d_{11} [-d_{33445678} - d_{2334} Q_1 \quad + \quad Q_2]$$
$$Q_1 = -d_{5678} - d_{4678} - d_{4578} + d_{4567} + d_{4568}$$
$$Q_2 = d_{22} \quad [\quad -d_{44} Q_3 \quad + \quad d_{33} (2d_{4457} + 2d_{4468} + Q_1)]$$
$$Q_3 = d_{5678} + d_{3678} + d_{5367} - d_{5368} - d_{5378}$$

For i = 2,3 & 4, the corresponding results may be readily obtained by symmetry.

For i = 5, the constants are:

$$C_1 = d_{1234678}\,Q_4 \;/\; [(d_5 + d_7)\,Q]$$

$$C_2 = d_{12347}(d_6 - d_8)\,Q_4 \;/\; [(d_5 + d_7)\,Q]$$

$$\begin{aligned}C_3 = [&d_{2233446778} - d_{1224477}(d_{36} - d_{38} + d_{68})(d_3 - d_1) + \\ &d_{11}\;\{d_{33446778} + d_{233}\,(d_{44677} - d_{44778} - d_{46778}) + \\ &\quad d_{2233}(d_{6778} - d_{4677} + d_{4778} - 2d_{4477} - 2d_{4468})\;\}]/ \\ &[(d_5 + d_7)\,Q]\end{aligned}$$

$$\begin{aligned}C_4 = -[&d_{2334678}\,(d_{24} - d_{27} + d_{47}) + \\ &d_{11}\,\{\,d_{344678}(-d_3 + d_7) - d_{24}\,(d_{77}Q_7 + d_{33}Q_6 + d_{33477}\,) + \\ &\quad d_{22}(d_{4678}(d_4 - d_7) + d_{33}Q_9 - d_3Q_5\;)\,\} + \\ &d_{13}\,\{\,-d_{3446778} + d_{2477}\,Q_7 + d_{22}(-d_{44678} + d_{46778} + d_3Q_5\;)\}]/ \\ &[(d_5 + d_7)Q]\end{aligned}$$

$$C_5 = -d_{12347}\,Q_4 \,/\, [(d_5 + d_7)\,Q]$$

$$\begin{aligned}C_6 = \;-[&d_{223344678} + d_{122344}\;(-d_{678} + d_{378} - d_{367} + d_{368}) + \\ &d_{11}\{\;d_{3344678} + d_{2334}Q_6 + \\ &\quad d_{22}\;(d_{44678} + d_{344}(d_{67} - d_{68} - d_{78}) + d_{33}\;(-2d_{447} - Q_6\,))\}]\,/ \\ [(d_5 + d_7)\,Q]&\end{aligned}$$

$$C_7 = -[d_{24678}(d_{337} + Q_{10}) + d_{11}\,Q_{11} + d_1\{\,Q_{12}(-d_3 + d_4) + d_{22}Q_{13}\,\}]\,/\,[2(d_5 + d_7)Q]$$

$$C_8 = -[d_{24678}(-d_{337} + Q_{10}) - d_{11}\,Q_{11} + d_1\,\{Q_{12}\,(d_3 + d_4) + d_{22}Q_{13}\,\}]\,/\,[2(d_5 + d_7)Q]$$

where the additonal constants are:

$$Q_4 = d_{2347} + d_{1347} + 2d_{1234} - d_{1237} - d_{1247}$$

$$Q_5 = 2d_{4677} - 2d_{4778} - d_{6778} - d_{4467} + d_{4468} + d_{4477} + d_{4478}$$

$$Q_6 = -d_{678} - d_{478} + d_{467} + d_{468}$$

$$Q_7 = -\,d_{468} - 2d_{346} + 2d_{348} + d_{368}$$

$$Q_8 = d_{6778} - 2d_{4677} + 2d_{4778} + 2d_{4467} - 2d_{4468} - 2d_{4477} - 2d_{4478}$$

$$Q_9 = -d_{678} - d_{478} + d_{467} + d_{468} + d_{477}$$

$$Q_{10} = -\,d_{347} - 2d_{234} + d_{237} + d_{247}$$

$$Q_{11} = d_{346778} - 2d_{334678} + d_{336778} + d_2(d_{46778} + 2d_{34677} - 2d_{34778} - d_{36778} - 2d_{33}\,Q_9)$$

$$Q_{12} = d_{346778} - d_{277}Q_7$$

$$Q_{13} = 2d_{44678} - d_{46778} + d_3Q_8$$

For $i = 6, 7$ & 8 , the corresponding results may be obtained by symmetry.

Appendix B. The derivation of equation (5.14)

For elastic materials involving transverse anisotropy (or isotropy), the propagator matrices derived in Cartesian or cylindrical systems of vector functions are identical. The expansion coefficients U_L, U_M, U_N, T_L, T_M and T_N in these two systems satisfy the same linear differential equations.

The unknown displacement vector is expressed in the Cartesian system of vector functions:

$$\boldsymbol{u}(x,y,z)=\int\int_{-\infty}^{+\infty}[\;U_L(z)\boldsymbol{L}(x,y)+U_M(z)\boldsymbol{M}(x,y)+U_N(z)\boldsymbol{N}(x,y)\;]d\alpha d\beta \qquad \text{(B.1)}$$

where

$$\begin{aligned}
&\boldsymbol{L}(x,y)=S(x,y;\lambda,m)\boldsymbol{i}_z\\
&\boldsymbol{M}(x,y)=\frac{\partial S}{\partial x}\boldsymbol{i}_x+\frac{\partial S}{\partial y}\boldsymbol{i}_y\\
&\boldsymbol{N}(x,y)=\frac{\partial S}{\partial y}\boldsymbol{i}_x-\frac{\partial S}{\partial x}\boldsymbol{i}_y\\
&S(x,y;\lambda,m)=\frac{1}{2\pi}\exp[-i(\alpha x+\beta y)]
\end{aligned} \qquad \text{(B.2)}$$

Substituting (B.2) into (B.1), we have

$$\begin{aligned}
\boldsymbol{u}(x,y,z)&=\int\int_{-\infty}^{+\infty}[\;U_L(z)\boldsymbol{L}(x,y)+U_M(z)\boldsymbol{M}(x,y)+U_N(z)\boldsymbol{N}(x,y)\;]d\alpha d\beta\\
&=\int\int_{-\infty}^{+\infty}[\;U_L(z)S\boldsymbol{i}_z+U_M(z)(\frac{\partial S}{\partial x}\boldsymbol{i}_x+\frac{\partial S}{\partial y}\boldsymbol{i}_y)+U_N(z)(\frac{\partial S}{\partial y}\boldsymbol{i}_x+\frac{\partial S}{\partial x}\boldsymbol{i}_y)\;]d\alpha d\beta\\
&=\int\int_{-\infty}^{+\infty}[\;(U_M\frac{\partial S}{\partial x}+U_N\frac{\partial S}{\partial y})\boldsymbol{i}_x+(U_M\frac{\partial S}{\partial y}-U_N\frac{\partial S}{\partial x})\boldsymbol{i}_y+U_LS\boldsymbol{i}_z\;]d\alpha d\beta
\end{aligned} \qquad \text{(B.3)}$$

From the above, we have

$$\begin{aligned}
\boldsymbol{u}_x&=\int\int_{-\infty}^{+\infty}(U_M\frac{\partial S}{\partial x}+U_N\frac{\partial S}{\partial y})d\alpha d\beta\\
\boldsymbol{u}_y&=\int\int_{-\infty}^{+\infty}(U_M\frac{\partial S}{\partial y}-U_N\frac{\partial S}{\partial x})d\alpha d\beta\\
\boldsymbol{u}_z&=\int\int_{-\infty}^{+\infty}(U_LS)d\alpha d\beta
\end{aligned} \qquad \text{(B.4)}$$

From the strain-displacement relations we have

$$
\begin{aligned}
e_{xx} &= \frac{\partial u_x}{\partial x} = U_M \frac{\partial^2 S}{\partial x^2} + U_N \frac{\partial^2 S}{\partial x \partial y} \\
e_{yy} &= \frac{\partial u_y}{\partial x} = U_M \frac{\partial^2 S}{\partial y^2} - U_N \frac{\partial^2 S}{\partial x \partial y} \\
e_{zz} &= \frac{\partial u_z}{\partial z} = \frac{dU_L}{dz} S \\
2e_{xy} &= \frac{\partial u_x}{\partial y} + \frac{\partial u_y}{\partial x} = 2U_M \frac{\partial^2 S}{\partial x \partial y} + U_N \frac{\partial^2 S}{\partial y^2} - U_N \frac{\partial^2 S}{\partial x^2} \\
2e_{yz} &= \frac{\partial u_y}{\partial z} + \frac{\partial u_z}{\partial y} = \frac{dU_M}{dz}\frac{\partial S}{\partial y} - \frac{dU_N}{dz}\frac{\partial S}{\partial x} + U_L \frac{\partial S}{\partial y} \\
2e_{xz} &= \frac{\partial u_x}{\partial z} + \frac{\partial u_z}{\partial x} = \frac{dU_M}{dz}\frac{\partial S}{\partial x} + \frac{dU_N}{dz}\frac{\partial S}{\partial y} + U_L \frac{\partial S}{\partial x}
\end{aligned}
\tag{B.5}
$$

From the stress-strain relationship, we obtain the stresses expressed in terms of the coefficients of displacement

$$
\begin{aligned}
\sigma_{xx} &= C_{11}e_{xx} + C_{12}e_{yy} + C_{13}e_{zz} = \Big[\, C_{11}\big(U_M \frac{\partial^2}{\partial x^2} + U_N \frac{\partial^2}{\partial x \partial y}\big) + \\
&\qquad C_{12}\big(U_M \frac{\partial^2}{\partial y^2} - U_N \frac{\partial^2}{\partial x \partial y}\big) + C_{13}\frac{dU_L}{dz} \,\Big] S(x,y) \\
\sigma_{yy} &= C_{12}e_{xx} + C_{11}e_{yy} + C_{13}e_{zz} = \Big[\, C_{12}\big(U_M \frac{\partial^2}{\partial x^2} + U_N \frac{\partial^2}{\partial x \partial y}\big) + \\
&\qquad C_{11}\big(U_M \frac{\partial^2}{\partial y^2} - U_N \frac{\partial^2}{\partial x \partial y}\big) + C_{13}\frac{dU_L}{dz} \,\Big] S(x,y) \\
\sigma_{zz} &= C_{13}e_{xx} + C_{13}e_{yy} + C_{33}e_{zz} = \Big[\, C_{13}U_M\big(\frac{\partial^2}{\partial x^2} + \frac{\partial^2}{\partial y^2}\big) + \\
&\qquad + C_{33}\frac{dU_L}{dz} \,\Big] S(x,y) \\
\sigma_{xz} &= 2C_{44}e_{xz} = C_{44}\Big[\, U_L \frac{\partial}{\partial x} + \frac{dU_M}{dz}\frac{\partial}{\partial x} + \frac{dU_N}{dz}\frac{\partial}{\partial y} \,\Big] S(x,y) \\
\sigma_{yz} &= 2C_{44}e_{yz} = C_{44}\Big[\, U_L \frac{\partial}{\partial y} + \frac{dU_M}{dz}\frac{\partial}{\partial y} - \frac{dU_N}{dz}\frac{\partial}{\partial x} \,\Big] S(x,y) \\
\sigma_{xy} &= 2C_{66}e_{xy} = C_{66}\Big[\, 2U_M \frac{\partial^2}{\partial x \partial y} + U_N\big(\frac{\partial^2}{\partial y^2} - \frac{\partial^2}{\partial x^2}\big) \,\Big] S(x,y)
\end{aligned}
\tag{B.6}
$$

Except for special cases, the notation $\int\int_{-\infty}^{+\infty}[\ \cdot\ ]d\alpha d\beta$ is omitted. The traction vectors are defined as

$$\begin{aligned}\boldsymbol{T}(x,y,z) &= \sigma_{xz}\boldsymbol{i}_x + \sigma_{yz}\boldsymbol{i}_y + \sigma_{zz}\boldsymbol{i}_z \\ &= \int\int_{-\infty}^{+\infty}[T_L(z)\boldsymbol{L}(x,y) + T_M(z)\boldsymbol{M}(x,y) + T_N(z)\boldsymbol{N}(x,y)]d\alpha d\beta \\ &= \int\int_{-\infty}^{+\infty}\left[(T_M\frac{\partial S}{\partial x} + T_N\frac{\partial S}{\partial y})\boldsymbol{i}_x + (T_M\frac{\partial S}{\partial y} - T_N\frac{\partial S}{\partial x})\boldsymbol{i}_y + T_L S\right]d\alpha d\beta\end{aligned} \tag{B.7}$$

Comparing eqn.(B.6) with the above, we have

$$\begin{aligned}(T_M\frac{\partial S}{\partial x} + T_N\frac{\partial S}{\partial y})S &= C_{44}(U_L\frac{\partial}{\partial x} + \frac{dU_M}{dz}\frac{\partial}{\partial x} + \frac{dU_N}{dz}\frac{\partial}{\partial y})S \\ (T_M\frac{\partial S}{\partial y} - T_N\frac{\partial S}{\partial x})S &= C_{44}(U_L\frac{\partial}{\partial y} + \frac{dU_M}{dz}\frac{\partial}{\partial y} - \frac{dU_N}{dz}\frac{\partial}{\partial x})S \\ T_L S &= \left[C_{13}U_M(\frac{\partial^2}{\partial x^2} + \frac{\partial^2}{\partial y^2}) + C_{33}\frac{dU_L}{dz}\right]S\end{aligned} \tag{B.8}$$

From (B.8) we can immediately obtain three relations between the expansion coefficients

$$\begin{aligned}T_L &= -\lambda^2 C_{13}U_M + C_{33}\frac{dU_L}{dz} \\ T_M &= C_{44}(U_L + \frac{dU_M}{dz}) \\ T_N &= C_{44}\frac{dU_N}{dz}\end{aligned} \tag{B.9}$$

After substituting eqn. (B.6) into the equations of equilibrium, which are:

$$\begin{aligned}\frac{\partial\sigma_{xx}}{\partial x} + \frac{\partial\sigma_{xy}}{\partial y} + \frac{\partial\sigma_{xz}}{\partial z} &= 0 \\ \frac{\partial\sigma_{xy}}{\partial x} + \frac{\partial\sigma_{yy}}{\partial y} + \frac{\partial\sigma_{yz}}{\partial z} &= 0 \\ \frac{\partial\sigma_{xz}}{\partial x} + \frac{\partial\sigma_{yz}}{\partial y} + \frac{\partial\sigma_{zz}}{\partial z} &= 0\end{aligned} \tag{B.10}$$

and after some algebraic manipulations, we obtain the following three equations:

$$-\lambda^2 C_{11} U_M \frac{\partial S}{\partial x} - \lambda^2 C_{66} U_N \frac{\partial S}{\partial y} + C_{13} \frac{dU_L}{dz} \frac{\partial S}{\partial x} + \frac{dT_M}{dz} \frac{\partial S}{\partial x} + \frac{dT_N}{dz} \frac{\partial S}{\partial y} = 0 \tag{B.11a}$$

$$-\lambda^2 C_{11} U_M \frac{\partial S}{\partial y} + \lambda^2 C_{66} U_N \frac{\partial S}{\partial x} + C_{13} \frac{dU_L}{dz} \frac{\partial S}{\partial y} + \frac{dT_M}{dz} \frac{\partial S}{\partial y} - \frac{dT_N}{dz} \frac{\partial S}{\partial x} = 0 \tag{B.11b}$$

$$\lambda^2 C_{44} U_L + \lambda^2 C_{44} \frac{dU_M}{dz} + \lambda^2 C_{13} \frac{dU_M}{dz} - C_{33} \frac{d^2 U_L}{dz^2} = 0 \tag{B.11c}$$

We now differentiate these equations with respect to x and with respect to y. Finally, summing these results and making use of equation (B.9), we obtain:

$$\begin{aligned} &\frac{\partial T_L}{\partial z} - \lambda^2 T_M = 0 \\ &\frac{\partial T_N}{\partial z} - \lambda^2 C_{66} U_N = 0 \\ &-\lambda^2 C_{11} U_M + C_{13} \frac{\partial U_L}{\partial z} + \frac{\partial T_M}{\partial z} = 0 \end{aligned} \tag{B.12}$$

Appendix C. The derivation of equation (5.31)

The unit force $\boldsymbol{f}(r, \theta, z)$ can be expanded in the $\boldsymbol{L}(r, \theta)$, $\boldsymbol{M}(r, \theta)$ and $\boldsymbol{N}(r, \theta)$ system, as follows:

$$\begin{aligned} \boldsymbol{f}(r,\theta,z) &= f_r \cdot \boldsymbol{i}_r + f_\theta \boldsymbol{i}_\theta + f_z \cdot \boldsymbol{i}_z = \\ & \sum_m \int_0^{+\infty} \left[F_L(z)\boldsymbol{L}(r,\theta) + F_M(z)\boldsymbol{M}(r,\theta) + F_N(z)\boldsymbol{N}(r,\theta) \right] \lambda d\lambda \end{aligned} \tag{C.1}$$

By definition we have

$$\begin{aligned} \boldsymbol{L}(r,\theta) &= S(r,\theta;\lambda,m)\boldsymbol{i}_z \\ \boldsymbol{L}^*(r,\theta) &= S^*(r,\theta;\lambda,m)\boldsymbol{i}_z \\ S(r,\theta;\lambda,m) &= \frac{1}{\sqrt{2\pi}} J_m(\lambda r) e^{im\theta} \\ S^*(r,\theta;\lambda,m) &= \frac{1}{\sqrt{2\pi}} J_m(\lambda r) e^{-im\theta} \end{aligned} \tag{C.2}$$

From the above equations and the orthogonality of the system ($\boldsymbol{L}$, $\boldsymbol{M}$, $\boldsymbol{N}$) we have

For F_L:

$$\begin{aligned} & \int_0^{2\pi} \int_0^{+\infty} \boldsymbol{f}(r,\theta,z) \cdot \boldsymbol{L}^*(r,\theta) r dr d\theta = \\ & \quad \int_0^{2\pi} \int_0^{+\infty} \left[\sum_m \int_0^{+\infty} F_L(z) \boldsymbol{L}(r,\theta) \boldsymbol{L}^*(r,\theta) \lambda d\lambda \right] r dr d\theta = \\ & \quad \frac{1}{2\pi} \int_0^{2\pi} \int_0^{+\infty} \left[\int_0^{+\infty} F_L(z) J_m(\lambda r) J_m(\lambda r) \lambda d\lambda \right] r dr d\theta = \\ & \quad \frac{1}{2\pi} \int_0^{2\pi} F_L(z) d\theta = F_L(z) \end{aligned} \tag{C.3}$$

For F_M:

$$
\begin{aligned}
&\int_0^{2\pi}\int_0^{+\infty} \boldsymbol{f}(r,\theta,z)\cdot \boldsymbol{M}^*(r,\theta)\,r\,dr\,d\theta = \\
&\quad \int_0^{2\pi}\int_0^{+\infty}\left[\int_0^{+\infty} F_M(z)(\boldsymbol{i}_r\frac{\partial S}{\partial r}+\boldsymbol{i}_\theta\frac{\partial S}{r\partial\theta})(\boldsymbol{i}_r\frac{\partial S^*}{\partial r}+\boldsymbol{i}_\theta\frac{\partial S^*}{r\partial\theta})\lambda d\lambda\right] r\,dr\,d\theta = \\
&\quad \int_0^{2\pi}\int_0^{+\infty}\left[\int_0^{+\infty} F_M(z)(\frac{\partial S}{\partial r}\frac{\partial S^*}{\partial r}+\frac{\partial S}{r^2\partial\theta}\frac{\partial S^*}{\partial\theta})\lambda d\lambda\right] r\,dr\,d\theta = \\
&\quad \frac{1}{2\pi}\int_0^{2\pi}\int_0^{+\infty}\left\{\int_0^{+\infty} F_M(z)\left[\frac{\partial J_m(\lambda r)}{\partial r}\frac{\partial J_m(\lambda r)}{\partial r}+\frac{m^2}{r^2}J_m(\lambda r)J_m(\lambda r)\right]\lambda d\lambda\right\} r\,dr\,d\theta
\end{aligned}
\qquad \text{(C.4)}
$$

From the properties of Bessel functions,

$$J'_m(x)=\frac{J_{m-1}(x)-J_{m+1}(x)}{2}$$

we have

$$\frac{\partial J_m(\lambda r)}{\partial r}=\lambda\frac{\partial J_m(\lambda r)}{\partial(\lambda r)}=\frac{\lambda J_{m-1}(\lambda r)-\lambda J_{m+1}(\lambda r)}{2}$$

Substituting the above into equation C.4 yields:

$$
\begin{aligned}
&\int_0^{2\pi}\int_0^{+\infty} \boldsymbol{f}(r,\theta,z)\cdot \boldsymbol{M}^*(r,\theta)\,r\,dr\,d\theta = \\
&\quad \frac{1}{2\pi}\int_0^{2\pi}\int_0^{+\infty}\left\{\int_0^{+\infty} F_M(z)\left[\lambda^2\frac{J_{m-1}^2(\lambda r)-2J_{m-1}(\lambda r)J_{m+1}(\lambda r)+J_{m+1}^2(\lambda r)}{4}\right.\right. \\
&\quad \left.\left. +\frac{m^2}{r^2}J_m(\lambda r)J_m(\lambda r)\right]\lambda d\lambda\right\} r\,dr\,d\theta \quad .
\end{aligned}
\qquad \text{(C.5)}
$$

Also, from the properties of Bessel functions:

$$J_{\nu-1}(x) + J_{\nu+1}(x) = \frac{2\nu}{x} J_{\nu}(x)$$

we have

$$J_{m-1}(\lambda r) + J_{m+1}(\lambda r) = \frac{2m}{\lambda r} J_{m}(\lambda r)$$

Squaring the above, we have:

$$\frac{m^2}{r^2} J_m^2(\lambda r) = \lambda^2 \frac{J_{m-1}^2(\lambda r) + 2J_{m-1}(\lambda r)J_{m+1}(\lambda r) + J_{m+1}^2(\lambda r)}{4}$$

Substituting the above into the eqn (C.5), we have

$$\begin{aligned}
&\int_0^{2\pi}\int_0^{+\infty} \boldsymbol{f}(r,\theta,z)\cdot \boldsymbol{M}^*(r,\theta) r dr d\theta = \\
&\quad \frac{1}{2\pi}\int_0^{2\pi}\int_0^{+\infty} \left\{ \int_0^{+\infty} F_M(z)\left[\lambda^2 \frac{J_{m-1}^2(\lambda r) + J_{m+1}^2(\lambda r)}{2} \right] \lambda d\lambda \right\} r dr d\theta = \\
&\quad \frac{1}{2\pi}\int_0^{2\pi} d\theta \int_0^{+\infty} r dr \int_0^{+\infty} \lambda^2 F_M(z) \frac{J_{m-1}^2(\lambda r) + J_{m+1}^2(\lambda r)}{2} \lambda d\lambda = \\
&\quad = \lambda^2 F_M(z)
\end{aligned}$$

Dividing both sides by λ^2 yields the second equation in (5.31). The third equation in (5.31), which is

$$F_N(z) = \lambda^{-2} \int_0^{2\pi}\int_0^{+\infty} \boldsymbol{f}(r,\theta,z)\cdot \boldsymbol{N}^*(r,\theta) r dr d\theta$$

can be derived in a similar way.

Appendix D. The derivation of equation (5.32)

In Chapter 5, we assumed that a unit concentrated point load is located at depth $z = s$ along the z - axis and can be expressed in the following form

$$\begin{aligned} \boldsymbol{f}_h(r,\theta,z) &= \frac{1}{2\pi r_0}\delta(r_0)\delta(z-s)\boldsymbol{i}_h \\ \boldsymbol{f}_z(r,\theta,z) &= \frac{1}{2\pi r_0}\delta(r_0)\delta(z-s)\boldsymbol{i}_z \end{aligned} \tag{5.28bis}$$

where

$$\boldsymbol{i}_h = n_r\boldsymbol{i}_r + n_\theta\boldsymbol{i}_\theta = \cos(\theta-\theta_0)\boldsymbol{i}_r - \sin(\theta-\theta_0)\boldsymbol{i}_\theta \tag{5.29bis}$$

The cylindrical coordinates (r_0, θ_0, s) represent the position of the point force. Thus from the above two equations we have

$$\begin{aligned} f_r(r,\theta,z) &= \frac{1}{2\pi r_0}\delta(r_0)\delta(z-s)n_r = \frac{1}{2\pi r_0}\delta(r_0)\delta(z-s)\cos(\theta-\theta_0) \\ f_\theta(r,\theta,z) &= \frac{1}{2\pi r_0}\delta(r_0)\delta(z-s)n_\theta = \frac{1}{2\pi r_0}\delta(r_0)\delta(z-s)\sin(\theta_0-\theta) \end{aligned} \tag{D.1}$$

For F_L

$$\begin{aligned} F_L(z) &= \int_0^{2\pi}\int_0^{+\infty} \boldsymbol{f}\cdot\boldsymbol{L}^*(r,\theta)rdrd\theta = \\ &\frac{1}{\sqrt{2\pi}}\int_0^{2\pi}\int_0^{+\infty}\frac{1}{2\pi r_0}\delta(r_0)\delta(z-s)n_zJ_m(\lambda r)e^{-im\theta}rdrd\theta = \\ &\frac{n_z}{\sqrt{2\pi}}\delta(z-s)J_m(\lambda r_0)\frac{1}{2\pi}\int_0^{2\pi}e^{-im\theta}d\theta = \frac{n_z}{\sqrt{2\pi}}\delta(z-s) \end{aligned} \tag{D.2}$$

In the above, the following equation is used

$$\int_0^{2\pi} e^{i(m-n)\theta}d\theta = 2\pi\delta_{mn}$$

And from eqn. (D.2) we have

$$F_L(s) = \frac{n_z}{\sqrt{2\pi}}$$

Starting from equation (5.31), as derived in Appendix C, we have:

$$
\begin{aligned}
&F_M(z) = \lambda^{-2}\int_0^{2\pi}\int_0^{+\infty} \boldsymbol{f}(r,\theta,z)\cdot\boldsymbol{M}^*(r,\theta)\,r\,dr\,d\theta = \\
&\lambda^{-2}\int_0^{2\pi}\int_0^{+\infty}(f_r\boldsymbol{i}_r + f_\theta\boldsymbol{i}_\theta + f_z\boldsymbol{i}_z)(\boldsymbol{i}_r\frac{\partial S^*}{\partial r} + \boldsymbol{i}_\theta\frac{\partial S^*}{r\partial\theta})\,r\,dr\,d\theta = \qquad (D.3)\\
&\lambda^{-2}\int_0^{2\pi}\int_0^{+\infty}(f_r\frac{\partial S^*}{\partial r} + f_\theta\frac{\partial S^*}{r\partial\theta})\,r\,dr\,d\theta
\end{aligned}
$$

From the definition of S* (refer to equation C.2), we have

$$
\begin{aligned}
\frac{\partial S^*}{\partial r} &= \frac{1}{\sqrt{2\pi}}e^{-im\theta}\frac{\partial J_m(\lambda r)}{\partial r} \\
\frac{\partial S^*}{r\partial\theta} &= \frac{-im}{\sqrt{2\pi}r}e^{-im\theta}J_m(\lambda r)
\end{aligned}
\qquad (D.4)
$$

Substituting the above into (D.3), we have

$$
\begin{aligned}
F_M(z) &= \lambda^{-2}\int_0^{2\pi}\int_0^{+\infty}(f_r\frac{\partial S^*}{\partial r} + f_\theta\frac{\partial S^*}{r\partial\theta})\,r\,dr\,d\theta = \\
&\frac{\lambda^{-2}}{\sqrt{2\pi}}\int_0^{2\pi}\int_0^{+\infty}(f_r e^{-im\theta}\frac{\partial J_m(\lambda r)}{\partial r} - f_\theta\frac{im}{r}e^{-im\theta}J_m(\lambda r))\,r\,dr\,d\theta = \\
&\frac{\lambda^{-2}\delta(z-s)}{2\pi\sqrt{2\pi}}\int_0^{2\pi}\int_0^{+\infty}\frac{\delta(r_0)}{r_0}n_r\frac{\partial J_m(\lambda r)}{\partial r}e^{-im\theta}\,r\,dr\,d\theta - \qquad (D.5)\\
&\quad\frac{\lambda^{-2}\delta(z-s)im}{2\pi\sqrt{2\pi}}\int_0^{2\pi}\int_0^{+\infty}\frac{\delta(r_0)}{r_0}n_\theta J_m(\lambda r)e^{-im\theta}\,dr\,d\theta
\end{aligned}
$$

(i) when $m = 1$

$$
\begin{aligned}
F_M(z) = {} & \frac{\lambda^{-2}\delta(z-s)}{2\pi\sqrt{2\pi}}\int_0^{2\pi}\int_0^{+\infty}\frac{\delta(r_0)}{r_0}n_r\frac{\partial J_1(\lambda r)}{\partial r}e^{-i\theta}rdrd\theta - \\
& \frac{\lambda^{-2}\delta(z-s)i}{2\pi\sqrt{2\pi}}\int_0^{2\pi}\int_0^{+\infty}\frac{\delta(r_0)}{r_0}n_\theta J_1(\lambda r)e^{-i\theta}drd\theta = \\
& \frac{\lambda^{-1}\delta(z-s)}{2\pi\sqrt{2\pi}}\int_0^{2\pi}\int_0^{+\infty}\frac{\delta(r_0)}{r_0}n_r J_0(\lambda r)e^{-i\theta}rdrd\theta - \\
& \frac{\lambda^{-2}\delta(z-s)}{2\pi\sqrt{2\pi}}\int_0^{2\pi}\int_0^{+\infty}\frac{\delta(r_0)}{r_0}n_r\frac{J_1(\lambda r)}{r}e^{-i\theta}rdrd\theta - \\
& \frac{\lambda^{-2}\delta(z-s)i}{2\pi\sqrt{2\pi}}\int_0^{2\pi}\int_0^{+\infty}\frac{\delta(r_0)}{r_0}n_\theta J_1(\lambda r)e^{-i\theta}drd\theta = \\
& \frac{\lambda^{-1}\delta(z-s)}{2\pi\sqrt{2\pi}}J_0(\lambda r_0)\int_0^{2\pi}e^{-i\theta}\cos(\theta_0-\theta)d\theta - \\
& \frac{\lambda^{-2}\delta(z-s)}{2\pi\sqrt{2\pi}}\frac{J_1(\lambda r_0)}{r_0}\int_0^{2\pi}e^{-i\theta}\cos(\theta_0-\theta)d\theta - \\
& \frac{\lambda^{-2}\delta(z-s)i}{2\pi\sqrt{2\pi}}\frac{J_1(\lambda r_0)}{r_0}\int_0^{2\pi}e^{-i\theta}\sin(\theta_0-\theta)d\theta
\end{aligned}
\tag{D.6}
$$

After some algebraic manipulation, we have

$$
\begin{aligned}
& \int_0^{2\pi}e^{-i\theta}\cos(\theta_0-\theta)d\theta = \pi e^{-i\theta_0} \\
& \int_0^{2\pi}e^{-i\theta}\sin(\theta_0-\theta)d\theta = \pi i e^{-i\theta_0}
\end{aligned}
$$

Substituting the above into (D.6), we finally obtain

$$
\begin{aligned}
F_M(z) = {} & \frac{\delta(z-s)}{2\sqrt{2\pi}\lambda}J_0(\lambda r_0)e^{-i\theta_0} - \frac{\delta(z-s)}{2\sqrt{2\pi}\lambda^2}\frac{J_1(\lambda r_0)}{r_0}e^{-i\theta_0} - \\
& \frac{\delta(z-s)i^2}{2\sqrt{2\pi}\lambda^2}\frac{J_1(\lambda r_0)}{r_0}e^{-i\theta_0} = \frac{\delta(z-s)}{2\sqrt{2\pi}\lambda}J_0(\lambda r_0)e^{-i\theta_0}
\end{aligned}
\tag{D.7}
$$

Since the choice of the position of the point force is arbitrary, without loss of generality, if we set $r_0 = 0$ the above expression becomes

$$F_M(s) = \frac{e^{-i\theta_0}}{2\lambda\sqrt{2\pi}} \tag{D.8}$$

(ii) when $m = -1$

$$\begin{aligned} F_M(z) = {} & \frac{\lambda^{-2}\delta(z-s)}{2\pi\sqrt{2\pi}}\int_0^{2\pi}\int_0^{+\infty}\delta(r_0)n_r\frac{\partial J_{-1}(\lambda r)}{\partial r}e^{i\theta}rdrd\theta - \\ & \frac{\lambda^{-2}\delta(z-s)i}{2\pi\sqrt{2\pi}}\int_0^{2\pi}\int_0^{+\infty}\frac{\delta(r_0)}{r_0}n_\theta J_{-1}(\lambda r)e^{i\theta}drd\theta \\ = {} & -\frac{\lambda^{-2}\delta(z-s)}{2\pi\sqrt{2\pi}}\int_0^{2\pi}\int_0^{+\infty}\delta(r_0)n_r\frac{\partial J_1(\lambda r)}{\partial r}e^{i\theta}drd\theta - \\ & \frac{\lambda^{-2}\delta(z-s)i}{2\pi\sqrt{2\pi}}\int_0^{2\pi}\int_0^{+\infty}\frac{\delta(r_0)}{r_0}n_\theta J_1(\lambda r)e^{i\theta}drd\theta \\ = {} & -\frac{\lambda^{-1}\delta(z-s)}{2\pi\sqrt{2\pi}}\int_0^{2\pi}J_0(\lambda r_0)e^{i\theta}\cos(\theta_0-\theta)d\theta + \\ & \frac{\lambda^{-2}\delta(z-s)}{2\pi\sqrt{2\pi}}\frac{J_1(\lambda r_0)}{r_0}\int_0^{2\pi}e^{i\theta}\cos(\theta_0-\theta)d\theta - \\ & \frac{\lambda^{-2}\delta(z-s)i}{2\pi\sqrt{2\pi}}\frac{J_1(\lambda r_0)}{r_0}\int_0^{2\pi}e^{i\theta}\sin(\theta_0-\theta)d\theta \end{aligned} \tag{D.9}$$

From the following relations

$$\begin{aligned} & \int_0^{2\pi}e^{i\theta}\cos(\theta_0-\theta)d\theta = \pi\exp(i\theta_0) \\ & \int_0^{2\pi}e^{i\theta}\sin(\theta_0-\theta)d\theta = -\pi i\exp(i\theta_0) \end{aligned} \tag{D.10}$$

Equation (D.9) can be written as:

$$\begin{aligned} F_M(z) &= -\frac{\delta(z-s)}{2\lambda\sqrt{2\pi}} J_0(\lambda r_0) e^{i\theta_0} + \frac{\delta(z-s)}{2\lambda^2\sqrt{2\pi}} \frac{J_1(\lambda r_0)}{r_0} e^{i\theta_0} \\ &\quad + \frac{\delta(z-s) i^2}{2\lambda^2\sqrt{2\pi}} \frac{J_1(\lambda r_0)}{r_0} e^{i\theta_0} \\ &= -\frac{\delta(z-s)}{2\lambda\sqrt{2\pi}} J_0(\lambda r_0)(n_x + i n_y) \end{aligned} \tag{D.11}$$

Without loss of generality, we set $r_0 = 0$ and the above equation becomes

$$F_M(s) = -\frac{e^{i\theta_0}}{2\lambda\sqrt{2\pi}} \tag{D.12}$$

Writing (D.8) and (D.12) in a unified form we have

$$F_M(s) = \frac{\pm e^{\mp i\theta_0}}{2\lambda\sqrt{2\pi}} \qquad m = \pm 1 \tag{D.13}$$

F_N in eqn (5.32) can be derived in similar way and the procedure is omitted here for simplicity. Finally we get equation (5.32)

$$\begin{aligned} F_L(s) &= \frac{n_z}{\sqrt{2\pi}} \\ F_M(s) &= \frac{\pm e^{\mp i\theta_0}}{2\lambda\sqrt{2\pi}} \qquad m = \pm 1 \\ F_M(s) &= \frac{-i e^{\mp i\theta_0}}{2\lambda\sqrt{2\pi}} \qquad m = \pm 1 \end{aligned} \tag{5.32bis}$$

Appendix E. The derivation of equation (5.37)

From eqn (5.28):

$$f_h(r,\theta,z)=\frac{1}{2\pi r}\delta(r)\delta(z-s)\boldsymbol{i}_h$$
$$f_z(r,\theta,z)=\frac{1}{2\pi r}\delta(r)\delta(z-s)\boldsymbol{i}_z$$

And eqn (5.29):

$$\boldsymbol{i}_h=n_r\boldsymbol{i}_r+n_\theta\boldsymbol{i}_\theta=\cos(\theta-\theta_0)\boldsymbol{i}_r-\sin(\theta-\theta_0)\boldsymbol{i}_\theta$$

we have:

$$\begin{aligned}f_r(r,\theta,z)&=\frac{1}{2\pi r}\delta(r)\delta(z-s)n_r\\ f_\theta(r,\theta,z)&=\frac{1}{2\pi r}\delta(r)\delta(z-s)n_\theta\\ f_z(r,\theta,z)&=\frac{1}{2\pi r}\delta(r)\delta(z-s)\end{aligned}\qquad\text{(E-1)}$$

The stress discontinuities of $P(r,\theta)$, $Q(r,\theta)$ and $R(r,\theta)$ are expressed by eqn. (5.34)

$$P(r,\theta)=\sum_{m=-\infty}^{\infty}P_m(r)e^{im\theta}$$
$$Q(r,\theta)=\sum_{m=-\infty}^{\infty}Q_m(r)e^{im\theta}$$
$$R(r,\theta)=\sum_{m=-\infty}^{\infty}R_m(r)e^{im\theta}$$

For $m=+1$

$$\begin{aligned}P_{+1}(r)&=\frac{1}{2\pi}\int_0^{2\pi}P_re^{-i\theta}d\theta=\frac{1}{2\pi}\int_0^{2\pi}f_re^{-i\theta}d\theta\\ &=\frac{1}{4\pi^2}\frac{\delta(r)}{r}\delta(z-s)\int_0^{2\pi}e^{-i\theta}\cos(\theta-\theta_0)d\theta\end{aligned}\qquad\text{(E-2)}$$

Carrying out this integration:

$$\int_0^{2\pi} e^{-i\theta}\cos(\theta_0-\theta)d\theta = \int_0^{2\pi}(\cos\theta - i\sin\theta)(\cos\theta_0\cos\theta + \sin\theta_0\sin\theta)d\theta$$

$$= \int_0^{2\pi}\left[\cos^2\theta\cos\theta_0 + \cos\theta\sin\theta\sin\theta_0 - i(\sin\theta\cos\theta\cos\theta_0 + \sin^2\theta\sin\theta_0)\right]d\theta$$

$$= \pi(\cos\theta_0 - i\sin\theta_0) = \pi\exp(-i\theta_0) \tag{E-3}$$

Substituting the above into eqn. (E-2), we have

$$P_{+1}(r) = e^{-i\theta_0}\frac{\delta(r)}{4\pi r} \tag{E-4}$$

For m=-*1*

$$\begin{aligned} P_{-1}(r) &= \frac{1}{2\pi}\int_0^{2\pi} P_r e^{i\theta}d\theta = \frac{1}{2\pi}\int_0^{2\pi} f_r e^{i\theta}d\theta \\ &= \frac{1}{4\pi^2}\frac{\delta(r)}{r}\delta(z-s)\int_0^{2\pi} e^{i\theta}\cos(\theta-\theta_0)d\theta \\ &= \frac{1}{4\pi^2}\frac{\delta(r)}{r}\pi(\cos\theta_0 + i\sin\theta_0) \\ &= e^{i\theta_0}\frac{\delta(r)}{4\pi r} \end{aligned} \tag{E-5}$$

For $m \neq \pm 1$, by manipulation of trigonometric functions we can easily obtain

$$P_m(r) = 0 \tag{E-6}$$

Writing eqn. (E-4), (E-5) and (E-6) in a unified form, we have

$$P_{\pm 1}(r) = e^{\mp i\theta_0}\frac{\delta(r)}{4\pi r}, \qquad P_m(r) = 0 \quad for \quad m \neq \pm 1$$

$Q_m(r)$ and $R_m(r)$ can be derived in a similar way and written as follows

$$Q_{\pm 1}(r) = \pm i\, e^{\mp i\theta_0}\frac{\delta(r)}{4\pi r}, \qquad Q_m(r) = 0 \quad for \quad m \neq \pm 1$$

$$R_0(r) = \frac{\delta(r)}{2\pi r}, \qquad R_m(r) = 0 \quad for \quad m \neq 0$$

Thus, equation (5.37) is derived.

Appendix F.

The elements of the solution matrix [Z(z)] in eqn. (5.23)

Here, [Z(z)] is the type I solution matrix (see eqn. (5.23)), which is 4×4 in size. Suppose that x_1 and x_2 are the two roots of the characteristic equation as shown below

$$(C_{44}x^2 - C_{11})(C_{33}x^2 - C_{44}) + (C_{13} + C_{44})^2 x^2 = 0 \tag{F.1}$$

Depending on whether x_1 and x_2 have the same value or not, the elements of the solution matrix [Z(z)] are expressed in two separate forms.

Case 1: when $x_1 \neq x_2$

$$\begin{aligned}
Z_{11} &= c(x_1)\exp(\lambda x_1 z) \\
Z_{21} &= d(x_1)\exp(\lambda x_1 z) \\
Z_{31} &= \exp(\lambda x_1 z)/x_1 \\
Z_{41} &= \exp(\lambda x_1 z) \\
Z_{12} &= c(x_1)\exp(-\lambda x_1 z) \\
Z_{22} &= -d(x_1)\exp(-\lambda x_1 z) \\
Z_{32} &= -\exp(-\lambda x_1 z)/x_1 \\
Z_{42} &= \exp(-\lambda x_1 z)
\end{aligned} \tag{F.2}$$

Where

$$\begin{aligned}
c(x) &= (C_{11} + C_{13}x^2)/\left[(C_{11}C_{33} - C_{13}^2)x^2\right] \\
d(x) &= (C_{13} + C_{33}x^2)/\left[(C_{11}C_{33} - C_{13}^2)x\right]
\end{aligned} \tag{F.3}$$

Equation (F.2) only lists the first two columns of the solution matrix [*Z(z)*]. The last two columns, Z_{i3} and Z_{i4} can be obtained by simply replacing x_1 by x_2, in Z_{i1} and Z_{i2} respectively.

Case 2: when $x_1 = x_2$

In this case, the first and second columns (Z_{i1} and Z_{i2}) are the same as those in Case 1, and

$$\begin{aligned}
Z_{13} &= [c'(x_1)/\lambda + c(x_1)z]\exp(\lambda x_1 z) \\
Z_{23} &= [d'(x_1)/\lambda + d(x_1)z]\exp(\lambda x_1 z) \\
Z_{33} &= [-1/(\lambda x_1^2) + z/x_1]\exp(\lambda x_1 z) \\
Z_{43} &= z\exp(\lambda x_1 z) \\
Z_{14} &= [-c'(x_1)/\lambda + c(x_1)z]\exp(-\lambda x_1 z) \\
Z_{24} &= [d'(x_1)/\lambda - d(x_1)z]\exp(-\lambda x_1 z) \\
Z_{34} &= -[1/(\lambda x_1^2) + z/x_1]\exp(-\lambda x_1 z)/x_1 \\
Z_{44} &= z\exp(-\lambda x_1 z)
\end{aligned} \tag{F.4}$$

where

$$\begin{aligned}
c'(x) &= dc(x)/dx = -\frac{2(C_{13}+C_{44})C_{33}x}{C_{44}(C_{13}+C_{33}x^2)^2} \\
d'(x) &= dd(x)/dx = \frac{-C_{13}+C_{33}x^2}{(C_{11}C_{33}-C_{13}^2)x^2}
\end{aligned} \tag{F.5}$$

Appendix G

The elements of the layer matrix $\lfloor A_k^I \rfloor$ in eqn. (5.26)

The propagator matrix $\lfloor A_k^I \rfloor$ in eqn. (5.26) is a 4×4 matrix:

$$\left[A_k^I\right] = \begin{bmatrix} a_{11} & a_{12} & a_{13} & a_{14} \\ a_{21} & a_{22} & a_{23} & a_{24} \\ a_{31} & a_{32} & a_{33} & a_{34} \\ a_{41} & a_{42} & a_{43} & a_{44} \end{bmatrix} \tag{G.1}$$

The elements of $\lfloor A_k^I \rfloor$ are also dependant on two cases of the characteristic roots (x_1 and x_2) as described in Appendix F.

Case 1: when $x_1 \neq x_2$

$$\begin{aligned}
a_{11} &= \sum_{i=1}^{2} \frac{f(x_i)c(x_i)}{x_i} \cosh y_i \\
a_{21} &= -\sum_{i=1}^{2} \frac{f(x_i)d(x_i)}{x_i} \sinh y_i \\
a_{31} &= -\sum_{i=1}^{2} \frac{f(x_i)}{x_i^2} \sinh y_i \\
a_{41} &= \sum_{i=1}^{2} \frac{f(x_i)}{x_i} \cosh y_i \\
a_{12} &= \sum_{i=1}^{2} f(x_i)c(x_i) \sinh y_i \\
a_{22} &= -\sum_{i=1}^{2} f(x_i)d(x_i) \cosh y_i \\
a_{32} &= -a_{41} \\
a_{42} &= \sum_{i=1}^{2} f(x_i) \sinh y_i
\end{aligned} \tag{G.2}$$

$$a_{13} = -\sum_{i=1}^{2} f(x_i) c^2(x_i) \sinh y_i$$

$$a_{23} = \sum_{i=1}^{2} f(x_i) c(x_i) d(x_i) \cosh y_i$$

$$a_{33} = a_{11}$$

$$a_{43} = -a_{12}$$

$$a_{14} = -a_{23}$$

$$a_{24} = \sum_{i=1}^{2} f(x_i) d^2(x_i) \sinh y_i$$

$$a_{34} = -a_{21}$$

$$a_{44} = a_{22}$$

where

$$y_i = \lambda x_i h \qquad i = 1, 2$$
$$f(x) = \frac{x}{c(x) - x d(x)} \tag{G.3}$$

In the above, c(x) and d(x) are the same expressions as those given in Appendix F.

Case 2: when $x_1 = x_2$

For simplicity, the propagator matrix $\lfloor A_k^I \rfloor$ in this case can be expressed in the form

$$\left[A_k^I\right] = -\frac{x_1}{c'(x_1)}\left[B_k^I\right] = -\frac{x_1}{c'(x_1)}\begin{bmatrix} b_{11} & b_{12} & b_{13} & b_{14} \\ b_{21} & b_{22} & b_{23} & b_{24} \\ b_{31} & b_{32} & b_{33} & b_{34} \\ b_{41} & b_{42} & b_{43} & b_{44} \end{bmatrix} \tag{G.4}$$

The elements of the matrix $\lfloor B_k^I \rfloor$ are:

$$
\begin{aligned}
b_{11} &= -\frac{c'(x_1)}{x_1}\cosh y_1 - \frac{\lambda h c(x_1)}{x_1}\sinh y_1 \\
b_{21} &= \frac{d'(x_1)}{x_1}\sinh y_1 + \frac{\lambda h d(x_1)}{x_1}\cosh y_1 \\
b_{31} &= -\frac{1}{x_1^3}\sinh y_1 + \lambda h \frac{1}{x_1^2}\cosh y_1 \\
b_{41} &= -\frac{\lambda h}{x_1}\sinh y_1 \\
b_{12} &= -\left[\frac{c(x_1)}{x_1} + c'(x_1)\right]\sinh y_1 - \lambda h c(x_1)\cosh y_1 \\
b_{22} &= \left[\frac{d(x_1)}{x_1} + d'(x_1)\right]\cosh y_1 + \lambda h d(x_1)\sinh y_1 \\
b_{32} &= -b_{41} \\
b_{42} &= -\frac{1}{x_1}\sinh y_1 - \lambda h \cosh y_1
\end{aligned}
\tag{G.5}
$$

$$
\begin{aligned}
b_{13} &= c(x_1)\left[\frac{c(x_1)}{x_1} + 2c'(x_1)\right]\sinh y_1 + \lambda h c^2(x_1)\cosh y_1 \\
b_{23} &= -\lambda h c(x_1) d(x_1)\sinh y_1 \\
b_{33} &= b_{11}\ , \quad b_{43} = -b_{12}\ , \quad b_{14} = -b_{23} \\
b_{24} &= -d(x_1)\left[\frac{d(x_1)}{x_1} + 2d'(x_1)\right]\sinh y_1 - \lambda h d^2(x_1)\cosh y_1 \\
b_{34} &= -b_{21}\ , \quad b_{44} = b_{22}
\end{aligned}
$$

where y_1 is defined in (C.3). The functions $c(x)$, $d(x)$, $c'(x)$ and $d'(x)$ are defined in Appendix F. In particular, for the isotropic elastic case, we have

$$
\begin{aligned}
x_1 &= 1 \\
y_1 &= \lambda h \\
c(x_1) &= d(x_1) = \frac{1+\nu}{E} \\
c'(x_1) &= -\frac{2(1+\nu)(1-\nu)}{E} \\
d'(x_1) &= \frac{(1+\nu)(1-2\nu)}{E}
\end{aligned}
\tag{G.6}
$$

Appendix H. The expansion coefficients of the Green's functions for the full space

In this section, the expansion coefficients for the displacements and tractions for transversely isotropic material are listed. The form of formulations depends on the two cases of roots of the characteristic equation as shown in the Appendix F, that is, (1) Case 1, when $x_1 \neq x_2$, and (2) Case 2, when $x_1 = x_2$. In each case, we should also distinguish two different subcases of m = 0 and m = ± 1.

H1. Case 1, when $x_1 \neq x_2$

H1.1. when m = ± 1

$$
\begin{aligned}
U_N(z) &= -\frac{1}{2\bar{s}}\exp(-\lambda s d_1)\frac{\Delta T_N}{\lambda} \\
\frac{T_N(z)}{\lambda} &= -sign(z-h)\frac{1}{2}\exp(-\lambda s d_1)\frac{\Delta T_N}{\lambda} \\
U_L(z) &= sign(z-h)\frac{c(x_1)c(x_2)\exp(-\lambda x_1 d_1)}{2[c(x_1)-c(x_2)]}\Delta T_M \\
&\quad - sign(z-h)\frac{c(x_1)c(x_2)\exp(-\lambda x_2 d_1)}{2[c(x_1)-c(x_2)]}\Delta T_M \\
\lambda U_M(z) &= \frac{c(x_2)d(x_1)\exp(-\lambda x_1 d_1)}{2[c(x_1)-c(x_2)]}\Delta T_M \\
&\quad - \frac{c(x_1)d(x_2)\exp(-\lambda x_2 d_1)}{2[c(x_1)-c(x_2)]}\Delta T_M
\end{aligned}
\qquad \text{(H.1)}
$$

$$
\begin{aligned}
\frac{T_L(z)}{\lambda} &= \frac{c(x_2)\exp(-\lambda x_1 d_1)}{2x_1\left[c(x_1)-c(x_2)\right]}\Delta T_M \\
&\quad - \frac{c(x_1)\exp(-\lambda x_2 d_1)}{2x_2\left[c(x_1)-c(x_2)\right]}\Delta T_M \\
T_M(z) &= sign(z-h)\frac{c(x_2)\exp(-\lambda x_1 d_1)}{2\left[c(x_1)-c(x_2)\right]}\Delta T_M \\
&\quad - sign(z-h)\frac{c(x_1)\exp(-\lambda x_2 d_1)}{2\left[c(x_1)-c(x_2)\right]}\Delta T_M
\end{aligned}
$$

where

$$
d_1 = |z-h|
$$

The functions *c(x)* and *d(x)* are defined in Appendix F. $\bar{s}$ is a constant relating to the material elastic coefficients (see equation 5.21 in Chapter 5). $\triangle T_L$, $\triangle T_M$ and $\triangle T_N$ are discontinuity for the expansion coefficients of the traction vector caused by the point force vector (see equation 5.42).

H1.2. when m = 0

$$
\begin{aligned}
U_N(z) &= 0 \\
\frac{T_N(z)}{\lambda} &= 0 \\
U_L(z) &= \frac{x_1 c^2(x_1)\exp(-\lambda x_1 d_1)}{2\left[c(x_2)-c(x_1)\right]}\frac{\Delta T_L}{\lambda} \\
&\quad - \frac{x_2 c^2(x_2)\exp(-\lambda x_2 d_1)}{2\left[c(x_2)-c(x_1)\right]}\frac{\Delta T_L}{\lambda} \\
\lambda U_M(z) &= sign(z-h)\frac{x_1 c(x_1) d(x_1)\exp(-\lambda x_1 d_1)}{2\left[c(x_2)-c(x_1)\right]}\frac{\Delta T_L}{\lambda} \\
&\quad - sign(z-h)\frac{x_2 c(x_2) d(x_2)\exp(-\lambda x_2 d_1)}{2\left[c(x_2)-c(x_1)\right]}\frac{\Delta T_L}{\lambda}
\end{aligned}
\tag{H.2}
$$